Role of the chemical properties and the chemical transformations of organic matter with increasing thermal maturity on the development of the porosity of organic-rich shales

Amélie Cavelan

UNIVERSITÉ D'ORLÉANS

ÉCOLE DOCTORALE ENERGIE, MATERIAUX, SCIENCES DE LA TERRE ET DE L'UNIVERS

Institut des Sciences de la Terre d'Orléans

THÈSE présentée par :

Amélie CAVELAN

Soutenue le : **04 novembre 2019**

pour obtenir le grade de : **Docteur de l'Université d'Orléans**

Discipline/ Spécialité: Sciences de la Terre

Doctoral thesis in Geosciences

Role of the chemical properties and the chemical transformations of organic matter with increasing thermal maturity on the development of the porosity of organic-rich shales

THÈSE dirigée par/Supervised by:
Mohammed BOUSSAFIR, Senior Lecturer, University of Orléans

RAPPORTEURS/Reviewers:
François BAUDIN, Professor, Sorbonne University
Raymond MICHELS Researcher, CNRS, UMR Géoressources, University of Lorraine

Président du Jury/ Jury President:
Mikael MOTELICA-HEINO Professor, University of Orléans,

JURY:
François BAUDIN, Professor, Sorbonne University, Reviewer
Mohammed BOUSSAFIR, Senior Lecturer, University of Orléans, Supervisor
François GELIN Research Engineer / Project Manager, Total, Guest scientist
Isabelle KOWALEWSKI Research Engineer/Project Manager, IFPEN, Examiner
Fatima LAGGOUN-DEFARGE Research Director, CNRS, UMR ISTO, Examiner
Raymond MICHELS Researcher, CNRS, UMR Géoressources, University of Lorraine, Reviewer
Mikael MOTELICA-HEINO Professor, University of Orléans, Examiner and jury president

Role of the chemical properties and the chemical transformations of organic matter with increasing thermal maturity on the development of the porosity of organic-rich shale

Remerciements

Trois années de thèse, mais déjà 8 années passées à Orléans et tant de personnes à remercier…

Je souhaite commencer par mon encadrant, Mohammed Boussafir. Je te remercie pour avoir toujours été à mon écoute durant ces trois ans et m'avoir fait confiance. Merci d'avoir proposé ce sujet aussi intéressant, merci pour ta patience, ton enthousiasme constant pour ce projet et merci pour tous les conseils prodigués au cours de ces années. Je tiens également à remercier Claude Le Milbeau pour son aide précieuse. Un grand merci pour ta disponibilité et ta gentillesse quelles que soient les circonstances. Un grand merci également à Fatima Laggoun pour tous échanges et les précieux conseils prodigués durant ces trois ans.

Je tiens à remercier François Baudin et Raymond Michels pour avoir accepté d'être rapporteur sur mon travail. Merci également à Isabelle Kowalewski et Mikael Motelica-Heino pour avoir accepté d'examiner mon manuscrit. A tous, un grand merci pour tous ces échanges le jour de la soutenance et tous vos conseils.

Je tiens à remercier tout particulièrement François Gelin pour nous avoir permis d'obtenir ce précieux échantillon qui nous manquait tant. Merci d'avoir accepté de prendre part à mon jury de thèse et bien sûr, un grand merci pour tous tes conseils.

Je voudrais remercier chaleureusement toutes les personnes que j'ai rencontrées et avec qui j'ai passé de précieux instants. Je remercie notamment mes collègues de l'ICMN Sandrine Delpeux et Nathalie Mathieu avec qui j'ai passé de bons moments. Merci pour votre patience et votre aide, surtout durant cette dernière année. Merci pour le grand enthousiasme dont vous avez fait preuve pour ce projet et votre précieuse collaboration. Un grand merci à Olivier Rozenbaum du CEMTHI pour tous les conseils et l'aide apportée depuis mon stage de master. Merci pour ta disponibilité depuis plus de trois ans maintenant. Je souhaite également remercier Audrey Sauldubois pour les tous les conseils et l'aide apportée pour la préparation et les séances MET. Merci pour ta gentillesse !

Bien sûr, un grand merci à l'ensemble du personnel de l'ISTO et de l'OSUC pour leur disponibilité, leur gentillesse et leur amitié. Cela fait maintenant huit ans que je côtoie beaucoup d'entre vous. Merci notamment à tous ceux qui furent mes enseignants, et qui en me transmettant leur passion et leur soutien, m'ont permis d'arriver jusqu'à ce Doctorat.

Je tiens à remercier Rémi Champallier pour tout l'aide qu'il m'a apporté pour la mise en place des expériences de maturation. Merci à toi ainsi qu'à tous les collègues de l'atelier pour avoir été à l'écoute et disponible pour résoudre les divers petits soucis techniques rencontrés au cours de ces années. Je voudrais remercier chaleureusement Marielle Hatton et Rachel Boscardin non seulement pour leur aide au laboratoire mais aussi pour leur jovialité et leur bonne humeur. Je remercie également Nathalie Lottier pour son aide pour les analyses d'adsorption. Merci également à Ida Di Carlo, Patricia Benoist et Sylvain Janiec pour l'aide apportée lors des séances MEB, merci aussi à Fabrice Muller et à Philippe Penhoud pour les conseils et leur aide pour les analyses DRX. Et enfin un grand merci à Benjamin Moris-Muttoni pour le coup de main apporté lors des séances RAMAN.

Je tiens à remercier particulièrement mes voisins et voisines de bureau et toute la fine l'équipe présente lors de nos rendez-vous jeux de société hebdomadaires ! En particulier, un grand merci à Elodie Da Silva Machado, Clara Jodry et Bryan Cochelin pour m'avoir supporté pendant tous ces moments passés ensemble. Merci pour votre soutien. Merci à tous pour ces moments de détente qui m'ont aidée à décompresser, ces fou-rires partagés, et nos longues soirées à compter les moutons (les personnes concernées se reconnaitront !). Je vous souhaite, à tous, de réussir vos projets respectifs et de garder votre joie de vivre où qu'ils vous mènent.

Je tiens enfin à remercier mes parents pour m'avoir toujours encouragé et soutenu dans la réalisation de mes projets. Merci à mon frère pour m'avoir montré la voie et conseillé au cours de ces années. J'aimerai dédier ce travail à feu mon grand-père paternel, passionné à sa manière, par les sciences de la Terre.

Table of contents

Remerciements 3

Table of contents 5

Table of abbreviations 9

Résumé étendu en français 11

Introduction 23

Publications 26

International symposiums 26

National symposiums 26

1. Scientific background 29

2. Geological settings 47

2.1. The Kimmeridge Clay formation (KCF) 47

2.1.1. Geological background 47

2.1.2. OM composition and sedimentary cyclicities in the Yorkshire 49

2.1.3. Samples description and selection 51

2.2. The Vaca Muerta Formation (VMF) 52

2.2.1. Geological background 52

2.2.2. Mineralogy, organic matter composition and maturity 54

2.2.3. OM composition and sedimentary cyclicities in the VMF 55

2.2.4. Samples description and selection 55

3. Analytical methods 59

Introduction 59

3.1. Characterization of natural and thermally matured samples 60

3.1.1. Anhydrous confined thermal maturation 60

3.1.2. X-ray diffraction (XRD) 64

3.1.3. Petrography 65

3.1.4. Organic geochemistry 68

3.1.5. Porosity measurements 71

3.2. Characterization of isolated kerogen 73

3.2.1. Raman spectroscopy 74

3.2.2. Petrography 75

3.2.3. Small-Angle -X-ray scattering (SAXS) 77

4. Organic petrography and pore structure characterization of natural low-mature and gas-mature marine mudstones: insights into porosity controls in organic-rich source rocks. 81

Abstract 81

Introduction 82

4.1. Results 83

4.1.1. Mineralogy 83

4.1.2. Organic geochemistry 85

4.1.3. Petrographic observations 89

4.1.4. Porosity and pore size distribution 98

4.2. Discussion 105

4.2.1. Organic petrography, porosity and pore size distribution 105

4.2.2. Thermal maturity involvement in OM-hosted pore genesis 109

4.2.3. Secondary OM-hosted pores vs primary organic porosity 110

4.2.4. TOC and OM composition controls on pore genesis 112

Summary and conclusions 114

5. Concomitant organic matter geochemical transformation and porosity development during confined thermal maturation: insights into the influence of organic matter composition on pores development. 117

Abstract 117

Introduction 118

5.1. Results 119

5.1.1. Mineralogy 119

5.1.2. Petrography 120

5.1.3. Bulk and molecular OM geochemical characterization 129

5.1.4. Pore volume and pore size distribution 146

5.1. Discussion 150

5.1.1. Composition, porosity and maturity of the original OM precursor 150

5.1.2. OM thermal transformations during anhydrous confined thermal maturation 152

5.1.3. Thermal maturity and OM geochemical composition as controlling factor of KCF mudstones porosity 155

Summary and conclusions 165

6. Influence of thermal maturation on the structure of the isolated OM of organic-rich mudstones 169

Abstract 169

Introduction 170

6.1. Results 171

6.1.1. Elemental composition and Raman spectroscopy 171

6.1.2. SEM and TEM residual OM texture observations 176

6.1.3. SAXS measurements 182

6.2. Discussion 185

6.2.1. Assessment of thermal maturity and OM structure evolution during thermal maturation using Raman spectroscopy 185

6.2.2. Concomitant evolution of the texture, the structure and porosity of KCF isolated OM with increasing thermal maturity 187

Summary and conclusions 192

7. Does the duration of the confined thermal maturation experiments influence the evolution of the porosity of organic-rich source rocks? 195

Abstract 195

Introduction 196

7.1. Results 197

7.1.1. Evolution of bulk and molecular OM geochemical composition during 104 days of thermal maturation 197

5.1.2. Evolution of pore volume and surface area during 104 days of maturation and comparison with shorter duration experiments. 210

5.2. Discussion 217

5.2.1. How useful is it to combine different models for nitrogen adsorption measurements? 217

5.2.2. Effect of the duration of confined thermal maturation on OM thermal degradation 218

5.2.3. Does the duration of confined thermal maturation affect the evolution of porosity? 220

Summary and general discussion 227

Conclusions 235

References 239

Table of abbreviations

VMF: Vaca Muerta Formation

KCF: Kimmeridge Clay Formation

OM: Organic Matter

AOM: amorphous organic matter

TOC: Total Organic Carbon

HC: hydrocarbons

ARO: aromatic hydrocarbons

POL: polar hydrocarbons

SAT: saturated hydrocarbons

Phe: phenanthrene

DBT: dibenzothiophene

Flu: fluoranthene

Pyr: pyrene

Biph: biphenyle

Naph: naphthalene

PSD: pore size distribution

MPI: mercury intrusion porosimetry

SAXS: small angle X-ray scattering

Rc: mean calculated vitrinite reflectance (%)

Rm: mean measured vitrinite reflectance (%)

Rr: mean equivalent vitrinite reflectance calculated by Raman spectroscopy (%)

Résumé étendu en français

En réponse à la demande croissante d'énergie, l'exploration et l'exploitation des réservoirs non conventionnels ont fait l'objet d'une attention toute particulière. En réponse à l'amélioration significative des rendements issus des techniques d'extraction, l'importance économique de ces formations n'a fait que croître ces deux dernières décennies. En 2016, la production de gaz de schiste aux États-Unis a même dépassé la production de gaz issue des réservoirs conventionnels. Les formations argileuses peuvent jouer un rôle important dans ces systèmes pétroliers en agissant, à la fois comme roches mères dans les systèmes classiques, mais aussi comme réservoir dans les systèmes non conventionnels. Souvent peu perméables, ces formations contiennent parfois d'importantes quantités de matière organique (MO) et peuvent présenter une porosité relativement importante (jusqu'à ≈10%). Ces caractéristiques très singulières peuvent permettre à des quantités significatives d'hydrocarbures, liquides ou gazeux, formées par le craquage thermique de la MO d'être piégées et de s'accumuler au sein de la porosité au cours de l'enfouissement de ces formations dans les bassins sédimentaires. La capacité de stockage, les voies par lesquelles les hydrocarbures peuvent s'écouler ainsi que les techniques d'extraction dépendent alors étroitement de la porosité et de la perméabilité de ces couches argileuses riches en MO. C'est pourquoi l'identification des facteurs influençant le développement et l'évolution de la porosité de ces argilites pétroligènes est devenue un axe de recherche majeur au cours de la dernière décennie.

Bien que ces réservoirs non conventionnels soient étudiés depuis de nombreuses années, les processus à l'origine de la formation et l'évolution de leur porosité restent, dans l'ensemble, assez mal compris. La difficulté réside notamment dans la caractérisation du réseau poral de ces roches, dont le diamètre des pores varie souvent de l'ordre du nanomètre à la dizaine de micromètres (Chalmers and Bustin, 2008; Ross and Bustin, 2009; Loucks et al., 2012) et dont le développement dépend de nombreux paramètres géologiques (composition minéralogique, distribution, teneur, composition et maturité thermique de la MO…). La porosité associée à la MO a fait l'objet d'une attention croissante ces dernières années. Prédominante dans de nombreux réservoirs, cette porosité hébergée au sein même de la MO semble contribuer fortement à la surface spécifique et donc à la capacité de ces formations à stocker des hydrocarbures (Chalmers et al., 2012; Loucks et al., 2012; Bernard et al., 2012b; Curtis et al., 2012; Fishman et al., 2012; Hackley and Cardott, 2016; Hackley, 2017; Ko et al., 2018; Katz

and Arango, 2018). Cependant, de nombreuses inconnues demeurent quant aux facteurs à l'origine de ce réseau poral.

La littérature de ces dernières années montre que les processus de maturation thermique de la MO au cours de l'enfouissement et la production des hydrocarbures qui en découle peuvent influencer le développement des pores au sein de la MO (Chalmers and Bustin, 2008; Bernard et al., 2012a; Loucks et al., 2012; Bernard et al., 2012b; Curtis et al., 2012; Chen and Xiao, 2014; Ko et al., 2016; Hackley, 2017; Katz and Arango, 2018). Ce processus est d'ailleurs largement considéré par ces auteurs comme le principal facteur contrôlant le développement de la porosité des argilites pétroligènes. Bien qu'on considère souvent que la porosité diminue avec l'enfouissement en raison des réarrangements structuraux qui se produisent sous l'effet de la compaction et de l'occlusion possible de certains pores par des bitumes emprisonnés (Loucks et al., 2009), la porosité de la MO augmente généralement avec la profondeur (Bernard et al., 2012a; Curtis et al., 2012; Chen and Xiao, 2014; Ko et al., 2016; Han et al., 2017; Ko et al., 2018). L'effet de la maturation thermique sur la porosité n'est néanmoins pas très clair et de nombreuses contradictions existent entre les différents modèles présentés par la littérature (Katz and Arango, 2018). Ces divergences concernent aussi bien l'endroit où se forment ces pores (kérogène, bitume résiduel…) le moment où ils se forment (production des huiles, des gaz ?) que les processus à l'origine de leur développement. Ces contradictions s'expliquent notamment par le fait que la taille, la forme et la quantité de pores observés dans les particules organiques peuvent fortement varier d'une formation à l'autre (Katz and Arango, 2018). De plus, la porosité observée au sein d'une même formation pour un même degré de maturité thermique présente parfois, elle aussi, des variations significatives (Curtis et al., 2012; Milliken et al., 2013; Löhr et al., 2015). Cela indique que d'autres facteurs que la maturation thermique de la MO sont en jeu. Certains travaux suggèrent notamment que la teneur, et surtout, la composition de la MO puissent influencer localement, et de manière significative, le développement de la porosité (Loucks et al., 2012; Curtis et al., 2012; Fishman et al., 2012; Milliken et al., 2013; Löhr et al., 2015; Ko et al., 2018). Ces processus pourraient être à l'origine des variations de porosité parfois observées entre des échantillons durant la maturation thermique. Néanmoins, isoler l'influence de ce facteur sur la porosité s'avère être un exercice complexe si bien que de nombreuses zones d'ombre persistent encore aujourd'hui (Katz and Arango, 2018). L'influence relative de la teneur en MO, et plus particulièrement l'effet de la composition et de la dégradation thermique de la MO sur le développement de la porosité de ces argilites pétroligènes doivent être clarifiés.

Cette thèse s'est donc intéressée à l'influence que peut avoir les processus de dégradation thermique, la composition géochimique globale et la composition moléculaire de la MO sur le développement et l'évolution de la porosité d'argilites pétroligènes riches en MO au cours de l'enfouissement. Afin de déterminer le plus précisément possible l'évolution de la structure globale, de la composition de la MO et de la porosité de ces roches mères pendant la maturation thermique, ce travail se base sur les connaissances établies par la littérature de ces deux dernières décennies (synthétisées dans le premier chapitre de ce manuscrit) et sur de nouvelles données expérimentales.

La première partie de ce travail s'est attachée, tout particulièrement, à l'identification des différents facteurs influençant la nature, la structure et la distribution des pores dans des roches mères naturelles riches en MO de différents degrés de maturité thermique. Ces échantillons sont issus de la « Kimmeridge Clay Formation » (KCF) du Yorkshire (UK, immature) et du Viking graben (mer du Nord, fenêtre à huile) et de la « Vaca Muerta Formation » (VMF) d'Argentine (fenêtre à gaz). Ces deux formations contiennent toutes deux des teneurs élevées d'une même MO de type II initialement de bonne qualité pétroligène et déposée dans des environnements marins anoxiques comparables. C'est d'ailleurs pourquoi ces deux formations sont souvent considérées comme équivalentes en termes de composition de la MO et d'environnement de dépôt (Uliana et al., 1999). Cette première étude visait, en particulier, à documenter la composition organique et inorganique globale de ces argilites et à comparer la structure de leur réseau poral en fonction de la maturité thermique de la MO et la composition minéralogique. Pour cela, les compositions organique et minérale ont été caractérisées par diffraction des rayons-X (DRX), pyrolyse Rock-Eval, observations pétrographiques et étude du palynofacies. Les caractéristiques du réseau poral ont été documentées par des observations au microscope électronique à balayage (MEB), de la porosimétrie au mercure et par des analyses d'adsorption de diazote à basse pression. Sur la base de ces résultats, les relations entre la géochimie organique, la minéralogie et la porosité ont été examinées et comparées en fonction du degré de maturité. Néanmoins, les petites variations de la composition minéralogique entre les formations étudiées et la composition de la MO source, pas toujours identifiable, ont rendu difficile l'identification du rôle exacte de la composition initiale et de la maturité thermique de la MO sur la mise en place de la porosité de ces échantillons naturels. Réduire la complexité associée à ces systèmes naturels, et trouver un moyen de suivre pas à pas l'évolution de la porosité en fonction de la composition originale de la MO au cours de la maturation se sont donc avéré nécessaires pour la suite de ce travail.

Ainsi, la deuxième partie de cette thèse a consisté en la réalisation d'expériences de maturations thermiques artificielles en milieu anhydre et confiné sur six argilites immatures de la KCF. Au total, 5 degrés de maturité thermique ont été atteints allant des échantillons immatures (R_m =0.43%) jusqu'à la fenêtre à gaz sec (R_m =2.12%). L'évolution de la composition moléculaire a notamment été suivie par des analyses GC-TCD et GC/MS. L'évolution de la structure de la roche a été documentée par imagerie MEB et adsorption de diazote. Bien que la composition minéralogique des échantillons sélectionnés soit similaire, la teneur et la composition de la MO présentent des variations. Comparées aux observations réalisées sur les analogues naturels, ces expériences ont donc permis d'évaluer l'effet que peut avoir de légères variations de la composition de l'assemblage particulaire de la MO sur le développement de la porosité d'argilites pétroligènes au cours de l'enfouissement. Afin de mieux comprendre la contribution réelle de la MO sur l'évolution observée du volume poral lors de ces expériences, le résidu de MO a été isolé après maturation thermique. L'évolution de la composition, de la structure chimique et de la porosité de la MO a alors été documentée avec l'augmentation du degré de maturité à l'aide d'une combinaison de différentes techniques (analyses élémentaires, MEB, microscope électronique à transmission (MET), spectroscopie Raman, diffusion des rayons X aux petits angles).

Les résultats issus d'expériences de maturation artificielle antérieures ont montré que l'augmentation de la durée de maturation thermique et l'abaissement des températures expérimentales pouvaient avoir une influence sur le rendement, la composition et la cinétique de craquage thermique de la MO (Landais et al., 1994). Compte tenu de la forte relation qui semble exister entre la porosité des roches mères étudiées, les processus de dégradation thermique de la MO et la production des huiles et des gaz qui en découle, il nous a paru alors essentiel d'évaluer l'influence que peut avoir les couples durée-température choisis pour nos expériences de maturation sur l'évolution de la MO et la porosité qui en découle. Il s'agissait notamment de tester la représentativité des résultats obtenus lors de nos expériences en laboratoire. Dans ce but une deuxième série de maturation artificielle, plus lente (104 jours), utilisant des températures plus faibles, a finalement été mise en place sur les mêmes échantillons. Les résultats ont été comparés avec les expériences de courte durée (72 heures) précédemment réalisées.

Les expériences de maturation thermique, mises en place sur les échantillons immatures de la KCF, comparées aux analogues naturels du Viking graben (fenêtre à huile) et de la VMF (fenêtre à gaz), corroborent les hypothèses de la littérature. Ils montrent que les processus de

dégradation thermique de la MO sont effectivement responsables de changements importants de la porosité. La Fig.1 résume les principales observations faites sur les échantillons de la KCF avec l'augmentation du degré de maturité thermique. Bien que les pores soient principalement associés à la matrice minérale dans les échantillons immatures ou de faible maturité thermique, cela n'est pas vrai pour les stades de maturité plus élevée (fenêtre à gaz, Rm=1.39-2.12%), où la porosité hébergée par la MO est largement prédominante (Fig.1).

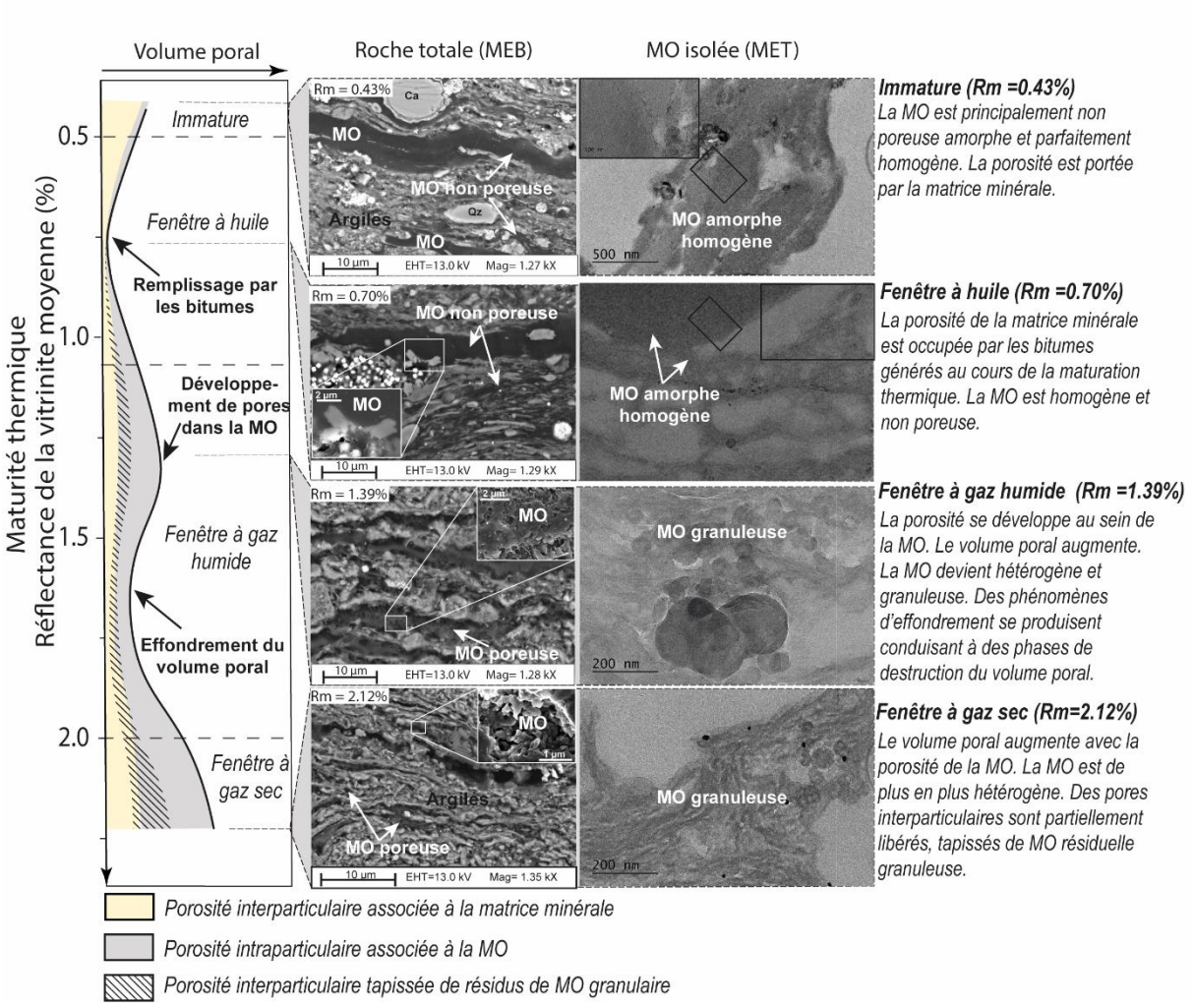

Fig.1. Résumé des principales évolutions du volume poral total (adsorption de diazote à basse pression), de la structure de la roche (images MEB en électrons rétrodiffusés) et de la structure de la matière organique isolée (MET) au cours de la maturation thermique des argilites de la KCF. MO : matière organique. Rm : réflectance de la vitrinite moyenne (%). Qz : quartz. Ca : carbonate.

Au cours de la fenêtre à huile, la migration des bitumes générés par la dégradation thermique de la MO dans la porosité interparticulaire adjacente entraîne une augmentation significative de la connectivité des composés organiques dans les échantillons et une forte diminution du volume poral associé à la matrice minérale (Fig.1). En parallèle, les variations

de la structure de la MO résiduelle à l'échelle nanoscopique et les variations de volume engendrées par la production des hydrocarbures conduisent à la formation d'un réseau de pores de plus en plus développé au sein de la MO, qui devient alors le principal contributeur de la porosité (Fig.1). Les similitudes observées entre l'évolution du volume poral des argilites totales et la porosité de la MO isolée suggèrent que l'évolution de la structure et de la composition chimique du kérogène est le principal facteur responsable du développement et de l'évolution des pores. Ce processus semble débuter dès le pic de production des huiles (Rm = 0,85%) et se poursuit jusqu'au stade de production des gaz secs (Rm= 2.12%). Nos observations au MET montrent effectivement que ces processus sont accompagnés d'un changement progressif de la structure du kérogène et des bitumes résiduels passant d'une texture parfaitement homogène avant maturation à une texture hétérogène granuleuse et poreuse jusqu'à l'échelle nanoscopique (Fig.1). Cela semble confirmer les hypothèses Keel (2015) et de Romero-Sarmiento et al. (2014) qui suggèrent que la création de pores au sein de la MO serait liée à l'organisation progressive de la structure de la MO avec l'augmentation du degré de maturité thermique. De plus, la porosité élevée mesurée sur la MO isolée du KCF (jusqu'à 20 %) indique que la MO peut effectivement contribuer de façon significative à la capacité de stockage de ces réservoirs argileux. Ainsi, en contrôlant les différentes étapes auxquelles les hydrocarbures liquides et gazeux sont produits et l'aromatisation progressive de la structure de la MO résiduelle, nos résultats confirment que les processus de dégradation thermique sont en effet le principal facteur contrôlant la porosité de ces argiles pétroligènes.

Toutefois, les différences de volume poral et de taille de pore observés entre les échantillons de la KCF au cours des expériences de maturation artificielle montrent que le simple fait de considérer le type de la MO et le degré de maturité est insuffisant pour estimer la porosité de ces formations. Si en dessous de 5.5 wt.% de teneur en carbone organique total (COT) le volume poral augmente avec le COT dans la fenêtre à gaz humide (Rm=1.39%), pour des échantillons plus riches en MO, cette relation n'est plus très nette. Si la MO apporte l'essentielle de la porosité à ce stade de maturité, cela montre que d'autres processus sont effectivement en jeu. Nos recherches révèlent que lors des expériences de maturation thermique, les échantillons riches en MO orangée pétroligène d'origine phytoplanctonique, qui apparaît sous forme de particules de bituminite larges et ductiles sur les sections de roches brutes polies, ont généré des quantités plus importantes d'hydrocarbures enrichis en composés saturés et aromatiques plus légers. Cela semble avoir conduit à une meilleure imprégnation de la matrice minérale par les bitumes formant un « réseau organique » bien interconnecté, mais

ductile (ou fragile selon le degré de maturité) (en vert, à droite, Fig.2). Avec l'augmentation du degré de maturité, la conversion plus efficace de ce « réseau organique » en hydrocarbures gazeux a permis la formation d'une porosité bien développée au sein de la MO mais plus vulnérable aux phénomènes de compaction. Cela semble avoir entrainé des effondrements plus importants du réseau poral et la destruction d'une partie des pores (Fig.2).

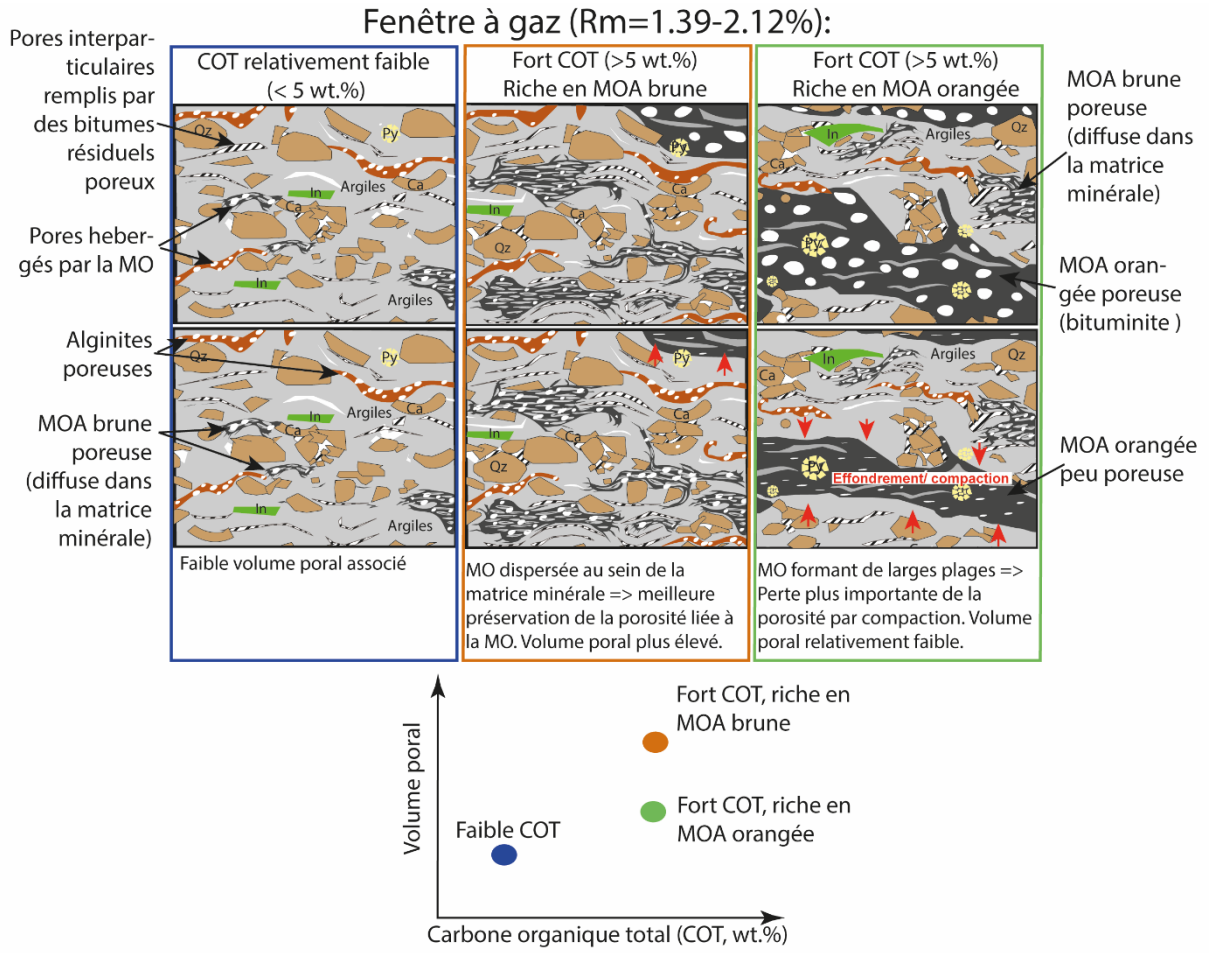

Fig.2. Principales différences observées entre les échantillons de la KCF en fonction de la composition de la MO et de la teneur en carbone organique total (COT) au cours de la fenêtre à gaz. En gris clair : minéraux argileux. In : fragments d'inertinite (restent non poreux tout au long de la maturation thermique). Py : framboïdes de pyrite.

Malgré une forte teneur en MO, ces échantillons possèdent donc un volume poral relativement faible après maturation thermique (Fig.2). Au contraire, dans les échantillons présentant une proportion plus élevée de MO brune d'origine algaire (en orange, Fig.2), la MO est dispersée au sein de la matrice minérale formant un « réseau organique » moins bien connecté mais mieux protégé par cette matrice qui l'englobe. Malgré la porosité probablement plus faible formée au sein de cette MO durant la conversion moins efficace de ces composés moins pétroligènes, cette porosité semble alors avoir été mieux préservée des phénomènes d'effondrement. Ainsi, ces

échantillons présentent systématiquement une plus grande taille de pores dans la fenêtre à gaz humide et un volume poral plus important dans la fenêtre à gaz sec (Fig.2). Contrairement à ce qui est donc généralement admis dans la littérature (Chen et al., 2015; Katz and Arango, 2018), ces résultats montrent que la capacité des argilites étudiées à préserver la porosité et donc le volume poral final diminue fortement avec l'augmentation de la quantité d'hydrocarbures gazeux générée pendant la maturation et la qualité pétroligène initiale de la MO. (Chen et al., 2015), suggèrent qu'un kérogène de type I a un potentiel environ 40 fois plus élevé pour le développement de pores qu'un kérogène de type III. Pour lui, la capacité du kérogène à développer une porosité dépend fortement de sa prédisposition à générer des huiles. Même si le volume poral qui se forme pendant la maturation dépend de la teneur en MO (qui héberge la plus grande partie de cette porosité) et de sa qualité pétroligène, nos résultats révèlent toutefois que cette relation n'est pas simple. Il est vrai que les fragments d'inertinite, ne présentent aucun développement de pore pendant la maturation thermique indiquant que les composants organiques de type III, inertes, ont, en effet, une faible capacité à développer des pores. Néanmoins, nos recherches sur un kérogène de type II indiquent que la forme et la distribution des différents macéraux ainsi que leur capacité à former un réseau de MO connecté et ductile influence fortement la capacité de la roche à préserver la porosité formée pendant la maturation des phénomènes de compaction et d'effondrement (Orange, au centre, Fig.2). Par conséquent, il n'existe aucune corrélation linéaire positive directe entre la porosité, la teneur et la qualité pétroligène de la MO pour les échantillons étudiés. Cela explique probablement la diversité des tendances observées dans ces formations argileuses où la composition de la MO est souvent hétérogène. On peut envisager que ces variations, associées à la composition initiale de la MO, peuvent localement masquer l'effet de la maturité thermique. Cela pourrait expliquer pourquoi la teneur en MO semble parfois avoir un contrôle plus important sur la porosité que le degré de maturité thermique dans certaines formations (Milliken et al., 2013; Pan et al., 2015). En outre, les relations similaires existant entre le COT et le volume poral des échantillons de la KCF maturés artificiellement (Rc=1.24%) les échantillons de la VMF naturellement matures (Rc=1.65%), et les tendances observées par Milliken et al. (2013) dans le Marcellus ou par Pan et al. (2015) dans la formation de la région du Yangtze inférieur, laissent entendre que les processus mis en évidence dans ce travail s'appliquent également aux systèmes naturels.

Les différences observées entre les échantillons apparaissent principalement liées à des phénomènes de compaction différentielle contrôlés par la composition et la distribution des macéraux dans la roche. Néanmoins, l'effet de la composition de la MO sur l'évolution de la

structure même du kérogène isolé n'a pas été documenté. Ces processus méritent donc d'être étudiés plus en profondeur. Evaluer l'effet des différences de composition de la MO sur l'évolution de la structure chimique et la porosité du kérogène à l'échelle nanoscopique pourrait, par exemple, permettre d'expliquer une partie des différences observées entre les échantillons étudiés.

Bien que la fraction organique représente souvent bien moins de 15% en poids de la roche totale, ces résultats montrent que la composition initiale de la MO et ses transformations au cours de la maturation thermique sont des facteurs cruciaux contrôlant la capacité de ces roches mères marines à développer et à préserver leur volume poral au cours de l'enfouissement. Cela semble particulièrement vrai pour ces formations très argileuses riches en MO (>50 % en poids de minéraux argileux) où la plupart des pores interparticulaires associés à cette matrice minérale, relativement ductile, sont rapidement réduits par compaction ou remplis par les bitumes générés et emprisonnés dès les premiers stades de la maturation thermique. Dans ces systèmes, les pores formés au sein de la MO au cours de la maturation thermique deviennent rapidement, les principaux contributeurs de la porosité. La teneur, la composition et la maturité thermique de la MO sont alors les principaux facteurs contrôlant les caractéristiques de ce réseau poral. Si certains pores interparticulaires présents au sein de la matrice minérale sont partiellement libérés pendant le craquage secondaire, apparaissant alors sous la forme de pores interparticulaires tapissés de MO résiduelle granulaire (Fig.1), la formation de ces pores dépend étroitement du taux de conversion de la MO, de sa composition et de son degré de maturité. Même si ces pores ne peuvent pas être considérés comme des pores hébergés par la phase organique, leur abondance et leurs caractéristiques restent étroitement liées aux propriétés même de la MO. Ces tendances pourraient, toutefois, être très différentes dans les systèmes contenant une proportion de minéraux « rigides » plus élevée (comme le quartz, les carbonates ou les feldspaths), où un plus grand volume de pores interparticulaires est associé à la matrice minérale. Dans ce cas, la contribution de la MO est probablement beaucoup plus faible et l'effet des caractéristiques de cette dernière sur la porosité moins importante. Seule l'augmentation du nombre d'expériences de maturation artificielle et un plus grand nombre de comparaison avec des roches mères de composition variable pourrait permettre de confirmer ces hypothèses et d'identifier l'amplitude de ces variations sur l'évolution globale de la porosité. Cela pourrait également contribuer à l'établissement de modèles d'évolution de la porosité plus représentatifs de la complexité des systèmes naturels. Bien qu'une simulation expérimentale parfaite des processus de maturation thermique de la MO

ne soit pas réalisable, les similitudes existant entre nos échantillons maturés artificiellement, des équivalents naturels issues de la VMF et du Viking graben et les tendances observées dans la littérature (même évolution des biomarqueurs et, de la composition moléculaire des huiles et des gaz et, des variations semblables de la porosité et de la texture de la MO au MEB…), indiquent néanmoins que nos expériences en milieu anhydre et confiné donnent des résultats relativement comparables à ceux obtenus dans les bassins sédimentaires.

Toutefois, les résultats des expériences de maturation thermique de longue durée (104 jours) suggèrent que les températures plus faibles et la durée plus longue des processus de dégradation de la MO dans les bassins sédimentaires pourraient conduire à une conversion plus progressive et plus efficace de la MO. En effet, si l'augmentation de la durée des expériences de maturation thermique n'a pas permis de modifier la quantité de bitume générée au cours de la fenêtre à huile, elle semble favoriser la dégradation des composés polaires en composés saturés et aromatiques. De plus, en limitant la rupture précoce des liaisons chimiques de faible énergie au sein de la MO, la température plus basse de ces expériences de longue durée conduit à des variations de la concentration des gaz générés et du timing auquel ils sont produits. Il est important de noter que ces processus n'influencent pas l'évolution générale du volume des pores au cours de la maturation, mais cela semble renforcer les différences entre les échantillons dont la composition de la MO diffère. On constate, par exemple, que l'augmentation de la durée des expériences de maturation provoque une baisse plus importante du volume poral des échantillons les plus riches en MO orangée d'origine phytoplanctonique au cours de la fenêtre à gaz. Cela suggère que les différences observées en fonction de la composition de la MO au cours de ces travaux pourraient être bien plus prononcées dans les bassins sédimentaires.

Enfin, l'absence totale de variation de la composition minéralogique et de la structure des minéraux argileux avec l'augmentation du degré de maturité des échantillons de la KCF montrent que nos expériences de maturation ne permettent pas de rendre compte des transformations diagénétiques que subit la phase minérale au cours de l'enfouissement. Or, les processus physiques et l'altération chimique de la phase inorganique, comme la conversion progressive des smectites en feuillets d'illite de plus en plus ordonnés ou la précipitation de ciments, influencent très probablement le développement et surtout la préservation des pores pendant la maturation (Day-Stirrat et al., 2008; Schieber, 2010). Une comparaison de ces résultats avec des équivalents naturels de minéralogie variable reste donc désormais essentielle pour mieux comprendre le rôle exact de la phase organique vis-à-vis de la phase minérale sur le développement des pores.

Introduction

Introduction

In response to the rising energy demand, the exploration and the exploitation of unconventional reservoirs receive a specific attention the past two decades. Due to the significant improvement of the recoveries from hydraulic fracturing and horizontal drilling technologies, these formations became of commercial importance. Hence, since 2016, the production of shale gas exceeds the production of conventional gas reservoirs in the United States. Mudstones can play a significant role in petroleum systems as source rocks as well as reservoirs in unconventional plays. Mudstones form generally low permeability layers which can, sometimes, host significant amount of organic matter (OM) (> 2 weight %). Contrary to conventional reservoirs, where the relatively high permeability of the formations allows the migration of most of the generated hydrocarbons to a reservoir, the low permeability of mudstones is responsible for the incomplete expulsion of hydrocarbons (oil and gas) generated during burial, which remain partly entrapped in rocks. While the permeability of these rocks is low, these mudstones can however, hosted a significant porosity (up to ≈10%). Therefore, considerable amounts of oil and gas remain entrapped in these formations which act both as source rocks and reservoir, hence their economic interest. The assessment of the oil and gas generation potential of these formations and production techniques closely depend on the porosity and the permeability of the rock. The amount and the distribution of the porosity control the amount of hydrocarbon that can be stored, the assessment of the factors influencing porosity in gas shales has thus become a major research focus the last decade.

While these unconventional reservoirs have been studied for many years, the development and the evolution of gas shale pore systems remains incompletely understood (Katz and Arango, 2018). The difficulty lies especially in the characterization of their pore network whose pore sizes can ranging over six orders of magnitude (Chalmers and Bustin, 2008) and whose development can depend on many geological parameters including, for example, mineralogy, rock framework, thermal maturity, OM content and OM composition. The porosity associated with the OM receives a growing attention these last years. Predominant in many gas shale systems studied the past ten years, this porosity appears to have a significant contribution to the specific surface area and thus to the gas storage capacity of these formations (Katz and Arango, 2018). However, numerous research questions still open about the main factors controlling the origin of this pore network. It has been well documented by the available literature that OM thermal maturation processes with burial and the resulting oil and gas

generation can influence the development of pores in OM. But this effect of maturity is no clear and many contradictions exist with regard to the place where these pores form (kerogen, bitumen) and the processes of their development. While the size, the shape and the volume of pores observed in the OM can be relatively similar with increasing burial, two formations of a same maturity and containing a similar type of OM can exhibit very different porosity suggesting that other factors than thermal maturation are at play (Fishman et al., 2012; Milliken et al., 2013). In particular, recent works suggest that the composition of the OM may have locally a significant influence on porosity (Ko et al., 2018). This process may lead to variations of the evolution of the pore volume between samples. Nevertheless, to isolate the influence of this factor on porosity turns out to be a complex exercise. The process of pores development during hydrocarbon generation, the relative influence of total organic carbon content, and more specifically the influence of the composition of the OM precursor needs to be clarified.

This project is intended to explore how the bulk and the molecular geochemical composition of the OM and its degradation processes during thermal maturation influence the development and the evolution of the porosity of organic-rich source rocks during burial. We built this work on the knowledge base established by the available literature of the past ten years (presented in the first chapter of this manuscript) and on new experimental data in order to determine as accurately as possible the evolution of the structure of the rock framework, the OM composition and porosity of source rocks with increasing maturity. The origin and the choice of the sample selected for this work and the different methods used for their characterization are presented in chapter 2 and 3 respectively.

The first part of this work aimed to better identify the different parameters influencing the nature, the structure and the distribution of pores in natural organic-rich source rocks of various thermal maturities. This chapter investigates thus 21 low-mature, 1 oil-mature and 12 gas-mature rocks presenting various OM content from the Kimmeridge Clay formation (KCF) of the Yorkshire (United kingdom), the Viking graben (North Sea) and from the Vaca Muerta Formation (VMF, Argentina) respectively. In particular, this first study aims to document the overall organic and inorganic composition of these mudstones and to compare their pore structure as a function of the OM thermal maturity and mineral composition. Hence, the OM composition was investigated using Rock-Eval, petrographic observations and palynofacies analysis; and finally, their pore structure was characterized with SEM, MIP, and low-pressure nitrogen adsorption measurements. Based on these results, the relationships between organic geochemistry, mineralogy and porosity were examined and compared as a function of thermal

maturity. However, slight variations of mineralogy exist between VMF and KCF samples and the composition of the OM precursor in thermally mature VMF samples is not identifiable. This makes it difficult to really understand the role of the original OM composition on pores development.

To reduce the complexity existing in natural mudstones, and to better follow step by step the progressive evolution of the porosity as a function of the original OM composition from the immature stage to the dry gas zone, the second part of this work (chapter 5) focuses on the confined anhydrous thermal maturation of 6 of the immature KCF mudstones. These rocks were selected for their similar mineralogy but their slightly different type II kerogen composition and total organic carbon content (TOC). Compared with the observations made on natural analogues, this chapter aims to investigate how the slight variations in the composition of the total particulate OM assemblage and maceral types influence the evolution of the size, the distribution and the abundance of pores of these organic-rich marine mudstones with increasing maturity. Then, in order to better understand the specific contribution of the OM structure on the evolution of the pore volume observed during these experiments, the residual OM was isolated by acidic treatments after laboratory thermal maturation. The evolution of the composition, the chemical structure and the porosity of kerogen from the immature stage to the dry gas zone were documented using a combination of elemental analysis, SEM, TEM imaging techniques, Raman spectroscopy and SAXS. This work is presented in chapter 6.

Previous results from artificial thermal maturation experiments showed that increasing thermal maturation duration and lowered experimental temperatures could significantly influence the yield, the composition and the timing at which bitumen and gas are generated during thermal maturation (Landais et al., 1994). In view of the strong relation existing between organic-rich source rocks porosity, OM thermal degradation processes and oil and gas generation, these differences may influence the formation of pores during maturation. The last chapter (chapter 7) aims thus to investigate the influence of the duration-temperature-pairs chosen for our laboratory thermal maturation experiments on the evolution of the OM and the porosity of the KCF source rocks with increasing maturity. In particular, this work aims to test the representativeness of the results obtained from our artificial maturation experiments. Longer duration (104 days) thermal maturations, bulk, molecular geochemical OM characterization (Rock Eval, GC-TCD, GC/MS) and nitrogen adsorption porosimetry measurements were thus applied on the same six type II KCF mudstones and the results were compared with the shorter duration experiments (72 hours).

This work has been the subject of several publications and communications in congresses under the following references:

Publications

Cavelan, A., Boussafir, M., Rozenbaum, O., & Laggoun-Défarge, F. (2019). Organic petrography and pore structure characterization of low-mature and gas-mature marine organic-rich mudstones: Insights into porosity controls in gas shale systems. Marine and Petroleum Geology, 103, 331-350.

Cavelan, A., Boussafir, M., Le Milbeau, C., Rozenbaum, O., & Laggoun-Défarge, F. (2019). Effect of organic matter composition on source rock porosity during confined anhydrous thermal maturation: Example of Kimmeridge-clay mudstones. International Journal of Coal Geology, 103236.

International symposiums

Cavelan, A., Boussafir, M., Le Milbeau, C., Delpeux, S., Rozenbaum, O., Laggoun-Défarge, F. Influence of organic matter properties of Kimmeridge clay source rocks during laboratory thermal maturation. 29th International Meeting on Organic Geochemistry (IMOG) 2019, September 1-6, Gothenburg, Sweden. Oral communication.

Cavelan, A., Boussafir, M., Le Milbeau, C., Rozenbaum, O., & Laggoun-Défarge, F. Organic Matter Influence on Porosity of Kimmeridge-Clay Source-Rocks: Insights from Organic Petrography and Laboratory Thermal Maturation. 81st EAGE Conference and Exhibition 2019, June 3-6, London, United Kingdom. Oral communication.

Cavelan, A., Boussafir, M., Rozenbaum, O., Le Milbeau, C., & Laggoun Defarge, F. Do chemical properties of organic matter affect the porosity during confined pyrolysis of organic rich shales? EGU General Assembly 2018, April 7-12, Vienna, Austria. Oral communication.

National symposiums

Cavelan, A., Boussafir, M., Rozenbaum, O., Le Milbeau, C., & Laggoun Defarge, F. Effet des propriétés chimiques de la matière organique sur la porosité d'argilites pétroligènes au cours d'une pyrolyse artificielle en milieu confiné. FROG IV, 4ème Réunion des Géochimistes Organiciens Français 2018, July 10-11, Villeurbanne, France. Oral communication.

Cavelan, A., Boussafir, M., Rozenbaum, O., Le Milbeau, C., & Laggoun Defarge, F. Impact of organic matter chemical transformations on shale porosity during the confined pyrolysis of organic rich shales: a complement to the observations of natural systems. 5th YNHM 2018, March 6-10, Paris, France. Oral communication.

Cavelan, A., Boussafir, M., Delpeux, S., Le Milbeau, C., Rozenbaum, O., & Laggoun Defarge, F. Effect of organic matter chemical properties on thermal maturation of organic rich shales: experimental approach. 26ème Réunion des Sciences de la Terre 2018, October 22-26, Lille, France. Oral communication.

Cavelan, A., Pierre, G., Boussafir, M., Delpeux, S., Le Milbeau, C., Rozenbaum, O., & Laggoun Defarge, F. Do experimental duration and temperature of confined pyrolysis experiments influence the evolution of the porosity of organic-rich shales? 26ème Réunion des Sciences de la Terre 2018, October 22-26, Lille, France. Poster.

Chapter 1: Scientific background

1. Scientific background

1.1. Organic matter in mudstones

1.1.1. Definitions

Many terms exist in the available literature to describe the different components of organic matter (OM) and shales. In order to avoid any possible confusion, it is necessary to redefine some terms that are crucial to understanding this work. The terminology ‘shale’ has been widely and too often used to designate all fine-grained sedimentary rocks. These last years, the use of ‘mudstone’ or ‘mudrock’ is thus preferred rather than the use of "shale”. Hence and according to the recommendations of (Lazar et al., 2015), the terminology ‘mudstone’ was thus adopted in the present study to refer specifically to rocks containing more than 50% of mud-size grains (<62.5 µm, clay minerals and silts).

OM is widely used to refer to any solid or liquid materials rich in organic carbon. Yet, OM includes, many components such as kerogen, bitumen, solid bitumen and pyrobitumen. Depending on the authors, the definitions of these terms vary. The definitions adopted in this work need thus to be defined. According to Tissot and Welte (1984) kerogen consists in the part of the OM preserved in sedimentary rocks which is insoluble in organic solvents. Kerogen is made up of complex polymer structures (macromolecules) derived from the early diagenesis of biological organic remains (e.g. plant tissues, microplankton, algal matter, etc.) which can be partly converted into liquid and gaseous hydrocarbons with increasing thermal maturity (depending on the thermal maturity and the original composition of kerogen). Bitumen (called ‘pre-oil bitumen’ by Curiale (1986) corresponds to the liquid, solid/viscous OM fraction which is soluble in organic solvents (Dow, 1977; Tissot and Welte, 1984). This fraction mainly derived from the thermal cracking of kerogen under immature to relatively low-mature conditions. Bitumen is hydrocarbon-rich and contain generally high amounts of N, S, O, asphaltenes and resins. The composition of bitumen is detailed in Fig. 1.1. Solid bitumen (included in pre-oil bitumen in the literature) corresponds to very viscous bitumen which is solidified in the subsurface and difficult to dissolve in organic solvents (Curiale, 1986). Pyrobitumen, often called post-oil bitumen or secondary solid bitumen (Curiale, 1986), is the solid OM residue remaining after the secondary cracking of bitumen in source rocks and reservoirs. It is insoluble in organic solvents and non-volatile (Tissot and Welte, 1984; Hunt, 1996).

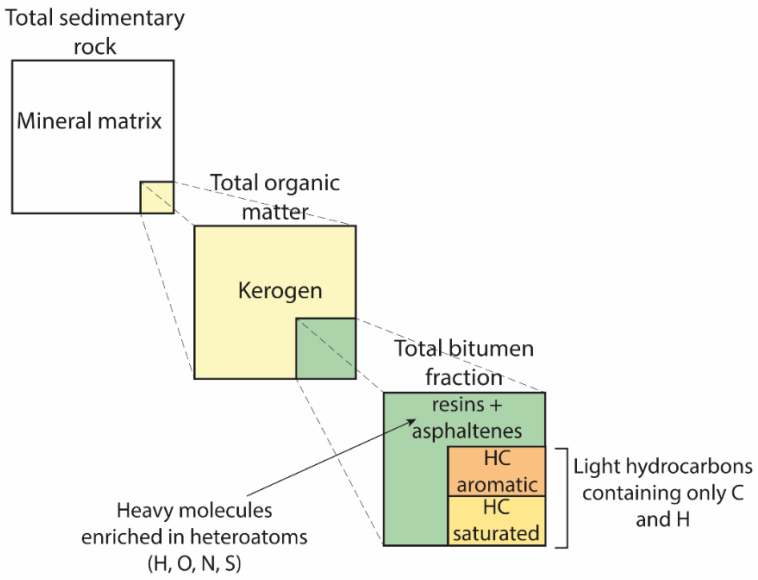

Fig. 1.1. Simplified diagram showing the different fractions of the organic matter in sedimentary rocks (modified from Tissot and Welte, 1984).

1.1.2. Accumulation and preservation of organic matter

Mudstones are often considered as 'good source rocks' when the total organic carbon content (TOC) exceeds 2 wt.% (Tissot and Welte, 1984; Jarvie et al., 2007). While mudstones are one of the most widely distributed rocks on Earth, not all mudstones are organic-rich. The preservation and the accumulation of such amount of OM required a combination of a multitude of specific conditions such as a high primary productivity leading to a higher exportation from the photic zone, an intermediate to high sedimentation rate allowing a quick burial of the OM isolating it from the oxygenated water column without diluting it, and an anoxic water-sediments interface (Killops and Killops, 2004; Dembicki, 2017).

While some macromolecules, naturally resistant to degradation are selectively preserved (such as lignin, algaenan or cutan, (Tegelaar et al., 1989), the most part of the OM (≈90%) is quickly degraded in the water column or in the water-sediments interface (Hedges and Keil, 1995; Drouin, 2007). The anoxia of the depositional environment is often considered as the main factor influencing the preservation of OM in sediments (Killops and Killops, 2004; Dembicki, 2017). The development of anoxic conditions in the water column, just above the water-sediment interface (i) limits the oxidation and the degradation of the OM by benthic grazer organisms; (ii) prevents the development of microbial activity and the reworking of the water sediment interface (Killops and Killops, 2004; Peters et al., 2007); (iii) enhances the

proliferation of sulphate-reducing bacteria favoring the incorporation of sulfur in lipidic molecules rendering them degradation-resistant (Boussafir and Lallier-Vergès, 1997). This process is called natural sulfurization. Hence, different environments can be favorable to the preservation of the OM and to the formation of good source rocks. Distal zones of deltas; early marine incursion in rift basins; environments where stratified water columns can be developed such as barred basin, epicontinental seas or anoxic lakes; open marine anoxic environments in upwelling zones are the most cited environments supposed to be favorable to the formation of source rocks (Dembicki, 2017).

1.1.3. Transformations of OM with burial

Early OM diagenesis and formation of kerogen

After deposition, the OM is mainly composed of biomolecules inherited from living organisms such as lipids, proteins or carbohydrates. During the first few hundred meters of burial, these OM components endure a strong biogeochemical degradation through an intense bacterial activity (Tissot and Welte, 1984). Firstly, the biomolecules are degraded into monomers by bacteria (Tissot and Welte, 1984). This leads to the loss of chemical functional groups and results in a depletion of N, O and to the release of CO_2, N_2, H_2S (Fig. 1.2). Biogenic methane is also generated by the intense bacterial activity. Then, the recondensation of these monomers leads to the formation of complex insoluble polymers resistant to degradation which become increasingly integrated to the sediment. These geopolymers form the kerogen.

The structure, the initial hydrogen content and thus the initial oil proneness of kerogen in mudstones strongly depend on the source of the OM. Hence, kerogen is generally classified into three types. This classification, based on H/C and O/C kerogen atomic ratios is generally plotted in a Van Krevelen diagram (Fig. 1.3, Tissot and Welte (1984). Type I kerogen is often associated to lacustrine environments. Oxygen-poor (O/C < 0.1), this type is the most hydrogen-rich type of kerogen (H/C >1.5). Composed of the accumulation of aliphatic membranes derived from some bacteria and algae (such as *Botryococcus*), this highly oil-prone kerogen type is however rare in source rocks (less than 3%). Type II kerogen contains relatively high amount of hydrogen (H/C =1-1.5) and relatively low content of oxygen (O/C =0.1-0.2). Often associated with marine environments, type II kerogen is mainly composed of phytoplanktonic materials reworked by bacterial activity and can sometimes contain a mix of spores, pollens, phytoplankton, land plant debris, bacterial, algal matter and land plant inputs. This is the major

type of kerogen in source rocks. Type III kerogen is hydrogen-poor (H/C < 1.0) and oxygen-rich (O/C >0.2). This kerogen type is mainly composed of debris derived from land plants. This type of kerogen is not sufficiently rich in hydrogen to be oil-prone but can be gas-prone.

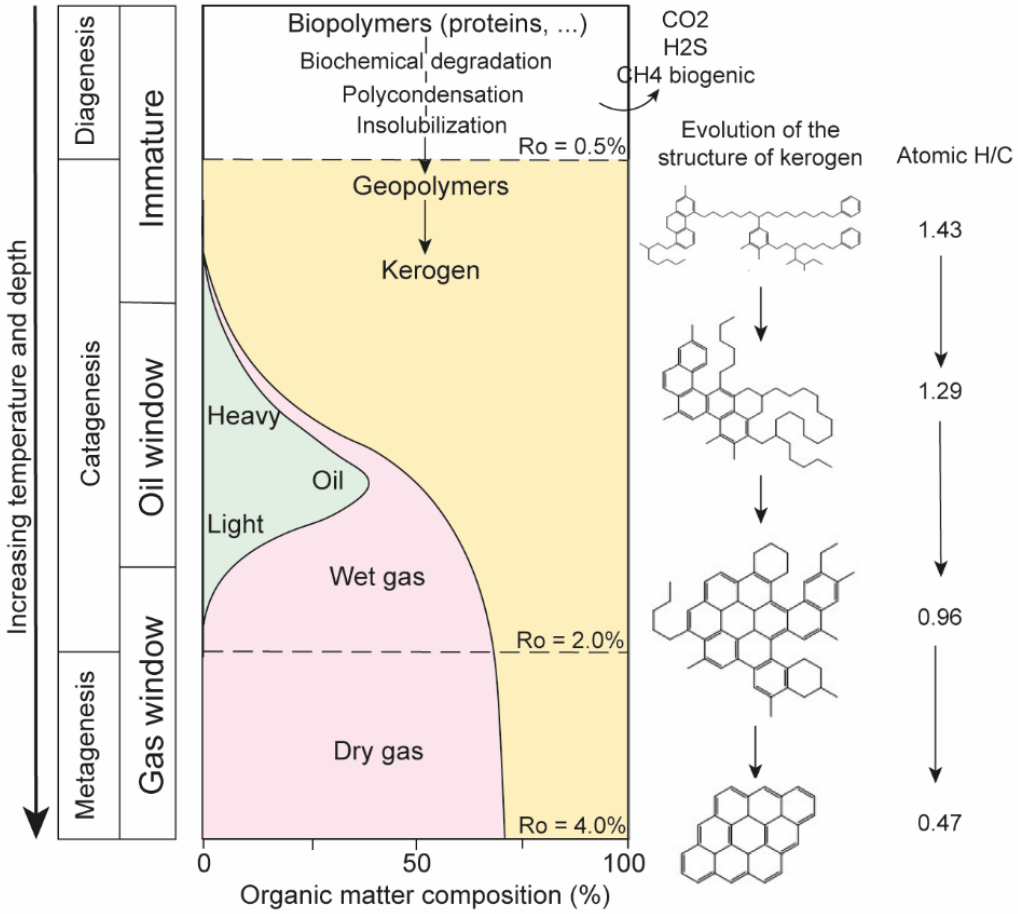

Fig. 1.2. General evolution of sedimentary OM with increasing temperature and burial (modified from Tissot and Welte, 1984; Hunt, 1996). Ro: vitrinite reflectance.

Thermal degradation of kerogen

During burial and the increase of temperature (40-50°C), the kerogen, unstable, endure many geochemical processes leading progressively to the production of oil and gas (Tissot and Welte, 1984; Behar and Vandenbroucke, 1987; Hunt, 1996). Firstly, (between 40-80°C) the rupture of the C-O chemical bonds existing between kerogen macromolecules lead to a strong depletion of kerogen in oxygen and to the released of CO_2, H_2O and viscous heavy molecules enriched in heteroatoms (N, S, O). These polar components, called resins and asphaltenes, are soluble in organic solvents and took part of bitumen. At temperatures ranging from 100 to 140°C, the catagenesis begins (Fig. 1.2). The thermal cracking of C-C bonds in kerogen, resins and asphaltenes, results in the production of heavy liquid hydrocarbons (15 to 40 C number)

which became increasingly lighter with increasing depth and temperature (oil). The thermal degradation of these newly formed hydrocarbons leads also to the production of lighter aliphatic components, conducing to the progressive increase of the relative proportion of saturated hydrocarbon in the bitumen fraction. These processes result in the progressive depletion of hydrogen (decrease of H/C), the densification and the aromatization of kerogen (Fig. 1.2, 1.3, Tissot and Welte, 1984; Behar and Vandenbroucke, 1987; Hunt, 1996). Except small methyl groups, most of the kerogen is composed of a condensed aromatic structure.

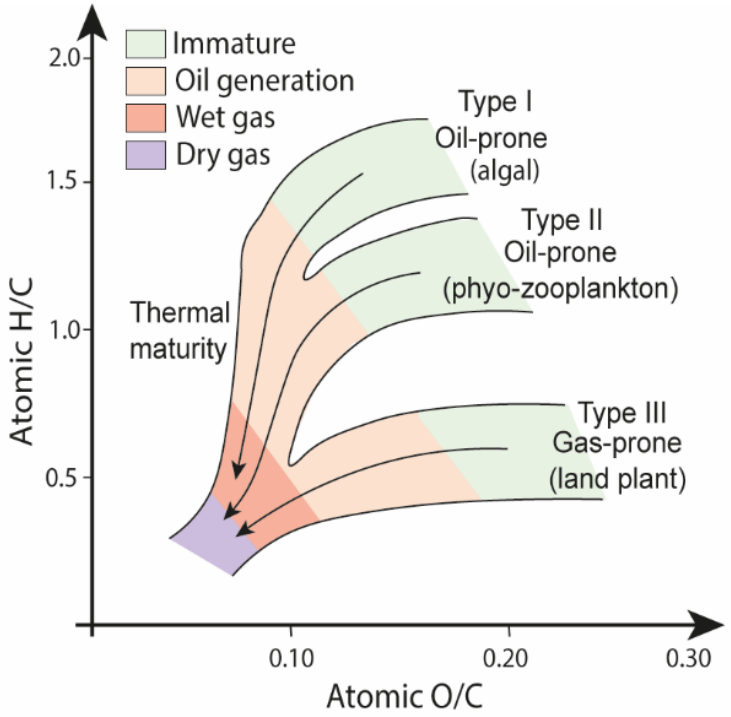

Fig. 1.2. Van Krevelen diagram showing the classification of kerogen based on H/C and O/C atomic ratios and its evolution with increasing thermal maturity.

At higher depth, when temperature ranges between 180-220°C, the remaining methyl groups of kerogen are released to form methane. The liquid hydrocarbons still entrapped in source rocks endure a secondary thermal cracking resulting in the production of lighter gaseous hydrocarbons and carbon-rich residues called pyrobitumen (Tissot and Welte, 1984). This is the metagenesis (Fig. 1.2). The residual kerogen becomes enriched in nm-size graphene-like polyaromatic layers which tend to pile up into increasingly well-order and larger basic structural units separated by nanopores (Boulmier et al., 1982; Oberlin, 1989; Rouzaud and Oberlin, 1989; Hunt, 1996).

1.2. Porosity of mudstones

1.2.1. Generalities

Assessing the quality of mudstone reservoirs depends closely on the volume and the arrangement of the pore system as they control both the pathways for hydrocarbon flow and their storage capacity. It is thus primordial to identify the factors at the origin of this porosity to better understand the nature and the features of the pore system. Gas shale systems have been studied for many years, but the origin and the evolution of their porosity remain incompletely understood. The difficulty lies especially in the characterization of these heterogeneous rocks whose pore sizes are on the order of nm to µm (Chalmers and Bustin, 2008; Ross and Bustin, 2009; Chalmers et al., 2012; Loucks et al., 2012).

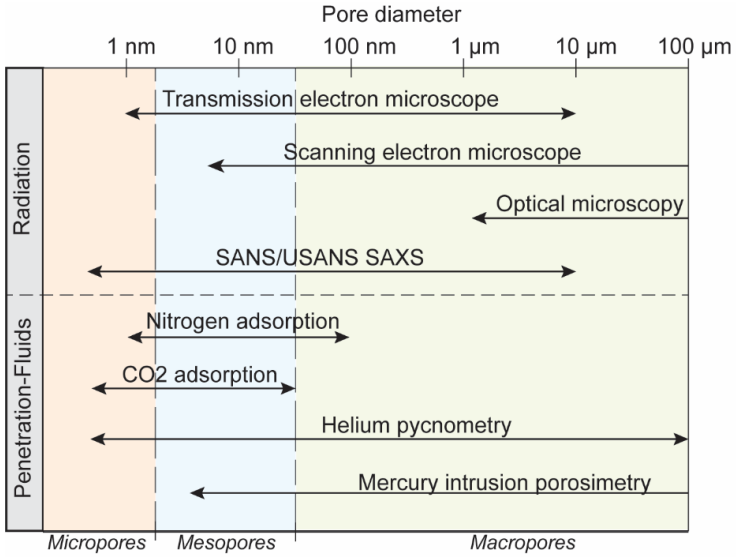

Fig. 1.4. Pore size range accessible by the methods commonly used to estimate porosity and pore size distributions in shale reservoirs (modified from Clarkson et al., 2012).

The porosity of these mudstones is generally dominated by mesopores (pore width between 2–50 nm, pore size as defined in Rouquerol et al. (1994)) but it can also contain variable amounts of macropores (> 50 nm) and less abundant micropores (< 2 nm in diameter) (Chalmers and Bustin, 2008; Ross and Bustin, 2009; Chalmers et al., 2012; Mastalerz et al., 2013). Due to this wide range of pore sizes, a combination of different techniques is often required for the assessment of porosity. High magnification imaging techniques such as scanning electron microscopy (SEM) and transmission electron microscopy (TEM) coupled with argon-ion-beam milling for sample preparation have provided many information on the distribution, the size of pores and the evolution of the porosity of mudstones with burial (Loucks

et al., 2012; Bernard et al., 2012b; Curtis et al., 2012; Fishman et al., 2012; Rodriguez et al., 2014; Romero-Sarmiento et al., 2014; Keel, 2015; Hackley et al., 2017; Ko et al., 2018). These high magnification techniques are not always sufficient to assess the full range of pores in these rocks. Previous studies reveal that a significant number of pores are often less than 5 nm in mudstones (King et al., 2015; Klaver et al., 2015; Mathia et al., 2016). Imaging techniques are generally not able to fully assess this nanoporosity. For example, the results from Mathia et al. (2016) on the Lower Toarcian Posidonia Shale indicate that the porosity estimated using SEM does not exceed 25% of the total rocks porosity. Klaver et al. (2015) showed that the porosity derived from visual SEM estimations is less than 1.7% in the Haynesville Formation, whereas MIP indicates values up to 9.2%. Hence, other analytical approaches are commonly used such as nitrogen and carbon dioxide adsorption measurements (Rouquerol et al., 1994; Kuila et al., 2012; Chalmers et al., 2012; Tian et al., 2013; Chen and Xiao, 2014; Tian et al., 2015; Pan et al., 2015; Song et al., 2019), mercury intrusion porosimetry (MIP) (Clarkson et al., 2013; Mastalerz et al., 2013), helium pycnometry (Yang et al., 2016), small-angle and ultra-small angle neutron scattering (USANS and SANS) (Mastalerz et al., 2012; Clarkson et al., 2013) and small-angle X-ray scattering (SAXS) (Leu et al., 2016). Each of these techniques provides information on different pore attributes or on various pore size ranges (Fig. 1.4) and cannot therefore be compared easily (Bustin et al., 2009; Mastalerz et al., 2012; Clarkson et al., 2013). The total porosity, not always well-interconnected, can be, indeed, strongly different from the volume accessible to gas or fluids flowing through the rock. This already complex situation is further complicated by the presence of a multitude of pore types.

1.2.2. Classification and distribution of pores

The porosity of organic-rich mudstones generally comprises various pore types associated with OM, clay minerals and rigid grains (Chalmers and Bustin, 2008; Ross and Bustin, 2009; Loucks et al., 2009; Chalmers et al., 2012; Loucks et al., 2012; Kuila et al., 2014). According to Loucks et al. (2012) three main types of pores exist in mudstones pore systems: (i) the interparticle pores, (ii) the intraparticle pores and (iii) the OM-hosted pores. The complete description of these pores is presented in Fig. 1.5. The interparticle pores are located between particles and are mainly tied with the presence of rigid mineral grains which can resist to compaction and protect pores and ductile grains from compaction (Schieber, 2010; Loucks et al., 2012). Yang et al. (2016) suggest that some of the large interparticle pores may also partly

result from the partial dissolution of carbonates and feldspars. Generally, less interconnected than interparticle pores, intraparticle pores correspond to the pores within inorganic particles (Loucks et al., 2012). The formation of these pores appears mainly driven by the dissolution of fossils or mineral grains in response, for example, to the formation of organic acids during kerogen transformation (Schieber, 2010; Loucks et al., 2012; Yang et al., 2016). The OM-hosted pores are located within OM particles.

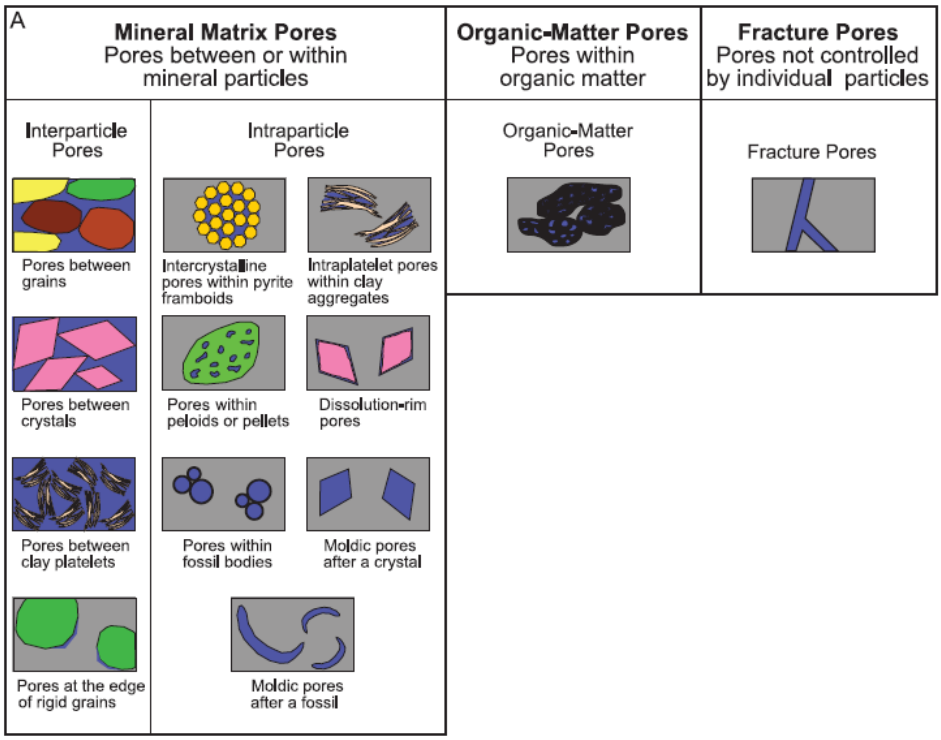

Fig. 1.5. Classification of pore types occurring in mudstones (from Loucks et al., 2012).

This OM porosity is generally subdivided into two groups: (i) primary OM-hosted pores, mainly inherited from features initially present in kerogen; for example, from the original structure of cellulose, lignaceous debris or spaces between adjacent cells of colonial algae (Löhr et al., 2015; Reed, 2017). An example of these primary pores observed by Löhr et al. (2015) in the Stuart Ranges formation is shown in Fig. 1.6. This primary OM-hosted porosity is thus, often associated with fragments derived from plant tissues; (ii) secondary pores are supposed to be formed in pyrobitumen and/or kerogen during thermal maturation (Chalmers and Bustin, 2008; Bernard et al., 2012a, b; Loucks et al., 2012; Curtis et al., 2012; Milliken et al., 2013; Mastalerz et al., 2013; Chen and Xiao, 2014; Cardott et al., 2015; Ko et al., 2016, 2018; Katz and Arango, 2018). These secondary OM-hosted pores can be classified into different categories. According to the observations of Milliken et al. (2013) on the Marcellus Formation, four different types of OM-hosted pores can be distinguished (Fig. 1.7): (i) discrete small

isolated pores dispersed in OM particles; (ii) sponge-like pores; (iii) complex large pores; (iv) mineral-associated pores which consist in interparticle pores between mineral and OM.

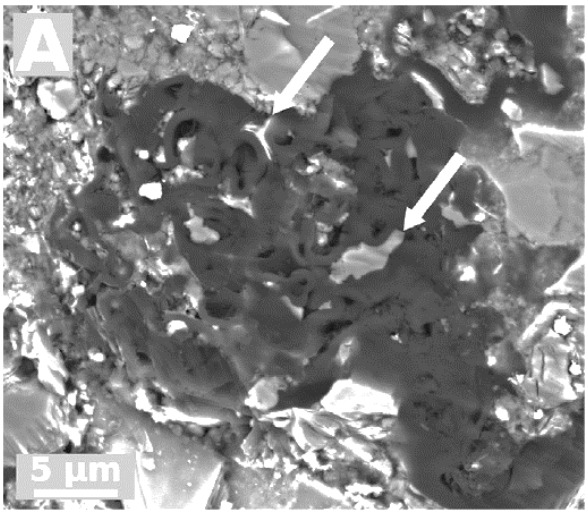

Fig. 1.6. Example of primary pores observed in immature kerogen of colonial algal origin (Stuart Ranges formation, Ro= 0.5%, from Löhr et al. (2015).

Imaging (Loucks et al., 2012; Bernard et al., 2012b; Curtis et al., 2012; Fishman et al., 2012; Hackley and Cardott, 2016; Hackley et al., 2017; Ko et al., 2018) and gas adsorption techniques (Kuila et al., 2012; Chalmers et al., 2012; Pan et al., 2015; Pan et al., 2015) revealed that these secondary OM porosities are frequently the main component of gas shales pore volume. Given the significant volume of OM-hosted pores in many shale reservoirs, and thus, the important contribution of the OM to the hydrocarbons storage capacity, the OM-hosted porosity became a major research focus these last years. However, the type and the origin of this porosity is often difficult to identify due to the small size of these pores and the great heterogeneity of shale reservoirs (Loucks and Reed, 2014). Therefore, many contradictory results exist in the available literature about the relative proportion of primary and secondary OM-hosted pores or on their sites of formation (kerogen, solid-bitumen?) (Loucks et al., 2009; Bernard et al., 2012a, b; Loucks and Reed, 2014; Reed et al., 2014; Katz and Arango, 2018). Bernard et al. (2012b) suggest that most of pores in the Barnett Shales is provided by nanopores hosted by pyrobitumen while for Loucks et al. (2009), OM pores are mainly located in kerogen. Yet, this OM-linked porosity can control many reservoir properties including total porosity or methane sorption capacities (Ross and Bustin, 2009; Strąpoć et al., 2010; Milliken et al., 2013; Ko et al., 2016; Chalmers and Bustin, 2017; Song et al., 2019), hence the importance of clearly to understand the factors impacting its development.

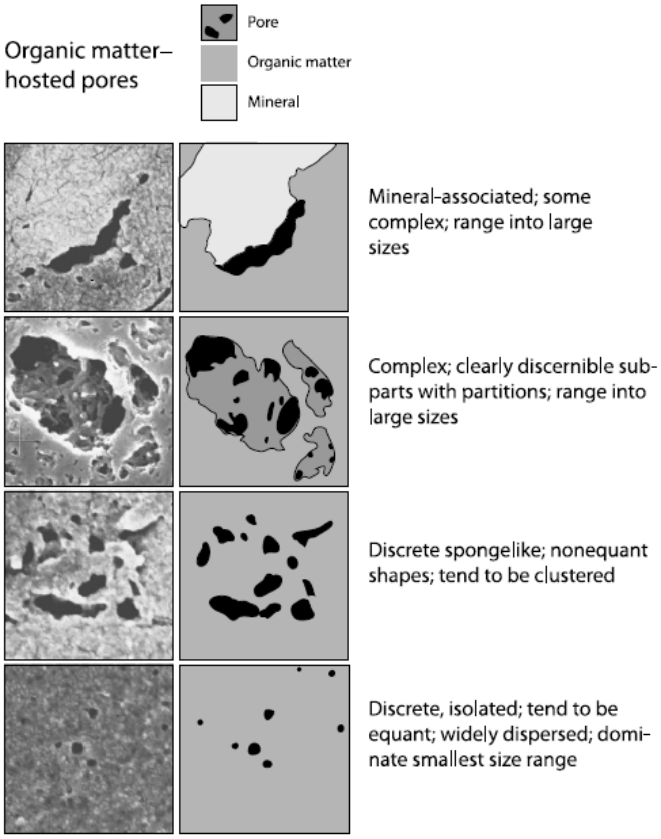

Fig. 1.7. Different categories of organic-matter-hosted pores observed in the Marcellus Formations (from Milliken et al., 2013).

1.2.3. Controlling factors of porosity

Many geological parameters influence the distribution of pores in organic-rich mudstones, hence the difficulty to evaluate and predict their pore network. The OM abundance (TOC), kerogen type, thermal maturity, the mineral composition and the rock fabric are the most frequently cited parameters in the literature (Loucks et al., 2009; Chalmers et al., 2012; Milliken et al., 2013; Kuila et al., 2014; Ko et al., 2016; Chalmers and Bustin, 2017; Ardakani et al., 2018; Ko et al., 2018; Katz and Arango, 2018; Song et al., 2019). However, their respective effect on porosity is often complex to isolate.

1.2.3.1. Influence of thermal maturity

In recent years, a special attention was paid to the effect of thermal maturity in the formation of OM-hosted pores in mudstones (Chalmers and Bustin, 2008; Loucks et al., 2009; Bernard et al., 2012a, b; Loucks et al., 2012; Curtis et al., 2012; Chen and Xiao, 2014; Ko et al., 2016). The increase in maturity with burial and kerogen thermal degradation is widely

considered as the main factor controlling the development of pores in organic-rich source rocks (Chalmers and Bustin, 2008; Loucks et al., 2009; Bernard et al., 2012a, b; Curtis et al., 2012; Chen and Xiao, 2014; Yang et al., 2018). While the interparticle porosity has been thought to decrease with burial due to structural rearrangements under compaction and possible occlusion by entrapped bitumen (Loucks et al., 2009; Modica and Lapierre, 2012), the OM-hosted porosity generally increases with increasing depth (Bernard et al., 2012a; Curtis et al., 2012; Reed et al., 2014; Chen and Xiao, 2014; Ko et al., 2016; Han et al., 2017; Ko et al., 2018). While primary OM-hosted pores, likely inherited from the original organic material structure (e.g. structure of cellulose, lignaceous debris, spaces between adjacent cells of colonial algae etc.) are sometimes observed in low-mature kerogen (Pommer and Milliken, 2015; Löhr et al., 2015; Reed, 2017; Katz and Arango, 2018), pores are rarely observed in amorphous type II OM (Bernard et al., 2012a, b; Curtis et al., 2012; Kuila et al., 2014; Katz and Arango, 2018).

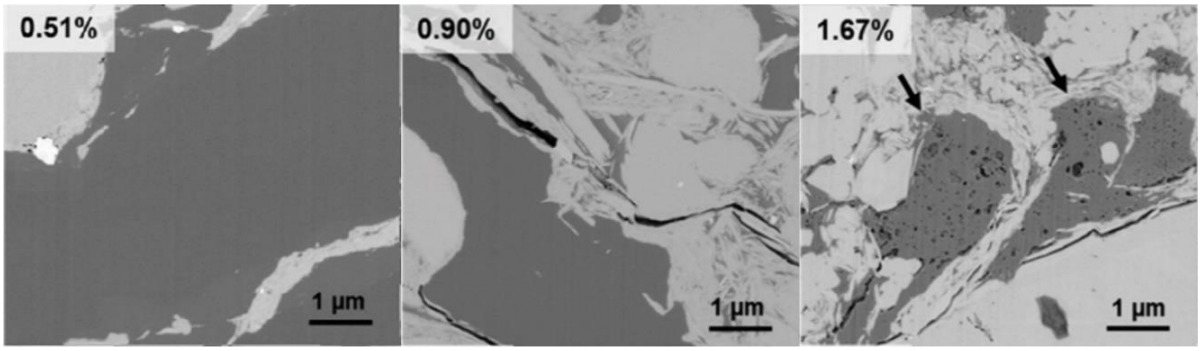

Fig. 1.8. BSE images of samples from the Woodford Shale showing the evolution of the organic matter-hosted porosity with the increase of thermal maturity from Ro=0.51% to 1.67% (from Curtis et al., 2012).

Yet, a significant volume of OM-hosted pores is widely present in thermally mature mudstones (Fig. 1.8, Loucks et al., 2009; Bernard et al., 2012b; Curtis et al., 2012; Kuila et al., 2014). The use of anhydrous laboratory thermal maturation revealed that these variations of porosity appear closely tied with the OM thermal transformations (Chen and Xiao, 2014; Wu et al., 2015; Ko et al., 2017). Even if the influence of thermal maturity on OM porosity has been studied for many years, the factors controlling the evolution of this porosity remains poorly understood and many contradictions exist between pore evolution models.

A decrease of the OM porosity is currently observed in various source rocks up to maturity corresponding to Ro of ≈0.90% (Furmann et al., 2016; DiStefano et al., 2016; Han et al., 2017; Ko et al., 2018; Katz and Arango, 2018; Wang et al., 2019). For example, while Katz and Arango (2018) observed the presence of primary pores associated to detritic OM up to Ro

≈0.63% in the Kimmeridge Clay formation, the OM is totally non-porous during the main oil generation stage. The occlusion of pores by retained bitumen is often an obvious explanation for these phenomena (Sanei et al., 2015; Zargari et al., 2015; Löhr et al., 2015; Furmann et al., 2016; Han et al., 2017). Previous studies suggest however, that the swelling of kerogen by retained oil (Mathia et al., 2016), pore compaction, ductile deformations, collapse of the kerogen structure due to its more important plasticity at the highest temperature and/or changes in the physical and chemical properties of kerogen may also partly explained this loss of pore volume during oil generation (Guo et al., 2018). Then, the progressive conversion of kerogen and the significant variation of volume created by oil and gas generation and expulsion are known to result in the growth of the secondary OM-hosted porosity (Jarvie et al., 2007; Chalmers and Bustin, 2008; Loucks et al., 2012; Bernard et al., 2012b; Curtis et al., 2012; Chen and Xiao, 2014; Ko et al., 2016; Han et al., 2017; Yang et al., 2018; Ko et al., 2018). This phenomenon seems tied with the significant variation of the pore sizes which tend to increase during wet gas generation, likely due to the coalescence of pores (Loucks et al., 2009; Mastalerz et al., 2013). With increasing thermal maturity some solid bitumen and pyrobitumen can be formed during the thermal cracking of pre-existing bitumen into oil and gas (Tissot and Welte, 1984; Lewan, 1993; Behar et al., 1997; Reed et al., 2014). Pyrobitumen is often the predominant maceral in gas-mature mudstones (Hackley and Cardott, 2016; Hackley, 2017) and is generally considered to be the main contributor to the porosity (Bernard et al., 2012b; Milliken et al., 2013; Hackley and Cardott, 2016; Hackley et al., 2017). The bubble-like shape of some OM-hosted pores in gas-mature mudstones has been interpreted as evidence that this growth of OM porosity in the secondary products of OM thermal degradation is the result of oil and gas generation and expulsion, that leave behind abundant devolatilization vacuoles (Bernard et al., 2012a, b; Milliken et al., 2013). This hypothesis remains nevertheless controversial since some evidence show that pores can also be widely developed in residual kerogen particles (Loucks et al., 2009; Reed et al., 2014; Katz and Arango, 2018) or can form at lower maturity, during the peak of oil generation, (Ro of 0.8-0.9%, Loucks et al., 2009; Reed et al., 2014; Chen and Xiao, 2014; Juliao et al., 2015; Ko et al., 2017; Han et al., 2017).

Other hypotheses have thus been proposed. SEM and Raman spectroscopy investigations of Keel (2015) in the Ordovician Vila Group, the Cretaceous Niobrara Formation and the Silurian ‘hot shales’ suggest that the formation of pores in type II and III OM is mainly due to the creation of void spaces formed by the released of volatiles which surround ‘aromatic islands. For them, the formation of these aromatic units is tied with the kerogen macromolecules

restructuring and the increase of aromaticity during maturation. Alternatively, Romero-Sarmiento et al. (2014) suggest that the disorientation of the kerogen polyaromatic layers at the nanoscopic scale is responsible for most of the development of the porosity of gas-mature rocks from the Barnett Shales. For Curtis et al. (2012) and Pommer and Milliken (2015), the development of pores occurs mainly within the late oil window (Ro= 0.90-1.23%) and stops at higher maturity stages. However, in the Upper Permian of the southern Junggar Basin and the Upper Permian of the northern Sichuan Basin the organic porosity increases up to very advance levels of maturity (Ro > 3.6%) (Fig. 1.9, Chen and Xiao (2014).

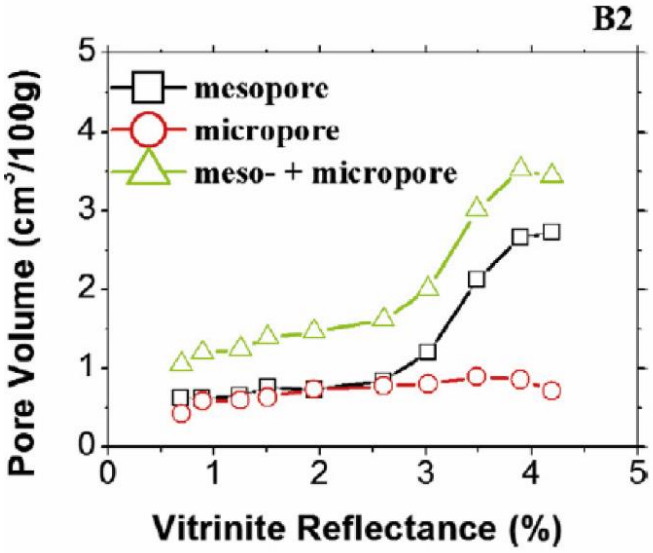

Fig. 1.9. Variations of pore volume of an organic-rich sample (TOC = 8.63 wt.%) from the Upper Permian outcrop of the northern Sichuan Basin (from Chen and Xiao, 2014).

While many contradictions exist about why, where and when OM-hosted pores are generated, the relation between thermal maturity, OM molecular transformations and porosity is not clear (Schieber, 2010; Curtis et al., 2012; Fishman et al., 2012; Milliken et al., 2013; Pan et al., 2015; Löhr et al., 2015; Guo et al., 2018; Ko et al., 2018; Katz and Arango, 2018). For example, Loucks et al. (2012) reveal that no linear apparent correlation can be observed between the OM porosity of the Barnett Shale and thermal maturity. The OM-hosted porosity can however, vary greatly between OM particles of the Woodford Shale for a given maturity (Fig. 1.10, Curtis et al. (2012). These evidences indicate that the impact of thermal maturity on porosity may also strongly depend on the original OM composition (Loucks et al., 2012; Curtis et al., 2012; Mastalerz et al., 2013; Ko et al., 2017; Ardakani et al., 2018; Ko et al., 2018) and the OM content (Milliken et al., 2013; Pan et al., 2015; Ko et al., 2017) explaining the multitude of trends observed in shale reservoirs.

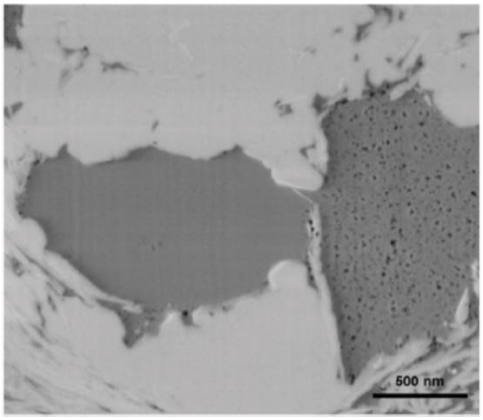

Fig. 1.10. BSE image showing the juxtaposition of a porous and a non-porous organic-matter particle in a Woodford Shale sample (Ro= 1.4%, from Curtis et al., 2012).

1.2.3.2. Role of the organic matter richness

Some studies reveal that the OM content (TOC) can sometimes have a stronger influence on OM-hosted pores development than maturity. While TOC influences the number of pores provided by the OM and thus the total porosity, the relation between TOC and organic-rich shales porosity appears more complex. For example, in oil-mature (Ro= 1.0%) and gas-mature (Ro= 2.1%) mudstones from the Marcellus formation, Milliken et al. (2013) show that a positive correlation exists between porosity and TOC but only for TOC values less than 5.5 wt%. Above, samples exhibit a reduce pore volume and contain smaller pores (Fig. 1.11).

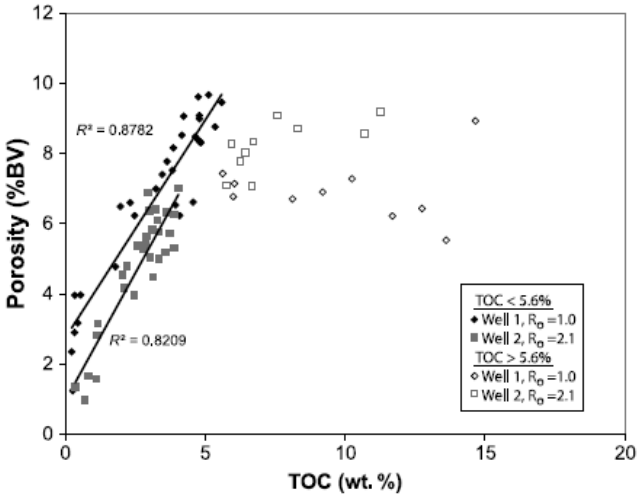

Fig. 1.11. Evolution of porosity with total organic carbon content (TOC) in the Marcellus formation at different thermal maturity (Milliken et al., 2013).

For these authors, this particular relationship could stem from a more important pore collapse of the porosity in the organic-rich samples, facilitated by the greater ductility of the rock

framework. According to these results Milliken et al. (2013) suggest that TOC could be a key control of porosity in mudstones. Similar trends were observed by Wang et al. (2013) in the Lower Cambrian and the Upper Ordovician-Lower Silurian shales from the Sichuan Basin for TOC values > 5 wt.% or by Pan et al. (2015) in overmature samples (Ro > 2.0%) from the Gufeng, the Longtan and the Dalong formations above 12 wt.% of TOC. For Wang et al. (2013), this phenomenon may result in variations of the rock fabric influencing its ability to resist to compaction. This hypothesis provides support to the suggestion of Fishman et al. (2012) who propose that the stability of the OM-hosted porosity and its ability to be preserved in thermally mature rocks could be related to the relative proportion of ductile components (clay minerals, amorphous OM particles) versus rigid mineral grains (calcite, quartz, feldspar).

1.2.3.3. Influence of the organic matter composition

In addition to OM thermal degradation processes and organic-richness, many works show that the initial kerogen composition, controlled by dispositional conditions and early diagenetic processes, can also strongly influence the evolution of porosity (Loucks et al., 2012; Curtis et al., 2012; Fishman et al., 2012; Milliken et al., 2013; Cardott et al., 2015; Ko et al., 2016; Ko et al., 2017; Ko et al., 2018). Source rock kerogen can be composed of particles of various origins, with distinct morphologies, internal structure and chemical composition. This may influence the primary OM porosity but also, the timing and the ability of rock to generate oil, gas and solid bitumen during burial (Tissot and Welte, 1984). This may lead to variation in the character, the distribution and the timing at which pores are generated during maturation. For example, no OM-hosted pores development is generally observed for type III kerogen, but vitrinite often contain mesopores tied with the original vitrinite microstructure (Mastalerz et al., 2012; Zargari et al., 2015). For Löhr et al. (2015), the primary OM porosity inherited from biological structures may influence the development of secondary organic pores during thermal maturation, leading to inhomogeneity in the OM-hosted pore distribution at more elevated maturities. For them, this impact of the primary OM-hosted porosity is however restricted to the relatively low thermal maturation stages (Ro ≤ 1.50%); above, the porosity is rather controlled by the secondary OM porosity formed in pyrobitumen. Ko et al. (2018) showed that the different abundance of Tasmanites between the Eagle Ford and Barnett mudstones has an impact on the pore evolution models with increasing maturity. The results of Chen et al. (2015) indicate that different kerogen types exhibit different ability to develop pores during maturation. These authors suggest that type I kerogen has a greater potential to develop pores than type II

or III kerogen. For them, OM type is thus a key factor for the development of the OM-hosted porosity. This is in accordance with the conclusion of which suggest that the initial OM oil and gas generation potential has a prime control on OM-hosted pores development. While the evolution of the bulk and the molecular composition of OM as a function of the OM origin and thermal maturity have been well documented (Tissot and Welte, 1984; Monthioux et al., 1985; Boreham et al., 1988; Radke, 1988; Behar et al., 1992; Landais et al., 1994; Peters et al., 2007), the influence of these evolutions on source rock porosity remains however, poorly understood.

Conclusions

This review of the available literature shows that the OM-hosted porosity is a key component of the porosity of shale reservoirs. While thermal maturation processes appear to be the main factor controlling its development, many contradictions exist with respect to the relative influence of the OM composition and TOC. The relative contribution of the primary OM-hosted pores versus the secondary OM porosity formed during maturation is not clear and discrepancies still remain in regard to when the OM porosity develops and where (kerogen, pyrobitumen, both?). It is clear that there are number of issues that need to be clarified about the development of the OM-hosted porosity in mudstones. This issue leads us to ask the following questions. Firstly, what is the importance of the influence of the OM composition and maturity on porosity? What is its contribution to the gas-mature mudstones porosity? Where and when develop this OM porosity? Does a slight variation of the composition of the total particulate OM assemblage can affect the evolution, the size, and the abundance of pores during thermal maturation? One of the main challenges when studying organic-rich mudstones is the great variability that often exists within a same gas-shale reservoir with respect to the original OM composition (not identifiable in thermally mature rocks), the TOC and mineralogy. To isolate the effect of the OM composition, porosity and thermal maturity is thus a complex exercise. In reducing the complexity that exists in natural systems, the use of laboratory simulations may thus be a key to better understand and discriminate the influence of factors other than maturity on porosity. This is the reason why this artificial maturation experiments is increasingly used in the community (Chen and Xiao, 2014; Ko et al., 2016; Liu et al., 2018; Ko et al., 2018). It’s also the reason why this laboratory scientific approach was selected for the present study.

Chapter 2: Geological settings

2. Geological settings

2.1. The Kimmeridge Clay formation (KCF)

2.1.1. Geological background

The KCF consists of organic-rich marine claystones widely distributed in several European basins throughout the Jurassic graben and rifting fault systems of the North Sea area (Herbin et al., 1995, Fig. 2.1).

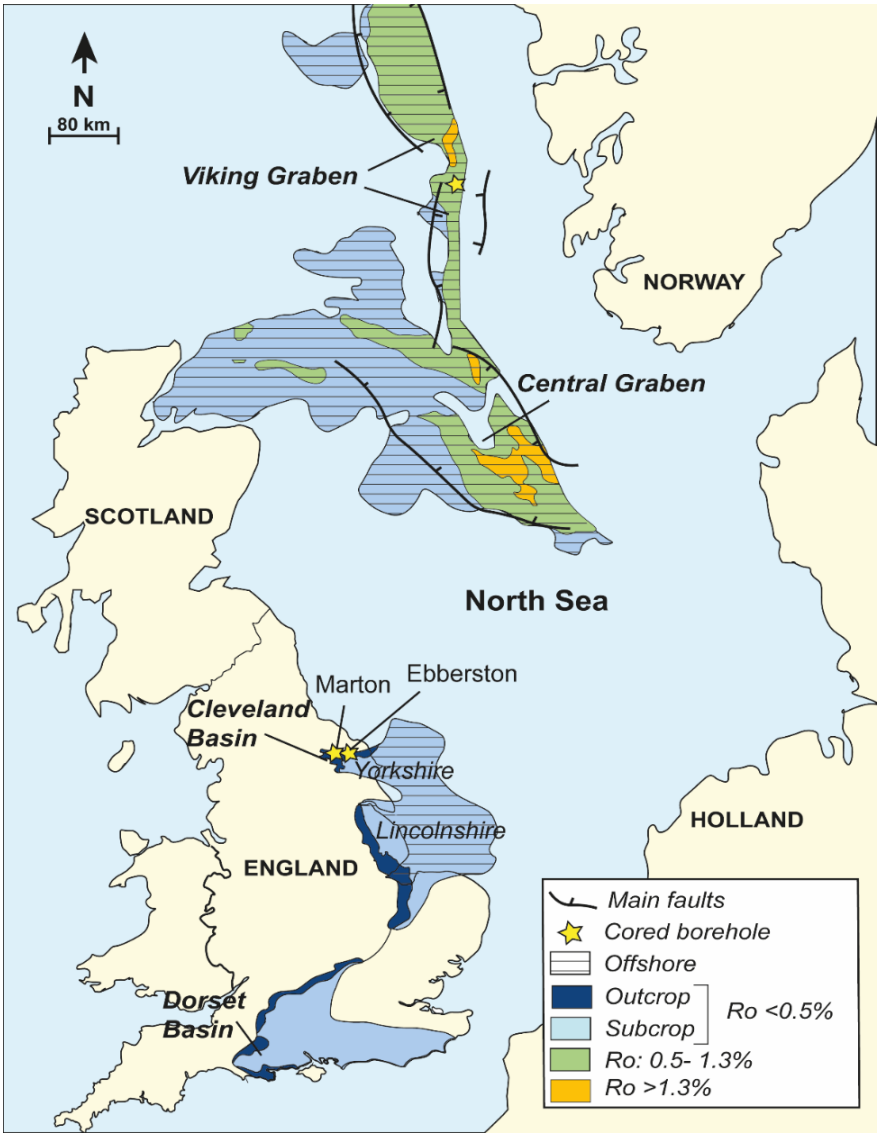

Fig. 2.1. Kimmeridge clay formation outcrops, subcrops and approximate thermal maturity across England and North Sea. Location of the studies boreholes (modified from (Ramanampisoa and Disnar, 1994; Gallois, 2004; Johnson et al., 2005).

This formation was deposited from the Kimmeridgian to the Tithonian (locally, the deposition can extend to the lower Berriasian) during the important marine transgression of the Upper Jurassic (Cox and Gallois, 1981; Rawson and Riley, 1982; Herbin et al., 1995; Fig. 2.2). During this period, the high primary productivity and the limited connections to the open sea led to the development of anoxic to suboxic conditions, particularly favorable to the accumulation of OM (Rawson and Riley, 1982; Ramanampisoa and Disnar, 1994; Boussafir et al., 1995a; Lallier-Vergès et al., 1995; Herbin et al., 1995).

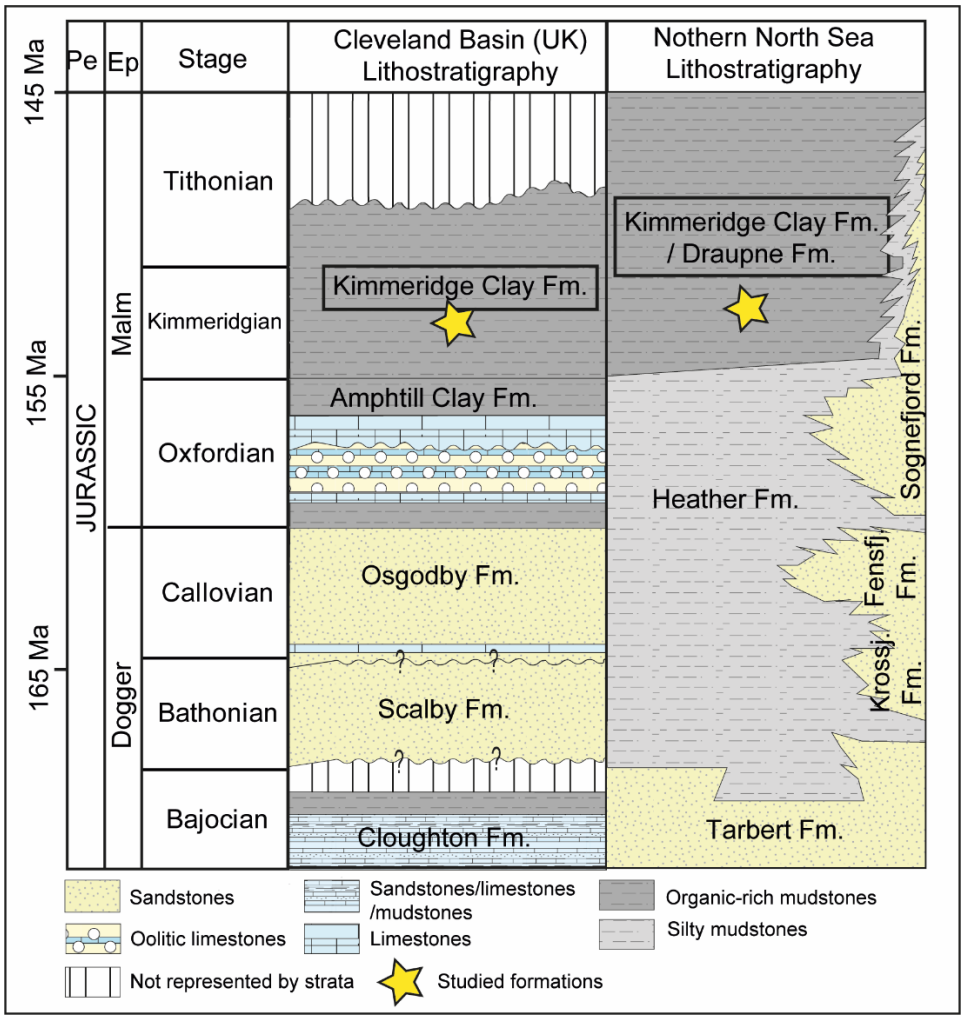

Fig. 2.2. Simplified lithostratigraphy of the Middle and the Upper Jurassic of the Cleveland Basin (UK) and the Northern North Sea (modified from Powell, 2010; Patruno et al., 2015; Cavelan et al., 2019b).

This formation is considered as the major source unit responsible for most of the North Sea conventional oil and gaseous hydrocarbon resources and exhibit also a significant potential as an unconventional hydrocarbons reservoir (Cornford, 1984; Cooper et al., 1995; Gallois, 2004; Gautier, 2005). This formation is thus of great economic importance (Gallois, 2004; Gautier, 2005).

Onshore, the KCF outcrops in England from the Dorset coast to the north Yorkshire (Rawson and Riley, 1982). In this area the formation consists mainly of several hundred meters (100 -400 meters of thickness) of organic-rich mudstones alternating with marls, interbedded coccoliths, and diagenetic limestones (Rawson and Riley, 1982; Herbin et al., 1995). Its lower boundary is marked by an erosive non-sequence with the Ampthill Clay formation while its upper boundary is often truncated by erosion (Fig. 2.2) (Cox and Gallois, 1981; Powell, 2010). Offshore the KCF is largely distributed throughout the Northern, Central and Southern North Sea, where it reaches a huger thickness and higher thermal maturities (Boulmier et al., 1982; Goff, 1983; Field, 1985, Fig. 2.1). In this area, the KCF comprises 260 (Southern) to 1400 meters (Northern North Sea) of organic-rich fissile mudstones with local alternations of siltstones, limestones sandstones and conglomerates (Wiliams et al., 2001; Johnson et al., 2005; Patruno et al., 2015). In the Northern and Central North Sea, the KCF is sometimes topped by sandstones, limestones or sandstones and generally overlies the mudstones from the Heather Formation (Fig. 2.2).

2.1.2. OM composition and sedimentary cyclicities in the Yorkshire

Formed during pronounced sea-level and climate fluctuations at the Milankovitch-scale, KCF mudstones are locally internally marked by strong short-term cyclic variations in lithology, OM content and OM composition (Cox and Gallois, 1981; Oschmann, 1988). According to these variations, Oschmann (1988) has distinguished different organic cycles of several orders with duration ranging between on year (four-order cycles) to 3.10^7 years (first-order cycles). For this author, the first- and second-order cycles are tied with sea-level fluctuations while third-order cycles (5.10^3 to 15.10^3 years long) are controlled by climatic variations. These cyclicities were well-observed in the Yorkshire and the southern England (Cox and Gallois, 1981; Oschmann, 1988; Boussafir et al., 1995a; Lallier-Vergès et al., 1995). Dominated by a type II marine kerogen, previous SEM, TEM, bulk and molecular geochemical investigations have indeed, revealed that significant variations of TOC, OM composition and OM oil generation potential exist in the short-term cycle I and II of Marton and in the cycle III of Ebberston boreholes in the Yorkshire (UK, Fig. 2.1, 2.3, Herbin et al., 1991; Lallier-Vergès et al., 1995; Herbin et al., 1995; Boussafir and Lallier-Vergès, 1997). In this section, the OM is mainly composed of three distinct types of marine amorphous organic matter (AOM) (orange, brown and black AOM in order of decreasing abundance) with a minor contribution of

structured constituents derived from plant tissues and zooplankton (Boussafir et al., 1995a; Boussafir et al., 1995b; Boussafir and Lallier-Vergès, 1997).

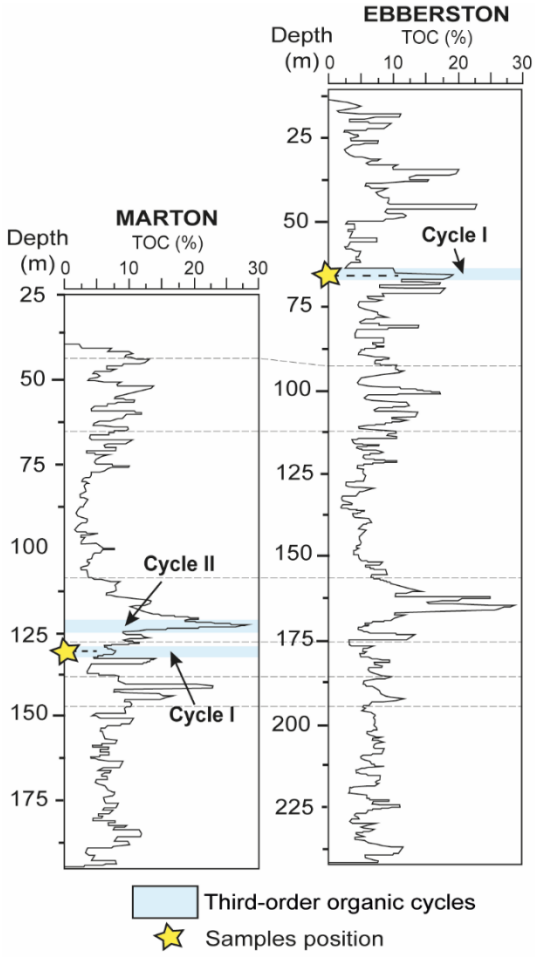

Fig. 2.3. Total organic carbon (TOC) variations with depth in Ebberston and Marton boreholes and samples location (modified from Herbin et al., 1995).

The relative proportions of these compounds vary as a function of the position on the cycle. For these authors, these fluctuations occur in parallel with variations in the organic productivity and the oxygenation of the dispositional environment in response to climate change (Boussafir et al., 1995a; Boussafir et al., 1995b; Lallier-Vergès et al., 1995; Boussafir and Lallier-Vergès, 1997). Hence, the organic-rich facies of the cycle (middle part, Herbin et al., 1995) were formed in more anoxic conditions during periods of higher primary productivity (Boussafir et al., 1995b; Boussafir and Lallier-Vergès, 1997). These facies are characterized by higher contents of gel-like orange Amorphous Organic Matter (AOM) consisting in highly oil-prone phytoplanktonic OM preserved essentially by sulfurization (Boussafir et al., 1995b; Lallier-Vergès et al., 1995; Boussafir and Lallier-Vergès, 1997). OM in the beginning and the end of the cycle was deposited during periods of lower productivity and is composed of lower contents

of organic compounds with a lower oil generation potential (mainly brown AOM, Boussafir et al., 1995b; Boussafir and Lallier-Vergès, 1997).

2.1.3. Samples description and selection

For this work, a total of twenty-one samples were selected in the well-documented cycle I of Ebberston and Marton boreholes, in the Cleveland Basin (Pickering Vale, Yorkshire, UK, Fig. 2.1, Fig. 2.2). These two boreholes were sampled by the "British Geological Survey" and the "Institut Français du Pétrole (IFP)" in 1987. These rocks were sampled between 128.15-129.20 meters deep in Marton and between 69.11-70.65 meters deep in Ebberston (Fig. 2.2). Based on previous studies (see 2.1.2), the studied samples were selected in the whole cycle I and cycle III of Marton and Ebberston wells respectively, in order to cover a wide range of TOC, OM compositions and OM oil generation potential but relatively similar mineralogy. Previous X-ray diffraction investigations from Herbin et al, (1991) and Desprairies et al. (1995) have showed indeed, that Marton (cycle I) and Ebberston (cycle III) rocks show a relatively monotonous lithology consisting of finely laminated organic-rich marine mudstones. In Marton, these rocks are composed of ≈ 4-20 wt% of carbonates, 7-26 wt% of quartz, 60-80 wt% of clay and less than 10 wt% of pyrite, feldspar and gypsum while in Ebberston, rocks contain 44-80 wt% of clay, 5-15 wt% of Quartz, 7-29 wt% of carbonates and less than 10 wt% of pyrite, feldspar and gypsum (Desprairies et al., 1995). The composition of clay minerals is also relatively constant with 34-43% of detritic kaolinite, 12-18% of illite and 43-52% of illite/smectite interstratified which probably derived from the diagenetic transformation of smectite during burial (Herbin et al., 1991). These mudstones are characterized by high type II OM contents raging in from 2–10 wt.% of Rock-Eval® 6 TOC in Marton and from 2-20 wt.% in Ebberston (Fig. 2.3) and exhibit a high petroleum potential varying from ≈400 to 700 mg of HC/g of TOC depending to their position on the cycle (Herbin et al., 1991; Ramanampisoa and Disnar, 1994; Disnar and Ramanampisoa, 1995). With a Rock Eval Tmax ranging from 420 to 431°C and a mean vitrinite reflectance of ~0.5%, these low-mature rocks have just reached the limit of the oil window (Ramanampisoa and Disnar, 1994).

The strategy adopted for this work consists partly on the comparison of different source rocks of various thermal maturity but similar original OM composition and mineralogy to investigate the role of the original OM composition, content and maturity on the evolution of the global rock structure with increasing burial or during laboratory thermal maturation. With

their high TOC, their low-maturity, their variable OM composition but their homogeneous mineral composition, these highly oil-prone KCF mudstones are thus, the perfect candidates for these investigations. In order to compare the porosity and the OM composition of these low-mature samples with natural mature rocks with an equivalent original OM composition, one oil-mature KCF sample (Ro ≈ 0.7-0.85%, Fig. 2.1) was obtained from the Viking Graben (3913 meters depths) and gas-mature samples were selected in the Vaca Muerta Formation. The exact location of the sample of the Viking graben is unknown (Fig. 2.1). Lithostratigraphy of the Viking Graben area is presented on Fig. 2.2.

2.2. The Vaca Muerta Formation (VMF)

2.2.1. Geological background

The Vaca Muerta Formation (VMF) is a marine deposit widely developed in the southern part of the Neuquén Basin (Central West Argentina, Fig. 2.4).

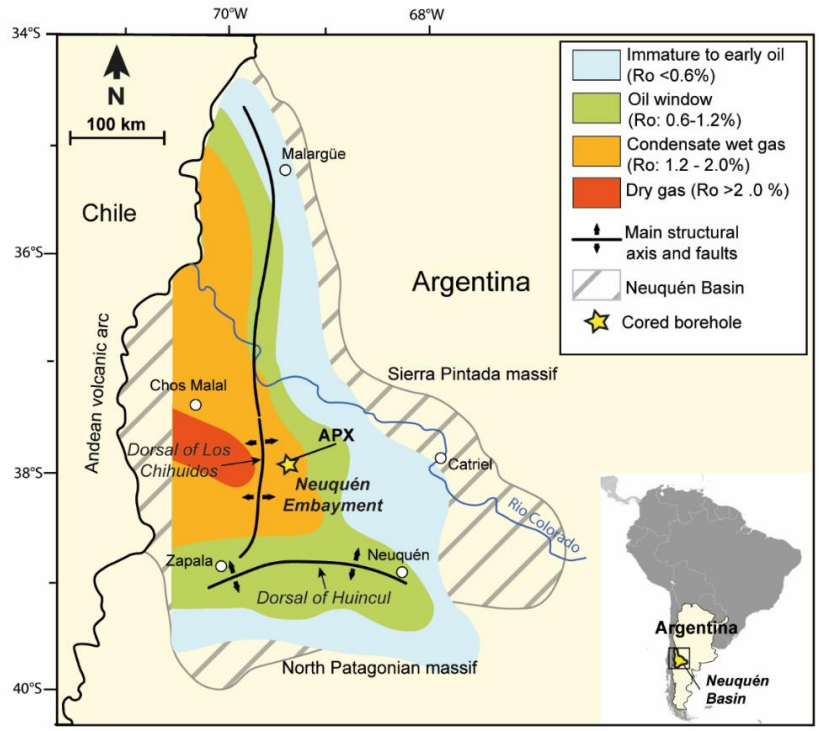

Fig. 2.4. Location of the Aguada Pichana borehole and thermal maturity of the VMF across the Neuquén Basin, central-west Argentina (modified from Legarreta and Villar, 2015).

This basin extends from the central-western Argentina to the eastern Chile and exhibits a complex geologic evolution, largely driven by the changes in tectonic regime of the Gondwana

western margin since the Upper Triassic (Legarreta and Uliana, 1991; Uliana et al., 1999; Howell et al., 2005; Mosquera et al., 2006).

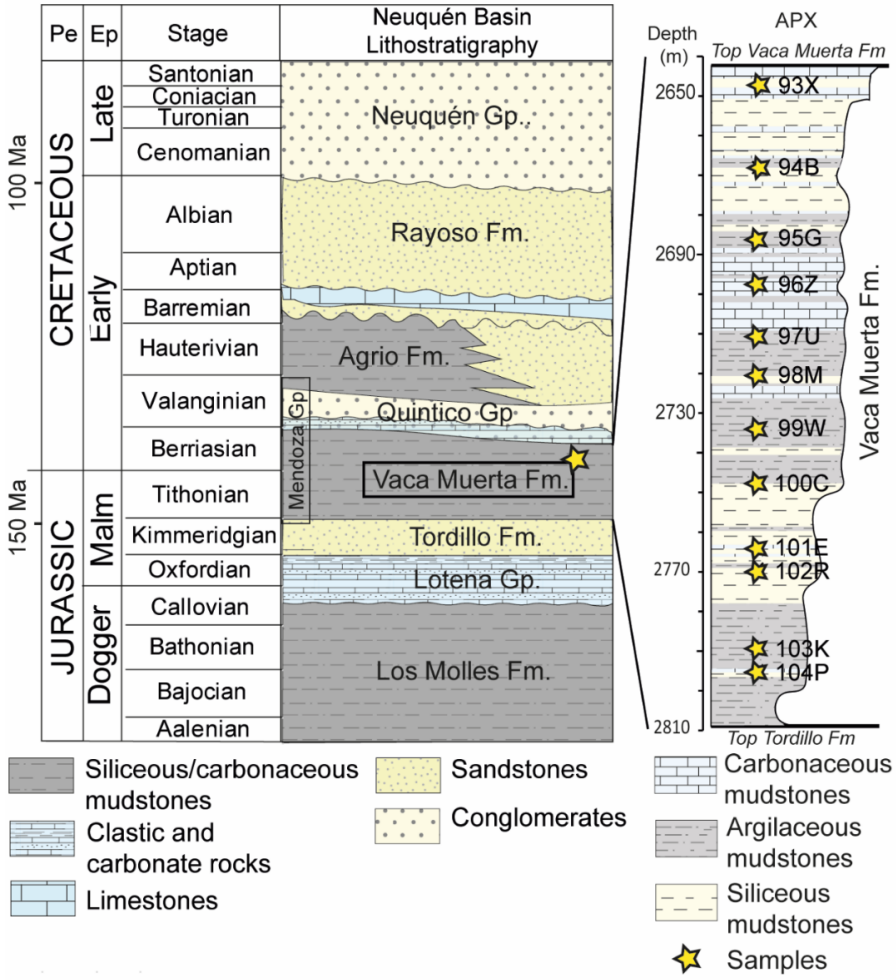

Fig. 2.5. Simplified stratigraphic column in the studied area and distribution of samples in the investigated well. Lithostratigraphy after Howell et al. (2005) and Vergani et al. (2011).

Considering to be the primary source rocks of conventional oil resources in the Neuquén Basin, the VMF exhibits also a well-recognized unconventional resource potential; it is indeed, the most important shale-gas and shale-oil reservoir of Argentina (Kietzmann et al., 2014; EIA, 2015; Legarreta and Villar, 2015). The VMF deposited from the Tithonian to the Lower Valanginian (Fig. 2.5) in response to a widespread marine transgression from the Pacific Ocean. (Legarreta and Uliana, 1991, 1996; Kietzmann et al., 2011, 2014). The VMF overlies the continental deposits of the Tordillo Formation and was topped by the alternation of the siliciclastic sediments and carbonates of the shallow marine deposits of the Quantico group (Fig. 2.5) (Legarreta and Uliana, 1991, 1996; Howell et al., 2005; Garcia et al., 2013). According to Stinco and Barred, (2014) and Bishop (2015), the Vaca Muerta deposit is often associated with facies of distal ramp which prograde from east to west. The VMF belongs to

the Lower Mendoza Group and consists of a succession of 25 to 450 meters of marine black shales, marls, limestones and dark calcareous siltstones interbedded with fined-grained organic-rich mudstones (Fig. 2.5) deposed in shallow marine environment under low energy (Mitchum and Uliana, 1985; Legarreta and Uliana, 1991, 1996; Howell et al., 2005; Legarreta and Villar, 2011; Garcia et al., 2013; Kietzmann et al., 2014; Bishop, 2015). This has favored the development of anoxic conditions and the accumulation and the preservation of high amounts of OM.

2.2.2. Mineralogy, organic matter composition and maturity

Previous studies reveal that the mineralogy of the Vaca Muerta source rocks exhibits significant variations depending on the basin location (Garcia et al., 2013). Generally, the most abundant components are quartz with contents ranging from 16 to 63 wt.%, and plagioclase (1 to 28 wt.%) (Garcia et al., 2013; Kietzmann et al., 2016). According to Kietzmann et al. (2016), the proportion of carbonates, inversely correlated to the content of quartz, fluctuates greatly over the formation from 0 to 51 wt.%. Higher clay minerals content is observed in the southwestern part of the basin, where it generally does not exceed ~30 wt.% (Garcia et al., 2013; Kietzmann et al., 2016). In the immature to low-mature samples, clays are dominated by mixed layer illite-smectite and smectite while the most mature rocks contain mainly chlorite, illite and mixed layer illite-smectite (Kugler, 1985).

Vitrinite reflectance ranging from ≈0.6 to 2.0% (Legarreta and Villar, 2015). While immature to low-mature rocks are located along much of the eastern coast and on the Neuquén Dorsal, VMF rocks are gas-mature in the western and the central zone of the basin (Kugler, 1985; Legarreta and Villar, 2015). With TOC contents ranging from 3 to 12 wt.% and oil generation potential varying between 400 to 800 mgHC/g TOC, the VMF source rocks are characterized by high type II highly oil-prone OM contents (Mitchum and Uliana, 1985; Legarreta and Villar, 2011; Sylwan, 2014). As for the KCF, the kerogen of the VMF is mainly dominated by marine algal AOM associated with variable amounts of marine microplankton and structured terrestrial materials (Uliana et al., 1999; Legarreta and Villar, 2015). According to the same authors, the OM composition is not homogeneous in the VMF, and exhibits variations depending to the grade of oxygenation and the distance to the coast in relation to changes in eustasy (Uliana et al., 1999; Legarreta and Villar, 2015).

2.2.3. OM composition and sedimentary cyclicities in the VMF

As for the KCF, the VMF was formed during pronounced sea-level and climate fluctuations and are marked by strong short-term cyclic variations of composition. Kietzmann et al. (2011) show that the VMF exhibits significant cyclic variations of lithology characterized by a decimeter-scale rhythmic alternation of marls, shales and limestones. More recently, Monkenbusch et al. (2017) and Lejay et al. (2018) have demonstrated that these cyclic variations affect also the quantity and the quality of the OM deposited in the VMF. Monkenbusch et al. (2017) show that variations of the HI, the OI and the TOC (a definition of these parameters are available in chapter 3.1.4) are driven by the precession, the long and the short eccentricity. For these authors, climate and sea level variations, triggered by the evolution of these orbital parameters, have influenced the sea bottom water circulation, the stratification of the water column and the intakes of nutriments in the basin, modifying the amount, the composition and the quality of the preserved OM.

2.2.4. Samples description and selection

For this work, 12 samples were collected in the central basin from the Aguada Pichana x1001 borehole (APX) located in the thickest and deepest zone of the formation in the east of the fault system of Los Chihuidos (Fig. 2.4). The organic-rich facies are often associated with clay-rich mineralogies. In order to cover a wide range of relatively high OM contents, the studied samples were collected between 2647 and 2808 meters and selected in the clay-mineral-rich facies throughout the all thickness of the formation (Fig. 2.5). These mudstones are considered to reach the gas window with a vitrinite reflectance of ≈1.2% to 2.0% (Legarreta and Villar, 2011). In order to better understand the different parameters influencing the nature, the structure and the distribution of pores in gas-source rocks and especially the effect of the OM content and composition, this study aims firstly to compare the features of the porosity of natural low-mature rocks (the KCF mudstones) with gas-mature shales of equivalent original OM composition and contents. According to previous studies, the VMF and the KCF contain high contents of a similar highly oil-prone type II OM precursor deposited under comparable environments. Besides, the two formations are often considered as equivalent in terms of both OM composition and depositional environment (Uliana et al., 1999). These gas-mature samples from the VMF seem thus, to be the perfect candidates for our investigations.

Chapter 3: Analytical methods

3. Analytical methods

Introduction

A combination of different techniques was used to simulate the thermal maturation of KF rocks, to assess the mineralogical composition, the bulk, the molecular OM composition and the structure of natural and thermally matured samples at different maturity stages from the microscopic to the nanoscopic scale (Fig. 3.1). All these techniques are presented below.

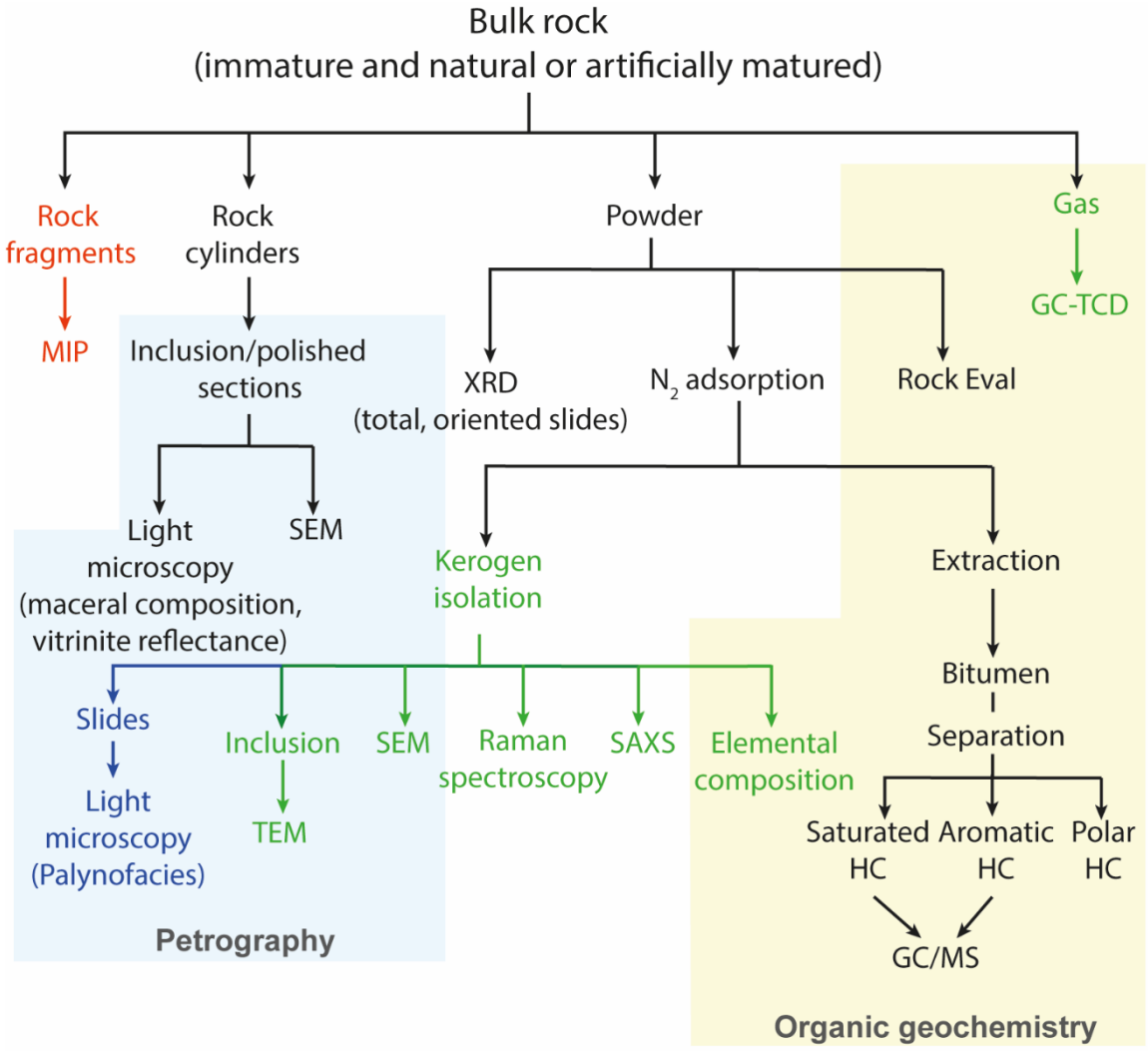

Fig. 3.1. Tree view showing the methods used for the characterization of VMF and KCF mudstones. In dark: methods applied for all samples. In blue: method used for KCF immature samples characterization only. In green: methods applied to immature and thermally mature KCF samples only. In red: methods use for natural samples characterization only. MIP: mercury intrusion porosimetry. SEM: Scanning electron microscopy. TEM: transmission electron microscopy. SAXS: Small-Angle X-ray scattering. XRD: X-ray diffraction. GC: gas chromatography. MS: mass spectrometry. HC: hydrocarbons.

3.1. Characterization of natural and thermally matured samples

3.1.1. Anhydrous confined thermal maturation

For limiting the complexity existing in natural shale reservoirs, laboratory simulations were increasingly used to assess the evolution of OM and porosity in organic-rich mudstones (Zhang et al., 2013; Chen and Xiao, 2014; Hu et al., 2015; Ko et al., 2016; Guo et al., 2017; Liu et al., 2018; Ko et al., 2018). Initially used to assess the factors controlling the thermal degradation of kerogen and the processes behind oil and gas generation (Behar et al., 1992; Lewan, 1997, 2008, 2010), previous studies reveal that the conditions under which these experiments were carried out (confinement pressure, temperature-duration pairs, presence of excess water etc.) may strongly influence the OM thermal degradation (Monthioux, 1988; Michels et al., 1992, 1994; Landais et al., 1994; Michels et al., 1995) and thus, potentially affect the evolution of porosity. Hence, the conditions used during this work where carefully selected based on the results available in the literature. The causes of this choice are outlined below.

Choice of thermal maturation conditions

While pressure is not considered as a major control factor on OM thermal degradation, previous investigations suggest that confined systems (under 300-700 bars) provide good results compared to closed systems (Fig. 3.2, Monthioux, 1988; Michels et al., 1994).

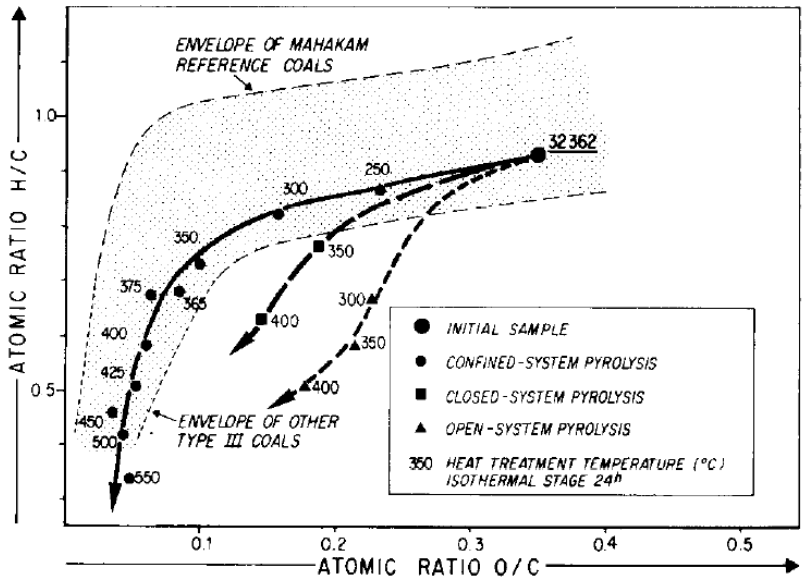

Fig. 3.2. Influence of confinement during artificial thermal maturation of Mahakam Coals (from Monthioux, 1988).

In confined systems, a hydrostatic pressure is applied on gold cells. However, contrary to hydrous systems, there is no contact between the pressurizing fluid and samples. The pressure is thus transmitted inside the gold cells via the products (CO_2, H_2O, etc.) generated by the thermal transformation of both OM and minerals (Landais et al., 1994). Under the low temperatures of natural basins, the kerogen is considered to be a closed and condensed systems able to maintain strong effluents partial pressures (Monthioux, 1988). But, under the high temperature required for laboratory simulations, the kerogen structure is dissociated and artificial confinement appears necessary to ensure a close contact between the products to allow kerogen transformations (Monthioux, 1988). For these reasons, confined artificial thermal maturation conditions were selected for this work.

Water is commonly present within the porosity of reservoir systems and is often considered to be the main source of hydrogen during OM thermal degradation processes (Lewan, 1997). However, the results from Landais et al. (1994) suggest that in sufficiently confined systems, no excess of water is necessary to simulate adequately OM thermal maturation. Furthermore, previous studies have demonstrated that the high temperature of laboratory experiments may greatly enhances the ability of water to enter the OM pore network, modifying the reactions between organic species (Michels et al., 1995; Lewan, 1997) and delaying the conversion of kerogen (Landais et al., 1994). Under the lower temperatures (60-150°C, Tissot and Welte, 1984) of sedimentary basins, the solubility of organic compounds is limited, and a lower amount of water is available for hydrogen exchange reactions (Michels et al., 1995). To limit these effects which can modify kerogen conversion processes and porosity during maturation, to use anhydrous artificial maturation conditions were preferred for this PhD work.

OM thermal degradation processes are governed by first order Arrhenius law, an infinity of duration-temperature pairs could thus be used to reach a similar rank of maturity (Wood, 1988; Landais et al., 1994). However, previous studies show that experimental temperature and duration are not really exchangeable parameters during artificial thermal maturations (Landais et al., 1994). These authors show that increasing thermal maturation duration and lowered experimental temperatures could influence the composition, the yield and the timing at which gas and bitumen are generated. To investigate the effect of the temperature-duration pairs choice of thermal maturation experiments on OM thermal degradation processes and, especially, on pore development, two series of laboratory simulation, a shorter (72 hours) and a longer (104 days), were carried out.

Experimental device and sample preparation

The first series of anhydrous confined thermal maturation was conducted simultaneously on about 1 g of six total rocks crushed into powder (< 250 µm) and on a small-diameter rock cylinders (5 mm in diameter; 1.5 cm in length, drilled perpendicular to the bedding) placed and sealed under argon atmosphere inside gold cells (L = 6.5 cm, i.d = 0.5 cm, wall thickness 0.45 mm, Fig. 3.3).

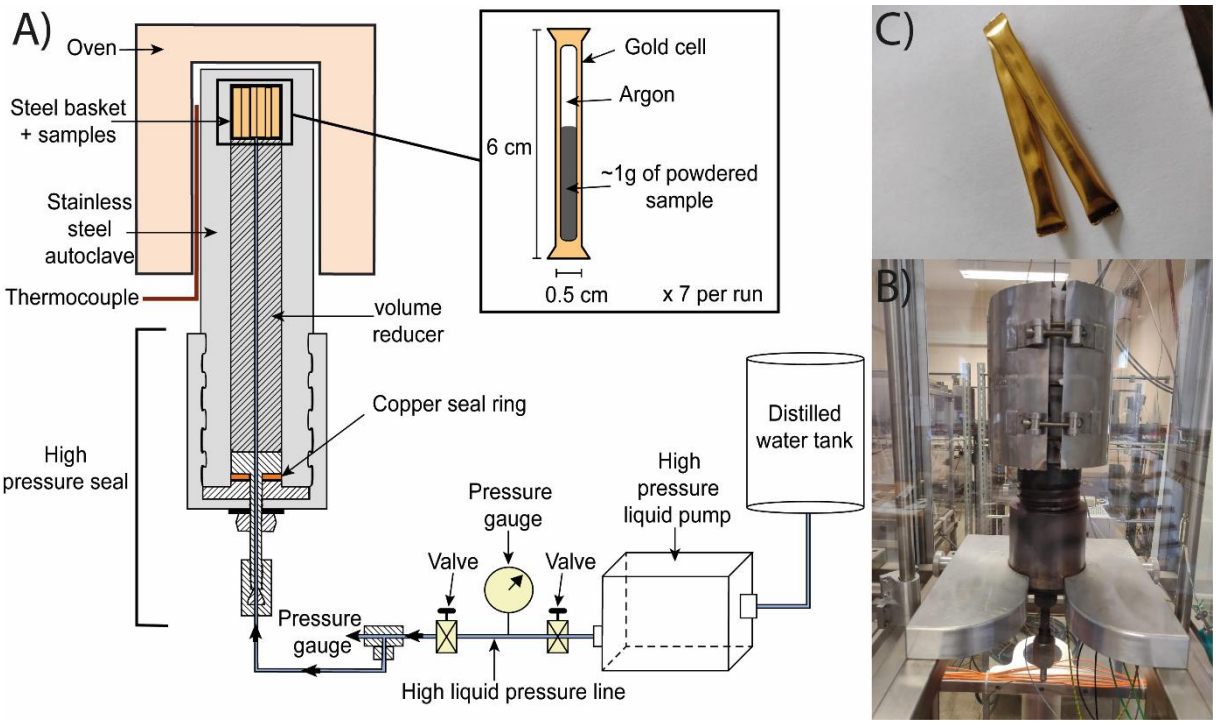

Fig. 3.3. A-B) Laboratory anhydrous confined thermal maturation system. The high-pressure stainless-steel autoclave is held vertically during heating. C) Gold cells used for thermal maturation experiments.

The small rock cylinders will be used for petrographic observations while powdered samples will be utilized for nitrogen adsorption measurements, GC-MS, GC-TCD analyses and Raman Spectroscopy. The selection of the six samples used for laboratory simulations was based on the results on palynofacies and Rock Eval analysis in order to cover a wide range of TOC and kerogen composition. The second series was conducted on the three powdered samples of this group which exhibit the best representative TOC and OM composition of the all series. Prior to loading the samples, open-ended tubes were heated to 550°C and washed with hydrochloric acid to remove potential organic material contaminants. The samples were dried 12 hours at 105°C to remove any potential free or adsorbed water. The cells were welded using an argon-arc welder and introduced into high-pressure stainless-steel autoclaves

pressurized with water inserted into a pyrolysis oven (Fig. 3.3). The temperature of the system was raised at 4.5°C min^{-1} to the final temperature. To avoid any rupture of the gold cells, a constant hydrostatic external pressure of 600 bars (pressure comparable with that observed at 2-4 km depth in natural sedimentary basins) was exerted on the samples by a system of valves connected to a pump during the experiments (Fig. 3.3A).

For the first/shorter thermal maturation series, the samples were then heated under isothermal conditions at temperatures ranging from 325°C to 470°C for 72 hours to reach five thermal maturities ranging from the early oil generation to the dry gas zone (Fig. 3.4). For the second series of laboratory simulation, samples were heated at temperatures ranging from 283°C to 390°C for 104 days in order to reach three thermal maturities equivalent to those previously reached by shorter duration experiments (Fig. 3.4). The temperatures used for these experiments were based on the results of Landais et al. (1994). At the end of the run, the oven was turned off and the autoclaves were slowly depressurized to avoid the rupture of the cells. The gold cells were then recovered and carefully cleaned with dichloromethane and sealed in separate glass bottles to collect gases.

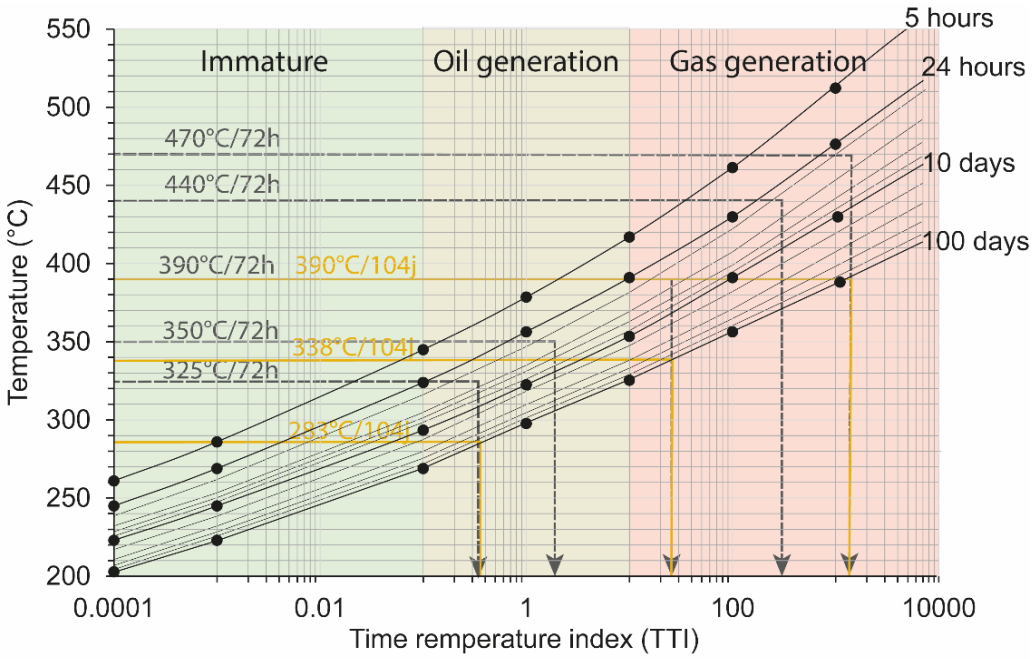

Fig. 3.4. Relation between maturity (expressed as time temperature index), experimental artificial thermal maturation temperature and duration. Grey: experimental duration-temperature pairs used for the shorter series (72 hours) of thermal maturation. Orange: experimental duration-temperature pairs used for the longer series (104 days) of thermal maturation. This chart was drawn after the data of Landais et al. (1994).

3.1.2. X-ray diffraction (XRD)

Inorganic constituents were analyzed by XRD carried out on natural and artificially matured total crushed samples (< 250 µm) and clay fraction-oriented slides to assess both the global mineralogy and the composition of clay minerals. Total rock powder analyses were conducted under Cobalt radiation using an INEL® diffractometer equipped with a CPS120 curved detector. The immature samples chosen for these analyses were selected throughout the entire Marton, Ebberston and VMF series to cover a wide range of depth and TOC contents. Relative mineral percentages were semi-quantified using the area under the curve for major diffraction peaks of each mineral and were then corrected using 4 artificial standard samples (laboratory mixtures with known abundances of mineral standards). This method, based on Fisher and Underwood (1995), assumes that there is a quantifiable relationship between peak area and the relative abundance of each mineral and that the factors are constant. This allows conversion from XRD to mineral abundances (Fisher and Underwood, 1995). The results were then normalized to 100% after TOC contents determined by Rock Eval pyrolysis. Based on the analysis of standard samples, the reproducibility averaged ± 3.7 wt.% for quartz, ± 4.9 wt.% for total carbonate, ± 1.3 wt.% for pyrite, ± 3.2 wt.% for gypsum, ± 4.4 wt.% for total clay and ± 8.3 wt.% for albite.

To prepare oriented clay slides, rock powders were firstly decarbonated and decarbonized by hydrochloric acid (37%) and hydrogen peroxide (30%) treatments respectively. The remaining fractions were then suspended into ultra-pure water and introduced in dialysis membranes placed in ultra-pure water baths to remove chloride ions. The water baths were changed every 12 hours up to the removal of all chloride ions (negative silver nitrate test). Samples were then left to decant for 12 hours in ultra-pure water. The suspension, which contains the purified clay fraction, was recovered, dried (50°C) and served then to carry out the oriented slides (Fig. 3.5). Two oriented slides were realized per samples, one was air-dried, and the other was treated with ethylene glycol to cause the swelling of clays. The analyses of the oriented slides were then conducted under copper radiations using a THERMO Fisher Scientific ARL X'TRA® diffractometer sets in a theta-theta Bragg-Brentano geometry. After the analyses, the slides treated with ethylene glycol were reanalyzed after to be heated at 550°C for 1 hours to allow the identification of kaolinite.

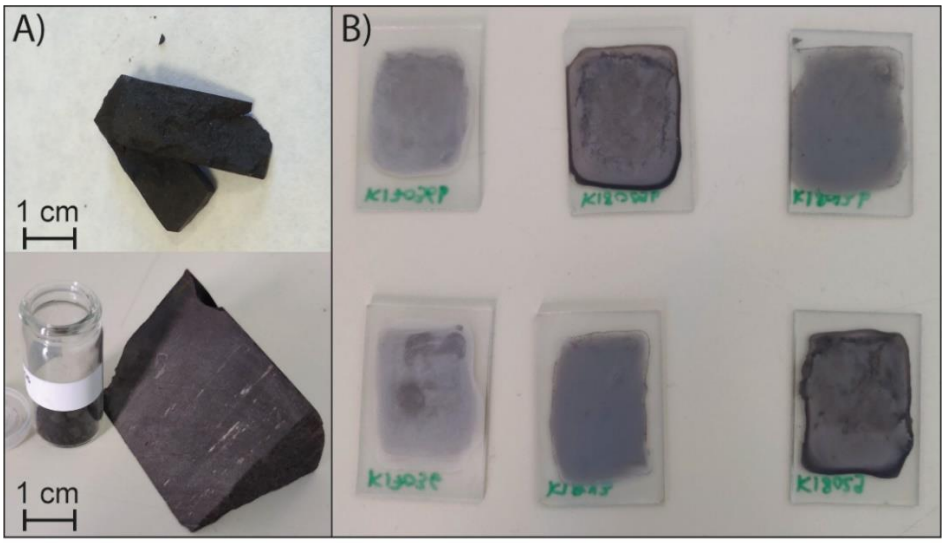

Fig. 3.5. A) Original natural samples and powdered sample. B) Clay mineral-oriented slides prepared for XRD analyses.

3.1.3. Petrography

3.1.3.1. Light microscopy

Maceral composition

The observation of polished sections (non-covered) under reflected light and UV-excitation is a useful technique to identify the in-situ OM components of rocks. These observations make possible to distinguish marine and terrestrial OM but also to differentiate primary kerogen, the OM having undergone diagenetic transformations, bitumen or pyrobitumen. To identify the different macerals of natural and artificially matured samples and their evolution with increasing thermal maturity, petrographic observations were carried out on bulk rock polished sections under oil immersion using both reflected light for the reflectance and UV-excitation for fluorescence (Leica® DMRX microscope). Polished sections of VMF, natural and artificially matured KCF samples were made from small sample blocks cylinders impregnated with epoxy resin (Fig. 3.6). The immature KCF thin sections used in this study were previously analyzed in Boussafir et al. (1995a) and (Boussafir and Lallier-Vergès, 1997).

To facilitate broad-beam argon-ion milling, the bulk rock sections were prepared by mechanical polishing perpendicular to bedding, using first abrasive grinding paper (up to P4000) and then alumina polishing suspensions (up to 0.04 µm). To improve the quality of this pre-polishing for SEM observations, each polished section was then argon-ion milled at 5 kV

for 1 hour (6*10 minutes separated by 10-minute breaks to avoid intense heating on the sample surface and the creation of artefacts). The sample rotation speed was set as 20 rpm and a 4° tilt rock angle were applied. Finally, samples were argon-ion milled 30 min (3*10 minutes) at 2 kV using a current of 220 µA (Gatan PECS model 682).

Fig. 3.6. Polished sections prepared from thermally matured KCF mudstones cylinders

Palynofacies analysis

Palynofacies analysis consists in the identification of plant debris, amorphous organic components, individual palynomorph as well as their relative proportions and their preservation states (Combaz, 1980). In complement with Rock Eval, this is a good tool to identify the OM depositional environment and evaluate its potential of bitumen and gas generation. In the present study, palynofacies analysis was carried out on the isolated kerogen (and the associated metal sulphides) of all immature KCF samples. The OM was isolated by a classical fluoridric/hydrochloric acid treatment according to Boussafir et al. (1995a, b). This microscopical examination enabled the relative proportion of the organic components of all immature KCF samples to be assessed. The observations were done using transmitted light under oil immersion with a 50× magnification objective (Leica® DMRX microscope). The quantification was considered as effective when at least a total of 500 particles were counted for each sample.

Vitrinite reflectance

Vitrinite reflectance measurements consist in the measure of the percentage of incident light reflected by the surface of vitrinite particles in a rock. Vitrinite is a type of maceral formed from humic gels derived from the ligno-cellulosic OM of higher plants (Teichmüller, 1989). This parameter is closely tied with thermal maturity. Vitrinite reflectance is thus a useful tool to estimate the thermal maturity of OM in sedimentary rocks. Where possible, measurements

of vitrinite reflectance (Rm) were carried out from bulk rock polished sections in order to confirm calculated/equivalent vitrinite reflectance (Rc, see paragraph 3.1.4). Measurements were carried out using a Leica® DMRX microscope equipped with a photometer and an 50x oil-immersion objective. Mean reflectance values were determined using at least 50 measurements. Calibrations were carefully made using glass-reflectance standards (Robert, 1971; Bertrand et al., 1993). Due to the very low content of vitrinite in the samples, only a few vitrinite reflectance values can be measured.

3.1.3.2. Scanning electron microscopy (SEM)

In complement to light microscopy, SEM was used to observe the OM surface texture and porosity of natural and artificially matured samples. SEM is based on the electron-matter interaction. An electron gun sends an ion beam toward the sample surface. The interaction between these electrons and the atoms of the rock causes the re-emission of different compounds including backscattered electrons (BSE) and secondary electrons (SE). The number of backscattered electrons increases with the atomic mass average of the observed section. BSE allow thus the differentiation of rock components. Heavier elements appear thus in white or light grey whereas, lighter components (such as OM appears) in dark grey. SE consist of low energy electrons emitted by the surface layers of the sample. The intensity of this radiation is thus directly controlled by the distance to the detector and thus to the rock surface texture. Hence, scanning electron microscope (SEM) observations were conducted using both BSE and SE modes to image the surface texture of samples and to assess the evolution of the OM texture with increasing thermal maturity. These analyses were carried out using a SEM Merlin Zeiss® equipped with an in-lens secondary electron detector at a working distance of 7.7 mm at 13 kV. The observations were conducted on the argon-ion beam polished sections of natural and artificially matured samples (Fig. 3.6) but also on the isolated kerogen of thermally matured KCF samples.

The estimation of the relative abundance of each type of particles observed in SEM on polished sections of thermally matured samples was performed at a 1250x magnification on 12 to 15 observation areas randomly distributed all across the samples. Pore size measurements were done from zooms of these same observation areas. BSE and SE were both used during quantification to clearly discriminate OM and pores. Quantifications were done by superimposing on each observation area a 57 µm square grid divided into 36 units of 9.3*9.3 µm. The total number of units occupied by each particle type was then counted for each sample

allowing the estimation of their relative abundance. The quantification was considered as affective when at least a total of 400 units were counted for each sample.

3.1.4. Organic geochemistry

Rock Eval pyrolysis

Rock-Eval pyrolysis is a classical method for determining the amount, type, hydrocarbons-quality and thermal maturity of OM preserved in source-rocks and sediments. Depending on the estimated OM content, 50 to 60 mg of dried sediment was used for new Rock-Eval 6® (Vinci Technologies, Rueil Malmaison) analysis. The pyrolysis program under inert gas (N_2) started with an isothermal stage (2 min. 200°C). Then, the oven temperature was raised at 30 °C/min to 650 °C (held 3 min). The oxidation phase corresponds to an isothermal stage at 400 °C, then the temperature was raised at 30 °C min^{-1} to 850 °C (held 5 min) under purified air. The significance of classical Rock-Eval parameters was explained by Espitalié et al. (1985a, b). The specific parameters given by the new Rock-Eval 6 device were presented by (Lafargue et al., 1998). The Rock-Eval parameters used here were: (i) total organic carbon (TOC, wt.%), which expresses the quantity of OM calculated from the spectrum integration of S_1, S_2 , S_3 which are respectively, free hydrocarbons, pyrolizable hydrocarbons, CO and CO_2 produced by the breakdown of kerogen under inert gas flux, and S_4 peaks which corresponds to the CO and CO_2 produced by pyrolysis and oxidation of residual carbon under purified air flux; (ii) the hydrogen index (HI, mg HC /gTOC), i.e. the amount of hydrocarbon (HC) produced during pyrolysis (S_2); (iii) the oxygen index (OI, mg CO_2 /gTOC), which is calculated from the S_3 peak and represents the oxygenated quality of OM; (iv)) T_{max} , which is deduced from the T_{pic} of Rock-Eval VI. T_{pic} is the temperature of the peak oil production during pyrolysis. T_{max} is often used as an OM maturity indicator (Espitalié et al., 1985a, b); (v) the production index ($PI=S_1/S_1+S_2$), an indicator of free petroleum content which naturally evolves as a function of maturity. (vi) the RC/TOC which represent the relative proportion of residual/inert carbon (RC) in samples. This ratio tends to increase with increasing thermal maturity.

Molecular organic matter composition

To analyze permanent and condensable gases (CO_2, C_1, C_2-C_5 n-alkanes), the gold tubes were pierced under vacuum in a glass bottle after maturation. 2 cm^3 of gases (at atmospheric pressure) were sampled with a gastight syringe and injected in a GC-TCD for characterization.

The molecular composition of the gas produced during maturation was determined using a Perkin Elmer® Clarus 580 gas chromatograph fitted with a Supelco® Carboxen 1010 Plot® Capillary column (30 m × 0.53 mm i.d., 0.15 µm film thickness). For the analysis, the temperature was held at 35°C for 5 min and then increased at 20°C.min^{-1} to 240°C. The final isotherm was held at 240°C for 40 min. The GC-TCD was purged before each analysis with an isothermal temperature held at 240°C for 25 min to avoid any contamination between samples. Helium was the carrier gas. Samples were injected splitless with the injector temperature set at 240°C. For the identification and quantification of H_2O, CH_4, CO_2, C_2H_6, C_3H_8, C_4H_{10} and C_5H_{12} concentrations, calibration curves were made using standard gases. The total number of moles of gas was quantified assuming ideal gas behavior and using their respective peak areas on chromatograms. H_2S was not quantified.

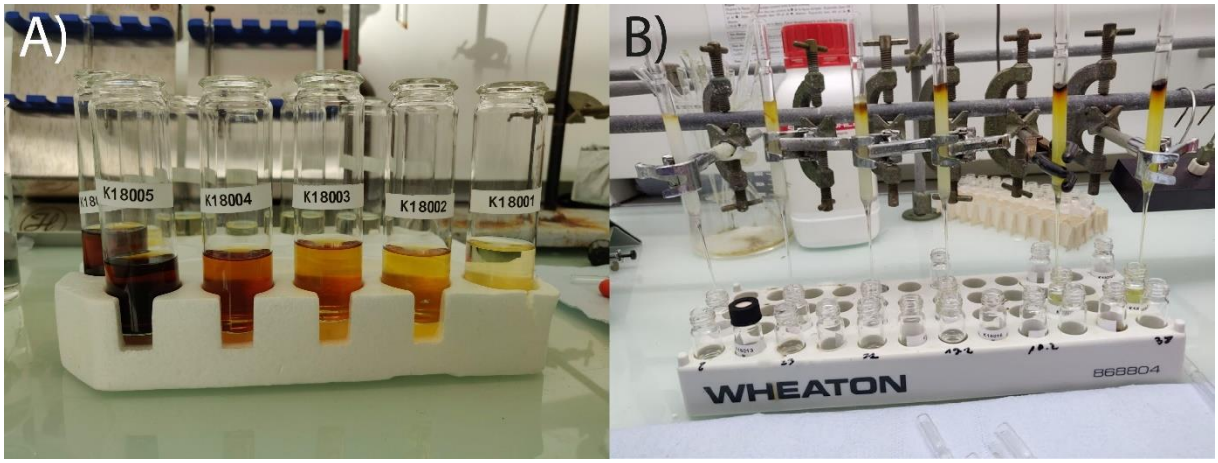

Fig. 3.7. A) Example of bitumen fraction obtained after dichloromethane/methanol extraction. B) Separation of bitumen into saturated, aromatic and polar fractions using deactivated silica gel chromatography column.

To quantify and assess the evolution of saturated (SAT), aromatic (ARO) and polar (POL) hydrocarbon concentrations of each KCF sample during thermal maturation, about 1g of each powdered sample was ultrasonically extracted (7×10 min) with a mixture of dichloromethane/methanol (1/1, v/v). After centrifugation, the supernatants were combined (Fig. 3.7), dried under nitrogen and weighed to determine the weight of the total extractible bitumen (EB). The extracts were desulfurized on copper and separated into SAT, ARO and POL fractions by a deactivated silica gel (5% with water) chromatography column (Fig. 3.7). The SAT (saturated hydrocarbon fraction) was recovered by elution with heptane. The ARO (aromatic HC) were recovered by the subsequent elution of a mixture of heptane/toluene (3/1) and (2/2). The POL (Polar HC) were recovered by elution with methanol. By difference of mass between the sum of the weight of POL, ARO and SAT and the weight of the total extract, the

amount of asphaltenes were determined and summed with the POL fraction. After removal of the solvents, each fraction was dried under nitrogen and weighed to obtain the total extracted mass of saturated, aromatic and polar compounds. The SAT and the ARO were then analyzed by Gas Chromatography-Mass Spectrometry (GC-MS).

GC-MS was performed on a Trace-GC Ultra gas chromatograph (GC) coupled to a TSQ Quantum XLS mass spectrometer fitted with an AS 3000 auto sampler (from Thermo Scientific). The GC was equipped with a Thermo Trace-Gold 5 MS capillary column (60 m × 0.25 mm i.d, 0.25 film thickness). The GC operating conditions were as follows: temperature held at 80°C for 1 min, then increased to 120°C at 30°C.min^{-1} and from 120°C to 300°C at 3°C. min^{-1}. The final isotherm was held at 300°C over 68 min. The sample was injected in splitless mode with an injector temperature set at 280°C. Helium was the carrier gas. The mass spectrometer was operated in the electron ionization mode at 70 eV ionization energy and scanned from m/z 50 to 600. The different molecular components were identified by comparison of their retention times and mass spectra with available published data and their concentrations were calculated accordingly using their respective peak areas in mass chromatograms. Squalane was used as internal standard.

Thermal maturity

Measurements of mean equivalent reflectance values of thermally matured KCF rocks (calculated vitrinite reflectance, Rc, %) were determined using the methylphenanthrene index (MPI-1), dimethylphenanthrene ratio (DPR) and methyldibenzothiophene ratio (MDBR) after the equation of Radke et al. (1986) and Boreham et al. (1988) (Eq.3.1 to 3.6). To this aim and to avoid possible coelutions, Phenanthrenes (Phe), dibenzothiophenes (DBT) and their methylated derivatives were quantified using the peak area on ion specific chromatograms (m/z 178+192+206 and m/z 184+198+212 respectively).

$$\mathrm{MDBR} = \frac{4.\,\mathrm{MDBT}}{1.\,\mathrm{MDBT}} \qquad \textit{(Eq. 3.1, Boreham et al., 1988)}$$

$$\mathrm{MDBR\ Rc\ \%} = 0.40 + 0.30 \times \mathrm{MDBR} - 0.094 \times \mathrm{MDBR}^2 + 0.011 \times \mathrm{MDBR}^3 \qquad \text{(Eq. 3.2, Boreham et al., 1988)}$$

$$DPR = ((2{,}6.DMP + 2{,}7.DMP + 3{,}5.DMP)/((1{,}3.DMP + 1{,}6.DMP + 2{,}5.DMP + 2{,}9.DMP + 2{,}10.DMP + 3{,}9.DMP + 3{,}1.DMP)) \qquad \text{(Eq. 3.3, Radke et al., 1986)}$$

$$DPR\ Rc\ \% = 1.50 + 1.34 \times log10\ (DPR)$$ (Eq. 3.4, Radke et al., 1986)

$$MPI.1 = 1.5 \times (2.MP + 3.MP) / (Ph + 1.MP + 9.MP)$$ (Eq. 3.5, Radke et al., 1986)

for Ro ≤ 1.4%, $MPI.1\ Rc\ (\%) = 0.7 \times MPI.1 + 0.22$

for Ro ≥ 1.4%, $MPI.1\ Rc\ (\%) = -0.55 \times MPI.1 + 3.0$ (Eq. 3.6, Radke et al., 1986)

Where MDBT are methyldibenzothiophenes, DMP are dimethylphenanthrenes and MP are methylphenanthrenes.

3.1.5. Porosity measurements

Mercury intrusion porosimetry (MIP)

MIP is a powerful but destructive technique to assess the open porous meso and microporous structure of solid materials (pore throat between 250 µm to 6 nm). This method is based on the intrusion of mercury under a controlled pressure into a solid sample structure. The PSD of macropores and large mesopores were measured by MIP using a Micrometrics® Autopore IV 9500 porosimeter. Due to its non-wetting properties, mercury do not spontaneously penetrate pores by capillarity. The intrusion of mercury was thus forced into the pores by the application of a controlled external pressure. The equilibrate pressure required for the intrusion of mercury is inversely proportional to the pore sizes. With the volume of intruded mercury at a given pressure, it is thus possible for the apparatus to quantify the pore volume and to assess the pore size distribution (PSD). For these analyzes, about 1.5 g of sample was crushed into fragments (~2 mm in diameter), degassed under vacuum at 105°C for 24 h and intruded with mercury up to 60,000 psia (414 MPa). The equilibration time was set to 10 s. Penetrometers with a stem volume of 0.390 cm^3 were used for the analysis. The pore throat radius was calculated assuming cylindrical pores by the Laplace-Washburn equation (Eq. 3. 7, Washburn, 1921):

$$p = -\frac{2\gamma \cos\Theta}{r}$$ (Eq. 3.7, Washburn, 1921)

Where p the absolute applied pressure, r the pore radius, γ the mercury surface tension (≈0.48 N/m) and Θ the mercury contact angle (≈ 140°). Measurements were then corrected for conformance errors (Sigal, 2009). MIP is destructive and required relatively high amounts of

materials, this method was thus only used for natural samples for which the quantity of samples was not limited.

Nitrogen adsorption measurements

Nitrogen adsorption is a widely used technique for the characterization of various porous materials including mudstones (Kuila and Prasad, 2013; Tian et al., 2015). The surface adsorption capacity of nitrogen in the surface of a solid material depends on the relative pressure of nitrogen P/Po. P is the nitrogen partial pressure and Po the saturated vapor pressure of nitrogen at 77K (temperature of liquid nitrogen). While MIP gives information on the meso- and the macroporosity, nitrogen adsorption gives information regarding the mesoporosity (2-50 nm) and the microporosity (<2 nm). As all gas adsorption methods, nitrogen adsorption is based on the theory of gas adsorption on solid surfaces. The curve showing the variation of the equilibrium adsorption capacity as a function of pressure is the adsorption isotherm. The analysis of this adsorption isotherm using different methods can allow the calculation of the specific surface area or the pore size distribution of porous materials.

For the shorter thermal maturation series and natural samples, low-pressure nitrogen adsorption measurements were carried out on a Quantachrome® NOVA 2200^{e} apparatus at 77K to measure the pore size distribution (PSD), the specific surface area and the volume of mesopores to large micropores. About 1 g of sample was powdered (<250 µm) and outgassed under vacuum at 105 °C for 24 h before analysis. Adsorption-desorption isotherms were obtained under the relative pressure P/Po ranging from 0.003 to ≈0.99. An equilibration time of 100 s was applied during the analysis. The total pore volume was determined after the liquid molar volume adsorbed at the relative pressure P/Po of 0.987. The specific surface area was determined using the Brunauer, Emmett and Teller method (BET) for adsorption in the best linear range between the relative pressure P/Po 0.03 and 0.33 (Brunauer et al., 1938). A minimum of 13 points was used for the BET surface-area analysis. The PSD was determined using the Barrett, Johner and Halenda (BJH) method (Barrett et al., 1951) between P/Po ranging from 0.042 and 0.993. This method was applied from the adsorption isotherm to avoid tensile strength effect phenomena that occur during desorption. The pore volume and the specific surface area of micropores were calculated from the t-plot method using the universal t-curve based on the Harkins-Jura model (De Boer et al., 1966), which was the most frequently used in the community.

For the analyses of the longer thermal maturation series, the remaining samples mass was not sufficient to allow a good estimation of the total pore volume with the Quantachrome® NOVA 2200^{e} apparatus. The analyses were thus conducted on a Micromeritics® ASAP -2420 apparatus at the Mulhouse Materials Science Institute (IS2M). Before analysis, the powdered samples were firstly oven-dried 48h at 105°C and outgassed at 65°C for 48 hours under vacuum in the apparatus. Adsorption and desorption isotherms were obtained at 77K. The relative pressure (P/P_o) ranges from 0.001 to ≈0.99 and an equilibration time of 10 s was applied during the analysis. Total pore volumes were determined after the liquid molar volume adsorbed at P/P_o = 0.993. The single point surface area at was determined at P/Po=0.320. To allow comparison with shorter maturation experiments, the same methods were used to determine the specific surface area (BET), the PSD (BJH) and the micropore volume and specific surface area (Harkins Jura model, HJ, see above). However, new methods were tested for a better estimation of the micropore volume and distribution. Hence, the PSD was also determined using the density functional theory (DFT) method (Webb and Orr, 1997), most suitable for the assessment of the microporosity. DFT method for slit-like pores was used. An infinite size slit distribution on a generic surface has been found to be most relevant for DFT distribution. An adjustment rate R of 0.01 was applied in order to eliminate the data out-of-model (zero point of the distribution). The microporosity was determined using the Dubinin-Radushkevich equation (DR, Dubinin, 1947) which is a common approach for the characterization of microporous carbons (Dubinin, 1966; Rouquerol et al., 2013). This method was applied between P/P_o ranging from 0.0001 and 0.01.

Clarkson et al. (2013) suggested that pore throats obtained by MIP are similar to pore bodies for some pore geometries including silt pores. In theory low-pressure nitrogen adsorption measurements and MIP should thus give similar results. Accordingly, pore throat size is often considered to be similar to pore size in shales (Wang et al., 2014). Kuila and Prasad (2011) showed that PSD curves from MIP and nitrogen adsorption exhibit a good correlation. Therefore, pore throat size from MIP was used as pore size in this study for convenience when comparing the nitrogen adsorption data.

3.2. Characterization of isolated kerogen

After thermal maturation, the kerogen of the sample containing the most intermediate OM composition of the all KCF studied series was isolated by fluoridric/hydrochloric acid

treatments at different range of thermal maturity and characterized by a combination of different techniques.

3.2.1. Raman spectroscopy

Sensitive to the molecular vibrations of specific chemical bonds, Raman spectroscopy can give information on the evolution of the organic-matter chemical structure during thermal maturation (Tuinstra and Koenig, 1970; Beyssac et al., 2002; Sadezky et al., 2005; Romero-Sarmiento et al., 2014; Keel, 2015; Schito et al., 2017). During Raman analysis, source of monochromatic light interacts with molecular vibrations of the sample resulting in the shift of energy of the re-emitted photons. This shift in energy can give useful information concerning the vibrational modes in the system and the chemical structure. Generally used to characterized the degree of organization of carbonaceous materials and evaluate the variations of metamorphic grade of carbon-rich metasedimentary rocks (Beyssac et al., 2002; Lahfid et al., 2010; Kouketsu et al., 2014), this method was also frequently used for the characterization of low-mature to gas-mature mudstones these last few years (Quirico et al., 2005; Liu et al., 2013; Romero-Sarmiento et al., 2014; Keel, 2015; Sauerer et al., 2017; Schito et al., 2017; Cheshire et al., 2017). Moreover, some studies showed that a relatively good correlation exists between some Raman parameters and OM thermal maturity allowing the estimation of the vitrinite reflectance (Quirico et al., 2005; Sauerer et al., 2017; Schito et al., 2017; Cheshire et al., 2017).

In order to assess the variations of kerogen chemical structure Raman spectroscopy was performed on artificially matured KCF isolated kerogen samples using a confocal Raman Renishaw® InVia Reflex micro-spectrometer. A 514.5 nm argon laser focused by a Leica® DM2500 microscope with a 100× magnification objective was used as the light source. The intensity of the laser power was set as 0.1% (=0.05 mW). Data were collected over the first order Raman spectrum (700 to 2300 cm^{-1}). These analyses were done at the BRGM in Orléans. For these analyses, the isolated kerogen powders were past on slides without any other preparation. For each sample, height measurements were performed on randomly selected areas on all the sample surface to ensure reproducibility of measurements and estimate standard errors. Each spectrum is the average of at least 10 scans. The Raman spectra were analyzed using PeakFit software. As suggested by Schito et al. (2017), the curve fitting and the deconvolution of bands were performed using mixed Gaussian-Lorentzian band profiles applied to six peaks and using a linear baseline. This appears to be the best solution to obtain

the better correlation with the Raman spectra using the minimum number of components. All spectra were deconvoluted using the same procedure.

3.2.2. Petrography

Scanning electron microscopy (SEM)

SEM observations were conducted using secondary electron (SE) modes to image the surface texture and assess the evolution of the isolated kerogen texture with increasing thermal maturity. These analyses were carried out using a SEM Merlin Zeiss® equipped with an in-lens secondary electron detector under the same conditions as previously used for total rocks. Isolated kerogen powder was fixed to SEM stubs with a cupper paste and coated with carbon (Fig. 3.8).

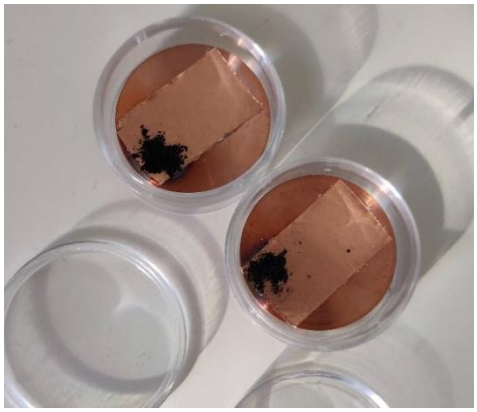

Fig. 3.8. Isolated kerogen from thermally matured KCF samples fixed to SEM stubs with cupper paste for SEM observations.

Transmission electron microscopy (TEM)

Transmission electron microscopy (TEM) is a major analytical technique used by many scientific fields such as in the chemical, biological or physical sciences. During TEM observations, a beam of electrons is transmitted through a very thin sample, generally an ultrathin section (< 100 nm thick), to form an image. This image result from the sample-electron interaction. These interactions between sample atoms and electrons can be used to observe the structure of OM particles at the nanoscopic scale (Boussafir et al., 1995b; Romero-Sarmiento et al., 2014; Keel, 2015). This method could be thus a powerful technique to assess the structure of isolated kerogen at the nanometer scale, its evolution with increasing thermal maturity and its possible link with porosity.

Hence, TEM observations were performed under 200 kV using a Philips® CM20 Transmission Electron Microscope, equipped with a LaB6 filament and an EDX detector (Interfaces, Containment, Materials and Nanostructures (ICMN), Orléans). The observations were conducted on ultrathin sections prepared from the isolated kerogen of one representative KCF samples at different thermal maturity. For these observations, isolated kerogen was prepared as follows: the kerogen was included in a 15 $g.L^{-1}$ agar-agar solution. After the cooling and the hardening of the agar-agar, samples were recut into small cubes (≈2 mm side) to ensure a good concentration of kerogen particles. The samples were then placed into glass tubes (≈2 mL) and immersed into a phosphate buffer solution.

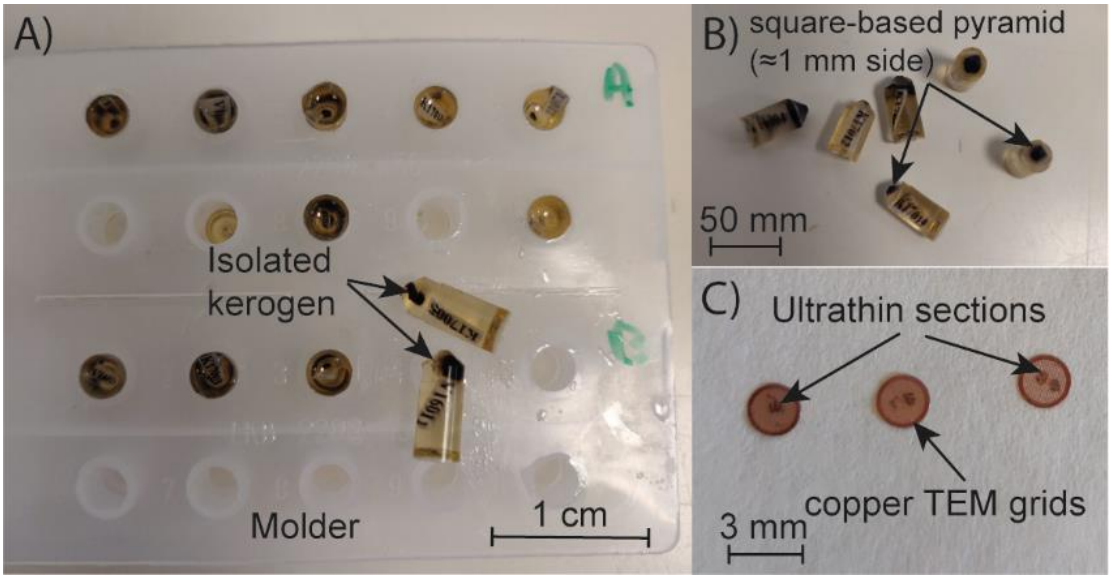

Fig. 3.9. A) Isolated kerogen samples inclusions. B) Samples carves into square-based pyramid for the preparation of ultrathin sections. C) Ultrathin sections on copper TEM grids.

The buffer solution was then replaced by osmium tetroxide (2%) for 5 hours for the fixation of OM. In creating artificial crosslinking in OM, the chemical fixation makes the organic molecules insoluble in water and in the organic solvents used during dehydration (alcohol, acetone etc.). According to the technique described by Boussafir (1994), the fixed samples were then dehydrated using a series of increasing acetone water solutions with percentage steps ranging from 10% to 100% and embedded in Low Viscosity Resin LV (Agar Scientific®) with a series of acetone/resin mixtures in the proportions 3:1 (for 12 hours) and 2:1 (for 24 hours) followed by a pure resin bath (24 hours). The samples were finally put in molds filled of pure resin and left to harden at 60°C in an oven for 48 hours (Fig. 3.9). The top of the samples was then carved into a square-based pyramid of about ≈1 mm side using a pyramidotome to facilitate the cutting of ultrathin sections. Ultrathin sections (about 0.5 nm thick) were then made using

a Diatome diamond knife mounted on an ultramicrotome (Centre de Microscopie Electronique, university of Orléans) and placed on copper TEM grids (Fig. 3.9).

3.2.3. Small-Angle -X-ray scattering (SAXS)

To assess the evolution of the total porosity of the isolated OM during maturation, small angle X-ray scattering (SAXS) experiments were performed on the ICMN device equipped with an X-ray tube delivering a monochromatic Cu Kα wavelength beam (λ=0.1541 nm^{-1}). The powdered isolated kerogen was placed into thin walled capillary glass tubes of 1 mm in diameter. These tubes were flame-sealed and placed vertically in a metal holder and investigated at room temperature (25 °C). The beam height on the capillary was about of 0.8 mm. According to the configuration of the apparatus (http://www.icmn.cnrs-orleans.fr/?SAXS-GISAXS), the scattering intensity of the sample was recorded by a 2D detector as a function of the diffusion vector q in the range 0.04 <q <7.5 nm-1 which corresponds to a pore size comprised between 0.8 to 160 nm in diameter. After the treatment of the raw data (angular summation of the 2D images, capillary scattering, thickness and adsorption correction), the scattering intensity was expressed as a function of the scattering vector q (q=4π sin θ/λ). SAXS data were presented as curves showing the logarithmic scattering intensity as a function of the magnitude of the scattering vector. After the correction of the scattering intensity in assuming a pore-matter system (see Cohaut et al., 2000), the porosity (P), the specific surface area (Sv), and the mean chord in pores ($\overline{l_p}$, mean pore size in nm) were calculated from the scattering power Q using the following equations (Cohaut et al., 2000):

$$Q = \int_{qmin}^{qmax} q^2 . I(q). dq = 2\pi Ie. Io. \Delta\rho^2 P(1-P)$$

$$Sv = \frac{4.P}{\overline{l_p}}$$

Where Ie is the Thomson factor, Io the incident beam intensity, $\Delta\rho^2$, the pores-matter electronic contrast calculated from the elemental composition of the kerogen (see below) assuming a maximum kerogen density of 2 cm3/g. Elemental analyses (C, H, N, S) were carried out on the studied samples using a Thermo Scientific Flash 2000 organic analyzer on three replicates and assuming an analytical error of ±0.05 %. The weight obtained after analysis were normalized to 100%. The oxygen content was graphically determined from H/C and mean calculated

vitrinite reflectance (Rc) using the Van Krevelen diagram (Fig. 3.10). These analyses permit also to compare the progressive evolution of the chemical composition of kerogen with SAXS porosity and Raman spectra during thermal maturation.

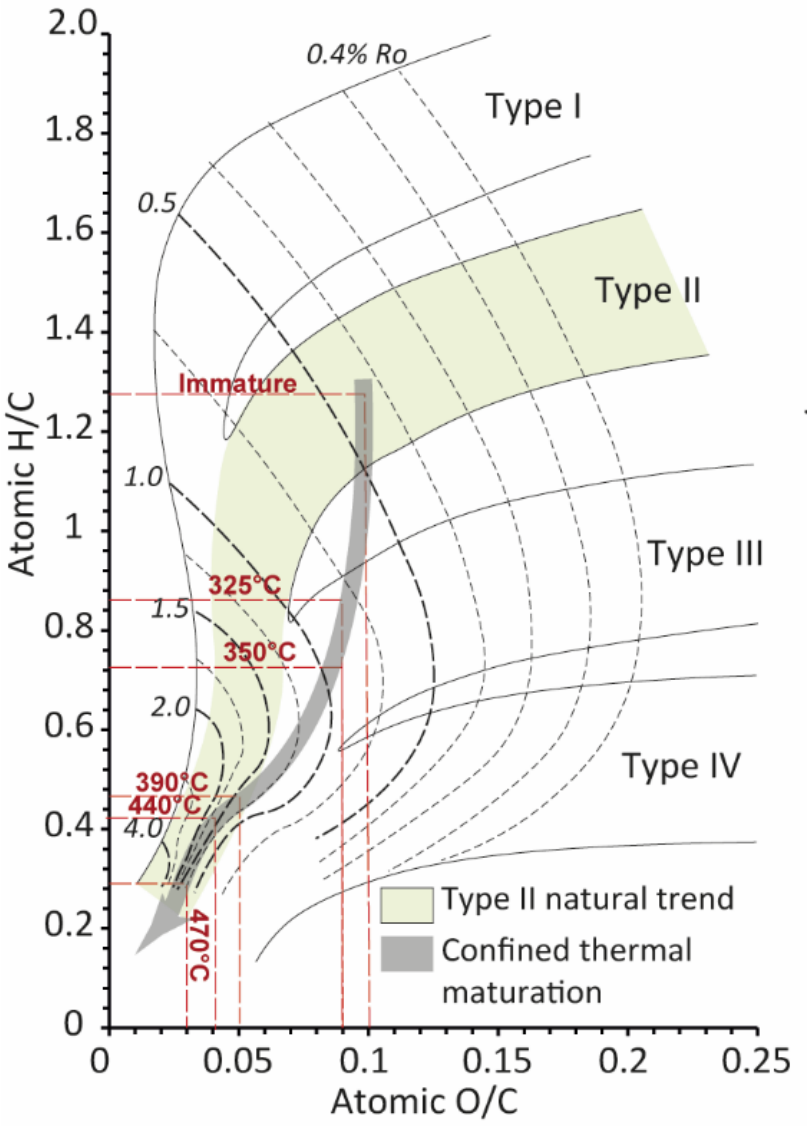

Fig. 3.10. Graphical determination of approximate O/C atomic ratios of KCF isolated OM after thermal maturation at 325-470°C for 72 hours using analyzed H/C atomic ratios, mean equivalent calculated vitrinite reflectance and van Krevelen diagram (modified from Hunt, 1996).

Chapter 4: Organic petrography and pore structure characterization of natural low-mature and gas-mature marine mudstones: insights into porosity controls in organic-rich source rocks

4. Organic petrography and pore structure characterization of natural low-mature and gas-mature marine mudstones: insights into porosity controls in organic-rich source rocks.

These results were published in Marine and Petroleum Geology under the title " Organic petrography and pore structure characterization of low-mature and gas-mature marine organic-rich mudstones: insights into porosity controls in gas shale systems." (Cavelan et al., 2019b).

Abstract

During this chapter, analyses of low-mature mudstones from the KCF and gas-mature mudstones from the VMF were performed using petrographic and SEM observations to characterize the organic and inorganic components of the rocks and their relationship with porosity. The porosity analyses using nitrogen adsorption measurements and MIP were then evaluated as a function of both composition and thermal maturity. Despite the absence of variation in the pore size distribution and the total pore volume with maturity, which is controlled by TOC, this study demonstrates that the pore network of these mudstones varies considerably with maturity. Contrary to immature KCF samples, whose porosity depends on mineral interparticle pores, the porosity of thermally-mature VMF rocks is mainly influenced by OM-hosted pores. OM porosity appears to increase during thermal maturation in response to the conversion of the OM, to become predominant in gas-mature rocks. It can therefore be considered that thermal maturation is a major process for the development of the OM porosity. However, the OM of high-TOC (>5.5 wt.%) gas-mature rocks contains smaller pores than low-TOC mudstones probably due to a difference in the original OM composition between these high- and low-TOC samples. By analogy with the KCF formation, which is often considered as time equivalent in terms of OM composition, the high-TOC VMF samples appear to have originally contained greater proportions of oil-prone amorphous OM and thus a better OM intrinsic quality for oil generation. This difference of OM composition and petroleum potential between VMF mudstones appears to have strongly influenced the OM-hosted pore genesis during maturation. These first results show that thermal maturity is not the only process that can explain OM-hosted pore genesis in gas shale systems. The OM composition seems also greatly influence the evolution of porosity during maturation. Organic composition and OM thermal maturity may therefore have a complementary effect, explaining the diversity of trends observed in natural formations.

Introduction

A multitude of factors seems to be responsible for OM-hosted pore genesis and stability in organic-rich mudstones. It is commonly assumed that OM-related porosity increases with thermal maturity in response to the thermal cracking of type II kerogen (Bernard et al., 2012a, b; Loucks et al., 2012; Chen and Xiao, 2014; Ko et al., 2016, 2018). The relationship between maturity and OM-hosted porosity is however not straightforward. In order to better understand the different parameters influencing the nature, the structure and the distribution of pores in natural organic-rich source rocks, this chapter investigated 21 low-mature, 1 oil-mature and 12 gas-mature rocks presenting various TOC from the KCF and the VMF respectively. These two formations are often considered as equivalent in terms of OM composition and depositional environment (Uliana et al., 1999). This study first documented the overall organic and inorganic composition and thermal maturation of these mudstones to compare their pore structure as a function of OM maturity and mineral composition. Then the OM composition of low-mature and gas-mature mudstones was investigated using Rock-Eval, petrographic observations and palynofacies analysis; and finally, their pore structure was characterized with SEM imaging techniques, MIP, and low-pressure N_2 adsorption measurements. Based on these results, the relationships between organic geochemistry, mineralogy and porosity were examined and compared as a function of thermal maturity. Most of these results has been published in *Marine and Petroleum Geology* under the title " Organic petrography and pore structure characterization of low-mature and gas-mature marine organic-rich mudstones: insights into porosity controls in gas shale systems." (Cavelan et al., 2019b).

4.1. Results

4.1.1. Mineralogy

Bulk mineralogy

Mineralogical data from XRD analyses are shown in Tab. 4.1 and Fig. 4.1. Quartz, calcite, clay minerals, feldspar and pyrite are the main mineral compounds in KCF and VMF samples (Tab. 4.1, Fig. 4.1). Both the VMF and the KCF formations show similar carbonate contents ranging from 6.6 to 29 wt.% ± 4.9 wt.% and relatively high pyrite contents (0.2–6.4 wt.% ± 1.3 wt.%, Tab. 4.1). However, some differences can be noted. KCF samples are 10 to 20 wt.% richer in clay minerals (~53.0 wt.% ± 4.4 wt.%) than VMF rocks (~26.0 wt.% ± 4.4 wt.%) and are thus argillaceous mudstones.

Tab. 4.1. Mineralogical composition obtained using X-ray diffraction analysis (in weight %) for KCF (Ebberston, Marton boreholes and VG: Viking graben) and VMF samples (APX).

Sample no.	***Well***	***Depth (m)***	***Quartz (wt.%)***	***Carbonate (wt.%)***			***Total carbonate (wt.%)***	***Gypsum (wt.%)***	***Albite (wt.%)***	***Total clay (wt.%)***	***Pyrite (wt.%)***
				Calcite	Siderite	Dolomite					
Eb 4	Ebberston	69.14	15.9	8.5	0	0	8.5	2.0	2.5	57.6	6.4
Eb 19	Ebberston	69.98	8.7	17.6	0	0	17.6	0.8	3.0	53.6	5.7
Eb 28	Ebberston	70.01	19.8	22.4	0	0	22.4	0	6.1	46.6	2.0
Eb 40	Ebberston	70.28	7.8	13.8	0	0	13.8	1.4	1.5	54.6	5.0
Eb 48	Ebberston	70.65	15.8	19.5	0	0	19.5	1.0	1.9	54.8	1.0
	Min		***7.8***	***8.5***	***0***	***0***	***8.5***	***0***	***1.5***	***46.6***	***1.0***
	Max		***19.8***	***22.4***	***0***	***0***	***22.4***	***2.0***	***6.1***	***57.6***	***6.4***
	Mean		***13.6***	***16.4***	***0***	***0***	***16.4***	***1.0***	***3.0***	***53.4***	***4.02***
Blc 2	Marton	128.15	19.7	16.3	4.6	0	20.9	1.1	2.6	52.5	0.2
Blc 13	Marton	128.40	21.5	19.7	4.4	0	24.1	1.7	0	49.0	0.7
Blc 30	Marton	128.75	14.3	15.0	0	0	15.0	0.8	6.2	46.0	6.4
Blc 31	Marton	128.78	14.3	17.0	1.0	0	18.0	0.6	2.7	54.1	3.5
Blc 50	Marton	129.20	12.4	6.5	13.7	0	20.2	1.1	3.8	59.1	1.3
	Min		***12.4***	***6.5***	***0***	***0***	***15.0***	***0.8***	***0***	***46.0***	***0.2***
	Max		***21.5***	***19.7***	***13.7***	***0***	***24.1***	***1.7***	***6.2***	***59.1***	***6.4***
	Mean		***16.4***	***14.9***	***4.7***	***0***	***19.6***	***1.1***	***3.1***	***52.1***	***2.42***
VK1	VG	3913	22.4	10.4	0	0	10.4	0	12.8	50.3	1.9
94B	APX	2668	31.5	10.0	0.3	0.5	10.8	0	21.1	30.0	1.6
96Z	APX	2697	15.6	28.8	0.2	0	29.0	0	23.6	22.2	2.4
98M	APX	2720	33.7	14.2	0.1	0	14.3	0	22.8	22.1	1.6
100C	APX	2747	39.1	8.1	0	0	8.1	0	26.4	21.7	1.5
102R	APX	2769	27.7	12.8	0.2	0	13.0	0	27.9	23.3	1.4
103K	APX	2789	22.1	6.5	0.1	0	6.6	0	24.6	36.1	1.6
	Min		***15.6***	***6.5***	***0***	***0***	***6.6***	***0***	***21.1***	***21.7***	***1.4***
	Max		***39.1***	***28.8***	***0.3***	***0.5***	***29.0***	***0***	***27.9***	***36.1***	***2.4***
	Mean		***28.3***	***13.4***	***0.1***	***0.1***	***13.6***	***0***	***24.4***	***25.9***	***1.7***

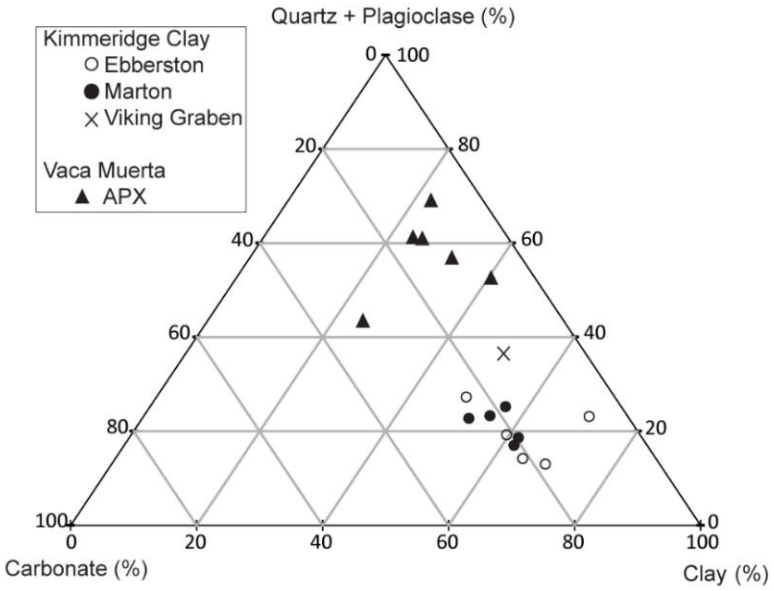

Fig. 4.1. Mineralogical ternary diagram based on the normalized data from Tab. 4.1 (in wt %).

Samples from the Viking graben, Marton and Ebberston boreholes exhibit the same mineralogy. VMF samples which contain higher amounts of feldspar (~24.0 wt.% ± 8.3 wt.%) and quartz (28.0 wt.% ± 3.7 wt.%) are siliceous mudstones. Traces of gypsum are observed in KCF samples (Tab. 4.1) as previously noted by Desprairies et al. (1995).

Clay mineralogy

The clay mineral assemblage is similar in samples from Marton, Ebberston boreholes and the Viking graben (Fig. 4.2). The two peaks at 7.18Ä (d001) and 3.52Ä (d002), which disappear after heating at 550°C, show the presence of significant amounts of kaolinite. The peak at 10.03Ä (d001), which is shifted towards 12Ä after glycolation, and the peaks at 5.00Ä (d002) and 3.33Ä (d003) indicate the presence of abundant mixed-layered illite/smectite (I/S). The contribution of muscovite cannot be excluded. In the VMF, I/S are still abundant but the less important shift of the peak at 10.2Ä after glycolation suggest that I/S contain a higher proportion of illite (Fig. 4.2). The resolution and the relative intensity of the pic at 3.33Ä increase from Ebberston to the VMF indicating a growing diagenetic evolution. Small peaks, not affected by the heating at 550°C and glycolation, are present at 14.3Ä and 7.2Ä. This suggests the presence of chlorite. It is very likely that muscovite are also present in samples. These slight variations of clay composition between VMF and KCF, well substantiate the higher diagenetic evolution of VMF samples.

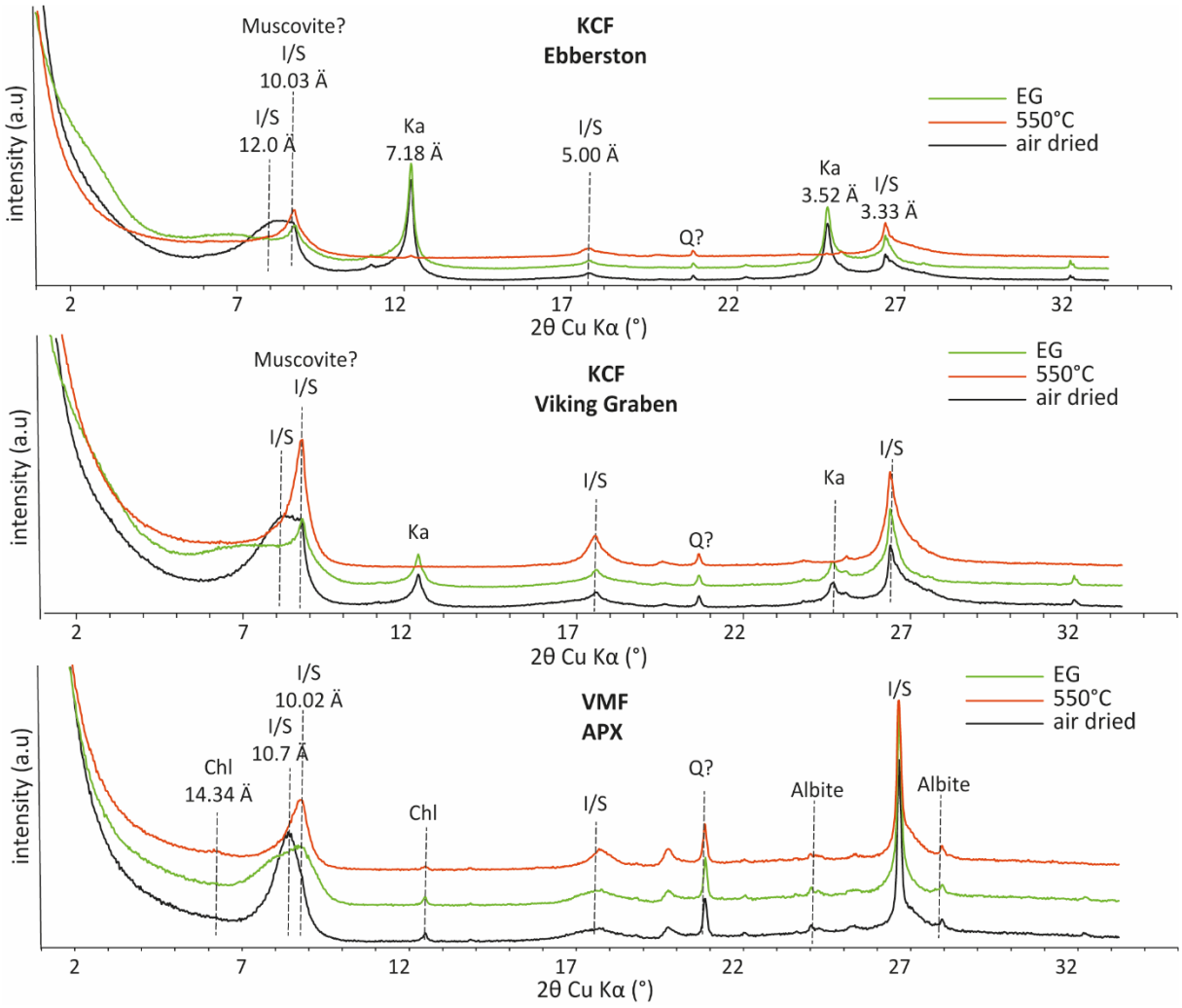

Fig. 4.2. XRD diffractogrammes of KCF and VMF clay minerals-oriented slides. EG: ethylene glycol. Chl: chlorite. I/S: mixed layered illite/smectite. Q: quartz. Ka: kaolinite.

4.1.2. Organic geochemistry

Organic geochemistry data from Rock Eval pyrolysis are shown in Tab.4.2 and Fig. 4.3 and their variations with depth in Marton, Ebberston and APX boreholes are illustrated in Fig.4.4. All samples are organic-rich with TOC contents higher than 2 wt.% (Tab.4.2; Fig.4.4). VMF samples exhibit low S_2 (< 2.2 mg/g rock), HI (< 49 mg/g TOC) and OI (< 20 mg/g TOC) values regardless of TOC content. As such, these samples plot near the origin in the pseudo-Van Krevelen diagram and the type of kerogen is non-identifiable (Fig. 4.3). The high T_{max} values (~500°C) indicate a high maturity of OM corresponding to the gas window (Fig. 4.3B, 4.4C). The RC/TOC ratio is close to 1, indicating the OM of VMF samples is mainly composed of residual OM with a low residual petroleum potential (low HI and S_2 values) (Tab.4.2, Fig.

4.4C). The high HI (~527 mg/gTOC in Ebberston, ~452 mg/g in Marton) and low OI values (~20 mg/gTOC) of KCF samples from Marton and Ebberston show they are Type II kerogen (Tab.4.2, Fig. 4.3A). The low production index (PI < 0.1) and T_{max} values (< 435°C) indicate their low maturity (Fig. 4.3B). The RC/TOC ratio, far smaller than 1, (< 0.62), indicates that these samples contain a great fraction of pyrolizable OM (Tab.4.2).

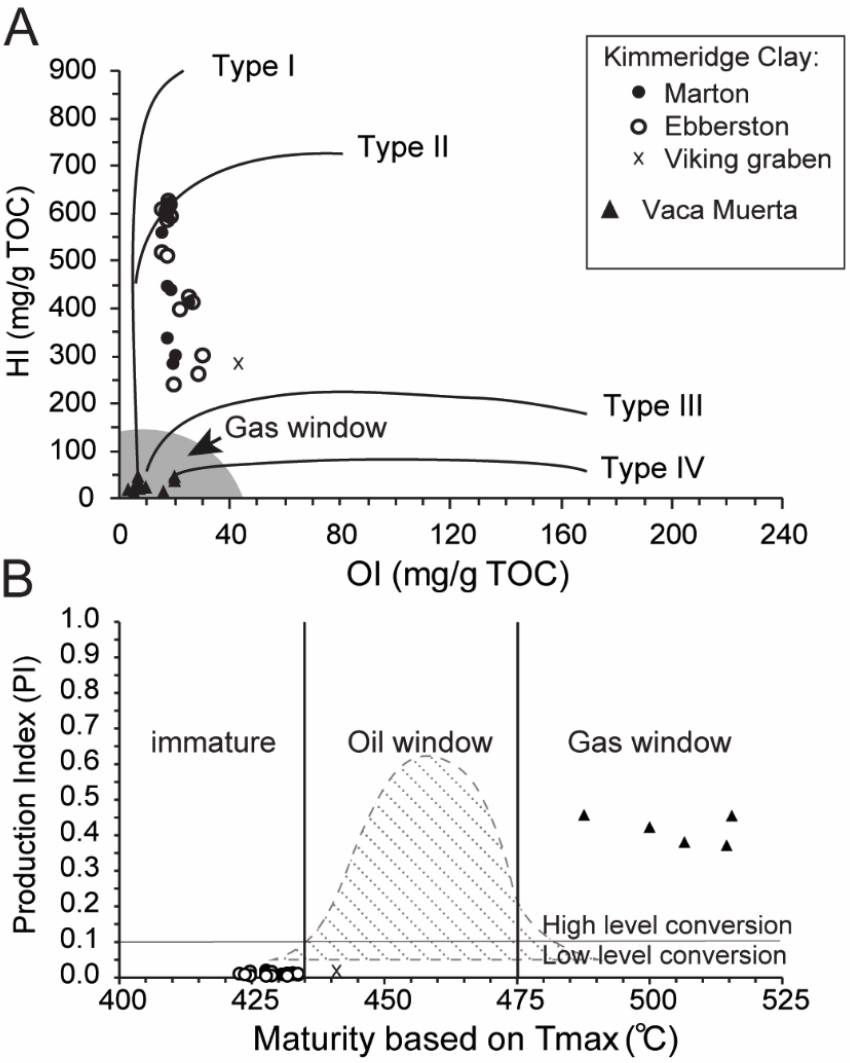

Fig. 4.3. A) Pseudo-Van Krevelen diagram of Vaca Muerta and Kimmeridge Clay samples. B) Production index as a function of T_{max} (data from Tab. 4.1).

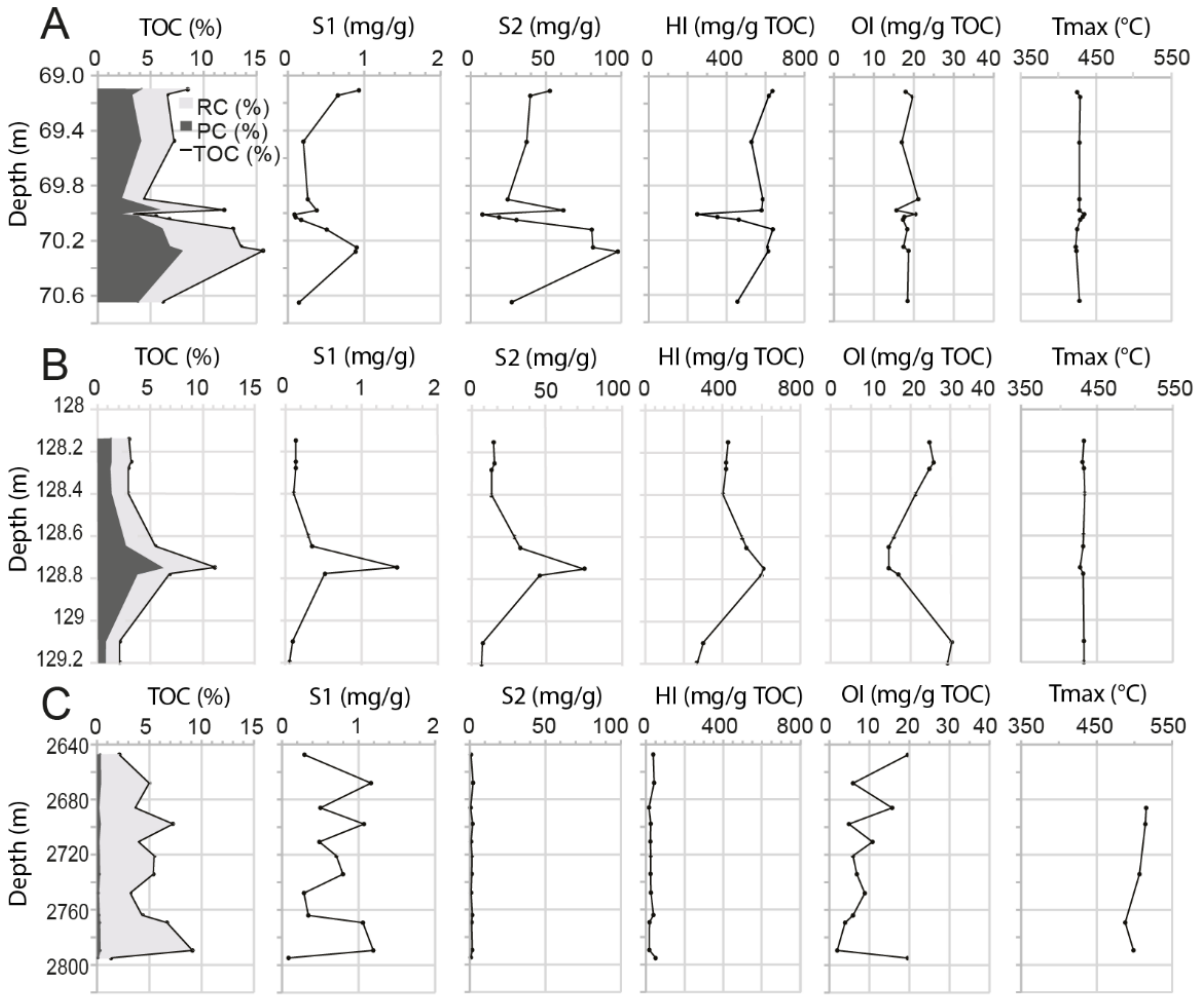

Fig. 4.4. Evolution of the main Rock Eval parameters with depth in Ebberston (A), Marton (B) (Kimmeridge Clay formation) and in the Vaca Muerta formation (C) (data from Tab. 4.1). RC: Residual Carbon. PC: pyrolizable carbon (in weight %).

Consistent variations of TOC, HI and S_2 values are observed in KCF samples (Fig.4.4A and B). OI values exhibit a negative correlation with TOC in Marton (Fig.4.4B). Some very high-TOC samples (Eb 19, Eb 40 and Blc 30) exhibit higher pyrite contents (Tab.4.2, and Tab. 4.1). In the Viking graben, the Tmax of 442°C indicate that the studied sample has reached the oil window (Tab.4.2, Fig. 4.3). However, the PI of 0.02, the relatively low RC/TOC (=0.73) and the low S_1 indicate that only the early oil generation stage has been reached. This samples exhibit similar HI, OI, S_1 and S_2 values than the lower oil-prone samples of Marton and Ebberston (such as Blc 43, Blc2) suggesting that these samples contain initially similar organic precursors (Tab.4.2).

Tab. 4.2. Main parameters from Rock Eval pyrolysis for VMF and KCF samples from Marton, Ebberston and the Viking graben (VG).

Sample no.	***Formation-well***	***Depth (m)***	***TOC (wt.%)***	***S1 (mg HC/g rock)***	***S2 (mg HC /g rock)***	***Tmax (°C)***	***HI (mgHC/ g TOC)***	***OI (mgCO2/ g TOC)***	***RC/ TOC***
Eb 3	KCF-Ebberston	69.11	8.3	0.9	52.7	425	636	18	0.47
Eb 4	KCF-Ebberston	69.14	7.1	0.2	37.2	428	528	17	0.57
Eb 8	KCF-Ebberston	69.48	6.4	0.7	39.6	429	616	20	0.49
Eb 11	KCF-Ebberston	69.9	4.2	0.3	24.6	428	586	21	0.51
Eb 19	KCF-Ebberston	69.98	10.6	0.4	61.5	428	580	15	0.52
Eb 28	KCF-Ebberston	70.01	3.2	0.1	7.9	434	249	20	0.78
Eb 30	KCF-Ebberston	70.03	5.4	0.1	18.9	432	353	18	0.71
Eb 32	KCF-Ebberston	70.05	6.6	0.2	30.5	429	462	17	0.62
Eb 34	KCF-Ebberston	70.12	12.6	0.5	80.4	425	638	18	0.48
Eb 38	KCF-Ebberston	70.25	13.4	0.9	81.3	423	607	17	0.50
Eb 40	KCF-Ebberston	70.28	15.9	0.9	97.7	424	613	19	0.49
Eb 48	KCF-Ebberston	70.65	6.0	0.1	27.3	428	456	18	0.62
		Mean	**8.3**	**0.4**	**46.6**	**427**	**527**	**18**	**0.56**
	KCF-Ebberston	**Min**	**3.2**	**0.1**	**7.9**	**423**	**249**	**15**	**0.47**
		Max	**15.9**	**0.9**	**97.7**	**434**	**638**	**21**	**0.78**
Blc 2	KCF-Marton	128.15	3.0	0.1	13.3	433	439	25	0.63
Blc 4	KCF-Marton	128.25	3.2	0.1	13.8	431	428	27	0.62
Blc 8	KCF-Marton	128.28	2.9	0.1	12.4	433	427	26	0.64
Blc 13	KCF-Marton	128.40	3.0	0.1	12.3	434	414	22	0.65
Blc 23	KCF-Marton	128.65	5.6	0.3	29.8	432	537	15	0.56
Blc 30	KCF-Marton	128.75	11.2	1.5	70.2	428	628	15	0.48
Blc 31	KCF-Marton	128.78	6.9	0.5	42.2	432	615	18	0.49
Blc 43	KCF-Marton	129.10	2.2	0.1	6.7	433	307	31	0.74
Blc 50	KCF-Marton	129.20	2.1	0.1	5.7	433	275	30	0.76
		Mean	**4.4**	**0.3**	**22.9**	**432**	**452**	**23**	**0.62**
	KCF-Marton	**Min**	**2**	**0**	**6**	**428**	**275**	**15**	**0.48**
		Max	**11**	**1**	**70**	**434**	**628**	**31**	**0.76**
VK1	KCF-VG		2.2	0.1	6.6	442	292	44	0.73
93X	VMF-APX	2647	2.1	0.3	0.8	/	38	19	0.95
94B	VMF-APX	2668	5.0	1.2	2.2	/	43	5	0.94
95G	VMF-APX	2685	3.6	0.5	0.6	/	16	15	0.97
96Z	VMF-APX	2697	7.3	1.1	1.8	515*	25	5	0.96
97U	VMF-APX	2710	3.9	0.5	0.9	/	23	11	0.97
98M	VMF-APX	2720	5.5	0.7	1.4	/	25	6	0.97
99W	VMF-APX	2734	5.4	0.8	1.3	507*	24	7	0.96
100C	VMF-APX	2747	3.2	0.3	0.8	/	26	9	0.97
101E	VMF-APX	2764	4.3	0.3	1.7	/	39	6	0.96
102R	VMF-APX	2769	6.7	1.1	1.3	488*	19	4	0.97
103K	VMF-APX	2789	9.1	1.2	1.6	500*	18	2	0.96
104P	VMF-APX	2794	1.3	0.1	0.7	/	49	20	0.90
		Mean	**4.8**	**0.7**	**1.3**	**502**	**29**	**9**	**0.96**
	VMF-APX	**Min**	**1.3**	**0.1**	**0.6**	**488**	**16**	**2**	**0.90**
		Max	**9.1**	**1.2**	**2.2**	**515**	**49**	**20**	**0.97**

*/: unmeasurable Tmax due to a flat S2 peak. *: Tmax values which appear to be correct despite a low S2 peak.*

4.1.3. Petrographic observations

Vaca Muerta formation

In petrographic observations of VMF samples, OM is mainly comprised of highly reflective (grey) non-fluorescent particles often associated with pyrite (Fig. 4.5).

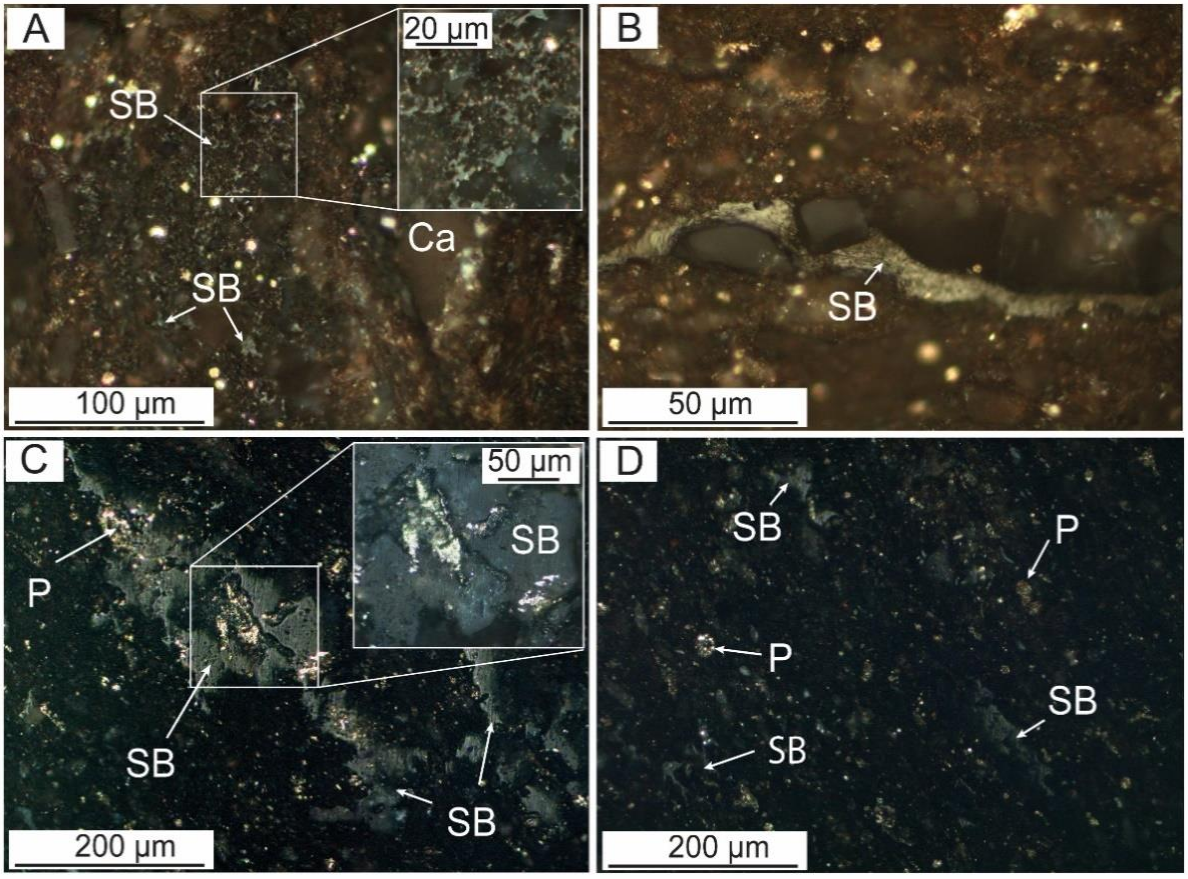

Fig. 4.5. Incident white light photomicrographs of VMF mudstones (~1.65% , TOC = 5.0 wt.%). A) Solid bitumen/pyrobitumen (SB) network. Insert in A shows solid bitumen embayed against small euhedral crystals of carbonates. B) Solid bitumen streak (grey-white). C-D) Pyrobitumen accumulations with a granular/pitted surface texture. P: pyrite. Ca: carbonate.

Some of these particles show a fracture-filling texture (Fig. 4.5B) or form abundant groundmass (Fig. 4.5A) with pitted surface texture (Fig. 4.5C). No identifiable biological structures are present, corroborating the high maturity of OM. These particles have been identified as pyrobitumen which is the dominant organic component in thermally mature organic-rich mudstones (Hackley and Cardott, 2016; Hackley, 2017).

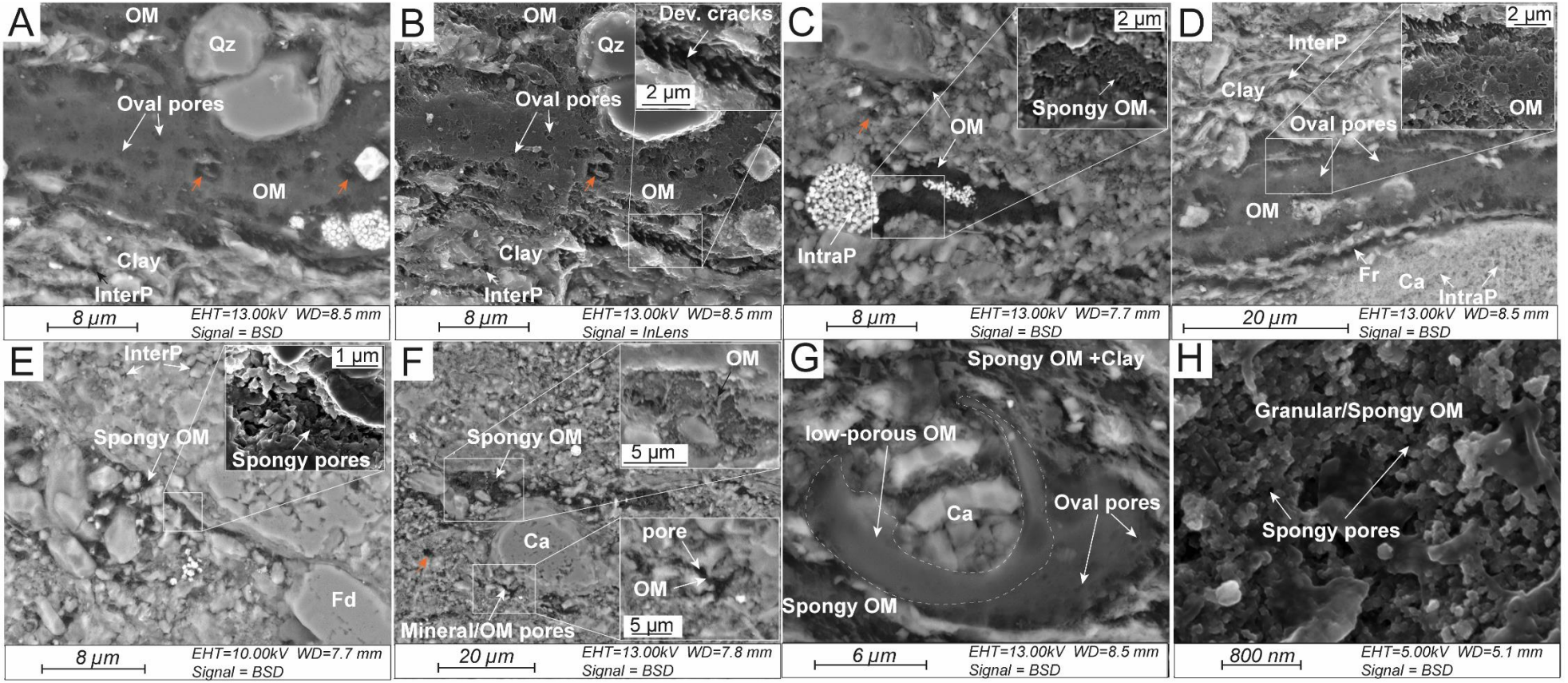

Fig. 4.6. SEM images of gas-mature VMF samples (A-B, TOC=6.7 wt.%; E-H, TOC=5.0 wt.%). A, B, D) Backscattered electron (BSE) and secondary electron (SE) images. Insert in B shows the presence of devolatilization cracks (Dev.cracks). C, E-F) BSE images showing spongy/ granular OM embayed in the mineral matrix. H and inserts in C-E show SE images of spongy subangular OM-hosted pores. Insert in F: BSE image of pores located between mineral and residual OM (mineral/OM pores). G) BSE image showing a less-porous OM area. Ca: calcite. Qz: quartz. InterP: interparticle pores. IntraP: intraparticle pores. Fr: microfracture. Some large macropores (orange arrows) and microfractures are interpreted as artefacts of polishing.

In SEM images, this residual OM appears as particles hosting nanometer-scale spongy pores (Fig. 4.6F, H). A continuous spongy OM-hosted pore network is observed inside these carbon-rich residues (Fig. 4.6). These spongy pores are abundant, closely spaced and exhibit subangular shapes (Fig. 4.6E, H). The subangular spongy pores are the most abundant (Fig. 4.6E, H) but many oval pores (bubble-like pores) are also observed Fig. 4.6A, B, D). These OM-hosted pores appear to be mainly composed of mesopores and macropores with diameter smaller than 200 nm (Fig. 4.6H); the larger pores probably come from the merging of smaller pores. Some pores are located between OM and mineral grains (Fig. 4.6F). These mineral/OM pores cannot be classified as OM-hosted pores and are interpreted as mineral interparticle pores containing relics of OM. The residual porous OM is dispersed in a fine and compact mineral matrix, which appears in the SEM images to be mainly composed of clay mineral sheet aggregates, quartz and calcite grains (Fig. 4.6). While some interparticle macropores are located between quartz, calcite grains or clay-sheets (Fig. 4.6A, C, D), some intraparticle macropores are located inside pyrite framboids and calcite grains (Fig. 4.6C, D). Most of the clay mineral aggregates are located near the OM (Fig. 4.6A, B, D). In these thermally-mature samples, only a few OM particles are non-porous or exhibit a low porosity (Fig. 4.6G). Some devolatilization cracks were also observed in the OM (Fig. 4.6B). Some of the large macropores (orange arrows, Fig. 4.6) and the microfractures observed in these samples are interpreted as artefacts due to sample preparation.

Kimmeridge Clay formation

KCF mudstones from Marton and Ebberston boreholes show a relatively heterogeneous OM distribution. In these immature samples, OM is composed of several terrestrial and marine macerals dispersed in a fine mineral matrix (Fig. 4.7, 4.8). In SEM images, this mineral matrix appears to be composed of clay mineral aggregates, quartz, calcite-grains, pyrite framboids (Fig. 4.9) and some microfossil remains (Fig. 4.9A, D, F).

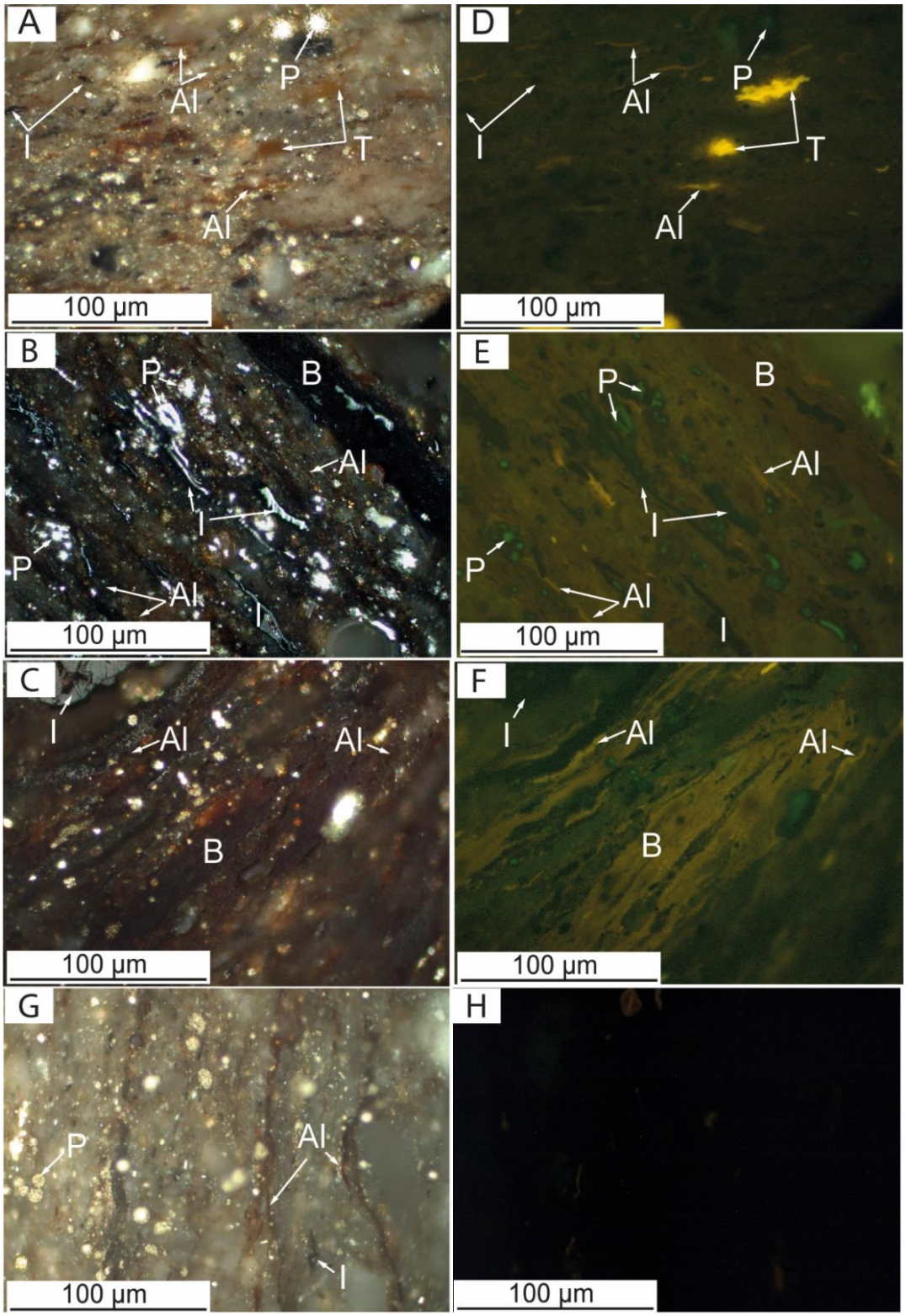

Fig. 4.7. Incident white light (A-C, G) photomicrographs of KCF mudstones from Marton, Ebberston boreholes (A, TOC= 5.6 wt.%; B =10.9 wt.%; C, TOC =15.9 wt.%) and the Viking graben (G, TOC= 2.2 wt.%). D-F, H) Same field as A, B, C and G under UV-fluorescence light. Al: lamellar alginite macerals. T: Tasmanite *algal body. B: elongated bodies of dark/brown AOM identified as 'bituminite' macerals. I: inertinite fragments. P: pyrite framboids.*

Terrestrial macerals, mainly represented by inertinite (Fig. 4.7), form a large proportion of the structured OM (~15%, Fig. 4.10). Phytoclasts, observed in palynofacies include some cuticular fragments, woody fragments and various debris of plant tissues (Fig. 4.8 E–J). The predominant marine amorphous OM (AOM) (~75%) is supplemented by a minor contribution of structured organic components derived from preserved phytoplanktonic organic-walled and algal spores (~10%, Fig. 4.8 K, L; 4.10). This structured marine OM is present as brightly fluorescent thin bodies identified as *Tasmanite* spores (Fig. 4.7).

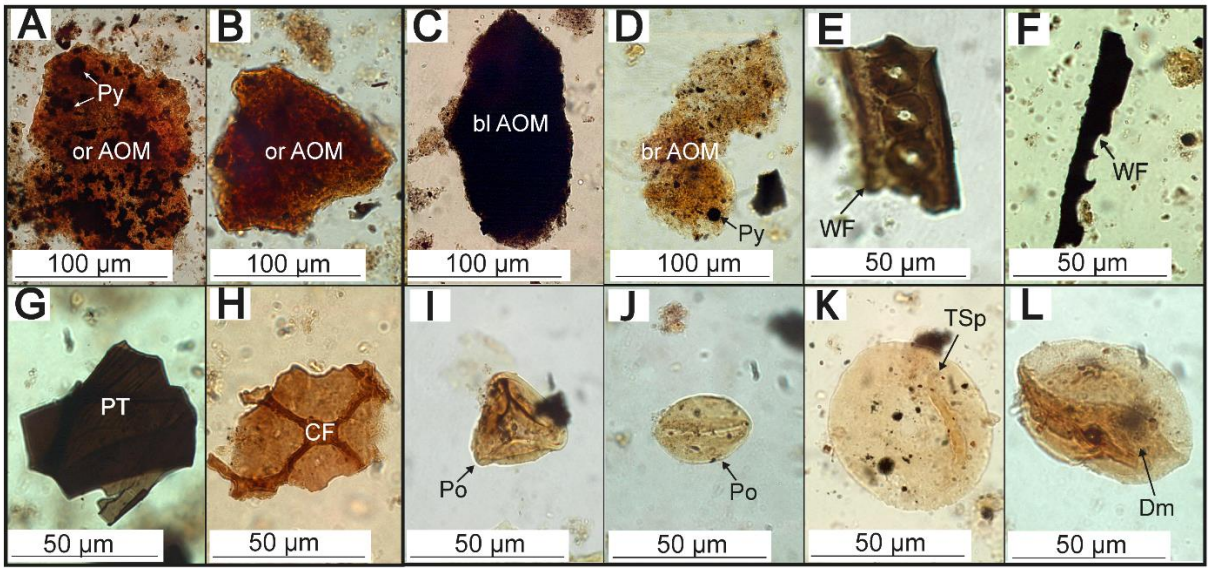

Fig. 4.8. Different types of AOM (A-D) and isolated structured organic matter (E-L) observed in KCF samples by optical microscopy (transmitted light, oil immersion). A, B): orange amorphous organic matter (or AOM) with black pyritic inclusions (Py). C: black amorphous organic matter (bl AOM). D: brown amorphous organic matter with pyrite and oxidized debris inclusions. E: woody oxidized fragment (WF). F: opaque oxidized debris from plant tissue (WF). G: gelified membranes of plant tissue (PT). H: cuticular fragments (CF). I and J: pollen grains (Po). K: well preserved Tasmanite*-like megaspore (Tsp). L: degraded megaspore (Dm).*

Three distinct types of AOM were identified: brown, orange and black AOM (Fig. 4.8 A-D). Black AOM is the least abundant amorphous fraction (~10%, Fig. 4.10). Previously observed in the KCF (Boussafir et al., 1995a, b), brown AOM does not correspond to any macerals in light microscopy, and seems to be dispersed in the organoclay-mineral matrix. This marine OM is probably responsible for the high fluorescence of the mineral matrix in light microscopy (Fig. 4.7D-F). Orange AOM is generally associated with pyrite framboids (Fig. 4.8A). In polished sections, these macerals are observable as thick elongated bodies oriented parallel to the bedding with a low brown/orange fluorescence (Fig. 4.7).

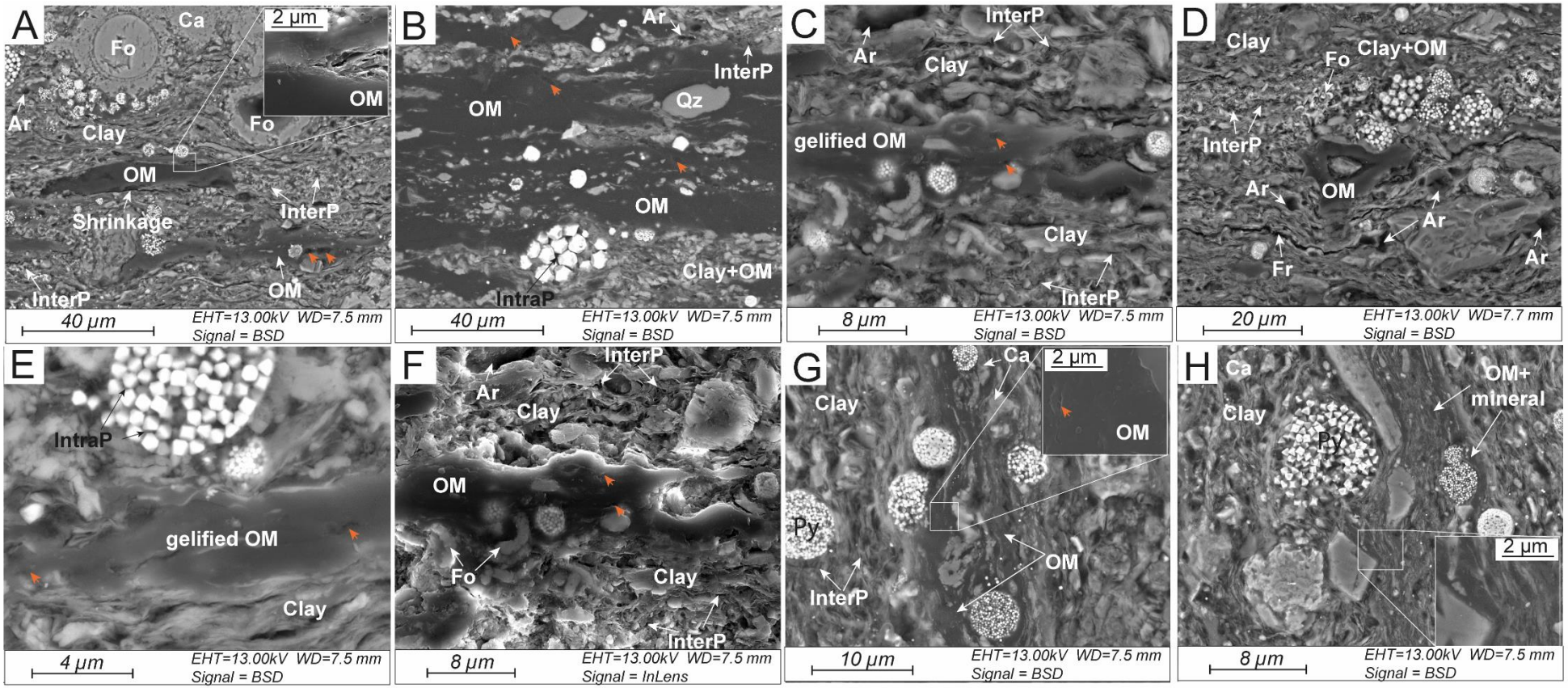

Fig. 4.9. SEM images of immature organic-rich KCF samples from Marton, Ebberston boreholes (A: TOC=15.9 wt.%; B: TOC=11.2 wt.%; C-F: TOC=5.6 wt.%) and oil-mature rocks from the Viking graben (G-H TOC=2.2 wt.%). F and insert in A show SE images of non-porous OM. Fr: microfracture. Ca : carbonate. Qz : quartz. InterP: interparticle pores. IntraP: intraparticle pores. Fo: microfossil debris. Rare pores are present in OM (orange arrows). Some of the large macropores (Ar) and the microfractures (Fr) are interpreted as artefacts due to sample polishing.

Abundant in high-TOC samples (Fig. 4.7B, C), these organic particles, so called 'bituminite' (Kus et al., 2017), were previously described in the KCF (Boussafir et al., 1995b; Boussafir and Lallier-Vergès, 1997). The same maceral types are observed in the studied sample from the Viking graben, but no fluorescence is observed well-substantiating the slightly higher thermal maturity of the sample (Fig. 4.7G, H). The alginite macerals observed in polished sections, is present as brightly fluorescent thin elongated bodies in SEM images (yellow-colored under UV excitation, Fig. 4.7).

In Marton and Ebberston boreholes, the abundance of these particles exhibits significant variations with TOC. In samples with TOC values < 6 wt.% the OM is rather composed of sparse fragments of inertinite with some alginites and rare *Tasmanite* algal bodies (Fig. 4.7A). Samples with very high TOC values (> 6 wt.%) show an increase in abundance of the fluorescent elongated organic particles including both alginites and bituminites (Fig. 4.7B, C). After normalization with TOC, palynofacies observations show that orange AOM and pyrite contents dramatically increase with TOC and HI values (Fig. 4.10; Tab.4.2) while brown and black AOM contents remain relatively stable (Fig. 4.10).

In SEM images, the OM is composed of elongated lamellar masses of kerogen particles (Fig. 4.9). This OM constitutes a homogenous gel with well-defined boundaries cementing mineral grains, clay mineral sheets and pyrite framboids (Fig. 4.9). Some horizontal fractures (Fr, Fig. 4.9), shrinkage OM pores (Fig. 4.9A) and rare OM-hosted mesopores with irregular shapes are visible (orange arrow, Ar, Fig. 4.9). Such fractures and some of the OM-hosted pores are interpreted as artefacts due to sample preparation after retrieval from subsurface and thus may not be present in the subsurface (Chalmers et al., 2012; Tian et al., 2015). The OM in these low-mature samples is thus mainly non-porous. Most of the macropores and mesopores are < 4 µm in diameter and seem located between clay sheets, inside microfossil remains or between calcite, and quartz grains (Fig. 4.9A, C, D). Some intraparticle pores are observed inside pyrite framboids (Fig. 4.9B, E). No differences are observed between samples from Marton, Ebberston and the Viking graben.

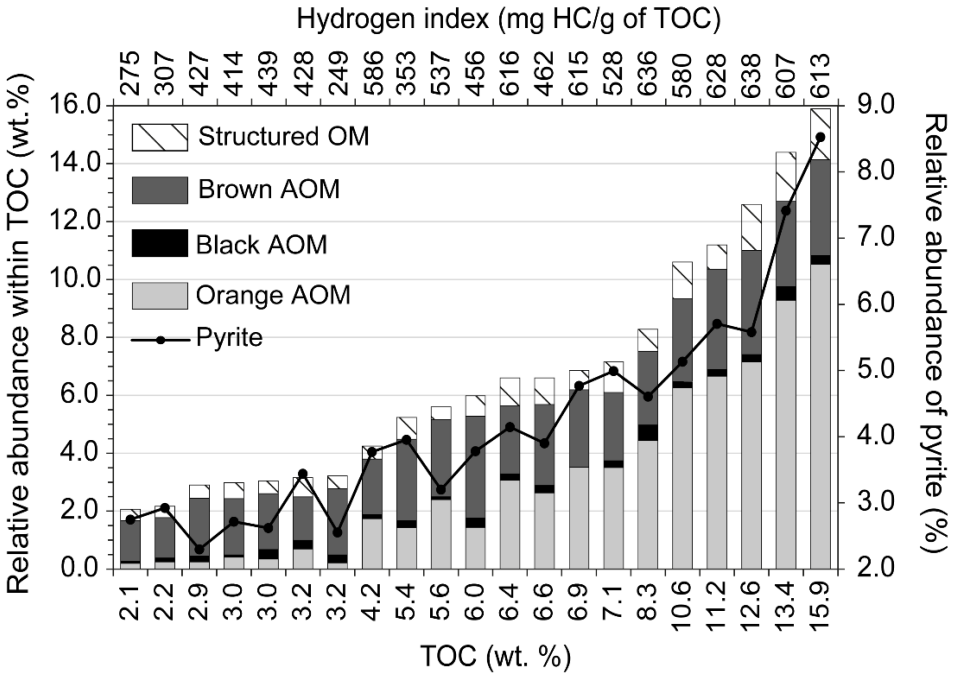

Fig. 4.10. Palynofacies composition versus TOC contents and hydrogen index of Kimmeridge Clay samples (including Marton and Ebberston samples). AOM: amorphous organic matter. Structured OM: structured organic matter composed of various phytoclasts including woody fragments, cuticular fragments and other plant tissues, pollen grains, spores and preserved phytoplankton.

The relationships between TOC, quartz and clay mineral contents are shown in Fig. 4.11. Clay mineral content exhibits no clear relationship with TOC contents in either of the formations (Fig. 4.11). A negative linear correlation between TOC and quartz contents is observed in the VMF (R^2=0.70, Fig. 4.11). A weaker negative linear correlation exists in the KCF between quartz and TOC (R^2=0.57, Fig. 4.11). The relationships between organic carbon contents and the specific surface area are shown in Fig. 4.12. VMF and KCF samples do not plot in the monolayer equivalent model trend such as Peru margin and Black-Sea sediments (Fig. 4.12, Hedges and Keil, 1995). This model represents the quantity of organic carbon that can be contributed by organo-clay interactions as a function of the specific surface area. VMF and KCF sediments thus contain organic carbon that cannot have been contributed solely by organo-clay interactions. Compared with Peru margin and Black-Sea sediments, our results suggest that other additional mechanisms have allowed the OM to be well-preserved in the KCF and VMF formations (Hedges and Keil, 1995).

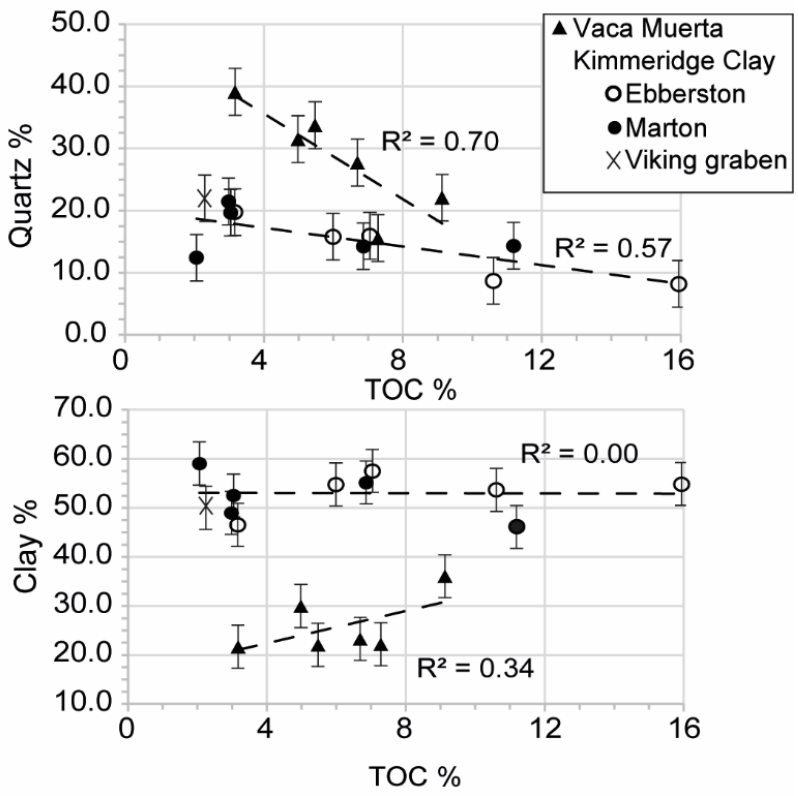

Fig. 4.11. Relationships between silica, clay minerals and TOC contents in KCF (Marton, Ebberston holes and Viking graben) and VMF samples (in weight %).

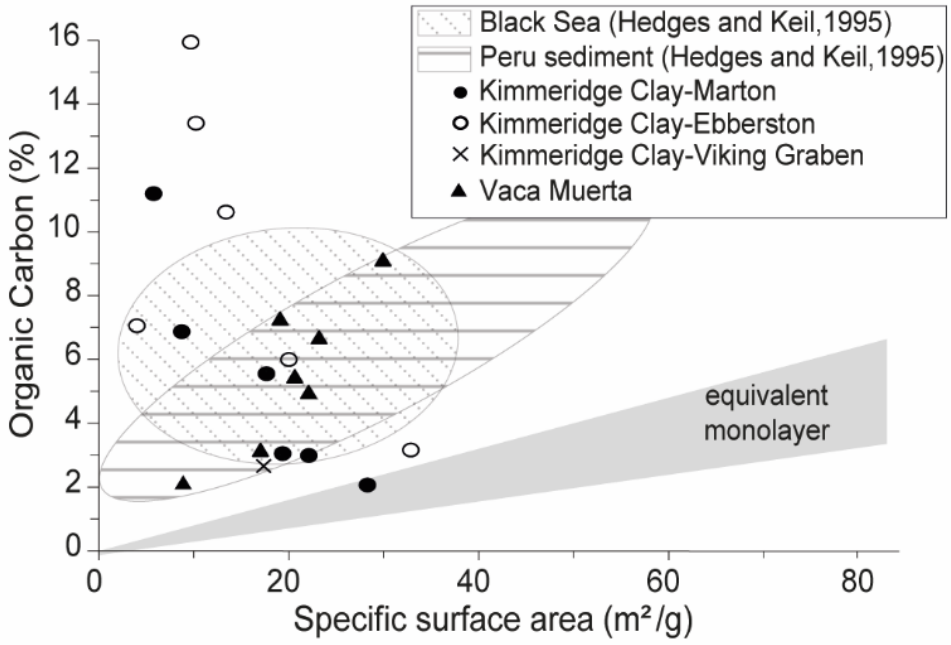

Fig. 4.12. Organic carbon content as a function of specific surface area of KCF and VMF samples. Comparison with the monolayer equivalent model from Hedges and Keil (1995).

4.1.4. Porosity and pore size distribution

Mercury intrusion porosimetry (MIP)

Data obtained from MIP are listed in Tab. 4.3. MIP measurements revealed a connected total porosity ranging from 15.69 to 23.40% in the KCF and from 16.69 to 28.68% in the VMF (Tab. 4.3).

Tab. 4.3. Porosity measurements obtained from MIP including raw data and corrected data from surface roughness for VMF and KCF mudstones (Marton, Ebberston boreholes, VG: Viking graben). Contribution of macropores corresponds to the contribution to the total pore volume of macropores ranging between 50 nm - 6µm in diameter. PV: pore volume. TP: Total porosity. MacroP (%): contribution of macropores in the total pore volume.

		Raw data				*Corrected data*			
Sample no.	***Well***	***PV (cm^3/ 100g)***	***TP (%)***	***skeletal density (g/cm^3)***	***bulk density (g/cm^3)***	***PV (cm^3/ 100g)***	***TP (%)***	***Cumulated PV at 50 nm (cm^3/100g)***	***Macro P (%)***
Eb 4	Ebberston	9.93	19.58	2.45	1.97	3.06	6.04	0.55	17.99
Eb 19	Ebberston	10.51	18.60	2.17	1.77	3.10	5.48	0.40	12.97
Eb 28	Ebberston	10.10	19.76	2.44	1.96	5.06	9.91	0.64	12.59
Eb 40	Ebberston	12.16	19.01	2.06	1.56	3.00	4.70	0.52	17.24
Eb 48	Ebberston	13.05	23.40	2.34	1.79	5.57	9.98	0.97	17.37
	Mean	**11.15**	**20.07**	**2.29**	**1.81**	**3.96**	**7.22**	**0.61**	**15.63**
Blc 2	Marton	9.72	19.49	2.49	2.01	2.61	5.23	0.28	10.80
Blc 13	Marton	8.35	16.91	2.44	2.02	2.39	4.85	0.27	11.12
Blc 30	Marton	10.59	18.84	2.19	1.78	1.89	3.37	0.43	22.84
Blc 31	Marton	8.33	15.69	2.24	1.88	2.14	4.03	0.49	22.75
Blc 50	Marton	10.13	20.13	2.49	1.99	3.07	6.09	0.33	10.63
	Mean	**9.42**	**18.21**	**2.37**	**1.94**	**2.42**	**4.71**	**0.36**	**15.63**
VK1	VG	12.2	22.9	2.44	1.88	3.12	5.87	0.27	8.65
93X	VMF	16.31	28.68	2.47	1.76	1.63	2.87	0.15	8.91
96Z	VMF	16.59	28.49	2.40	1.72	0.36	0.61	0.03	8.26
98M	VMF	15.96	28.10	2.45	1.76	1.31	2.29	0.09	6.69
103K	VMF	9.76	16.69	2.33	1.70	0.35	0.59	0.02	7.00
	Mean	**14.65**	**25.49**	**2.41**	**1.73**	**0.91**	**1.59**	**0.07**	**7.71**

Cumulative intrusion as a function of TOC and PSD are shown in Fig. 4.13 and 4.14. A significant number of pores are located in the 50–1000 µm pore size range for the KCF samples and in the 100–1000 µm for the VMF samples (Fig. 4.13A, C). Nevertheless, these large macropores which largely contribute to the total porosity were never seen in SEM and petrographic observations. The largest pores imaged by SEM are about 6 µm in diameter in both formations. The presence of pores > 6 µm is considered as conformance errors due to surface roughness, cracks and filling of the container (Sigal, 2009; Klaver et al., 2012). In order to provide more realistic MIP data, mercury intrusion curves, porosity and pore volumes were

thus corrected by excluding pores greater than 6 µm in diameter and by subtracting the first part of the intrusion data from the total (Fig. 4.13A, C).

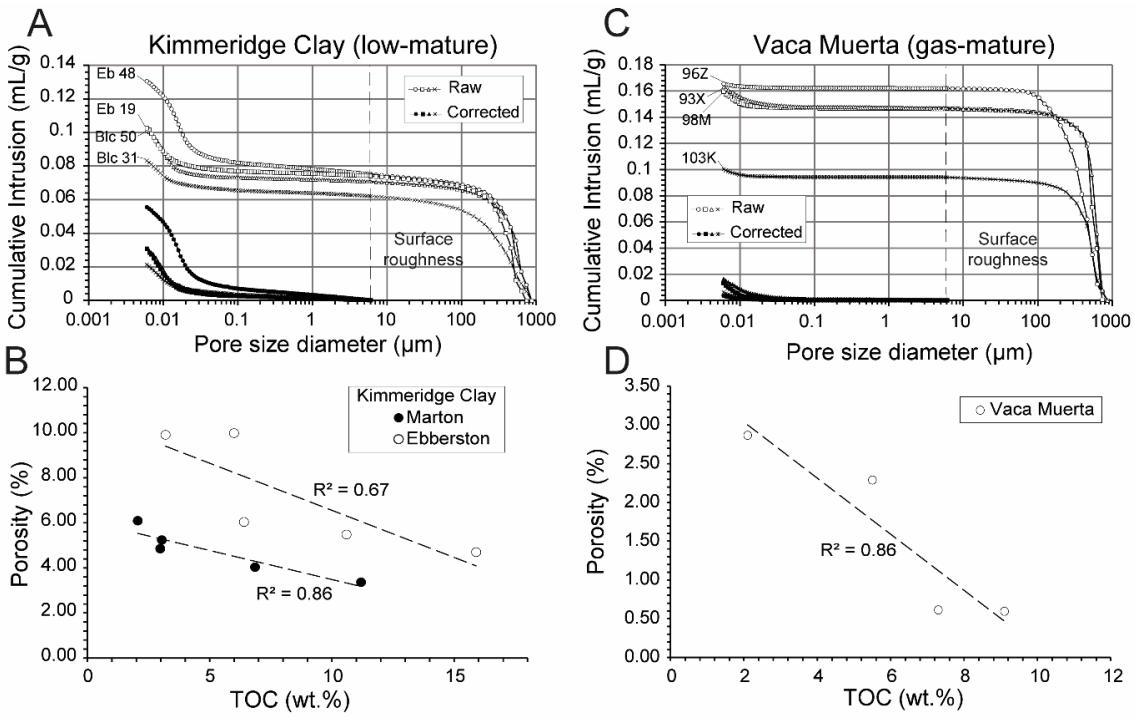

Fig. 4.13. A, C) Examples of cumulative intrusion curves derived from MIP as a function of pore size diameter before and after correction of conformance errors for KCF and VMF samples. B, D) Evolution of porosity as a function of TOC after correction.

Corrected porosity and pore volumes are listed in Tab. 4.3 and corrected PSD and cumulative intrusion curves are shown in Fig. 4.14. After corrections, the total porosity ranges from 3.37 to 9.98% and the total pore volume ranges from 1.89 to 5.57 cm^3/100g for KCF samples (Tab. 4.3). For VMF samples, their total porosities vary between 0.59 and 2.87% and the pore volume ranges from 0.35 to 1.63 cm^3/100g (Tab. 4.3), suggesting a very low macro- and mesoporosity (>6 nm). The bulk and the skeletal density of all samples decrease with increasing TOC likely due to the difference in density between OM and minerals (Tab. 4.3). All KCF and VMF samples are mainly composed of mesopores less than 30 nm in diameter with a great number of pores measuring less than 15 nm (Fig. 4.14). Only a few pores are in the 50 nm to 6 µm pore-size range in both formations (Fig. 4.14). These macropores account for ~15.63% of the total pore volume in the KCF samples from Marton and Ebberston, for 8.65% in the KCF sample from the Viking graben and for only ~ 7.71% in the VMF samples (Tab. 4.3). This suggests a less abundant macroporosity in the KCF Viking graben and VMF samples than in immature KCF samples. Similar pore size distribution is observed between low TOC samples (TOC ≈ 2.0 wt.%) from Marton/Ebberston boreholes and the Viking graben sample (Fig. 4.14).

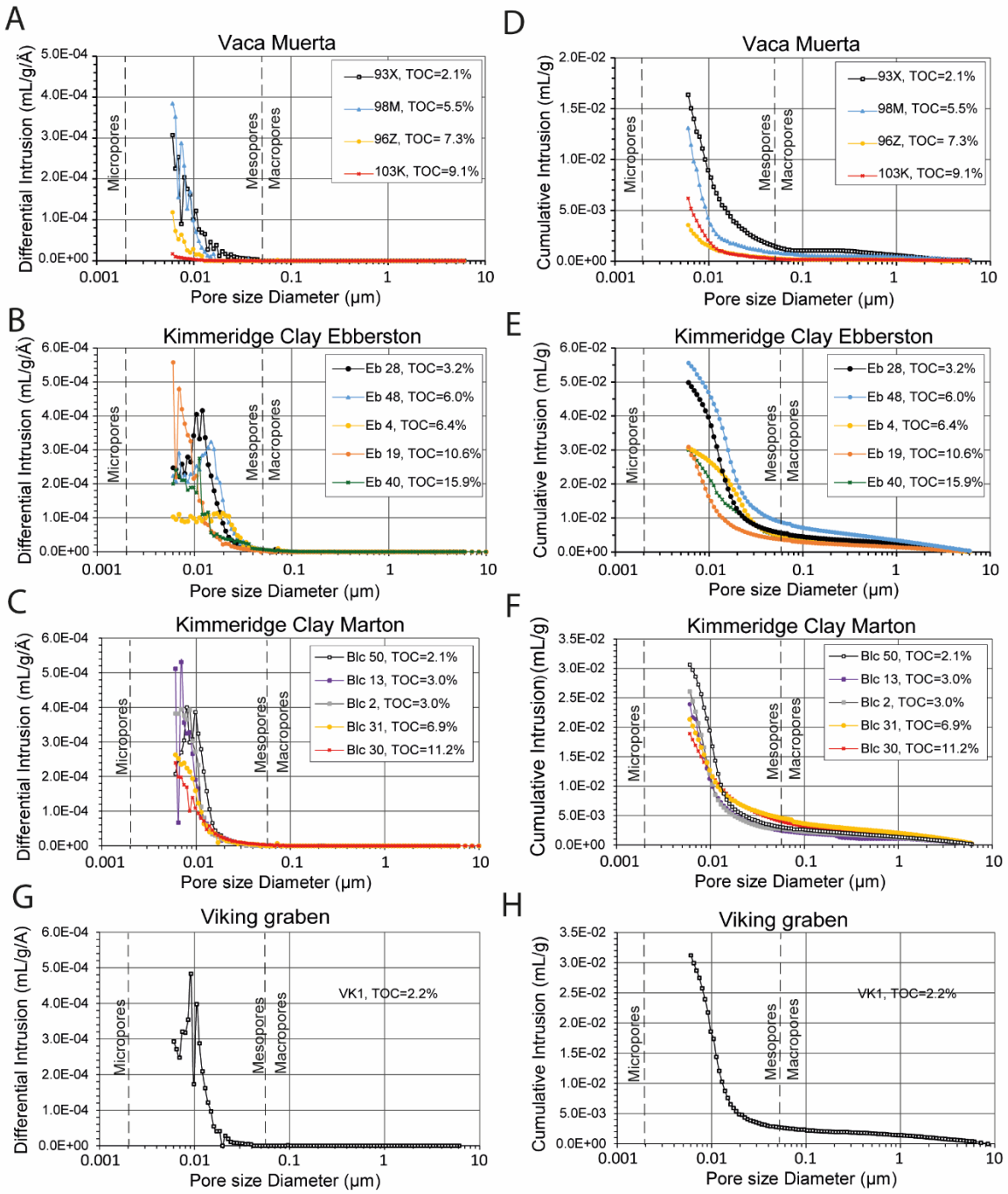

Fig. 4.14. Pore size distributions and cumulated pore volumes (after corrections) derived from mercury intrusion porosimetry measurements as a function of TOC (in weight %) for VMF (gas-mature) and KCF rocks from Marton, Ebberston boreholes (immature) and the Viking graben (oil generation).

The total pore volume and thus the porosity of KCF (Marton and Ebberston) and VMF mudstones decrease with increasing TOC (Tab. 4.3, Fig. 4.13B, D). KCF samples with more than 6 wt.% of TOC exhibit a lower number of pores in the 8 to 30 nm pore size range, and thus a lower porosity and total pore volume (Tab. 4.3, Fig. 4.13B, 4.14). Nevertheless, these high-

TOC samples can contain a significant amount of pores of less than 8 nm in diameter, such as Eb 19 or Eb 40 (Fig. 4.14). However, some of these small pores may be due to the additional creation of pore space during the crushing process at a high mercury pressure (up to 414 MPa) (Sigal, 2009; Comisky et al., 2011), and therefore these results must be interpreted with caution. VMF samples which contain more than 6 wt.% of TOC exhibit a lower porosity and total pore volume than samples with lower TOC contents due to a smaller number of mesopores in the 8–30 nm pore size range (Tab. 4.3).

Nitrogen adsorption

Data obtained from low-pressure nitrogen adsorption measurements are listed in Tab. 4.4. The pore size distributions (PSD) are shown in Fig. 4.15.

Tab. 4.4. Porosity measurements obtained by nitrogen adsorption analysis including BET specific surface areas (S_{BET}) and total pore volume (P_{vol}) for VMF and KCF samples (Marton, Ebberston boreholes, Viking graben). V_{micro}: micropore volume. S_{micro}: micropore specific surface area. S_{ext}: external specific surface area ($S_{micro} = S_{BET} - S_{ext}$). Vmicro contribution (%) is the contribution of the micropore volume to the total pore volume (%).

Sample no.	Well	TOC (wt.%)	S_{BET} (m^2/g)	P_{vol} ($cm^3/100g$)	S_{micro} (m^2/g)	S_{ext} (m^2/g)	V_{micro} ($cm^3/100g$)	V_{ext} ($cm^3/100g$)
93X	VMF	2.1	13.52	2.24	9.72	3.80	0.50	1.74
100C	VMF	3.2	17.54	2.76	15.99	1.54	0.80	1.96
94B	VMF	5.0	22.64	3.51	11.46	11.18	0.60	2.91
98M	VMF	5.5	21.07	3.57	7.39	13.68	0.30	3.27
102R	VMF	6.7	23.36	3.54	16.03	7.33	0.80	2.74
96Z	VMF	7.3	19.37	2.68	12.52	6.84	0.60	2.08
103K	VMF	9.1	29.92	3.54	23.43	6.49	1.10	2.44
	Mean	**5.6**	**21.1**	**3.1**	**13.8**	**7.3**	**0.7**	**2.4**
VK1	**VG**	2.2	17.21	3.18	/	/	/	/
Eb 4	Ebberston	7.1	15.53	4.42	4.85	10.68	0.10	4.32
Eb 19	Ebberston	10.6	12.06	3.63	7.42	4.65	0.40	3.23
Eb 28	Ebberston	3.2	33.96	5.41	9.28	24.68	0.50	4.91
Eb 38	Ebberston	14.4	10.32	2.82	1.61	8.70	0.10	2.72
Eb 40	Ebberston	15.9	9.59	3.17	1.29	8.30	0.10	3.07
Eb 48	Ebberston	6.0	20.01	5.62	0.73	19.28	0.00	5.62
	Mean	**9.5**	**16.9**	**4.2**	**4.2**	**12.7**	**0.2**	**4.0**
Blc 2	Marton	3.0	19.93	3.63	6.97	12.96	0.40	3.23
Blc 13	Marton	3.0	22.29	4.33	1.74	20.55	0.10	4.23
Blc 23	Marton	5.6	17.53	3.73	2.26	15.27	0.10	3.63
Blc 30	Marton	11.2	5.80	1.97	5.00	0.80	0.30	1.67
Blc 31	Marton	6.9	8.87	3.01	5.72	3.14	0.30	2.71
Blc 50	Marton	2.1	28.56	4.57	7.38	21.18	0.40	4.17
	Mean	**5.3**	**17.2**	**3.5**	**4.8**	**12.3**	**0.3**	**3.3**

/ method inapplicable (negative values).

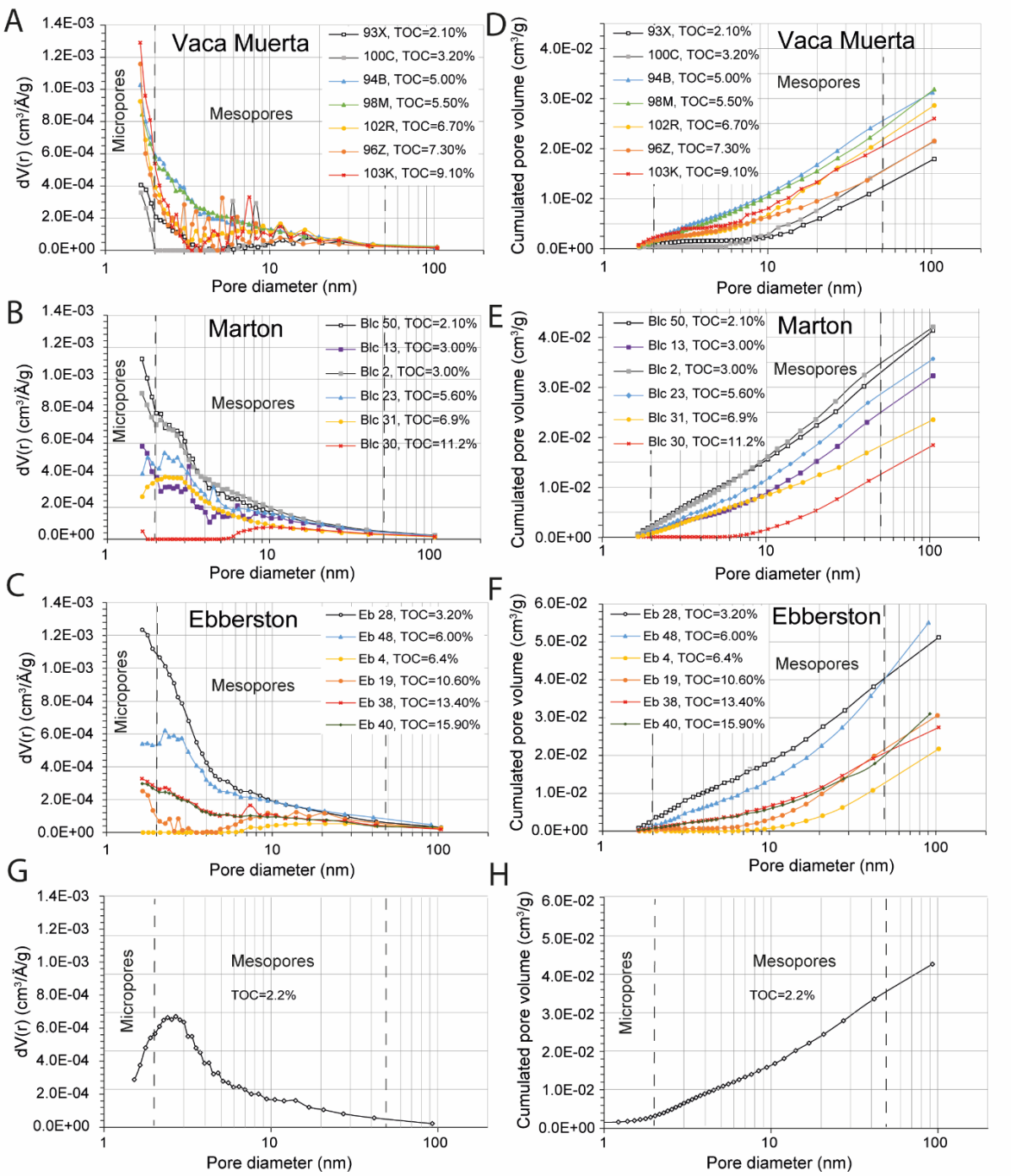

Fig. 4.15. Pore size distributions and cumulated pore volumes derived from the nitrogen adsorption branch for the isotherms of KCF (Marton, Ebberston, Viking graben) and VMF mudstones (BJH model) as a function of TOC (in weight %).

VMF exhibits total pore volumes varying from 1.97 to 4.57 cm^3/g (Tab. 4.4). In the KCF, total pore volumes range from 2.24 to 5.62 cm^3/g (Tab. 4.4). KCF samples exhibit low micropore volumes (< 0.50 $cm^3/100g$, Tab. 4.4) and low specific surface areas (< 9.3 m^2/g, Tab. 4.4). In these low-mature samples, micropores account for less than 15.2% of the total pore volume (Tab. 4.4). VMF mudstones exhibit higher micropore volumes (0.50–1.10 $cm^3/100g$) and

higher micropore specific surface areas (7.5–21.0 m^2/g, Tab. 4.4), suggesting a higher microporosity. In these thermally-mature rocks, micropores account for 8.4 to 31.1% of the total pore volume (Tab. 4.4). Despite this slightly higher microporosity in the VMF, total pore volumes of KCF and VMF are mainly provided by mesopores. Cumulative pore volumes show that the total pore volume is mainly provided by pores > 10 nm in diameter in both formations (Fig. 4.15D, E, F). PSD defined by low-pressure nitrogen adsorption analyses revealed that abundant micropores less than 8 nm are present in KCF and VMF samples (Fig. 4.15A-C, G), but have a low contribution to the total pore volume (Fig.4.15D-F, H). VMF samples show slightly higher specific surface areas than KCF samples (~21.0 m^2/g in the VMF, ~17.0 m^2/g in the KCF, Tab. 4.4). Even if lower number of micropores seems to be present in the KCF Viking graben sample, this sample exhibits relatively similar PSD as Marton and Ebberston rocks (Fig. 4.15).

Total pore volumes and specific surface areas of KCF (Marton and Ebberston) and VMF exhibit significant variations with TOC, but different trends are observed in the two formations (Fig. 4.15, 4.16A, B, E, F). OM content exerts thus a strong control on porosity which depends on the thermal maturity of these marine mudstones (Fig. 4.16). In KCF samples, the specific surface area, the total pore volume (Fig. 4.16 A, B) and the content of small mesopores and micropores (< 10 nm) decrease simultaneously with increasing TOC (Fig. 4.14, 4.15B, C). Similar trends are observed for the cumulated pore volumes in the 10-100 nm pore size range (Fig. 4.15E, F), suggesting the decrease in the number of pores > 10 nm in diameter with increasing TOC. KCF samples can be divided into two groups according to the texture of clay minerals in SEM observations (Fig. 4.16C, I, J). In lower clay samples, identified as group 1, phyllosilicate aggregates appear mainly isolated, dispersed in the mineral matrix with a more random orientation and accompanied by heterogeneous diffuse organo-mineral aggregates (Fig. 4.16C, D, J). In clay rich-samples, identified as group 2, the phyllosilicate aggregates are parallel to each other, more compact, with some interlayer pores (Fig. 4.16C, D, I). In this group, the OM is mainly composed of laminar pure OM without or with fewer insertions of clays. For both groups, the total pore volume strongly increases with quartz, carbonate and albite contents. In spite of the lower clay mineral contents of VMF samples, their specific surface area increases with increasing TOC content (Fig. 4.16F). However, the evolution of pore volume as a function of TOC appears more complex since no relationship can be discerned between differential pore volumes and TOC contents (Fig. 4.15A, D).

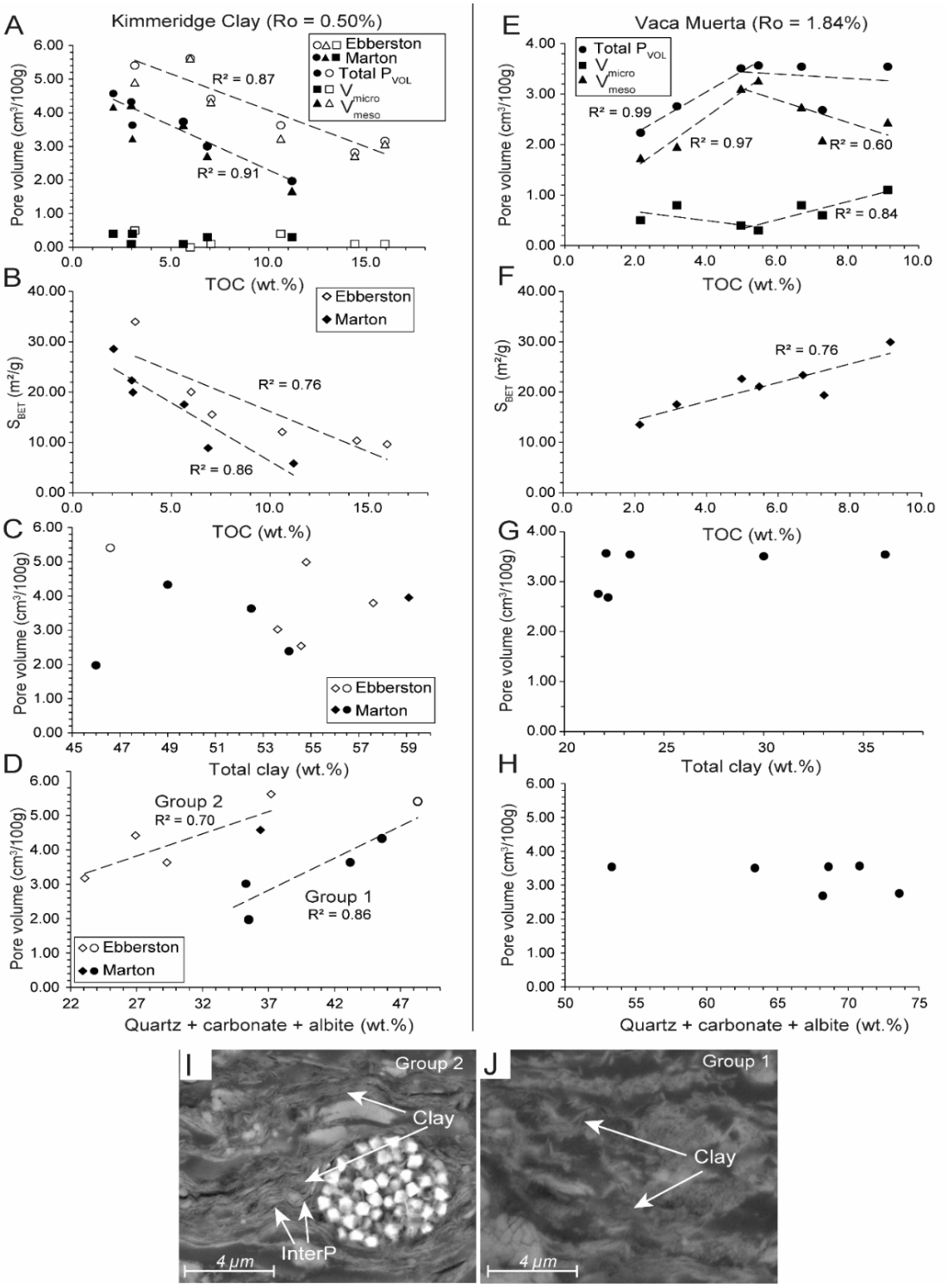

Fig. 4.16. A-H) Pore volumes and specific surface areas from nitrogen adsorption measurements as a function of TOC, clay, quartz, carbonate and albite contents for VMF and KCF rocks (Marton, Ebberston). C-D) The dots represent samples with relatively low clay mineral contents (group 1) and the diamonds stand for samples with relatively high clay mineral content (group 2). I-J) SEM images of broad ion beam milled thin sections of immature KCF samples showing differences in the texture of clay minerals between the group 1 (J) and 2 (I). InterP: interparticle pores.

The total pore volume (Fig. 4.16 E) and the cumulated pore volume (Fig.4.15 D) first increase with TOC contents but a lack of correlation is observed above 5.5 wt.%. That trend appears to be associated with the presence of smaller pores in organic-rich mudstones as evidenced by the decrease in the mesopore volume and the increase in the micropore volume above 5.5 wt.% of TOC (Fig. 4.16E) and the high content of mesopores less than 2 nm in diameter in very high-TOC samples (Fig. 4.15A). In contrast with low-mature samples, the total pore volume of VMF rocks exhibits no correlation with clay, quartz, feldspar and carbonate contents (Fig. 4.16G, H). Despite similar pore volumes and PSD, VMF and KCF mudstones exhibit therefore different pore characteristics.

4.2. Discussion

4.2.1. Organic petrography, porosity and pore size distribution

Petrographic and Rock Eval analysis show that KCF samples from Marton and Ebberston consist of low-mature organic-rich argillaceous mudstones with a high potential for oil generation (HI≈500 mg HC/g TOC) while VMF samples consist of gas-mature siliceous mudstones mainly composed of a residual OM with a low residual petroleum potential (RC/TOC > 0.90, low HI values, Tab. 4.2, Fig. 4.1, 4.3). The Viking graben sample is a perfect equivalent (similar macerals, HI, S2, TOC) of the least organic-rich samples from Marton and Ebberston boreholes (TOC ≈2.0 wt.%) but with a slightly higher thermal maturity corresponding to the early oil generation. This substantiates the %Ro of ~1.65% determined by Legarreta and Villar (2011) in the VMF, the %Ro of ~0.50% obtained by Ramanampisoa and Disnar (1994) in KCF mudstones from Marton and Ebberston boreholes and the range of maturity reached by the KCF in the Viking graben (Rm ≈ 0.5-1.3%, Johnson et al., 2005). In KCF samples, the OM components identified in petrographic observations can be grouped into three classes according to their origin: (1) the brown AOM (diffuse OM) (Fig. 4.8, 4.7) which are derived from the selective preservation of resistant cell-walls of green microalgae and bacterial biomacromolecules (Largeau et al., 1984); (2) terrestrial particles including spores, woody and cuticular fragments and black AOM (Fig. 4.7, 4.8) derived from bacterial macromolecules mixed with altered lignaceous debris (Boussafir and Lallier-Vergès, 1997); (3) the orange AOM interpreted as bituminite macerals (Fig. 4.7, 4.8, (Boussafir et al., 1995b; Lallier-Vergès et al., 1995; Boussafir and Lallier-Vergès, 1997). Previous studies suggest that these macerals have high hydrocarbon potentials and nanoscopically amorphous and homogeneous ultrafine structures in TEM observations, and are derived from phytoplanktonic

lipidic OM preserved by natural vulcanization (Ramanampisoa and Disnar, 1994; Boussafir et al., 1995b; Boussafir and Lallier-Vergès, 1997). In the KCF, periods of high productivity allow the metabolizable OM to enter the anoxic zone, favoring the development of sulphate-reducing organisms and thus the production of H_2S (Lallier-Vergès et al., 1995; Boussafir and Lallier-Vergès, 1997). Most of this H_2S diffuses from the sea sediments, while a part reacts with the reactive metals present in sediments to form sulphides (commonly pyrite). The excess of H_2S is then in part incorporated as organosulfur compounds in the metabolizable OM by natural vulcanization to form bioresistant AOM known as orange AOM (Boussafir and Lallier-Vergès, 1997). These processes of natural sulfurization have allowed the preservation of a large amount of metabolizable OM explaining why all KCF mudstones are not close to the monolayer equivalent field in the TOC versus specific surface area diagram (Fig. 4.12). Furthermore, this also explains the strong association of these hydrogen-rich amorphous OM with pyrite (Fig. 4.7, 4.9) and the relative increase of the OM quality in terms of oil-proneness with increasing TOC (Tab. 4.2, Fig. 4.10).

In SEM images, such OM exhibits a homogenous and gelified texture with well-defined boundaries and manifests a very low primary porosity (Fig. 4.9). In the high-TOC samples (≥ 5.4 wt.%, Tab. 4.2), the amorphous OM represents more than 85% of TOC based on observations with SEM (Fig. 4.10). These amorphous and homogeneous particles have lost their inherited biological structure due to reorganizations during preservation processes (Boussafir et al., 1995a; Boussafir et al., 1995b; Boussafir and Lallier-Vergès, 1997), probably explaining their low primary porosity. Furthermore, the increase in the pore volume, the porosity and the specific surface area with decreasing TOC (Fig.4.16A, B) suggests that the porosity of these low-mature mudstones is not provided by these rare OM-hosted pores. On the contrary, the gel formed by this amorphous OM appears to fill the interparticle mineral porosity, reducing the pore volume (Fig. 4.9, 4.16A, B). Most of the porosity in these low-mature rocks is thus composed of mineral-associated pores which are not filled by OM (Fig. 4.9). The strong increase in the pore volume with quartz, calcite and albite contents (Fig. 4.16D) indicates that the pores located between mineral grains (Fig. 4.9) largely contribute to the total porosity. Nevertheless, the behavior of the pore volume as a function of quartz, calcite and albite contents seems to be influenced by the texture of the clay minerals (Fig. 4.16). The slightly higher clay mineral contents of group 2 (Fig. 4.16C) seem to have favored the presence of thick phyllosilicate aggregates parallel to each other, more compact, with some interlayer pores (Fig. 4.16I). In samples with relatively low clay mineral contents (group 1), clay minerals,

mainly isolated, dispersed in the mineral matrix with a more random orientation and with the presence of heterogeneous diffuse organo-mineral aggregates appear to be less favorable to the presence of interlayer-pores between them (Fig. 4.16J). This observation suggests that clay mineral texture can influence the porosity of low-mature marine mudstones. However, the origin of this difference of texture and the link with clay mineral contents is unclear and further investigations are required. No real differences of OM texture and porosity are visible in light microscopy and SEM, images between the immature Marton and Ebberston samples and the oil-mature sample from the Viking graben (Fig. 4.7, 4.9). This suggests that no pores development seems to occur in OM in response to the early oil generation.

VMF samples exhibit very different features. The generation of HC with increasing maturity has led to the formation of a residual OM identified as pyrobitumen (Fig. 4.5). This carbon-rich residue was probably formed during the secondary cracking of liquid oil into gas (Tissot and Welte, 1984; Lewan, 1993; Behar et al., 1997; Bernard et al., 2012a; Reed et al., 2014). The large predominance of pyrobitumen was previously noted in most thermally mature mudstones (Bernard et al., 2012a; Hackley and Cardott, 2016; Hackley, 2017). In SEM and petrographic observations, this “grainy” OM exhibits a highly-developed and interconnected OM-hosted porosity compared to the KCF immature and early oil-mature organic “gel” (Fig. 4.6, 4.9). These nanometer-size OM-hosted pores exhibit variable shapes (Fig. 4.6). While most of them are subangular spongy OM pores, abundant oval pores (bubble-like) are visible in some OM particles (Fig. 4.6). Similar pores have been commonly described in thermally-mature mudstone reservoirs (Loucks et al., 2012; Bernard et al., 2012b; Curtis et al., 2012; Hackley and Cardott, 2016; Ko et al., 2017; Ko et al., 2018). These oval and subangular spongy pores are often considered to be formed in pyrobitumen during gas generation and expulsion from the end of the oil window to the dry gas zone (Bernard et al., 2012b; Ko et al., 2016). Not all the OM in the VMF is porous: some sparse and rare OM particles, probably kerogen (inertinite) are non-porous or exhibit a very low porosity (Fig. 4.9G). Similar observations were made in thermally mature KCF, Woodford and Marcellus mudstones (Curtis et al., 2012; Fishman et al., 2012; Hackley and Cardott, 2016), suggesting that residual kerogen evolves differently from pyrobitumen with increasing maturity. Contrary to the KCF, the strong increase in the specific surface area with TOC (Fig. 4.16F) demonstrates that the porosity of gas-mature mudstones is mainly provided by these OM-hosted pores. On the contrary, the absence of correlation between TOC and mineral contents (Fig. 4.16G, H) suggests that the

interparticle pores identified between clay sheets, calcite and quartz grains (Fig. 4.5) do not significantly contribute to the pore volume.

OM from the thermally mature VMF rocks is dominated by pyrobitumen (Fig. 4.5, 4.6). Due to the high maturity of these samples, this precursor OM is unidentifiable but previous studies have shown the presence of a KCF-like type II OM (Uliana et al., 1999; Legarreta and Villar, 2011, 2015). OM of low-mature VMF mudstones is mainly composed of hydrogen-rich type II OM derived from the early diagenesis of phytoplankton and algal bacterial contributions (orange and brown AOM observed in KCF) with variable amounts of alginite and terrestrial relics (Uliana et al., 1999; Legarreta and Villar, 2011, 2015). Highly oil-prone amorphous OM content increases with TOC content (3 to 12 wt.%, Legarreta and Villar, 2011, 2015), leading to fluctuations of HI (≈ 650 mg HC/g TOC) and OI (< 30–40 mg CO_2/g TOC, Legarreta and Villar, 2011, 2015) as a function of TOC as observed in KCF mudstones (Tab. 4.2). Therefore, in the present study VMF and KCF mudstones exhibit: (1) similar high pyrite contents which attests to natural sulfurization processes (Tab. 4.1); (2) a similar absence of correlation between clay and TOC contents (Fig. 4.11); (3) similar high TOC contents compared to their specific surface areas (Fig.15, Hedges and Keil (1995) showing the low contribution of organo-clay interactions regardless of vulcanization (orange AOM) and selective preservation processes (brown AOM). These formations thus contain three different maturity of similar OM which may allow comparison of their OM-hosted porosity as a function of maturity.

Previous work has demonstrated that clay minerals can act as catalysts in the acid-catalyzed cracking of kerogen into hydrocarbons during thermal maturation (Tannenbaum and Kaplan, 1985; Pan et al., 2009). Differences in clay mineral contents appear to mainly influence the kinetics of HC generation during the low stage of maturation (Tannenbaum and Kaplan, 1985). We can assume that variations in clay mineral content may lead to a different evolution of OM porosity in some formations during the oil generation stage. The catalytic influence of clays is, however, minor in higher maturation stage such as the gas window for our VMF samples (Tannenbaum and Kaplan, 1985). However, if we admit some catalytic effect in this higher maturation stage, and despite the lower clay mineral content of the VMF samples (Tab. 4.1, Fig. 4.1), most of the OM is integrated with or closely associated to clay mineral aggregates (Fig. 4.6A, B, D) as for the KCF. We can therefore assume that the catalytic effect of clay might be similar in the two formations and that the difference in mineralogy between them probably had a limited impact on OM porosity.

4.2.2. Thermal maturity involvement in OM-hosted pore genesis

The hydrous pyrolysis experiments of Chen and Xiao (2014) suggest that porosity and pore volumes increase with increasing maturity and thus thermally-mature mudstones will exhibit a higher porosity than low-mature rocks. Surprisingly, pore volumes determined from nitrogen adsorption show similar trends for both formations despite their difference in maturity (Tab. 4.4). This observation suggests that the relationship between thermal maturity and total pore volume is not straightforward. The porosity of both formations appears to be mainly mesoporous. The few numbers of mesopores in the 7-100 nm pore size range account for the most part of the pore volume (Fig. 4.15). KCF and VMF samples contain, however, abundant mesopores and micropores less than 8 nm in diameter which have a low contribution to the total pore volume (Fig. 4.14, 4.15). The presence of these very small mesopores (< 8 nm) and micropores has been previously noted in many gas shale systems (Chalmers and Bustin, 2008; Chalmers et al., 2012; Tian et al., 2015). The contribution of micropores to the total pore volume determined from nitrogen adsorption is higher in thermally-mature VMF mudstones (~21.0%) than in the KCF (~4.9 - 8.7%, Tab. 4.4). MIP measurements reveal that the macropores observed in SEM images do not greatly contribute to the porosity of KCF (≤23%, Tab. 4.3) and VMF mudstones (Fig. 4.9, 4.14). This may explain the low porosity and the low pore volumes of VMF samples measured using MIP (Tab. 4.3): the main part of the porosity of these thermally-mature mudstones is below the detection limit of MIP. This was especially true for VMF samples in which macropores account for less than 9% of the total pore volume obtained by MIP (Tab. 4.4). Moreover, VMF samples show slightly higher specific surface areas (Tab. 4.4). This result is quite surprising in view of the mineralogical compositions of these two series. Contrary to the observations, the higher content of clay minerals in KCF samples (Fig. 4.1) is expected to give them a greater specific surface area. This difference is likely related to the greater microporosity of VMF samples. This suggests a greater contribution in the KCF of the macropores observed between mineral grains and clay mineral aggregates in SEM images (Fig. 4.9). The higher thermal maturity and the greater depth of gas-mature samples have probably allowed a greater mineral matrix compaction than in low-mature KCF mudstones, thus probably reducing the number of macropores. Moreover, the presence of some mineral/OM pores and abundant pyrobitumen (Fig. 4.5, 4.6) suggests that the original mineral pores were partially filled during petroleum generation. Located between mineral grains (Fig. 4.6F), these ‘modified mineral pores’ are considered as original mineral pores, filled first by bitumen which was later extracted leaving behind residual pyrobitumen and smaller pores

(Ko et al., 2016; Ko et al., 2017). It can therefore be assumed that this process has also contributed to the progressive decrease in the number of primary macropores in thermally-mature samples.

The more fully developed spongy OM-hosted pores in gas-mature rocks suggests that they are essentially controlled by thermal maturation. This observation substantiates the common model of OM-hosted pore genesis which holds that the porosity increases during maturation in response to the volume lost during expulsion of the liquid and gaseous HC produced by the thermal primary and secondary cracking of the OM (Jarvie et al., 2007; Chalmers and Bustin, 2008; Loucks et al., 2012; Curtis et al., 2012). Recent studies show that these OM-hosted pores first formed in pyrobitumen since the oil window (Juliao et al., 2015; Hackley and Cardott, 2016; Ko et al., 2016) may further developed progressively to the dry gas zone and become predominant in gas-mature mudstones such as the VMF samples (Jarvie et al., 2007; Chalmers and Bustin, 2008; Loucks et al., 2012; Curtis et al., 2012; Chen and Xiao, 2014; Hackley, 2017; Ko et al., 2018). If this formation of OM-hosted pores starts during oil generation, the thermal maturity reached by the KCF sample form the Viking graben seems however not sufficient to allow any porosity development. Furthermore, while OM appears to be the major contributor to the total pore volume of these thermally-mature mudstones, the total pore volume does not increase linearly with TOC (Fig. 4.16E). This suggests that other factors than maturity are operating.

While the OM-hosted porosity increases strongly with maturity (Loucks et al., 2012; Curtis et al., 2012; Chen and Xiao, 2014; Hackley, 2017; Ko et al., 2017), this gain in volume may be counteracted by the decrease in the interparticle pores by compaction and diagenetic processes (Charpentier et al., 2003; Day-Stirrat et al., 2008; Milliken et al., 2013). The combination of these processes may not lead to a systematic variation in the total pore volume as a function of maturity (Tab. 4.3). As suggested by Milliken et al. (2013) and Pan et al. (2015) TOC may thus sometimes have a stronger control on these parameters than thermal maturity.

4.2.3. Secondary OM-hosted pores vs primary organic porosity

In contrast with SEM observations in immature and early oil-mature KCF mudstones which reveal a very low primary OM-hosted porosity, the presence of very porous OM has been previously noted in the Woodford shale, in the Monterey or in Stuart Range formations between Rm of 0.35-0.50% (Löhr et al., 2015). This suggests that some specific OM may contain abundant primary OM-hosted pores inherited from their biological structure. Löhr et al. (2015)

showed that this primary organic porosity may influence the development of secondary organic pores during thermal maturation, leading to inhomogeneity in the OM-hosted pore distribution at more elevated maturities. The presence of primary pores in originally deposited amorphous and structured OM of algal and terrestrial origin was previously noted in various thermally immature mudstones (Mastalerz et al., 2013; Löhr et al., 2015; Reed, 2017; Han et al., 2017) including the KCF (Fishman et al., 2012; Katz and Arango, 2018). Reed (2017) suggested that this primary OM porosity is closely related to the presence of terrestrial OM, probably inherited from the original structures of cellulose and woody fragments. The low content of these terrestrial organic materials in KCF samples (less than 15% of the TOC, Fig. 4.10) and the small area covered by SEM images probably may not allow the observation of these porous OM in the present study. This absence of pores is not a surprise for AOM particles of phytoplanktonic origin, known to have a perfect nanoscopically homogeneous ultrafine structure resulting from early diagenesis jellification processes (Boussafir et al., 1995b). While OM-hosted pores may subsist in biological figured particles as woody fragments and amorphous OM of algal and phytoplanktonic origin, they may not survive to the compaction and early diagenesis processes (such as microbial reworking) in our KCF samples. Schieber (2013) suggested that primary OM-hosted pores are more likely to be preserved in the presence of a protective rigid framework of grains which can hinder OM compaction. Our KCF samples are mainly composed of ductile components such as abundant clay mineral sheets, thick laminar AOM, thin elongated AOM particles and diffuses AOM domains mixed with clay minerals (Fig. 4.9) known to be particularly prone to compaction (Fishman et al., 2012; Milliken et al., 2014). The deformation of this ductile framework may have resulted in the destruction of a potential primary OM-hosted pore network and in the migration of deformed AOM in interparticle mineral-hosted pores at the origin of the AOM-mineral complex observed by SEM (Fig.10A-C). Furthermore, even if we assume that non-observed primary OM-hosted pores exist in low-mature KCF mudstones, these pores do not significantly contribute to the total pore volume, as shown by the decrease in porosity, the total pore volume and the specific surface area with increasing TOC (Fig. 4.13B, 4.16A).

While the difference in OM-hosted porosity between low-mature KCF and thermally-mature VMF mudstones is clearly illustrated in the present study, Fishman et al. (2012) demonstrated that in the offshore KCF mudstones, the size and abundance of this primary porosity varies with the maceral composition but is largely similar regardless of maturity variation between 0.5–1.3%Ro. Similar observations were also noted in the Woodford shale, in

the Monterey or the Stuart Ranges formations (Löhr et al., 2015). A hypothesis can be proposed to explain this difference with gas-mature rocks from the VMF. Once again, as suggested by Fishman et al. (2012), the plastic nature of the clay-rich KCF mudstones (Tab. 4.1, Fig. 4.1) could allow a greater compaction of pores developed during HC generation. The secondary OM porosity in KCF mudstones may thus have not been preserved like the VMF mudstones which exhibit a higher content of rigid minerals (quartz and feldspar, Tab. 4.2) and allow a better preservation of pores during compaction (Day-Stirrat et al., 2008; Schieber, 2010). Nevertheless, further investigations are needed to understand the connections which may exist between mineral compositions, compaction and secondary OM-hosted pores.

4.2.4. TOC and OM composition controls on pore genesis

Although thermal maturation appears to have significant effect on OM-hosted genesis, this process alone is insufficient to explain the decrease in the pore size with increasing TOC in thermally-VMF mature samples with TOC values greater than 5.5 wt.% (Fig. 4.16E). Similar trends were also previously observed by Milliken et al. (2013) and Pan et al. (2015). This observation may explain the lower pore volumes and MIP porosity of the two very high-TOC samples (7.3 wt% and 9.1 wt.%, Fig. 4.13D). Contrary to the lower-TOC samples (< 5.5 wt.%) which contain larger pores, the main part of the porosity of these high-TOC samples (> 5.5 wt.%) is below the detection limit of MIP. These samples contain a higher proportion of mesopores and macropores below the MIP detection limit (Tab. 4.3). The difference in the OM composition between high- and low-TOC samples could explain these pore-size variations as a function of TOC. In KCF mudstones, the increase of orange AOM content is responsible for higher values of HI and petroleum potential (S_2) and corresponds to periods of anoxia favorable to natural sulfurization processes (Boussafir et al., 1995a). These periods are marked by slightly lower quartz content (Fig. 4.11). By comparison, low-TOC samples correspond to periods marked by a greater proportion of quartz and terrestrial OM inputs (Fig. 4.10, 4.11), responsible for the decrease in the OM quality with respect to oil generation and in the TOC content (Fig.4.4A, B). Similar variations were previously documented in low-mature VMF mudstones (Legarreta and Uliana, 1991; Uliana et al., 1999; Legarreta and Villar, 2011, 2015). Similar variations in the original OM composition as a function of TOC can thus be expected in VMF mudstones and three explanations can be suggested: (1) As previously mentioned (Milliken et al., 2013; Pan et al., 2015), the smallest OM-pores of organic rich samples may represent a

more complete pore network collapse after petroleum migration caused by a higher HC production (or higher petroleum potential); (2) Alternatively, higher TOC samples from the VMF probably contained a greater content of well-preserved highly oil-prone OM which are less prone to the production of large *in-situ* OM mesopores during maturation. Well-preserved and more hydrogen-rich type II macerals (e.g., high HI values) produce liquid hydrocarbons, richer in light constituents, that are easy to migrate outward while more degraded and less oil-prone (e.g., low HI values) type II macerals produce heavier and more viscous oils (richer in asphaltenes, (Tissot and Welte, 1984; Bourbonniere and Meyers, 1996). During the secondary cracking of these viscous oils, abundant pyrobitumen and essentially gaseous HC are produced, which may result in a greater amount of mesoporosity. This may explain why TOC and pore volume are not systematically positively correlated. Moreover, some macerals such as inertinite (Fig. 4.6G) do not appear to develop pores with increasing maturity. This may explain the variations in porosity observed between nearby organic regions of the same sample in Woodford mudstones (Curtis et al., 2012). Changes in the relative proportion of these non-porous macerals may thus explain some variations between these samples. The importance of maceral types has been previously emphasized to explain porosity variations (Loucks et al., 2012; Fishman et al., 2012; Milliken et al., 2013; Cardott et al., 2015; Ko et al., 2017; Ko et al., 2018) (3) A close link seems to exist between the production of gas and OM-hosted pore genesis from the oil window to the dry gas zone (Bernard et al., 2012a; Milliken et al., 2013). Spongy pores in thermally-mature samples seem to form by the nucleation and the expulsion of gaseous HC produced by the thermal cracking of OM (Chalmers and Bustin, 2008; Bernard et al., 2012a; Loucks et al., 2012; Bernard et al., 2012b; Curtis et al., 2012; Milliken et al., 2013). Moreover, artificial maturation experiments have shown that the quantity of gas (CO, CO_2, CH_4, C_2-C_5) generated during the thermal diagenesis of OM can vary greatly between type I, II or III kerogen (Behar et al., 1992, 1997). It may be appropriate to assume that slight fluctuations in the OM composition may have led to the production of various quantity of gas during thermal maturation resulting in variations of the amount of spongy pores formed in residual OM between samples. This may explain in part why high- and low-TOC samples in the VMF exhibit different pore sizes and why porosity appears to be mainly controlled by TOC in some formations such as the Marcellus (Milliken et al., 2013) or in the Lower Yangtze region (Pan et al., 2015). This suggests therefore that thermal maturity and OM composition have a complementary effect which need to be clarified.

Summary and conclusions

The pore structure and the geochemistry of rocks of various thermal maturity from the KCF and the VMF were investigated and the following conclusions are drawn.

KCF rocks are low-mature marine mudstones mainly composed of low-porous marine AOM while VMF samples are gas-mature marine mudstones mainly composed of porous pyrobitumen. The OM composition of immature KCF samples manifests variations. High-TOC samples contain higher lipidic phytoplanktonic fractions and thus have a higher petroleum potential than low-TOC samples. Similar variations were observed in immature VMF mudstones. PSD shows a predominance of pores < 30 nm and the pore volume ranges between 2-5 cm^3/100g regardless of the degree of maturity. Nevertheless, pore networks significantly with thermal maturity. The porosity of low-mature mudstones is dominated by inorganic interparticle pores while the main contributor to the porosity of gas-mature rocks is OM. OM porosity, low in the immature and oil generation stages, appears to be formed in solid bitumen and increases during thermal diagenesis in response to HC generation.

Although the porosity of gas-mature mudstones is mainly controlled by OM, surprisingly no linear correlation is observed between TOC and pore volume above 5.5 wt.%. This observation is tied to the decrease of the pore sizes with increasing TOC. Differences in the composition of the precursor OM between high- and low-TOC samples may explain these pore-size variations.; three hypotheses can be put forward: (1) a stronger framework compaction of high-TOC samples in response to the volume lost during the expulsion of a greater amount of HC (higher petroleum potential); (2) The presence of well-preserved and more hydrogen-rich type II OM in high-TOC samples that is less favorable to the production of viscous oils and abundant porous pyrobitumen and thus less favorable to the formation of large mesopores (3) Variations in the quantity of gas generated during thermal maturation due to different composition of the OM precursor leading to variations in the quantity of pores formed in residual OM during gas expulsion. However, slight variations of mineralogy exist between VMF and KCF samples and the composition of the OM precursor in thermally mature VMF samples is not identifiable. This makes it difficult to really understand the role of the original OM composition on pores development and the different steps of the evolution of porosity during maturation. The use of artificial thermal maturations on immature KCF rocks can thus be a key to better understand the influence of OM composition during the progressive evolution of porosity during thermal transformations. This is the main goal of the next chapter.

Chapter 5: Concomitant organic matter geochemical transformation and porosity development during confined thermal maturation: insights into the influence of organic matter composition on pores development

5. Concomitant organic matter geochemical transformation and porosity development during confined thermal maturation: insights into the influence of organic matter composition on pores development.

A great part of this chapter has been published in the International journal of Coal Geology under the title 'Effect of organic matter composition on source rock porosity during confined anhydrous thermal maturation: example of Kimmeridge-clay mudstones.' (Cavelan et al., 2019a)

Abstract

To better understand how the original total particulate OM assemblage, maceral types, the geochemical composition of kerogen and the composition of the products generated during its thermal transformations can influence the ability of organic-rich source rocks to develop pores with increasing maturity, laboratory anhydrous thermal maturations were applied on the immature KCF mudstones. Nitrogen adsorption measurements, organic petrography (palynofacies and maceral analysis), SEM observations, bulk and molecular geochemical characterization (Rock Eval®, GC/MS, GC-TCD) were performed to examine the concomitant evolution of the OM geochemical properties and porosity for slightly different type II kerogen composition during maturation. Our results reveal that kerogen and bitumen transformations are mainly responsible for the formation, the occlusion and the destruction of pores with increasing maturity. After the thermal maturation, the initial bulk and molecular composition of the OM seem to be the dominant factors controlling the evolution of porosity. Samples with a higher phytoplanktonic OM content (orange AOM) contain higher content of thick ductile bituminite macerals and generated higher amounts of saturated and aromatic HC, richer in hydrogenated and lighter components (n- and isoalkanes…), leading to a more complete impregnation of the mineral matrix by bitumen and forming a well interconnected OM network. The more efficient secondary conversion of this OM network into C_1-C_5 HC resulted in the formation of a well-developed but more vulnerable OM porosity, more repeatedly altered by collapsing processes. Hence, for similar TOC, KCF rocks with a higher oil generation potential exhibit lower pore volume during gas generation stages. It therefore appears essential to consider clearly the identification of the composition of the original OM assemblage and to consider the geochemical properties of OM to better predict the amount of bitumen, oil and gas generated during thermal maturation and the associated pore development.

Introduction

Our previous works show that thermal maturity has indeed a major role in the development of the porosity of organic-rich mudstones in controlling the formation of pores in OM. However, difference of OM composition and petroleum potential between VMF mudstones appears to have dramatically influenced the OM-hosted pore genesis during maturation. Source rock kerogen can be composed of particles of various origins, with distinct morphologies, internal structure and chemical composition. The differences between these organic components in the same type of kerogen may influence the timing and the ability to generate oil, gas and solid bitumen during burial (Tissot and Welte, 1984). This may lead to variation in the character, the distribution and the timing at which pores are generated during maturation. However, isolating the influence of these factors on porosity during burial and thermal maturation turns out to be a complex task. Significant variations of mineralogy, OM composition and content can indeed exist within a same formation at various ranges of maturity. In reducing the complexity that exists in natural mudstones, the use of laboratory simulations can be a key to better understand and discriminate the influence of factors other than thermal maturity on porosity. To investigate how slight variations in the composition of the total particulate OM assemblage and maceral types affect the evolution of the size, the distribution and the abundance of pores during thermal maturation of organic-rich marine mudstones, anhydrous confined thermal maturation experiments were conducted on the immature KCF rocks. According to the previous results, six samples exhibiting slight differences in the total particulate OM assemblage and various TOC content were selected in Marton and Ebberston series for these experiments (B2, B23, B31, E19, E38 and E40). As shown earlier, the mineralogy of Marton and Ebberston samples is relatively homogeneous. The assessment of the composition of the OM precursor, its pore structure and its evolution with increasing thermal maturity was conducted using nitrogen adsorption measurements, XRD, organic and SEM petrography, bulk geochemical characterizations (palynofacies, maceral composition, vitrinite reflectance, Rock-Eval, GC-TCD), and molecular analysis (GC/MS). The question specifically addressed in this chapter is how slight differences in the relative proportion of individual OM components, maceral types and OM content throughout the same formation affect OM pores development and evolution during the maturation of organic-rich marine mudstones.

5.1. Results

5.1.1. Mineralogy

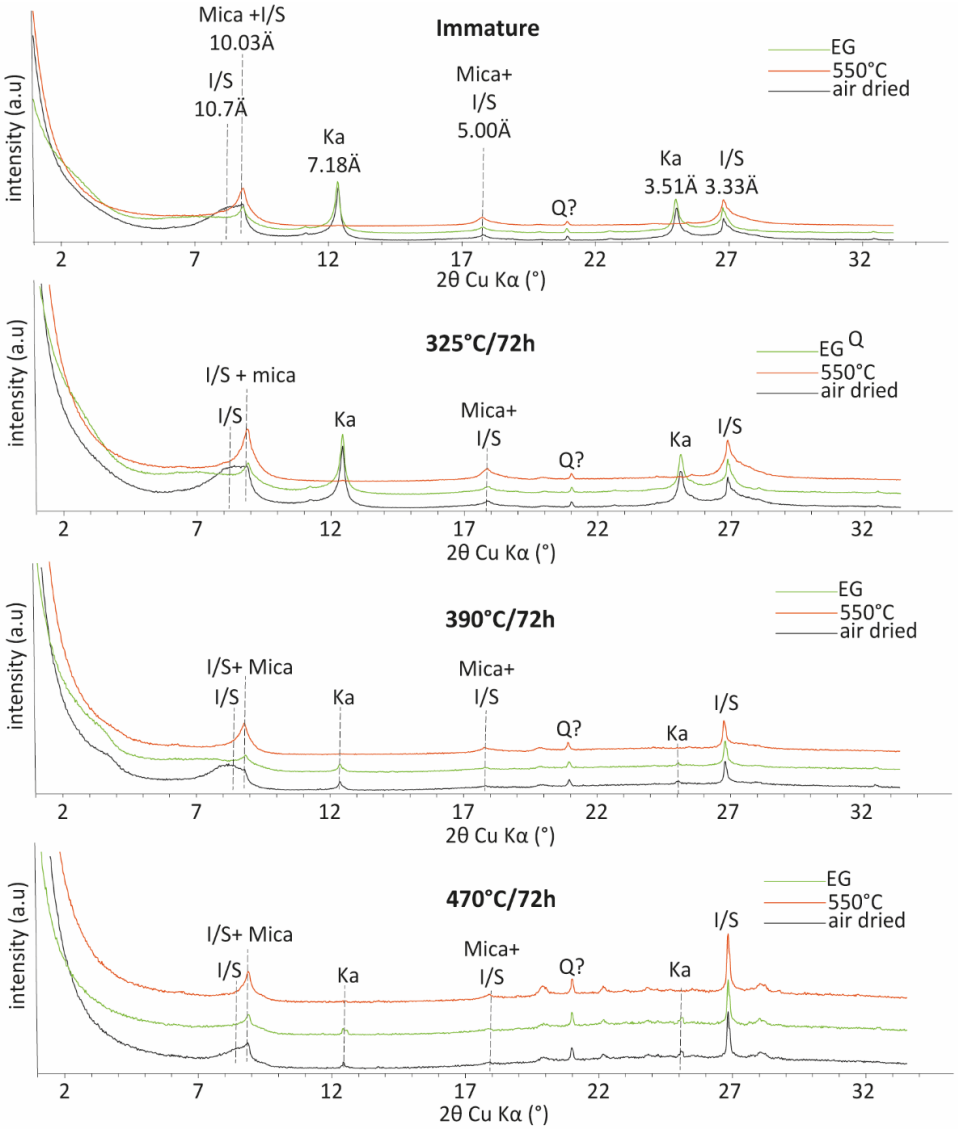

Fig. 5.1. XRD diffractograms of KCF clay mineral oriented slides after thermal maturation. EG: ethylene glycol. I/S: mixed layered Illite/smectite. Q: quartz. Ka: kaolinite.

The evolution of the clay-oriented slides XRD diffractograms before and after thermal maturation are presented in Fig. 5.1. As previously showed in chapter 4, clay minerals are mainly composed of mixed-layered Illite/Smectite and kaolinite. The composition of clay minerals is similar before and after thermal maturation. A slight increase of the resolution of the peak at 3.33Ä is observed after maturation suggesting a small increase of the illite crystallinity. This increase is however less important than those observed in natural samples (Fig. 4.2). Artificial maturation experiments are probably too short to properly simulate the diagenetic evolution of clay minerals.

5.1.2. Petrography

5.1.2.1. Light microscopy

Original maceral types and OM particulate assemblage

The detailed palynofacies composition of the samples selected for these works are presented in Tab. 5.1 and Fig. 5.2. These results are in accordance with our previous investigations.

Tab. 5.1. Abundance of AOM and isolated structured organic compounds, TOC, (wt.%), HI (mg HC/g TOC), and orange /brown AOM ratio (Or/Br AOM) of the selected KCF samples. PT: various phytoclasts including woody fragments, cuticular fragments and other plant tissues. Sp+Po: pollen grains, spores and preserved phytoplankton and algal fragments. Or: orange AOM. Br: brown AOM. Bl: black AOM. Gp A corresponds to samples with Or/Br AOM < 2.0 while group B corresponds to samples with Or/Br AOM > 2.0. OC: organic carbon.

			Relative abundance (%)					***OC contribution (in weight %)***					
Sample no.	***name***	***Gp***	***Or AOM***	***Br AOM***	***Bl AOM***	***Sp+ Po***	***PT***	***Or AOM***	***Br AOM***	***Bl AOM***	***Sp+ Po***	***PT***	***Or/Br AOM***
K16015	B2	A	8.4	63.5	13.8	8.1	6.2	0.3	1.9	0.4	0.2	0.2	0.2
K17001	B23	A	28.1	57.4	1.9	8.2	4.4	1.6	3.2	0.1	0.5	0.2	0.5
K16026	E19	A	42.5	34.0	3.6	5.1	14.8	4.4	3.5	0.4	0.5	1.5	1.3
K16019	B31	B	64.8	26.0	3.4	4.5	1.3	4.4	1.8	0.2	0.3	0.1	2.4
K16031	E38	B	73.0	17.8	2.0	4.6	2.6	10.5	2.6	0.3	0.7	0.4	4.0
K16032	E40	B	75.2	18.1	0.9	3.9	2.0	11.6	2.8	0.1	0.6	0.3	4.1

A progressive increase of HI, orange AOM content and orange/brown AOM ratio (Or/Br AOM) is observed from sample B2 to E40 (Tab. 5.1). Accordingly, to facilitate the discussion, the samples were divided in two groups (Tab. 5.1). The limit between these groups was subjectively determined considering the orange and brown AOM relative proportions but also the general behavior of samples during thermal maturation. Note however that the OM composition evolves slightly in each group and from one group to the other. Group A corresponds to samples B2, B23 and E19 that contain a relatively lower proportion of oil-prone orange AOM (Or/Br AOM < 2.0, Tab. 5.1), resulting in a slightly lower oil generation potential (HI<560 mg/g TOC). In polished sections, these samples are characterized by abundant inertinite fragments, alginite macerals and a lower amount of bituminite macerals (Fig. 5.2C-D). Group B corresponds to samples B31, E38 and E40 which are mainly composed of oil-prone orange AOM (> 50% of TOC, Or/Br AOM > 2.0, Tab. 5.1, Fig. 5.2). Group B samples are characterized by the presence of a greater amount of bituminite macerals in polished thin sections (Fig. 5.2A-B).

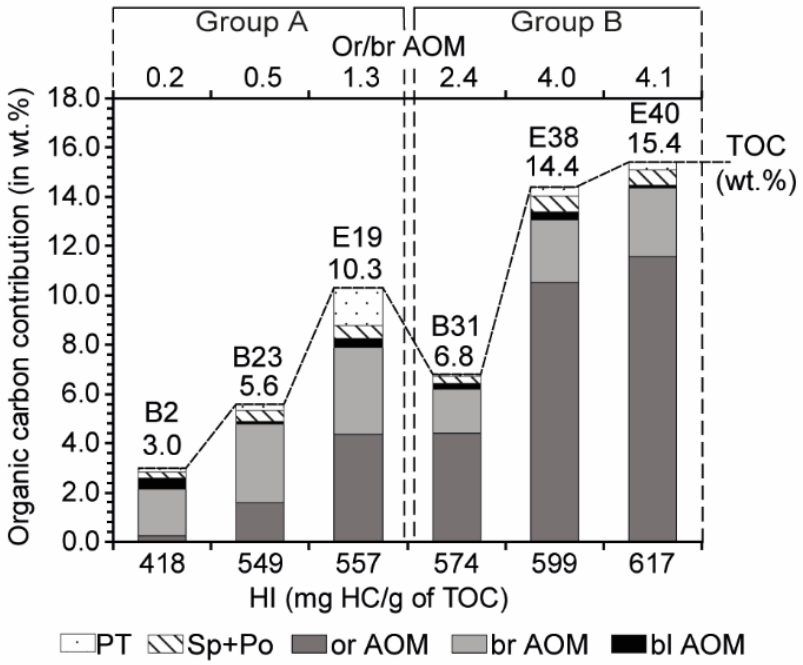

Fig. 5.2. Palynofacies composition, TOC, HI and orange/ brown AOM (Or/br AOM) of the six selected KCF samples. PT: various phytoclasts including woody fragments, cuticular fragments and other plant tissues. Sp+Po: pollen grains, spores and preserved phytoplankton and algal fragments. or: orange AOM. br: brown AOM. bl: black AOM. Group A corresponds to samples with Or/Br AOM < 2.0 while group B corresponds to samples with Or/Br AOM > 2.0.

Evolution of the maceral composition with increasing thermal maturity

After thermal maturation at 325°C for 72h, abundant highly grey-reflective solid bitumen accumulation is observable in polished sections but bituminite and alginite macerals are still predominant (Fig. 5.3E-F). Lamellar alginite, megaspores of *Tasmanaceae* and bituminite macerals still exhibit a relatively low fluorescence (Fig. 5.3F), suggesting that the peak of oil generation has not been reached. Some alginite and bituminite macerals exhibit a low-grey reflectance, suggesting their progressive conversion to oil (Fig. 5.3E). After the 390°C and 470°C/72h thermal maturation runs, the maceral composition is mainly composed of highly-grey reflectance and non-fluorescent macerals identified as solid bitumen (Fig. 5.3G-H). They mainly form an abundant groundmass or accumulations with a homogeneous or pitted surface texture (Fig. 5.3G-H). Their abundance in samples is closely related to the original TOC content and no notable differences between samples in group A and B were observed. At these high maturity stages, some inertinite fragments are present and are dispersed in the fine mineral matrix as well as abundant pyrite framboids (Fig. 5.3G-H).

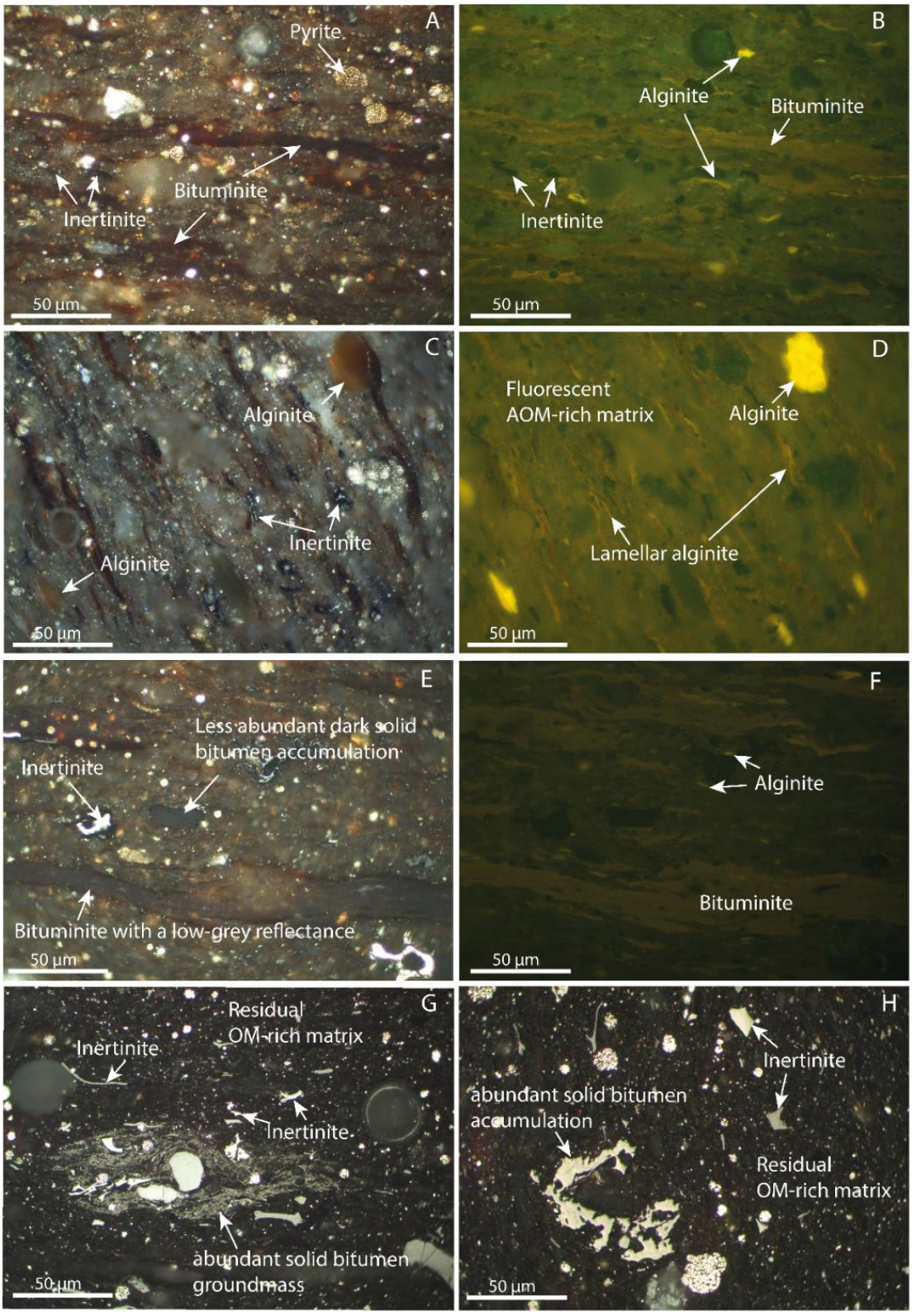

Fig. 5.3. Photomicrographs (oil immersion) of KCF samples. A) Immature (0.48% Ro) organic-rich (TOC=14.4 wt%) mudstone of group B. C) Immature (0.46 wt%) mudstone of group A (TOC=5.6 wt%). E) Oil window (0.68% Ro) organic-rich (TOC=14.2 wt%) mudstone. G) Organic-rich (13.0 wt%) condensate-wet gas-mature sample (1.20% Ro). H) Organic-rich (5.9 wt%) dry gas-mature sample (2.50% Ro). B, D, F) Same field as A, C and E under fluorescence from UV-excitation.

5.1.2.2. SEM observations

Intra- and inter-particle mineral pores

A compact mineral structure composed mainly of quartz, pyrite framboids and carbonated microfossil remains is present. These minerals are surrounded by abundant clay mineral lamellar aggregates composed of sheets oriented parallel to each other (Fig. 5.4, 5.5). Two types of mineral pores were observed (Fig. 5.4).

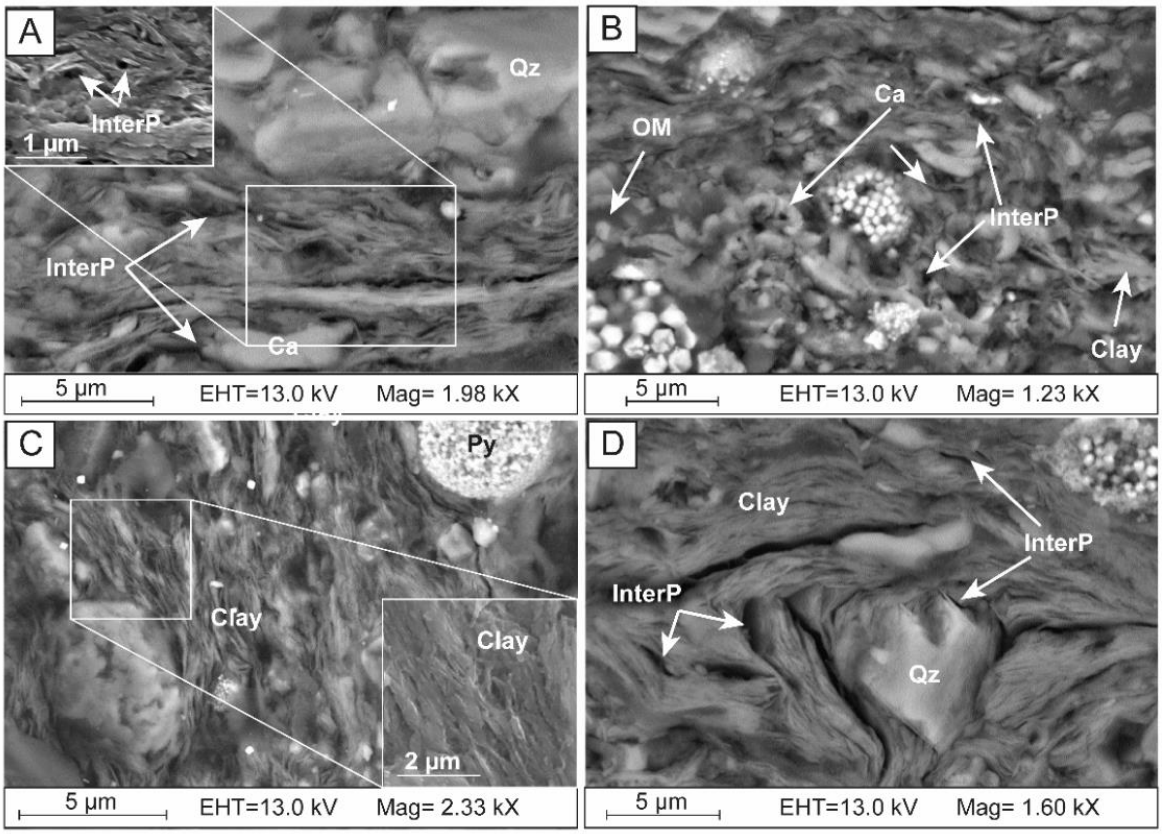

Fig. 5.4. BSE (A, B, C, D) and SE (inserts in A and C) images of broad ion beam milled thin sections showing examples of the predominant types of interparticle pores (InterP) present in KCF mudstones (mainly before thermal maturation). The length of most of these pores are ≤ 1 µm in diameter. A) Elongated pores located between clay minerals aggregates. B) Interparticle pores located between carbonate (Ca) microfossil fragments, clay and quartz (Qz) admixture. C, D) Elongated interparticle pores located between clay minerals mineral aggregates.

The elongated intra- and interparticle pores (≤500 nm wide and a few µm long) located within and between clay mineral layer aggregates (Fig. 5.4A, C, D) account for most of the porosity in immature samples (Fig. 5.5A). Interparticle angular pores (<1 µm in diameter) located between microfossil remains, quartz and clay admixture are locally abundant in immature mudstones (Fig. 5.4B). Most of the pores observed in KCF samples before thermal maturation are inter- or intraparticle macropores associated with minerals (Fig. 5.4, .5.5C).

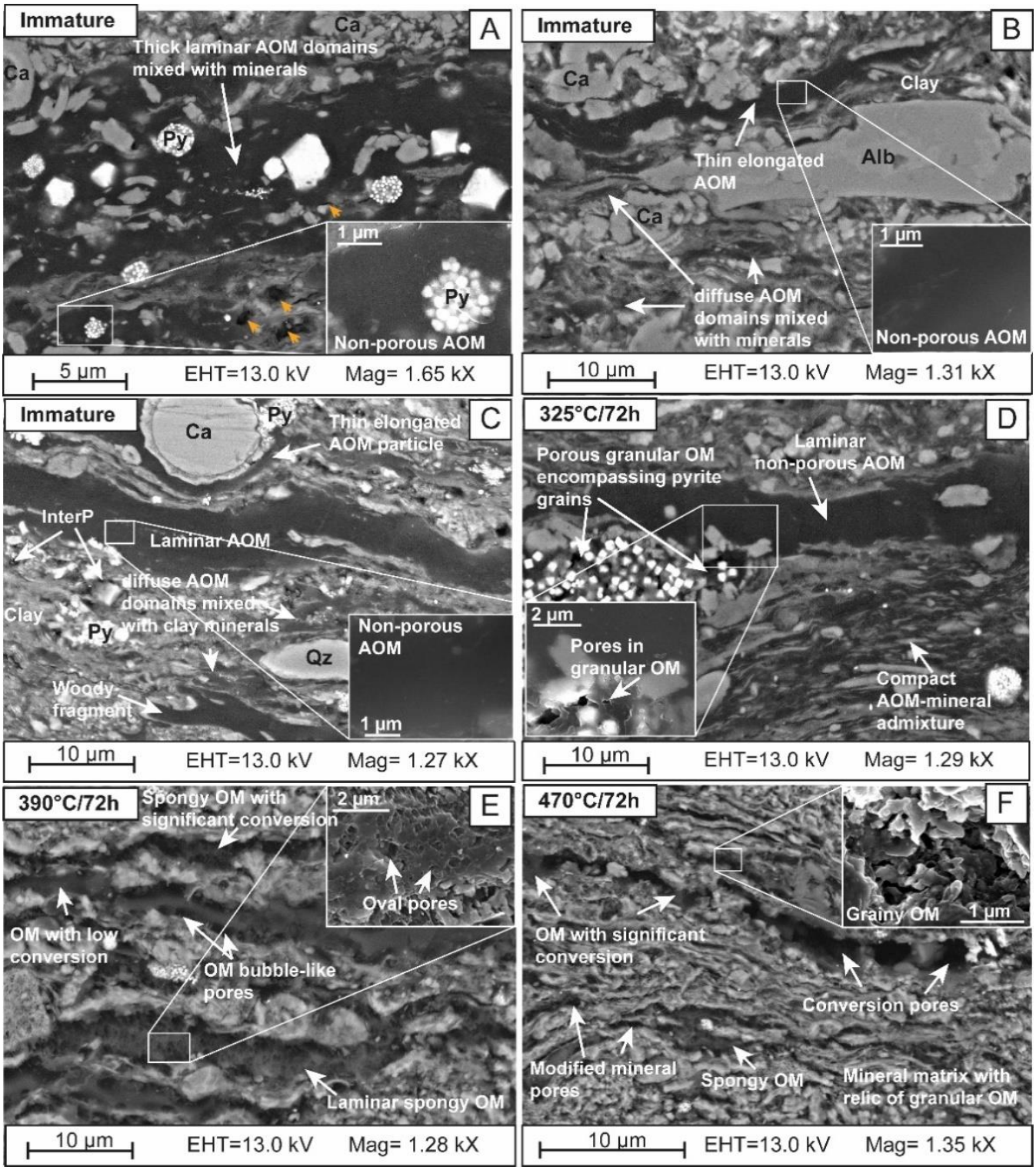

Fig. 5.5. BSE images of broad ion beam milled thin sections showing different types of OM particles and the evolution of the OM structure of organic-rich group A and group B mudstones with increasing maturity (A-C, TOC=10.3 wt%; D, TOC=10.2 wt%; E, TOC=7.2 wt%; F, TOC=7.0 wt%). The large macropores are probably artefacts from sample polishing (orange arrows). Py: pyrite. InterP: interparticle pores.

These intra and interparticle mineral pores become less abundant after maturation (Fig. 5.5). In the oil window, most of these pores have disappeared, filled by a diffuse structureless and homogeneous mass of OM which appears as a gel surrounding mineral grains (Fig. 5.5D, 5.6A, C). Some spongy OM particles are present. Most of the porosity is composed of modified mineral pores lined by relics of granular OM (probably pyrobitumen) composed of small spheres of OM. These pores result from the migration of petroleum into the surrounding mineral pores.

OM-hosted pores and surface texture

The shape and the size of OM particles vary widely (Fig. 5.5). 4 types of OM particles are observed in the immature samples. The first type is abundant marine homogeneous and non-porous thin elongated kerogen particles, oriented parallel to the bedding (Fig. 5.5B-C). The relative abundance of these particles decreases with the increase of the initial Or/Br AOM ratio of samples. Predominant in brown AOM-rich samples of group A but less abundant in group B samples (Tab. 5.2), these particles may derive from algal materials (same shape and size as the lamellar alginite observed by light microscopy, Fig. 5.3A-D) and exhibit a complete lack of primary OM-hosted porosity. Some thick (≈10-50 µm wide) AOM domains form homogeneous and non-porous laminar featureless particles embedding clay minerals, microfossil remains and especially, abundant pyrite framboids (Fig. 5.5A) which correspond to the bituminite macerals observed by light microscopy (Fig. 5.3A). Accordingly, these amorphous particles are less abundant in samples with low orange AOM contents (group A, Tab. 5.2), but predominant in samples with higher orange AOM contents (group B). Some sparse non-porous woody fragments of various shapes and sizes (2 to 20 µm long for 1-4 µm wide, Fig. 5.5C, 5.6H) are observed. The rest of the OM is composed of small diffuse domains of AOM particles, which do not show any distinct morphology, structure or fabric and are closely mixed with clay (Fig. 5.5B, C). Very abundant in brown AOM rich samples (group A), these diffuse AOM domains are less abundant in samples with lower brown AOM contents (group B). As previously documented (Boussafir et al., 1995a; b), these particles correspond to the brown AOM. While some rare interparticle pores are observed between OM particles, rigid grains and clay aggregates, most kerogen particles of both marine and terrestrial origin exhibit a complete lack of primary OM-hosted pores at the SEM detection limit (Fig. 5.5A-C). Similar observations were previously made for the natural oil-mature sample from the Viking graben (chapter 4).

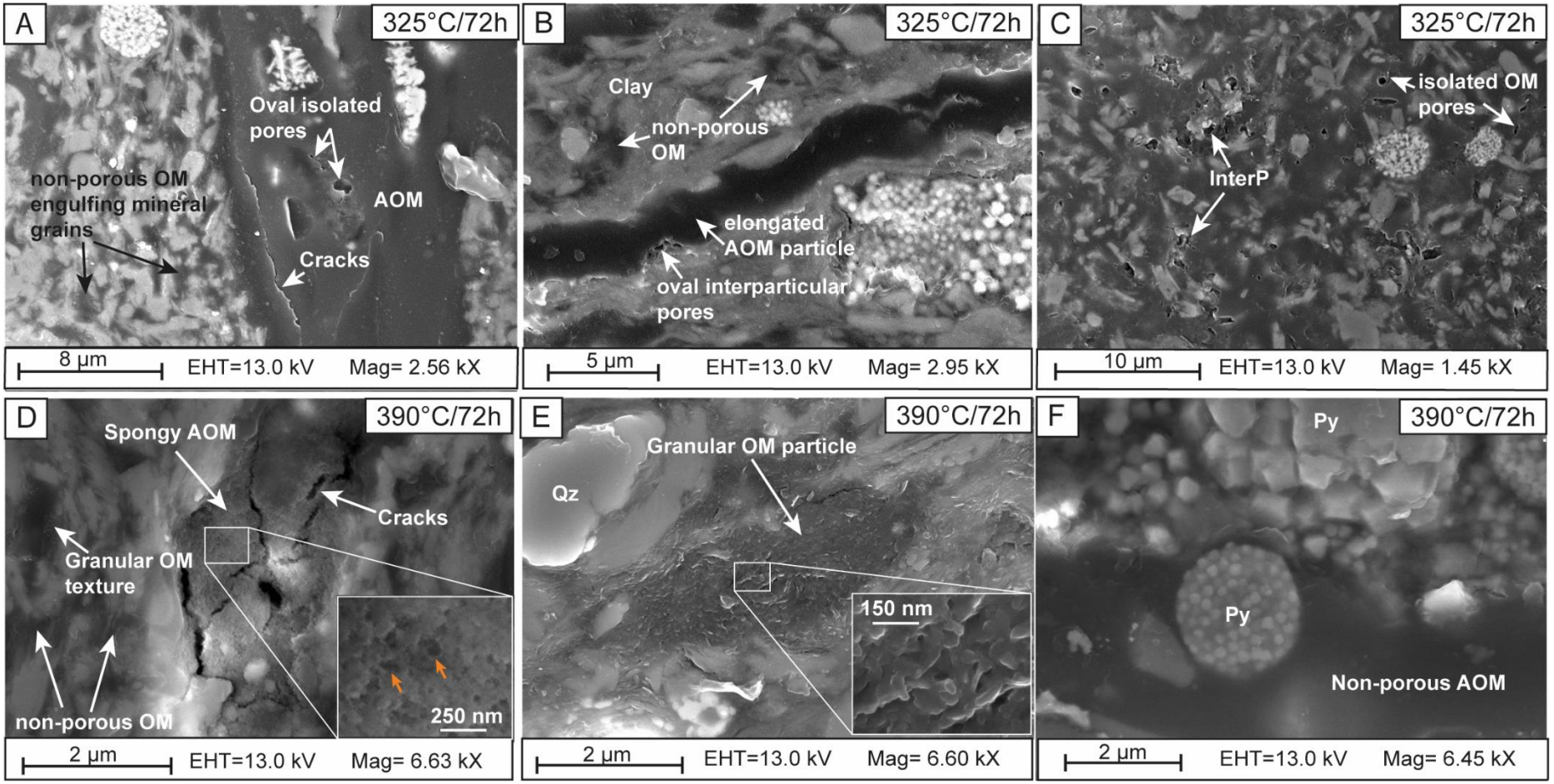

Fig. 5.6 (part 1). SE (A-F) and BSE (H) images of broad ion beam milled thin sections showing various types of OM pores and surface texture in KCF mudstones. Orange arrows show interconnected pores forming larger pores with a complex 3D internal structure. InterP: interparticle pores.

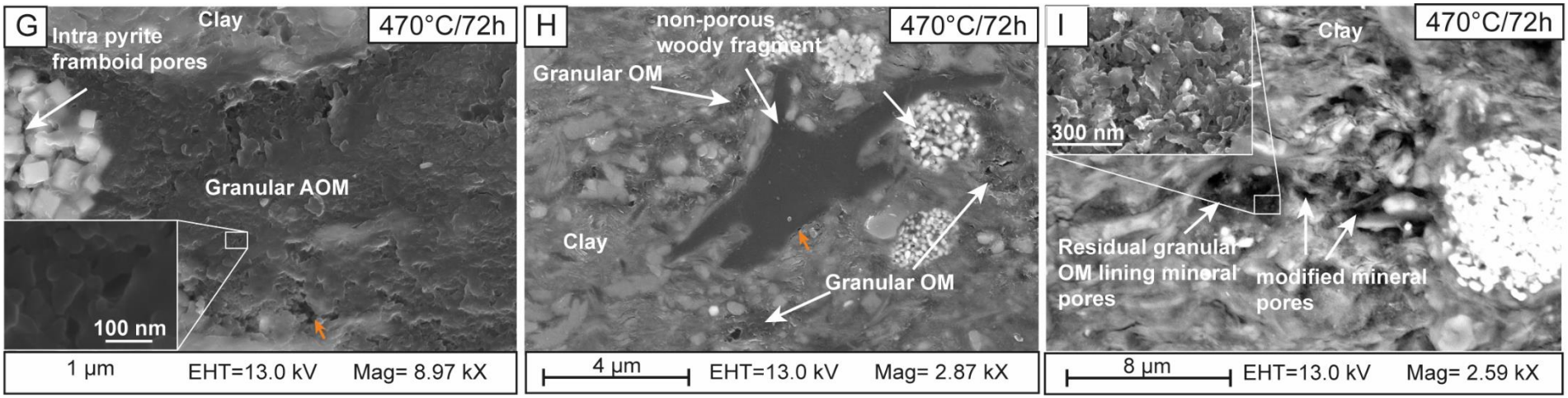

Fig. 5.6 (part 2). SE (G-H) and BSE (I) images of broad ion beam milled thin sections showing various types of OM pores and surface texture in KCF mudstones. Orange arrows show interconnected pores forming larger pores with a complex 3D internal structure. InterP: interparticle pores.

After thermal maturation at 325°C to 470°C for 72 hours, the OM surface texture varied widely (Tab. 5.2, Fig. 5.5). In the early oil generation stage, most of the pores previously related to minerals in thermally immature samples are filled by a diffuse gel-like AOM (Fig. 5.5D, 5.6A-C). Some of them appear to engulf pyrite grains (Fig. 5.5D).

Tab. 5.2. Mean relative abundance in SEM observations of the different types of OM in brown AOM-rich (Or/Br AOM < 2.0 group A) and orange AOM-rich (Or/Br AOM > 2.0, group B) samples before and after thermal maturation.

Thermal maturity	***Immature***		***Oil window (325°C/72h)***		***Wet gas zone (390°C/72h)***		***Dry gas zone (470°C/72h)***	
Sample group	***A***	***B***	***A***	***B***	***A***	***B***	***A***	***B***
Inter and intraparticle mineral pores associated with clay minerals and rigid grains	+++++	+++++	+	+	+	+	++	++
Thick non-porous laminar AOM domains encapsulating clay and pyrite	++ to +++	+++ to ++++	++ to +++	+++ to ++++	+	+++	O	O
Thin non-porous elongated AOM and diffuse AOM domains mixed with clay minerals	++++	+++	++++	++ to +++	+	+	O	O
Non-porous woody fragments	++	++	++	++	++	++	++	++
AOM with isolated oval pores	O	O	++	++	++	+++	O	O
OM cracks	O	O	O	O	+	+	+	+
Porous spongy OM	O	O	O	O	+ ++	++	+++	++++
Granular porous OM	O	O	+	+	++++	++	+++	++++
*Modified mineral and conversion pores with relic granular OM**	O	O	O	O	+	+	++++	+

*O: Absence of the corresponding OM/pore type. +: < 10%. ++: 10-20%. +++: 20-30%. ++++: 30-40%. +++++: ≥ 40%. * : Modified mineral and conversion pores are pores located between mineral and residual OM and interpreted as mineral interparticle pores containing relics of residual granular OM (pyrobitumen).*

As suggested in previous studies (Loucks et al., 2012; Milliken et al., 2013; Loucks and Reed, 2014; Ko et al., 2017; Guo et al., 2018; Ko et al., 2018) these particles may correspond to migrated material resulting from kerogen conversion (bitumen, oil or pre-oil gel-like solid bitumen) probably mixed with amorphous kerogen particles. Locally, these OM particles exhibit a porous granular texture (Fig. 5.5D, 5.6C). All the amorphous and structured kerogen particles exhibit an almost complete lack of OM-hosted pores considering the SEM detection limit (Fig. 5.5D). Only some isolated bubble-like pores are observed within AOM (Fig. 5.5A) but mainly at the edges of OM, in contact with clay mineral surfaces (Fig. 5.6B) or within diffuse AOM domains that appear to embed mineral grains (Fig. 5.6C). These isolated pores,

still abundant in the condensate/wet gas zone, become less common with increasing thermal maturity (Tab. 5.2). Some cracks and large pores are sometimes observed within thick laminar AOM domains in the early oil window (Fig. 5.6A), but they could be artefacts from sample polishing or caused by the high vacuum used during SEM observations.

As previously observed in the VMF (see chapter 4), in the gas window, granular and spongy macroporous OM of various shapes and sizes are more abundant (Tab. 5.2, Fig. 5.5E, F), indicating an intense OM-hosted pore development. OM with a granular texture appears to be composed of nanometer-scale spheres of OM separated by abundant interconnected pores which varied in size from a few dozen nanometers to one micrometer (Fig. 5.6E, G). Some OM particles contain abundant interconnected bubble-like pores and often large devolatilization vacuoles, giving them a spongy texture (Tab. 5.2, Fig. 5.5E, F, 5.6D). While most of these OM-hosted pores are mesopores (≤ 50 nm in diameter), neighboring pores are sometimes interconnected forming larger complex 3D pore structures (Fig. 5.6D, G). The laminar shapes of some granular and spongy AOM particles (Fig. 5.5E, F, 5.6D, G) and their often-strong association with pyrite (Fig. 5.6G) framboids suggest that these particles are residual marine kerogen particles. However, the origin of most of the OM is no longer identifiable (Fig. 5.6E). Although the OM in samples with lower Or/Br AOM ratio (group A) is largely porous with abundant spongy and granular OM, many laminar AOM particles, often associated with pyrite, are still non-porous at the SEM detection limit in samples with relatively higher Or/Br AOM ratios (Group B, Tab. 5.2, Fig. 5.6F). Some pores are observed between clay laminar aggregates, and mineral grains (Fig. 5.4E, 5.6I), but are mainly lined with relic granular OM, suggesting that these pores are original mineral modified pores, filled first by petroleum which was later extracted leaving behind residual pyrobitumen and smaller pores. These modified mineral pores, account for most of the porosity of samples with a higher relative proportion of brown AOM (group A) in the dry gas zone (Tab. 5.2) while they are relatively rare in samples with higher orange AOM contents (group B). Locally, a few large elongated pores are visible after maturation at 470°C (Fig. 5.5F). These pores, called conversion pores, may result from the near total conversion of some OM particles.

5.1.3. Bulk and molecular OM geochemical characterization

5.1.3.1. OM properties of immature KCF mudstones

The six selected KCF mudstones contain high amounts (3.0 -15.4 wt% of TOC) of well-preserved type II immature kerogen with a high oil generation potential (Fig. 5.7).

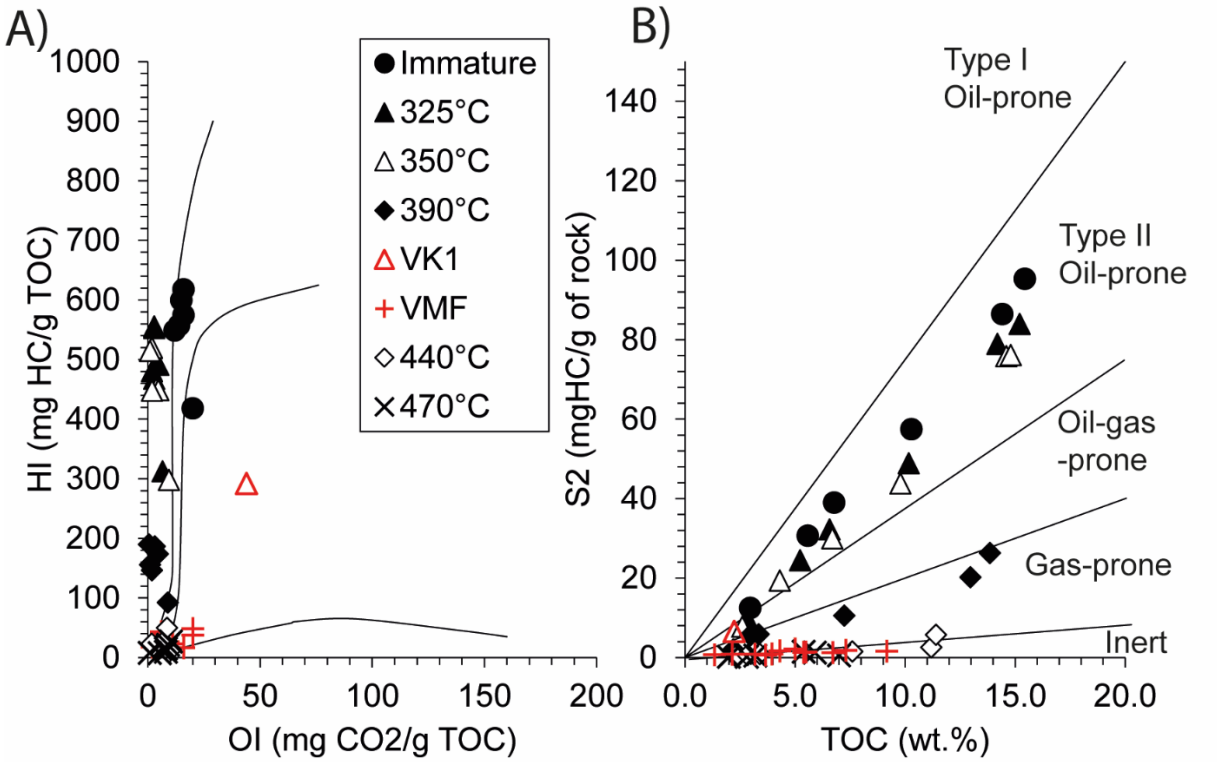

Fig. 5.7. A) Pseudo-Van Krevelen diagram of KCF samples showing the evolution of the HI and the OI with increasing maturation temperatures. B) Remaining hydrocarbon potential (S2) of samples versus TOC after thermal maturation. Comparison with samples from the VMF and the Viking Graben (VK1).

The Tmax is about 428°C, and the mean calculated vitrinite reflectance (Rc) is 0.48 ±0.02 (Tab. 5.3, 5.4). The bitumen fraction, which is low in samples before maturation, is mainly composed of polar hydrocarbons (POL, Tab.5.5, Fig. 5.8, 5.9). The mean vitrinite reflectance measurements (Rm) revealed that Rm is approximately ≈0.42% ±0.02 in these samples before maturation (Tab. 5.4). GC/MS analyses show that n-alkanes, steranes and hopanes are the prominent components of the saturated HC fraction (SAT) of bitumen before maturation (≥ 0.50 mg/g of TOC, Fig. 5.10, Tab. 5.5).

Tab. 5.3. Main Rock-Eval® parameters of KCF samples before and after thermal maturation. TOC: total organic carbon content (wt%). S_1: free hydrocarbon content (mgHC/g of rock). S_2: pyrolysable hydrocarbon content (mgHC/g of rock). HI: Hydrogen Index (mgHC/g TOC). OI: Oxygen Index ($mgCO_2$/g TOC). PI: Production Index. RC: Residual Carbon (wt%). Comparison with natural samples from the Viking graben (VK1) and the Vaca Muerta (VMF).

Sample no.	***Sample name***	***Well***	***Maturation conditions***	***TOC (wt%)***	***S1 (mg/g)***	***S2 (mg/g)***	***T_{max} (°C)***	***HI (mg/g TOC)***	***OI (mg/g TOC)***	***PI***	***RC/ TOC***
K16015	B2	Marton	Immature	3.0	0.1	12.4	429	418	20	0.00	0.64
K17001	B23	Marton		5.6	0.2	30.6	432	549	12	0.01	0.53
K16019	B31	Marton		6.8	0.2	38.9	431	574	16	0.01	0.51
K16026	E19	Ebberston		10.3	0.2	57.4	428	557	14	0.00	0.53
K16031	E38	Ebberston		14.4	0.5	86.4	422	599	15	0.01	0.49
K16032	E40	Ebberston		15.4	0.6	95.3	425	617	16	0.01	0.47
K17002	B2	Marton	325°C/72h	2.9	0.2	9.1	442	312	7	0.03	0.74
K17003	B23	Marton		5.2	0.5	24.5	442	468	3	0.02	0.60
K17004	B31	Marton		6.6	0.8	32.2	442	491	5	0.02	0.58
K17006	E19	Ebberston		10.2	1.0	48.9	442	481	2	0.02	0.59
K17007	E38	Ebberston		14.2	1.7	78.9	439	556	3	0.02	0.55
K17008	E40	Ebberston		15.2	1.5	84.0	438	553	3	0.02	0.54
K18001	B2	Marton	350°C/72h	2.6	0.6	7.7	450	298	9	0.07	0.72
K18002	B23	Marton		4.3	1.4	19.4	449	450	4	0.07	0.60
K18003	B31	Marton		6.7	3.4	30.0	444	449	5	0.10	0.58
K18004	E19	Ebberston		9.8	4.8	43.8	446	448	2	0.10	0.58
K18005	E38	Ebberston		14.6	11.6	75.8	442	519	2	0.13	0.53
K18006	E40	Ebberston		14.8	10.8	76.1	442	514	1	0.12	0.54
K17009	B2	Marton	390°C/72h	2.2	0.4	2.0	un	92	9	0.16	0.90
K17010	B23	Marton		3.0	1.2	5.6	un	187	3	0.17	0.81
K17011	B31	Marton		3.4	1.6	5.8	un	174	4	0.21	0.81
K17013	E19	Ebberston		7.2	4.6	10.6	470	146	2	0.30	0.81
K17014	E38	Ebberston		13.0	8.1	20.2	472	156	1	0.29	0.81
K17015	E40	Ebberston		13.9	10.3	26.3	475	190	0	0.28	0.77
K18007	B2	Marton	440°C/72h	2.3	0.2	0.3	un	13	10	0.53	1.00
K18008	B23	Marton		2.9	0.4	0.6	un	21	4	0.44	0.95
K18009	B31	Marton		3.4	1.0	0.9	un	26	7	0.41	0.97
K18010	E19	Ebberston		7.6	1.5	1.5	un	20	3	0.51	0.97
K18011	E38	Ebberston		11.2	2.4	2.6	un	23	2	0.48	0.96
K18012	E40	Ebberston		11.4	3.0	5.7	un	50	9	0.35	0.85
K17016	B2	Marton	470°C/72h	2.0	0.3	0.2	un	10	8	0.60	0.98
K17017	B23	Marton		2.8	0.3	0.2	un	8	1	0.67	0.98
K17018	B31	Marton		3.2	0.4	0.5	un	15	8	0.50	0.99
K17020	E19	Ebberston		7.0	0.7	0.5	un	7	5	0.58	0.98
K17021	E38	Ebberston		5.9	1.2	1.3	un	21	9	0.54	0.96
K17022	E40	Ebberston		5.4	1.0	1.5	un	27	10	0.44	0.95
K19001	VK1	VG	/	2.2	0.1	6.6	442	292	44	0.01	0.73
V16004	94B	VMF	/	5.0	1.2	2.2	/	43	5	0.35	0.94
V16011	102R	VMF	/	6.7	1.1	1.3	488	19	4	0.46	0.97

un: unmeasurable Tmax due to a flat S2 peak.

Tab. 5.4. Main biomarker parameter ratios of aliphatic and aromatic hydrocarbon fractions calculated (R_c) and measured (R_m) vitrinite reflectance values from the six selected KCF mudstones before and after thermal maturation. Comparison with natural samples from the Viking graben (VK1) and the VMF.

Sample no.	Gp	Rm (%)	St Dev.	MDBT[1]	R_{MDBT} (%)	MPI-1[1]	R_{MPI} (%)	DPR[1]	R_{DPR} (%)	Mean R_c (%)	St Dev.	MAS (I)/ (I+II)[2]	TAS(I)/ (I+II)[2]	20S/ (20S +R)[3]	22S/ (22S +R)[3]	Pr/n -C_{17}	Ph/ n- C_{18}	Pr/ Ph	CPI[4]	C_{14}- C_{25}	≥ C_{25}	DBT /Phe
K16015	A	0.42	0.03	0.36	0.50	0.33	0.45	0.17	0.47	0.47	0.03	2.91	2.22	0.12	0.34	3.01	1.48	1.14	1.73	0.08	0.06	0.46
K17001	A	0.40	0.04	0.37	0.50	0.30	0.43	0.16	0.43	0.45	0.04	4.72	4.55	0.17	0.42	3.38	1.47	1.07	1.40	0.09	0.07	0.46
K16026	A			0.31	0.48	0.34	0.46	0.18	0.50	0.48	0.02	2.58	3.94	0.19	0.40	2.88	2.06	0.60	1.71	0.08	0.10	0.49
K16019	B			0.30	0.48	0.32	0.44	0.21	0.58	0.50	0.07	2.69	4.22	0.18	0.47	1.70	2.16	0.72	1.42	0.11	0.11	1.24
K16031	B	0.43	0.03	0.35	0.49	0.39	0.49	0.17	0.46	0.48	0.02	2.05	11.18	0.10	0.39	1.78	2.29	0.90	1.52	0.12	0.15	1.62
K16032	B			0.30	0.48	0.40	0.50	0.20	0.56	0.51	0.04	6.02	18.55	0.14	0.35	2.24	2.56	0.73	1.98	0.15	0.16	1.47
Mean		**0.42**	**0.02**	**0.33**	**0.49**	**0.35**	**0.46**	**0.18**	**0.50**	**0.48**	**0.02**	**3.50**	**7.44**	**0.15**	**0.40**	**2.50**	**2.00**	**0.86**	**1.47**			**0.96**
K17002	A			1.19	0.64	0.82	0.79	0.27	0.74	0.72	0.08	22.54	24.03	0.36	0.49	1.06	0.68	1.30	1.10			
K17003	A	0.66	0.04	1.21	0.64	0.74	0.74	0.28	0.76	0.71	0.06	27.02	27.90	0.30	0.50	0.95	0.55	1.62	1.28			
K17005	A			1.50	0.68	0.81	0.79	0.28	0.76	0.74	0.06	9.17	38.34	0.31	0.51	1.11	0.63	1.37	1.18			
K17004	B	0.70	0.04	1.45	0.67	0.73	0.73	0.30	0.80	0.73	0.07	11.89	22.37	0.32	0.49	0.94	0.94	1.53	1.11			
K17007	B			1.40	0.67	0.70	0.71	0.26	0.72	0.70	0.03	7.30	40.89	0.46	0.50	0.95	0.90	1.15	1.02			
K17008	B			1.22	0.65	0.56	0.61	0.29	0.78	0.68	0.09	7.32	33.83	0.43	0.51	0.92	0.87	1.17	1.03			
Mean		**0.68**	**0.02**	**1.33**	**0.66**	**0.73**	**0.73**	**0.28**	**0.76**	**0.71**	**0.02**	**14.21**	**31.23**	**0.36**	**0.50**	**0.99**	**0.76**	**1.36**	**1.12**			
K18001	A			3.88	0.79	0.71	0.72	0.33	0.86	0.79	0.07	79.30	56.60	0.54	0.55	0.64	0.35	1.13	1.09			
K18002	A			3.44	0.77	1.01	0.93	0.36	0.90	0.87	0.09	76.10	60.40	0.50	0.54	0.72	0.44	1.44	1.01			
K18004	A			3.65	0.78	0.91	0.86	0.43	1.01	0.88	0.12	71.80	64.40	0.54	0.58	0.82	0.51	1.57	1.09			
K18003	B			3.75	0.78	0.96	0.89	0.38	0.94	0.87	0.08	61.60	58.60	0.54	0.57	0.70	0.58	1.62	1.07			
K18005	B			2.94	0.75	0.98	0.91	0.34	0.87	0.84	0.08	76.80	68.40	0.54	0.60	0.62	0.66	0.76	0.80			
K18006	B			2.62	0.74	0.92	0.86	0.40	0.96	0.85	0.11	69.9	63.6	0.53	0.58	0.68	0.66	1.28	1.07			
Mean				**3.38**	**0.77**	**0.92**	**0.86**	**0.37**	**0.92**	**0.85**	**0.03**	**72.58**	**62.00**	**0.53**	**0.57**	**0.70**	**0.53**	**1.30**	**1.02**			
K17009	A			5.89	1.15	1.45	1.24	0.66	1.26	1.22	0.06					0.05	0.05	0.38	1.09			
K17010	A	1.40	0.08	6.17	1.26	1.50	1.27	0.70	1.29	1.27	0.02					0.06	0.05	0.63	1.04			
K17012	A			6.25	1.29	1.59	1.33	0.69	1.28	1.30	0.03					0.10	0.07	0.93	1.04			
K17011	B	1.39	0.04	6.41	1.36	1.45	1.24	0.55	1.15	1.25	0.11					0.04	0.07	0.33	1.03			
K17014	B			5.99	1.19	1.44	1.23	0.57	1.17	1.20	0.03					0.03	0.03	0.46	1.06			
K17015	B			6.07	1.22	1.52	1.28	0.55	1.15	1.22	0.07					0.02	0.03	0.31	1.04			
Mean		**1.40**	**0.01**	**6.13**	**1.25**	**1.49**	**1.27**	**0.62**	**1.22**	**1.24**	**0.03**					**0.05**	**0.05**	**0.51**	**1.05**			
K18007	A			7.24	1.82	1.87	1.53	0.97	1.48	1.61	0.18					0.00	0.00	0.00				
K18008	A			7.12	1.74	1.93	1.57	0.90	1.44	1.58	0.15					0.00	0.00	0.00				
K18010	A			7.25	1.83	1.82	1.49	0.96	1.47	1.60	0.20					0.00	0.00	0.00				
K18009	B			7.37	1.73	1.46	1.24	0.90	1.44	1.47	0.25					0.00	0.00	0.00				
K18011	B			7.60	2.08	2.56	2.01	1.10	1.55	1.88	0.29					0.00	0.00	0.00				
K18012	B			7.34	1.89	2.29	1.82	0.92	1.45	1.72	0.24					0.00	0.00	0.00				

Mean				**7.32**	**1.85**	**1.99**	**1.61**	**0.96**	**1.47**	**1.67**	**0.14**					**0.00**	**0.00**	**0.00**	
K17022	A			*/	*/	*/	*/	*/	*/	*/	*/					0.00	0.00	0.00	
K17023	A	2.02	0.10	*/	*/	*/	*/	*/	*/	*/	*/					0.00	0.00	0.00	
K17025	A			8.22	2.62	0.72	2.60	5.60	2.50	2.57	0.06					0.00	0.00	0.00	
K17024	B	2.12	0.10	8.20	2.60	0.50	2.73	3.00	2.14	2.49	0.31					0.00	0.00	0.00	
K17027	B			7.98	2.40	0.50	2.73	4.50	2.38	2.50	0.20					0.00	0.00	0.00	
K17028	B			8.04	2.45	0.80	2.56	4.30	2.35	2.45	0.11					0.00	0.00	0.00	
Mean		**2.07**	**0.07**	**8.11**	**2.52**	**0.63**	**2.66**	**4.35**	**2.34**	**2.50**	**0.05**					**0.00**	**0.00**	**0.00**	
VK1	KCF	0.85	0.08	1.99	0.71	0.78	0.77	0.29	0.79	0.76	0.04	*/	10.0	0.40	0.53	1.06	0.80	0.77	1.08
94B	VMF	1.65	0.05	*/	*/	*/	*/	*/	*/	*/	*/					*/	*/	*/	
102R	VMF	1.69	0.10	*/	*/	*/	*/	*/	*/	*/	*/					*/	*/	*/	

**/: unquantifiable ratios due to too low concentrations of phenanthrenes and dibenzothiophenes. [1] For measurements, see appendix 1. [2] MA(I)/(I + II) (in %) where MA(I) = C_{21} ring-C monoaromatic steroids and MA(II) = C_{28} ring-C monoaromatic steroids. TA(I)/(I + II) (in %), where TA(I) is C_{20} triaromatic steroids and TA(II) = C_{28} triaromatic 20S + 20R isomers.[3] 20S/(20S+R) where 20S and 20R are epimers at C-20 in the C_{29} 5α,14α,17α steranes. 22S/(22S+R) where 22S is C_{32} 17α21β 22S hopane and 22R is C_{32} 17α21β 22R hopane. [4] Carbon preference index (CPI. Pr: pristane. Ph: phytane. DBT: dibenzothiophene. Phe: phenanthrene. Gp: sample groups. A: samples with higher relative proportion of brown AOM. B: samples containing higher relative proportions of orange AOM. C_{14}-C_{25}: total concentrations of n-alkanes > C_{14} and < C_{25} (mg/g TOC). Alk ≥ C_{25}: total concentrations of n-alkanes ≥ C_{25} (mg/g TOC).*

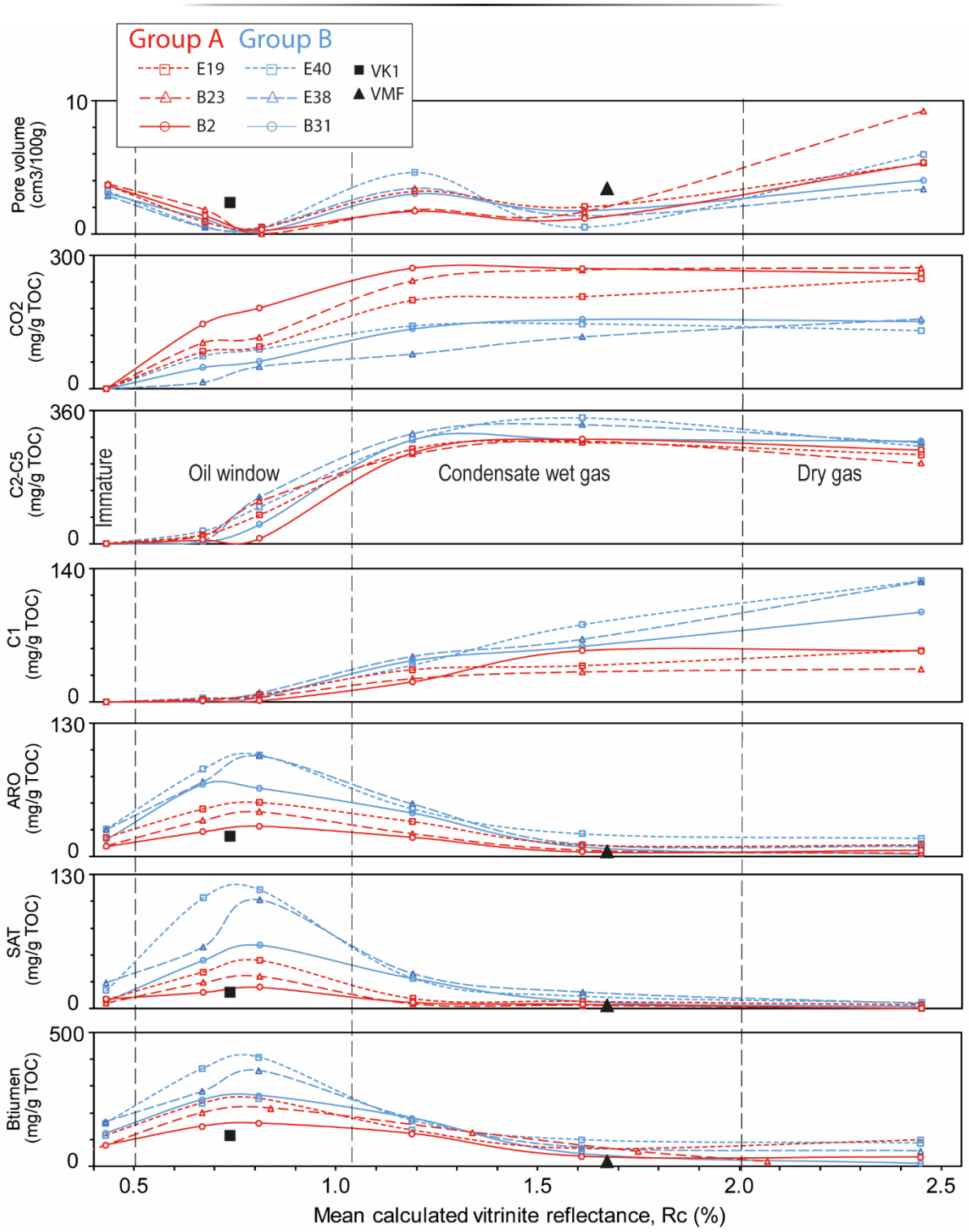

Fig. 5.8. Variations in total pore volume, gas, bitumen, aromatic (ARO) and saturated hydrocarbon (SAT) concentrations in KCF samples with increasing maturity (Rc calculated using MP1-1, DPR and MDBT ratios). Comparison with natural samples from the VMF and the Viking graben (VK1).

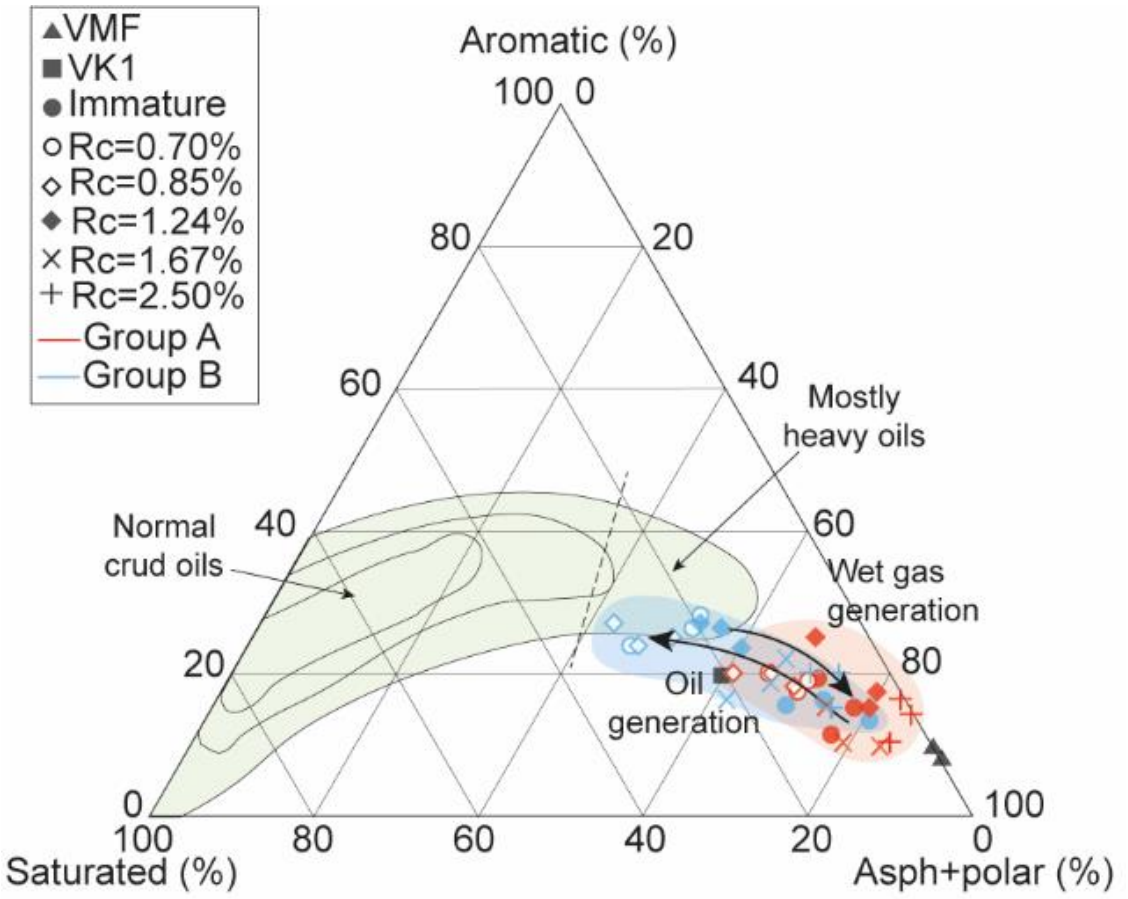

Fig. 5.9. Ternary diagram of saturated, aromatic and polar fractions (NSO) of bitumen extracted after confined thermal maturations.

As for the run at 325°C, CO_2 is the most abundant gas generated (in mass) after maturation at 350°C/72h, especially for group A (up to 182 mg/g of TOC) indicating the rapid pyrolytic reaction of oxygenated compounds of OM. After thermal maturations at 325-350°C for 72h, a strong decrease in hopane, sterane and MAS concentrations is observed in SAT and ARO fractions (Fig. 5.9).

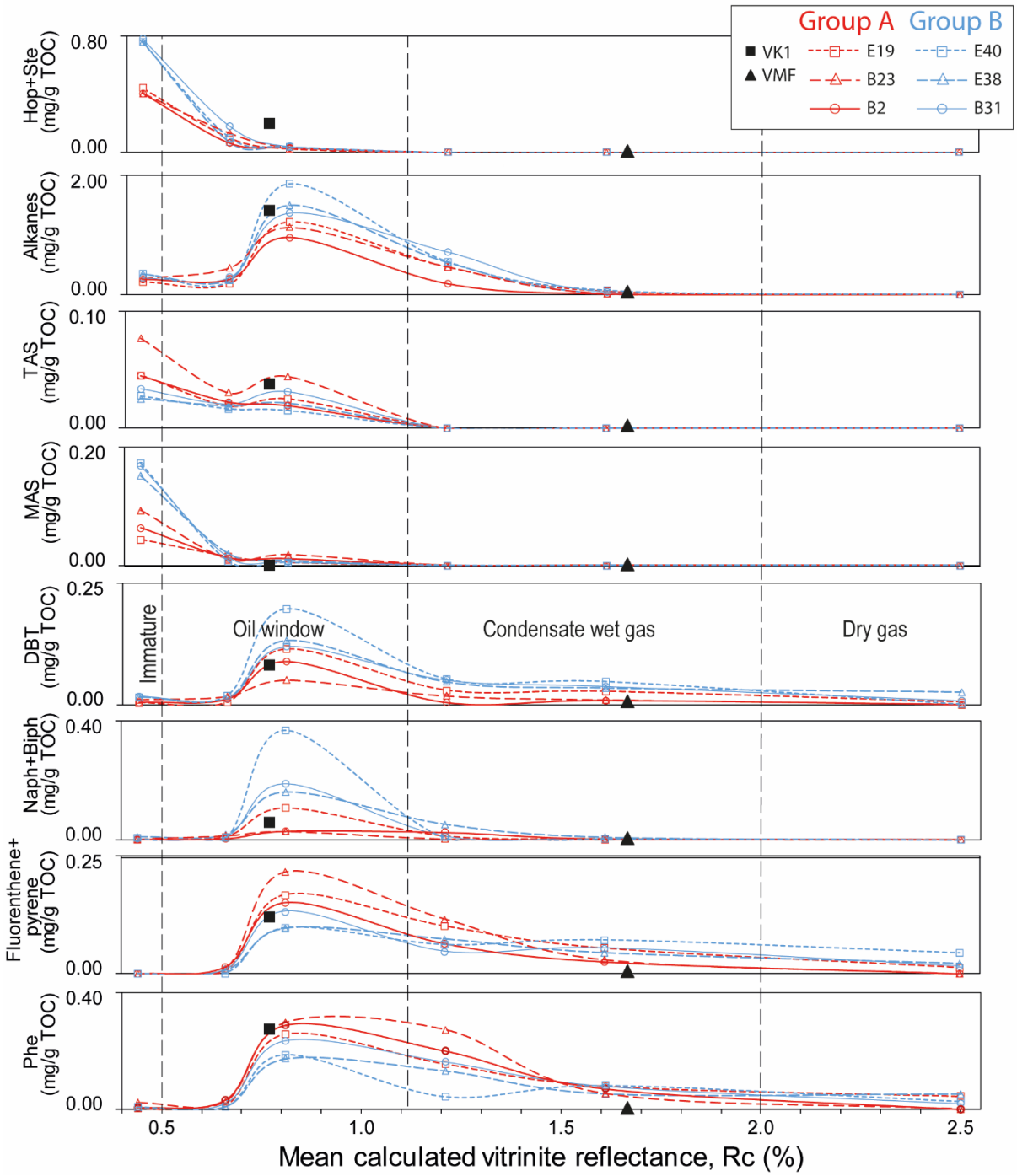

Fig. 5.10. Variations in the concentrations of fluorenthenes, pyrenes, phenanthrenes (Phe), dibenzothiophenes (DBT), n-alkanes, iso-alkanes, alkylcyclohexanes and alkylcyclopentanes (alkanes), tri- and tetramethylnaphtalenes (Naph), di- and trimethylbiphenyls (Biph), triaromatic steroids (TAS), C-ring monoaromatic steroids (MAS), hopanes, regular sterane, diasteranes and 4-methylsteranes (Hop+Ste) in KCF samples with increasing thermal maturity (Rc, mean calculated vitrinite reflectance). Comparison with natural samples from the VMF and the Viking graben (VK1).

Tab. 5.5. Condensable gases, bitumen concentrations and relative abundance of saturated (SAT), aromatic (ARO) and polar (POL, NSO compounds)) HC within bitumen before and after thermal maturation. Group A: brown AOM-rich samples. Group B: orange AOM-rich samples.

			Concentrations (mg/g of TOC)					***bitumen***		
Sample no.	**Gp**		**H_2O**	**C_1**	**C_2-C_5**	**CO_2**	**bitumen**	**SAT (%)**	**ARO (%)**	**POL (%)**
K16015	A	Immature	0	0	0	0	79.7	11.8	11.8	76.5
K17001	A		0	0	0	0	54.2	9.5	19.0	71.4
K16026	A		0	0	0	0	117.3	7.2	15.6	77.2
K16019	B		0	0	0	0	124.2	5.6	13.0	81.5
K16031	B		0	0	0	0	167.4	14.9	15.6	69.5
K16032	B		0	0	0	0	162.1	10.7	16.4	72.9
K17002	A	325/72h	16.6	1.2	9.3	145.8	150.2	10.5	15.8	73.7
K17003	A		5.3	3.2	22.1	103.6	201	12.5	17.5	70.0
K17005	A		3.1	3.1	23.5	83.6	236.7	14.9	19.4	65.7
K17004	B		8.3	0.6	4.2	48	249.1	18.8	28.1	53.1
K17007	B		3.3	1.9	9.1	14.7	280.3	21.4	26.0	52.7
K17008	B		2.3	4.4	33.7	73.5	365.1	29.5	23.3	47.2
K18001	A	350/72h	6.2	1.3	13.5	182.3	161.1	12.9	18.1	69.0
K18002	A		5.1	5	114	116.5	217.9	14.4	20.0	65.6
K18004	A		3.0	7.7	77	94.8	253.7	18.3	20.6	61.0
K18003	B		3.5	4.9	52.1	62.1	264.9	23.2	25.0	51.8
K18005	B		1.7	9.6	125	50.2	357.9	29.5	27.4	43.1
K18006	B		0.8	7.2	98.4	88.6	407.9	28.3	24.3	47.4
K17009	A	390/72h	5.9	21.3	245	271.6	122.3	5.0	15.0	80.0
K17010	A		4.4	24.4	242	242.8	128.4	3.4	17.2	79.3
K17012	A		9.2	33.9	255	199.6	136.8	7.0	24.6	68.4
K17011	B		10.1	43.6	281	134.8	180.5	16.3	23.3	60.5
K17014	B		2.9	48	298	78.3	180.6	18.8	28.2	52.9
K17015	B		2.7	39	280	141.4	171.6	17.2	26.9	55.9
K18007	A	440/72h	6.8	53.8	282	270.9	37.9	11.1	11.1	77.8
K18008	A		4.8	31.4	278	267.5	57.3	5.3	10.5	84.2
K18010	A		1.8	38.1	273	208	68.7	10.3	16.3	74.0
K18009	B		3.5	58.6	283	156.2	48.5	14.8	18.5	66.7
K18011	B		1.2	65.9	321	116.7	71.4	22.4	16.4	61.2
K18012	B		1.0	81.5	339	146	99.4	12.2	22.3	65.9
K17022	A	470/72h	20.6	53.6	253	259.8	34.9	0	16.7	83.3
K17023	A		6.3	34.6	217	272.3	20.1	0	14.3	85.7
K17025	A		41.1	54.2	240	247.7	100.5	3.6	10.7	85.7
K17024	B		9.1	94.5	277	151.9	12.4	10.2	19.9	69.9
K17027	B		21.7	126.3	273	157.1	58.5	8.3	16.7	75.0
K17028	B		22.2	127.6	262	130.8	87.2	6.7	20.3	73.3
VK1	KCF	/	/	/	/	/	105.2	16.4	14.5	69.1
94B	VMF	/	/	/	/	/	1.76	0	7.7	92.3
102R	VMF	/	/	/	/	/	2.38	0	9.4	90.6

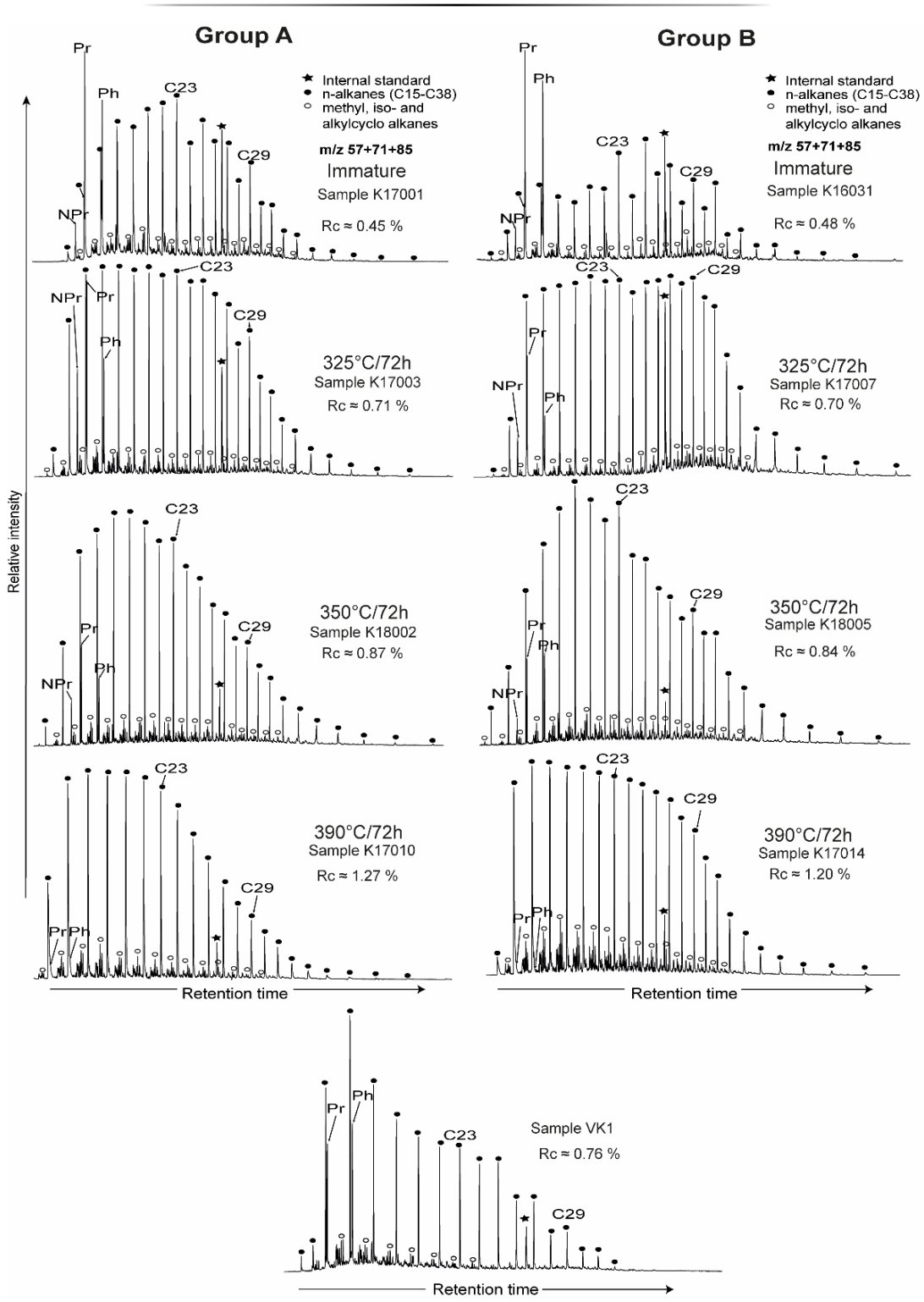

Fig. 5.11. Ion chromatograms of the alkanes (m/z 57+71+85) identified in the saturated HC fraction from two representative samples of group A and B at different thermal maturities. To improve the precision of the estimation of SAT and ARO concentrations, different amounts of standard (Squalane) were added to the samples depending on their bitumen richness. Group A is brown AOM-rich samples and group B is orange AOM-rich samples. NPr: norpristane. Pr: pristane. Ph: phytane. Comparison with the oil-mature sample from the Viking graben (VK1).

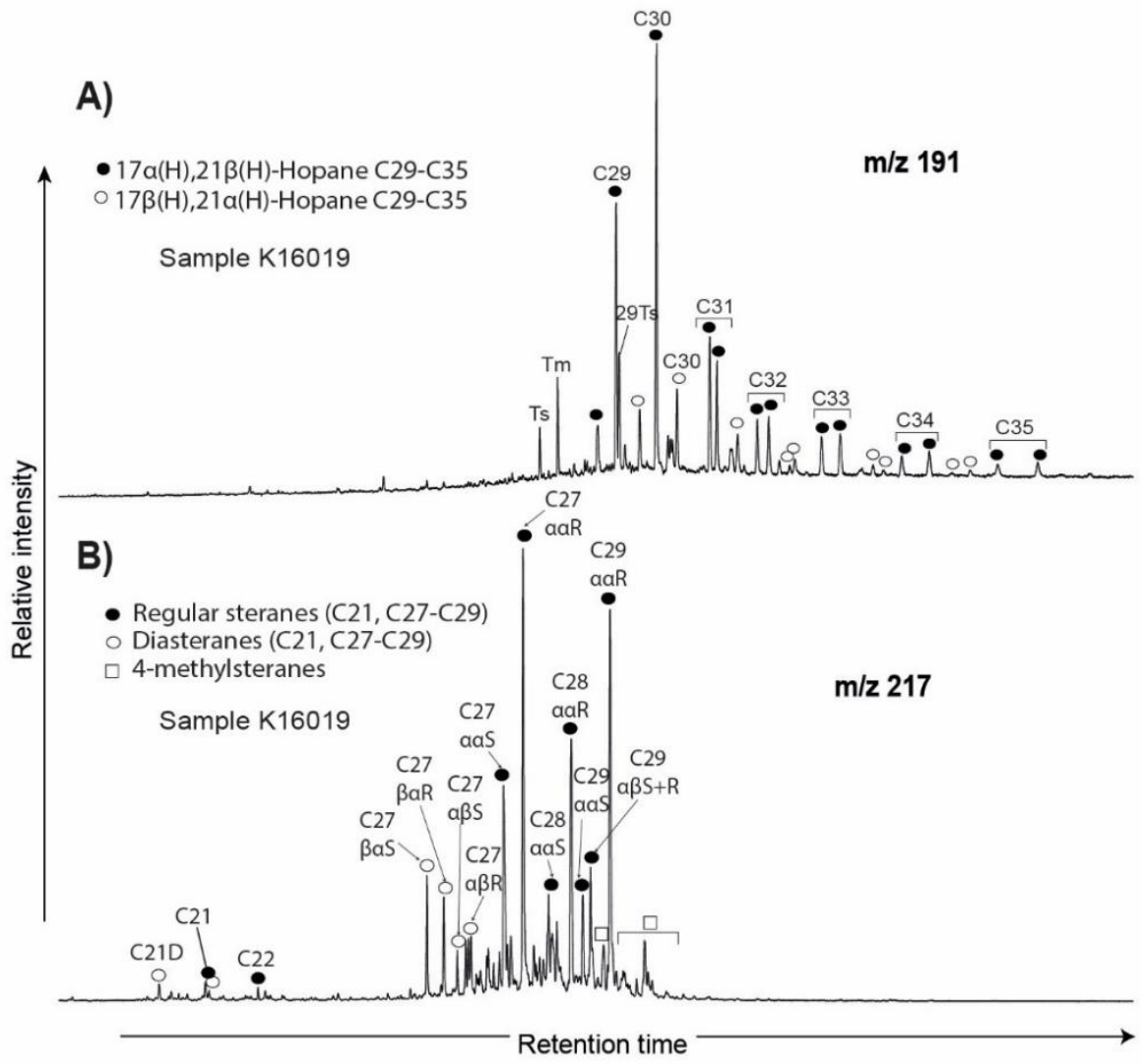

Fig. 5.12. Mass chromatograms showing the distribution of A) hopanes (m/z 191) and B) regular steranes, diasteranes (m/z 217) and 4-methysteranes in the aliphatic fraction from one representative KCF mudstone before thermal maturation. Ts: 18α(H)-22,29,30-trisnorhopane. Tm: 17α(H)-22,29,30–trisnorhopane.

Isoprenoid alkanes, alkylcycloalkanes (mainly alkylcyclohexanes and alkylcyclopentanes) and methyl-alkanes are also present but in lower amounts. N-alkanes exhibit a distribution maximizing at C_{23} with abundant C_{17}-C_{19} and C_{27}-C_{30} with a marked odd over even carbon number predominance (CPI ≈1.47), relatively high Pr/Ph (≈0.87), Pr/n-C_{17} (≈2.15) and Ph/n-C_{18} ratios (≈1.93) and similar proportions of n-alkanes C_{15}-C_{25} and ≥ C_{25} (Fig. 5.11, Tab. 5.4). No or only a few ≤ C_{14} n-alkanes are present in these immature samples. The hopane series extends from C_{27} to C_{35} with a prominent 17α(H), 21β(H) C_{30} hopane and a global predominance of 22R configurations (22S/(22R+S) < 0.50, Fig. 5.12A, Tab. 5.4). Moretanes (βα-Hopanes) are present in low amounts (Fig. 5.12A). The regular sterane series extends from C_{21} to C_{30} with a prominent 5α,14α,17α(H) 20R C_{27} and C_{29} and a large predominance of ααα

20R configurations (20S/(20S+R) < 0.20, Tab. 5.4, Fig. 5.12B). 4-methylsteranes are present. Triaromatic steroids (TAS) and C-ring monoaromatic steroids (MAS) are predominant in ARO (Fig. 5.10). TAS extends from C_{20} to C_{28} with abundant C_{26} 20R (Fig. 5.13A). MAS extends from C_{21} to C_{29} (Fig. 5.13A). Note the large predominance of long chain aromatic steroids (TAS(I)/TAS(I+II) and MAS(I)/MAS(I+II) < 8.0%, Tab. 5.4, Fig. 5.13A). Dibenzothiophenes (DBT), phenanthrenes (Phe) and their methylated derivatives (distribution in Fig. 5.14) are present in low amounts before maturation (≤ 0.02 mg/g of TOC, Fig. 5.9). SAT+ARO concentrations (less than 25% of the total bitumen fraction (Tab. 5.5) and S1 are linearly correlated with orange AOM initial contents ($R^2 \geq 0.90$; Fig. 5.15).

5.1.1.1. OM thermal transformations

After thermal maturation, a progressive decrease in the TOC, HI and the remaining HC potential is observed (Tab. 5.3, Fig. 5.7). Samples move progressively closer to the origin of the pseudo Van-Krevelen diagram (Fig. 5.7A). The increase in PI from ≈0.01 to ≈0.60 (Tab. 5.3) indicates the rise in the quantity of thermally generated HC. Thermal maturation at 325°C for 72 hours corresponds to a Tmax of ≈440°C and a mean Rc of 0.71% ± 0.02 (Tab. 5.3, 5.4). The mean Rm measured on these samples exhibits a similar value: 0.68% ± 0.02 (Tab. 5.4) indicating that the early oil generation stage has been reached. After heating at 350°C for 72 hours, Tmax and the mean Rc exhibit a slight increase and as expected, HI and S2 decrease (Tab. 5.3, Fig. 5.7). The HC potential remains, however, relatively high, especially for group B samples (S2 up to 76.1 mgHC/g of rock, Fig. 5.7B). The Tmax approaches 445°C and the mean Rc 0.85% ± 0.03 (Tab. 5.3, 5.4) suggesting that the peak of oil generation have been reached. The S1, relatively low after maturation at 325°C, exhibits a strong increase after maturation at 350°C, especially for the higher TOC samples (E38 and E40, Tab. 5.3).

Bitumen, SAT and ARO concentrations as well as the relative proportion of SAT, ARO in the bitumen fraction increase after heating at 325 and 350°C for 72h indicating oil production. As for immature rocks and samples matured at 325°C, SAT+ARO concentrations and S1 are positively correlated with the initial content of orange AOM after heating at 350°C for 72h ($R^2 \geq 0.88$, Fig. 5.15A). Samples of group B, especially E38 and E40, exhibit thus higher bitumen, SAT and ARO concentrations than B2 and B23 (group A). Similar proportion of SAT, ARO and POL (NSO) components were measured on the oil-mature sample from the Viking graben (Fig.5.8, 5.9, Tab.5.5). Only small quantities of gas are generated for these maturity stages (Fig. 5.8, Tab. 5.5).

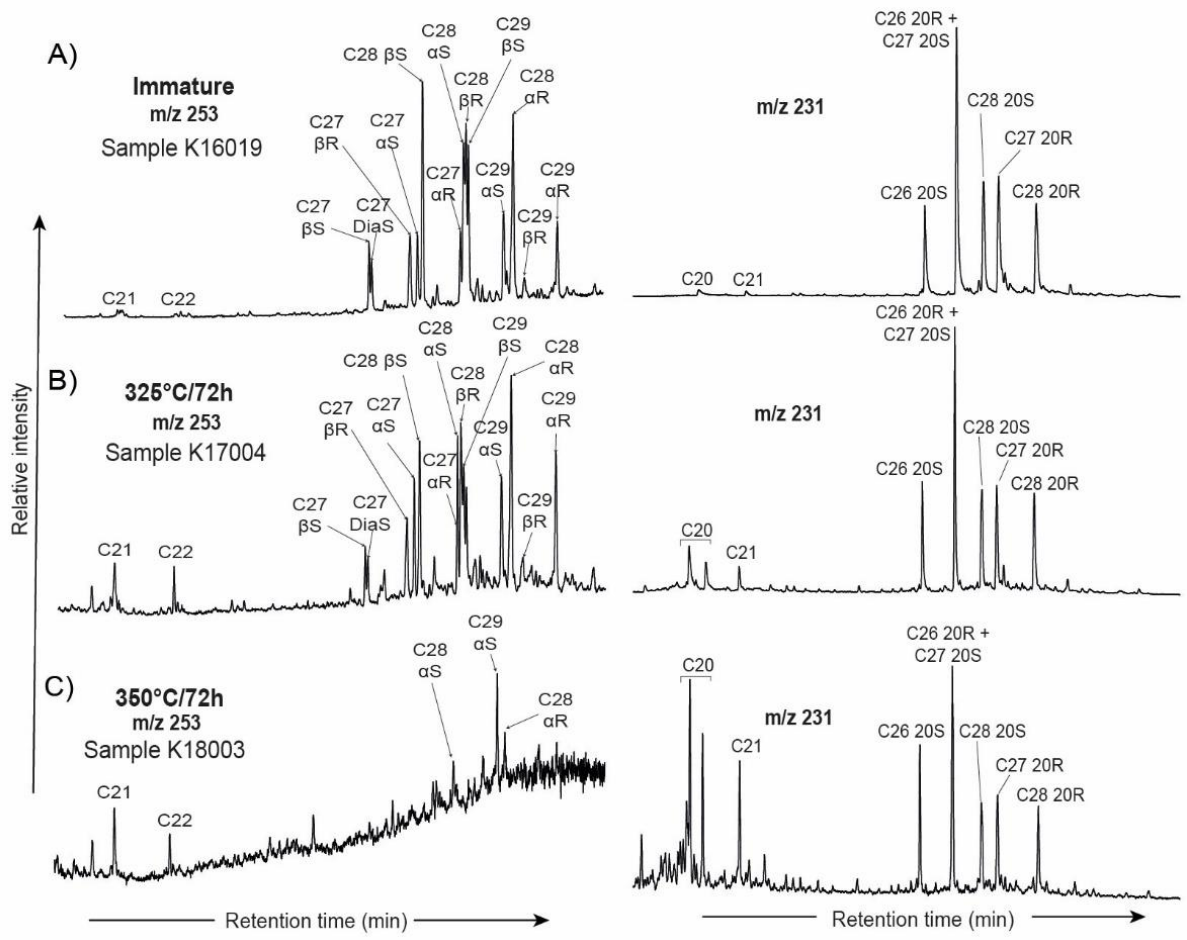

Fig. 5.13. Mass chromatograms showing the distribution of monoaromatic (m/z 253) and triaromatic steroids (m/z 231) in samples before (A) and after maturation at (B) 325°C and (C) 350°C for 72 hours.

TAS concentrations decrease slowly. On the contrary, the content of alkanes, Phe, DBT, fluorenthenes, pyrenes, naphthalenes and biphenyls increases, slightly after maturation at 325°C, and strongly after maturation at 350°C/72h (Fig. 5.10). As for SAT and ARO concentrations, differences in OM molecular composition are observable between samples of group A and B. Higher amounts of alkanes, DBT and diaromatic HC (naphthalenes and biphenyls) are present in group B after maturation at 325-350°C (Fig. 5.10). Conversely, group A shows higher concentrations of heavier polyaromatic HC such as fluorenthenes, pyrenes and Phe. The proportion of short-chain n-alkanes (mainly C_{14}-C_{25}), MAS and TAS and thus, TAS(I)/TAS(I+II) and MAS(I)/MAS(I+II) ratios increase (Tab. 5.4, Fig. 5.11, 5.12, 5.13). $<C_{14}$ n-alkanes are still present in very low amounts after maturation.

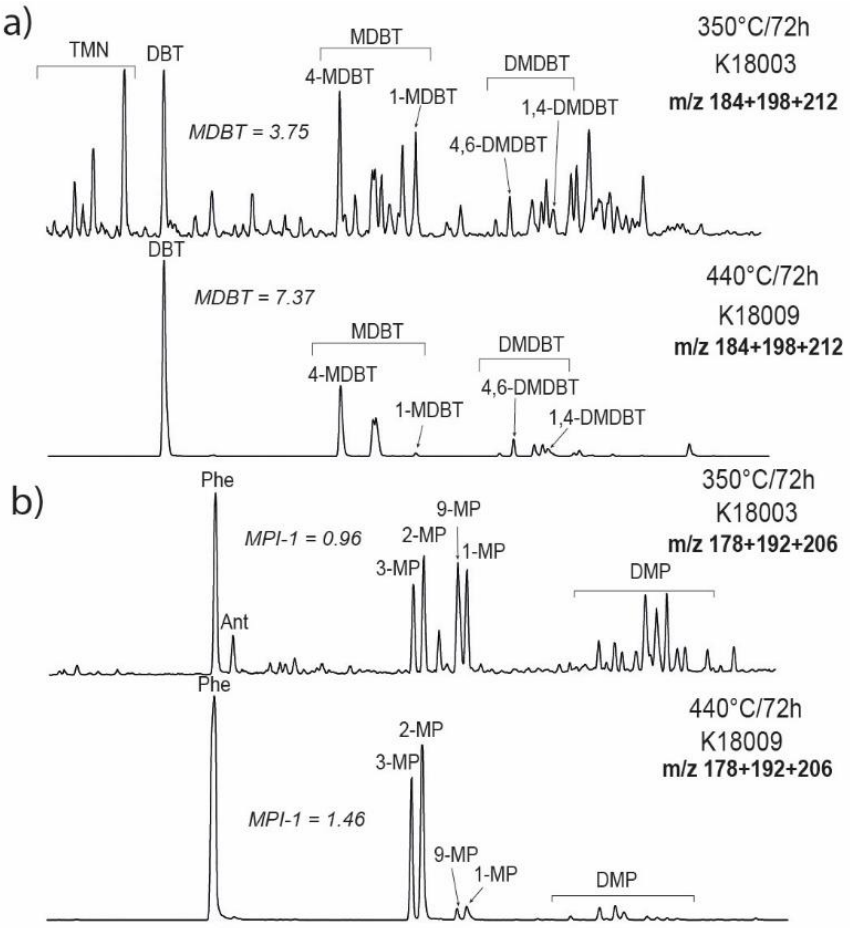

Fig. 5.14. Mass chromatograms showing the distribution of A) dibenzothiophenes (m/z 184+198+212) and phenanthrenes (m/z 178+192+206) in before (A) and after maturation at 325°C and 350°C for 72 hours. DBT: dibenzothiophene. MDBT: methyldibenzothiophenes. DMDBT: dimethyldibenzothiophenes. TMN: tetramethylnaphthalenes. Phe: phenanthrene. MP: methylphenanthrenes. DMP: dimethylphenanthrenes. MPI-1: methylphenanthrene ratio. MDBT: methyldibenzothiophene ratio.

For these early stages of maturation, the production of short-chain n-alkanes without odd over even carbon number predominance is responsible for the progressive decrease in the CPI up to ≈1.0 and for the decrease of Ph/n-C_{18} and Pr/n-C_{17} (Tab. 5.4, Fig. 5.16). Pr/Ph increase (Tab. 5.4, Fig. 5.17C). Similar Pr/Ph are obtained in naturally matured KCF source rocks (van Graas, 1990) or natural equivalents (Draupne Fm, Isaksen and Ledje, 2001). 20S/(20S+20R), 22S/(22R+22S), 4.6-DMDBT/1.4-DMDBT and MDBT ratios increase progressively (Fig. 5.17A, D). 20S/(20S+20R) and 22S/(22R+22S) reach their equilibrium after maturation at 350C° (Fig. 5.17A).

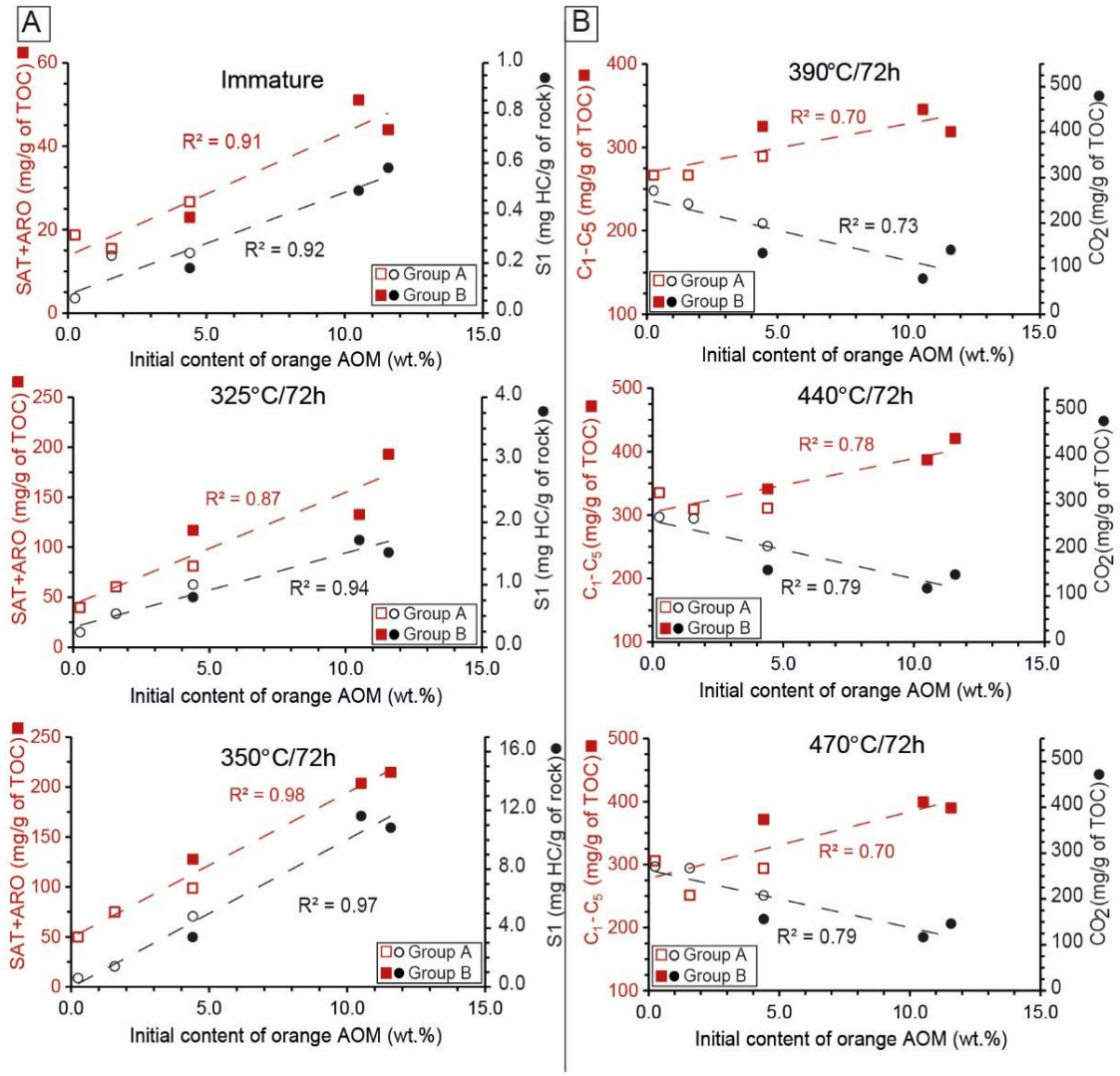

Fig. 5.15. Plot of S1 (points), saturated (SAT) and aromatic (ARO) HC concentrations (red squares) versus the initial content of orange AOM before and after thermal maturation at 325°C and 350°C. B) Plot of C_1-C_5 (red squares) and CO_2 concentrations (points) versus the initial content of orange AOM after thermal maturation at 390°C, 440°C and 470°C (gas window) in brown AOM-rich samples (group A) and orange AOM-rich samples (group B).

As previously shown by the Rock Eval parameters, the Viking graben sample seems to be an oil mature equivalent of sample B2 (Tab.5.3). Except the slightly higher alkanes, hopanes and steranes concentrations of sample VK1 (Fig.5.8, 5.10), after thermal maturation of the sample B2 at 325-350°C for 72 hours, B2 and VK1 exhibit similar biomarkers thermal maturity ratios, comparable SAT, ARO and POL relative proportions and similar concentrations of aromatic components (Fig.5.8, 5.10, 5.8, 5.16, 5.17, Tab.5.5, 5.4). Samples B2 and VK1 seems indeed to be good equivalents. After thermal maturation at 390 and 470°C, the Rc reaches respectively 1.24% ± 0.03 and 2.50% ± 0.05 (Tab. 5.4). This shows that the condensate-wet gas zone and the dry gas zone have been reached respectively.

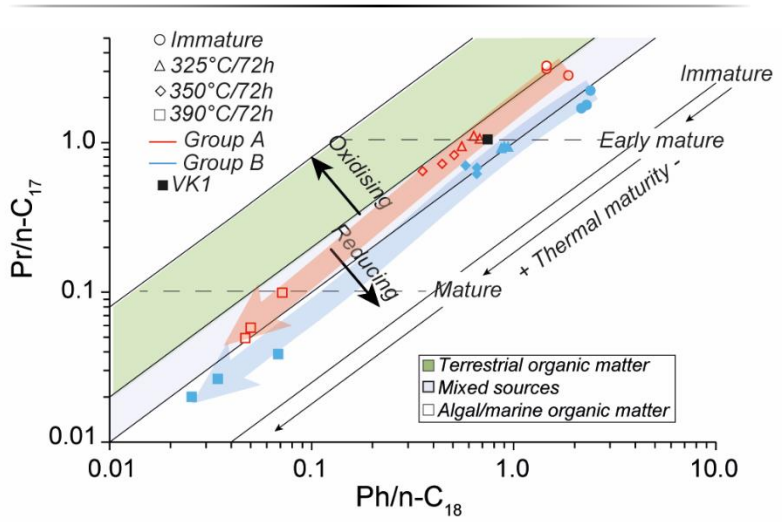

Fig. 5.16. Evolution of Pr/n-C17 versus Ph/n-C18 ratios (from Shanmugam, 1985) for brown AOM-rich (group A) and orange AOM-rich (group B) samples with increasing maturity. Comparison with the natural sample from the Viking graben (VK1).

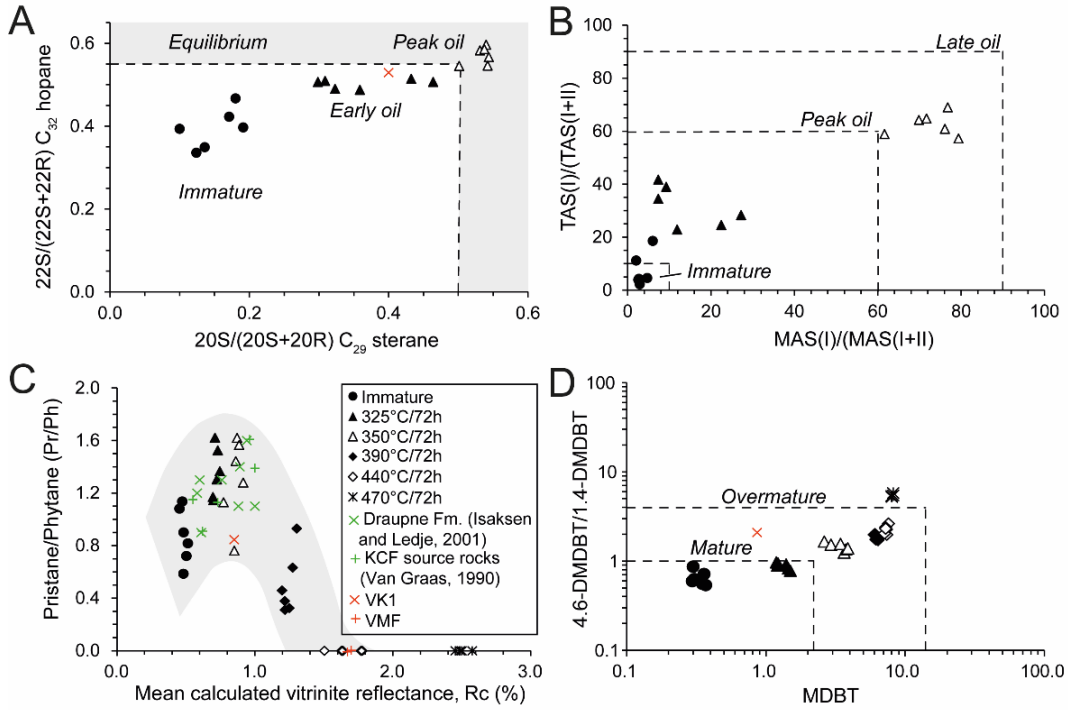

Fig. 5.17. A) Plot of 22S/(22S+22R) C32 hopane versus 20S/(20S+20R) C29 sterane ratios, where 22S is C32 17α21β 22S hopane, 22R is C32 17α21β 22R hopane, and 20S and 20R are epimers at C-20 in the C29 5α,14α,17α steranes. B) Plot of TAS(I)/TAS(I+II) versus MAS(I)/MAS(I+II) ratios, where TA(I) is C20 triaromatic steroids, TA(II) = C28 triaromatic 20S + 20R isomers, MAS(I) is C21 ring-C monoaromatic steroids and MAS(II) = C28 ring-C monoaromatic steroids. C) Plot of pristane/phytane (Pr/Ph) ratios versus Rc after thermal maturation. D) Plot of 4.6 dimethyldibenzothiophene/1.4-dimethyldibenzothiophene versus methyldibenzothiophene (MDBT) ratios. Comparison with the natural samples from the Viking graben (VK1) and the VMF.

The Rm measured on these samples (Rm) reaches respectively 1.40% ± 0.01 and 2.07% ± 0.07. After thermal maturation at 440°C, the mean Rc approaches 1.67% ± 0.14. At these maturity stages, samples exhibited a S_2 curve that was too flat to allow a correct estimate of T_{max} values after thermal maturation.

After maturation from 390 to 470°C for 72 hours, the OM is mainly composed of residual carbon (RC/TOC ≥ 0.77, Tab. 5.3). While samples show a low remaining HC potential for gas generation after maturation at 390°C (Fig. 5.7B), the TOC is composed of inert residual carbon without any remaining hydrocarbon potential at 440 and 470°C (S2 ≤ 1.1 mg HC/g rock, Tab. 5.3). The run at 390°C is characterized by the strong increase in CO_2 and C_2-C_5 concentrations and the decrease in total bitumen, SAT and ARO concentrations indicating the conversion of bitumen and kerogen into gas (Fig. 5.8, Tab. 5.5). Water is generated during thermal maturation, but the concentrations remains low (≤ 41.1 mg/g TOC). As expected, methane concentration, low after maturation at 390°C (≤ 48 mg/g TOC), increases after heating at 440°C and 470°C while C_2-C_5 and CO_2 concentrations are constant (Fig. 5.8, Tab. 5.5). C_1-C_5 concentration increases linearly with the initial orange AOM content throughout these three higher stages of maturity ($R^2 \geq 0.70$) while the amount of CO_2 decreases with increasing orange AOM content ($R^2 \geq 0.75$, Fig. 5.15B). In general, group B generated higher amounts of C_2-C_5 and lower amounts of CO_2 (Fig. 5.8, 5.15B). Hence, group A has generated 20% lower C_1-C_5 concentrations and 50% higher CO_2 concentrations during maturation (Tab. 5.5, Fig. 5.8). Despite similar initial orange AOM content between B31 and E19, brown AOM-rich E19 (group A) has led to the formation of significantly higher CO_2 and lower C_1-C_5 concentrations than B31 during maturation (group B, Tab. 5.5, Fig. 5.8). As for natural VMF samples, after maturation at 390°C, 440°C and 470°C, only heavy polyaromatic HC (Phe, fluorenthenes, pyrenes and DBT) are present in the residual total bitumen fraction (Fig. 5.8, 5.10). Alkanes in the C_{17}-C_{23} range are still relatively abundant, but Pr/Ph, Pr/n-C_{17} and Ph/n-C_{18} exhibit a strong decrease (Tab. 5.4, Fig. 5.11, 5.16, 5.17C). In the ARO, the MDBT, the MP1-I and the 4,6-DMDBT/1,4-DMDBT increase strongly (Tab. 5.4, Fig. 5.14, 5.17D). After thermal maturation at 440°C for 72 hours, KCF samples seems to have reached the same maturity than VMF samples (Tab.5.4, Fig.5.8, 5.10). The amount of residual bitumen (mainly POL) however slightly higher in the KCF (Tab.5.5, Fig.5.8, 5.10).

5.1.4. Pore volume and pore size distribution

Before maturation, the selected samples exhibit pore volumes and specific surface areas ranging between 2.82-3.73 $cm^3/100g$ and 8.87-19.93 m^2/g respectively (Tab. 5.6). The contribution of micropores is low (V_{micro} <0.4 $cm^3/100g$ and S_{micro} < 7.75 m^2/g, Tab. 5.6). Meso and macropores between 6-100 nm account for most of the pore volume (Fig. 5.18)

Tab. 5.6. BET specific surface areas (S_{BET}), total pore volumes (V_{tot}), micropore surface areas (S_{micro}) and pore volumes (V_{micro}), at different maturation temperatures. $\%V_{micro}$, $\%V_{meso}$, $\%V_{macro}$: contribution of the micropores (<2 nm), the mesopores (2-50 nm) and the macropores (>50 nm) to the total pore volume calculated from the percentage of cumulative pore volume at 2 and 50 nm in diameter.

Sample no.	Sample name	$T_{maturation}$ (°C)	S_{BET} (m^2/g)	V_{tot} ($cm^3/100g$)	S_{micro} (m^2/g)	V_{micro} (cm3/100g)	BJH		
							$\%V_{macro}$	$\%V_{micro}$	$\%V_{meso}$
K16015	B2	Immature	19.93	3.63	7.75	0.4	22.0	3.7	74.3
K17001	B23		17.52	3.73	1.60	0.1	18.0	4.0	78.0
K16019	B31		8.87	3.01	7.22	0.3	21.0	3.6	75.5
K16026	E19		12.06	3.63	5.66	0.4	28.0	1.6	70.4
K16031	E38		10.32	2.82	1.36	0.1	24.0	3.4	72.6
K16032	E40		9.59	3.17	1.12	0.1	34.0	2.8	63.2
K17002	B2	325°C	2.35	1.35	2.01	0.1	42.0	0.0	58.0
K17003	B23		2.50	1.79	0.36	0.0	46.0	0.0	54.0
K17004	B31		1.49	1.06	0.81	0.1	52.0	0.0	48.0
K17005	E19		0.63	0.90	0.10	0.2	51.0	0.0	49.0
K17007	E38		0.85	0.49	0.25	0.1	8.0	0.0	92.0
K17008	E40		0.52	0.52	0.52	0.2	65.0	0.0	35.0
K18001	B2	350°C	2.96	0.27	0.0	0.0	0.3	19.3	80.7
K18002	B23		un	un	un	un	un	un	un
K18003	B31		1.87	0.16	0.19	0.0	0.6	25.7	74.3
K18004	E19		5.26	0.48	0.0	0.0	0.0	18.1	81.9
K18005	E38		5.18	0.46	0.0	0.0	0.0	19.2	80.8
K18006	E40		4.66	0.43	0.0	0.0	0.4	22.2	77.4
K17009	B2	390°C	3.19	1.7	1.56	0.1	51	0.0	49.0
K17010	B23		3.25	1.79	3.02	0.1	59.1	0.0	40.9
K17011	B31		4.12	2.97	1.2	0.2	2.5	23.3	74.2
K17012	E19		2.14	3.98	0.69	0.3	53.1	0.0	46.9
K17014	E38		7.57	3.39	3.7	0.4	0.0	2.3	98.0
K17015	E40		11.53	4.58	3.68	0.6	0.0	20.9	79.1
K18007	B2	440°C	13.16	1.15	1.14	0.1	0.0	13.9	86.1
K18008	B23		17.72	1.65	0.0	0.0	0.0	13.6	86.4
K18009	B31		18.74	1.71	0.71	0.0	0.0	15.7	84.3
K18010	E19		21.86	2.02	0.23	0.0	0.0	14.3	85.7
K18011	E38		15.06	1.34	2.56	0.1	0.0	17.8	82.2
K18012	E40		5.73	0.48	0.35	0.0	0.0	21.7	78.3
K17022	B2	470°C	10.3	5.33	2.95	0.2	33.0	0.0	67.0
K17023	B23		15.2	9.20	5.90	0.3	42.0	0.0	58.0
K17024	B31		6.65	3.99	2.20	0.1	14.0	3.1	82.9
K17025	E19		17.44	8.22	5.45	0.3	36.0	0.0	64.0
K17027	E38		8.12	3.32	3.89	0.2	15.7	1.1	83.2
K17028	E40		19.52	5.95	5.65	0.4	13.2	2.1	84.7

un: unquantifiable values (below the detection limit of the apparatus).

Mesopores and micropores in the 1.6-5.0 nm pore size range are present, but make only a low contribution to the total pore volume because of their small size. No correlation exists between the pore volume, the TOC or the molecular composition.

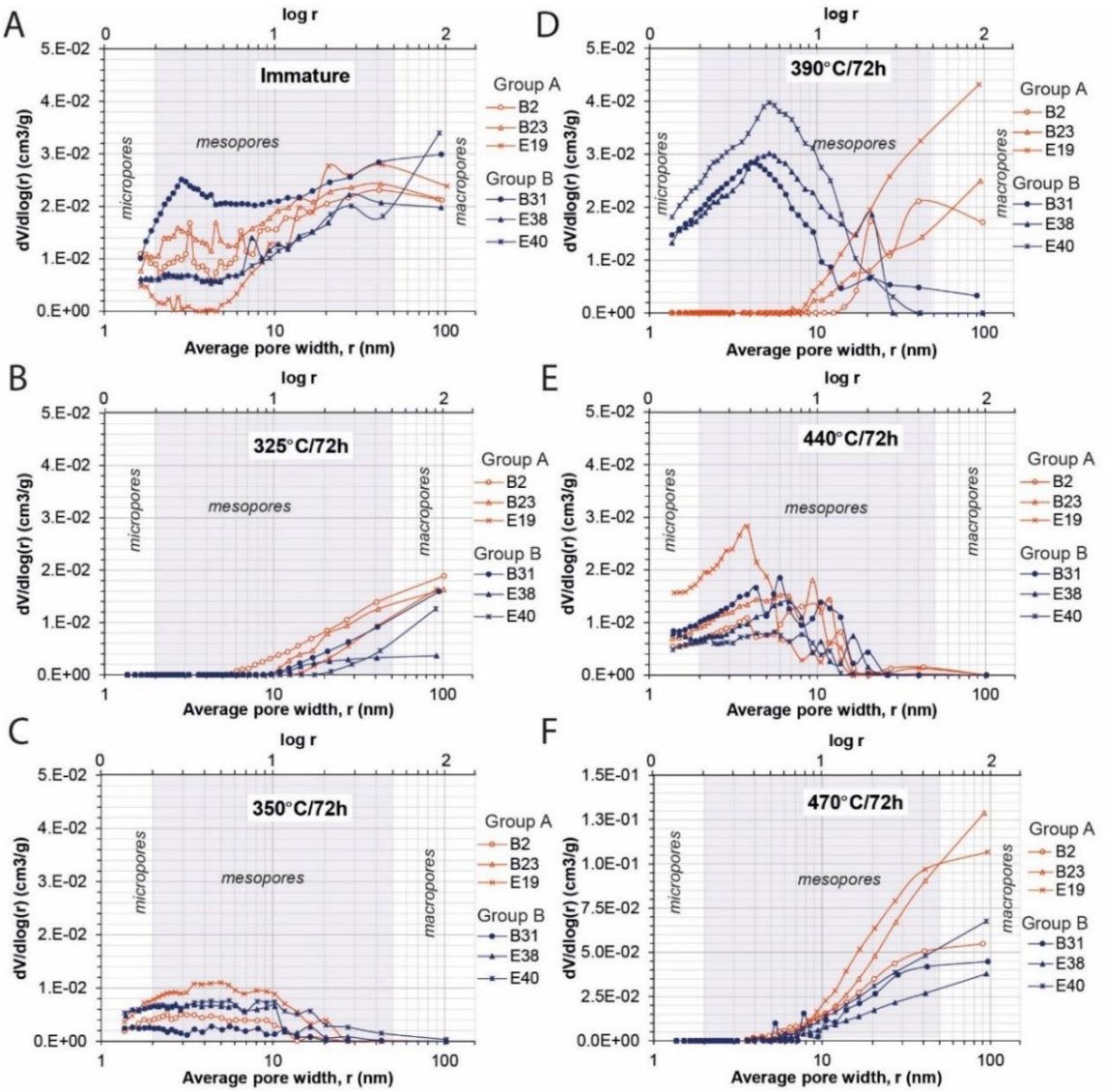

Fig. 5.18. Variations in BJH pore size distributions for KCF brown AOM-rich (group A, red) and orange AOM-rich samples (group B, blue) with increasing maturation temperature. Note that the plot of dV/dlog(r) versus r does not represent the real concentration of pores of various sizes but displays the relative contribution of pores over any ranges of pore sizes to the total pore volume. The Y-axis of F) is different from the other graphs.

After maturation at 325°C, total pore volumes show a strong decrease after heating at 350°C for 72h (Tab. 5.6, Fig. 5.8). Contrary to the stage at 325°C, where the residual pore volume is mainly composed of pores ≥ 10 nm with a relatively high contribution of macropores to the total pore volume (≈44%, Tab. 5.6, Fig. 5.18), after maturation at 350°C for 72h, the residual pore volume is mainly composed of pores ≤ 20 nm (Fig. 5.18) with a high contribution of mesopores (≈79%). While the total pore volume is inversely correlated with S1 (R^2=0.74) and SAT+ARO concentrations after heating at 325°C (R^2=0.64, Fig. 5.19A, C) and thus,

inversely correlated with the initial content of orange AOM (Fig. 5.15A), this correlation disappears after maturation at 350°C (Fig. 5.15B, D). Samples can be considered as non-porous after maturation at 350°C (V_{tot} ≤0.48 cm^3/100g, Tab. 5.6).

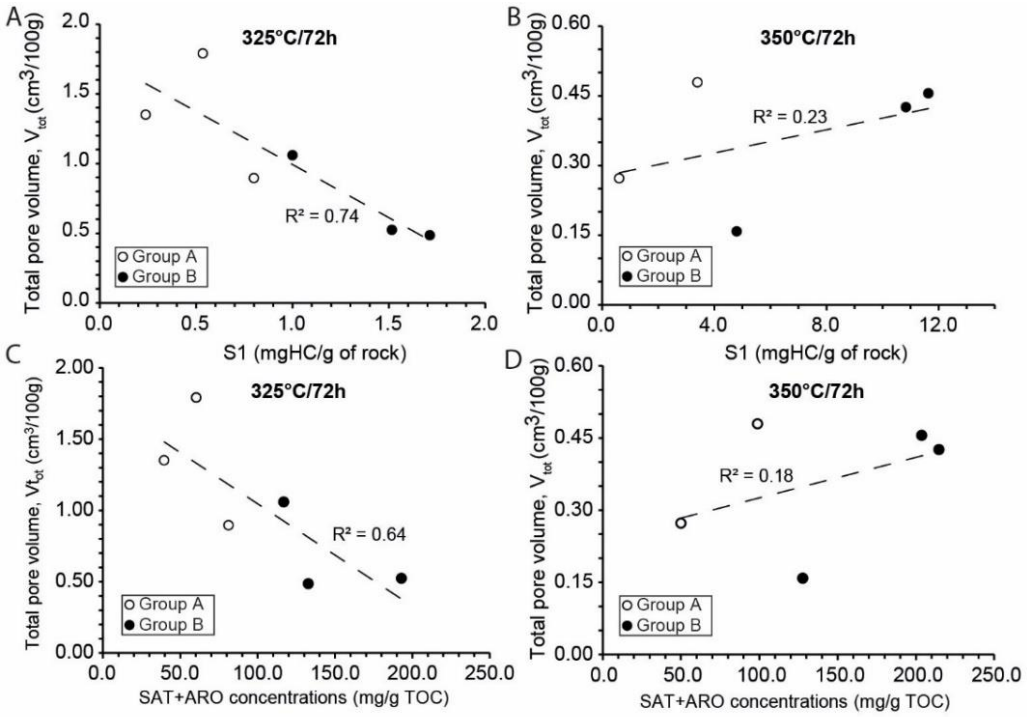

Fig. 5.19. Total pore volume as a function of S1, and SAT+ARO hydrocarbon concentration after thermal maturation at A, C) 325°C, B, D) 350°C (oil window). Group A: brown AOM-rich samples. Group B: orange AOM-rich samples.

After heating at 390°C for 72h, total pore volumes increase, especially for high-TOC samples (R^2=0.80, Fig. 5.20A). The PSD of group A samples differ from group B samples, even between E19 and B31 which exhibit similar initial orange AOM contents (Fig. 5.18, Tab. 5.1). Meso and micropores in the 1.6-10 nm range account for most of the pore volume of group B while the pore volume of group A is composed of pores in the 10-100 nm pore size range (Fig. 5.18D). No pores less than 4 nm were measured in group A. Some pores ≥ 10 nm are present in group B, but their contribution to the pore volume is small. Group B samples contain thus slightly higher specific surface areas and micropore volumes (Tab. 5.6). No correlation exists between pore volume, OM molecular composition and the concentration of C_1-C_5 generated at this maturity stage (Fig. 5.20C). The evolution of the pore volume after maturation at 440-390°C is characterized by a succession of phases of reduction and growth of the pore volume (Tab. 5.6, Fig. 5.8). After thermal maturation at 440°C for 72h, samples exhibit low pore

volumes (≤ 2.02 cm^3/100g), ≈83.8% of which is accounted for by mesopores, and relatively high specific surface areas (5.73-21.86 m^2/g, Tab. 5.6).

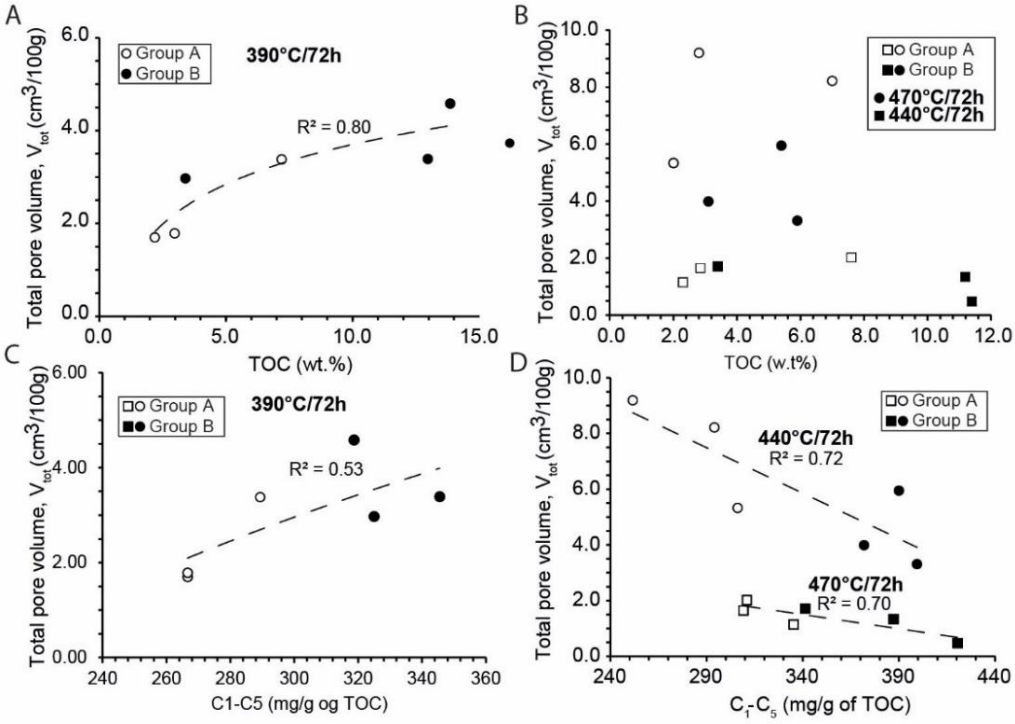

Fig. 5.20. Total pore volume as a function of total organic carbon content (TOC), and C_1-C_5 concentration after thermal maturation at A, C) 390°C, B, D) 440°C and 470°C (dry gas zone). Group A: brown AOM-rich samples. Group B: orange AOM-rich samples.

Most of the pores are less than 20 nm and no macropores are measured in the 50-100 nm pore size range (Fig. 5.18). After maturation at 470°C, pore volume exhibits a strong increase (V_{tot} ≥ 3.32 cm^3/100g, Fig. 5.8). Pores between 4-100 nm accounts for most of the pore volume (Fig. 5.18). All samples are characterized by the almost total absence of pores less than 4 nm. The increase in the number of mesopores ≥ 4 nm increases the total pore volume in group A (Tab. 5.6, Fig. 5.18). In group B, the increase in the number of pores in the 10-100 nm pore size range appears to partly compensate the strong decrease in the number of pores less than 8 nm (Fig. 5.18E-F). Mesopores ≥ 10 nm account for 64.0 to 84.7% of the pore volume (Tab. 5.6). No relationships between pore volume, specific surface area and TOC are visible at this high maturity degree (Fig. 5.20B). The pore volume decreases with increasing C_1-C_5 concentration (Fig. 5.20D) and thus, with increasing initial orange AOM content (Fig. 5.15B). Note that no correlation (R^2< 0.48) exist between the contents of quartz, carbonates or clay minerals previously determined (chapter 4) and the pore volume after thermal maturation.

5.1. Discussion

5.1.1. Composition, porosity and maturity of the original OM precursor

Rock-Eval and palynofacies analyses of KCF mudstones confirm that KCF mudstones contain a well-preserved type II oil-prone OM mainly composed of AOM derived essentially from resistant cell-walls of microalgae (brown AOM) and oil-prone phytoplanktonic lipidic components (orange AOM, Fig. 5.2, Fig. 5.7). This is well-substantiated by molecular analyses which show the presence of low molecular weight n-alkanes (C_{15}-C_{19}), known to be common constituents of phytoplankton, red and brown microalgae (Meyers, 2003; Sikes et al., 2009) and the predominance of mid molecular weight n-alkanes (C21-C25) known to be derived mainly from freshwater aquatic and marine macrophytes (Fig. 5.11; Huang et al., 1999; Ficken et al., 2000). As demonstrated by Tissot (1977) and Sikes et al. (2009), the high concentrations of high molecular weight C27-C31 n-alkanes with a pronounced odd over even predominance (CPI≈1.47, Tab. 5.4) observed in our samples confirms the presence of a supplemented background of terrigenous inputs in this OM (< 20% of the kerogen, Tab. 5.1). As expected, and according to the palynofacies observations and maceral composition, our results show real differences in molecular OM composition between samples. These differences stem from the modifications of depositional conditions and OM productivity that took place during KCF deposition previously discussed (see chapter 4 and Lallier-Vergès et al., 1995; Herbin et al., 1995; Boussafir and Lallier-Vergès, 1997). Samples in group A exhibit the typical characteristics of samples of the beginning of the cycle I of Marton with a kerogen composed of terrigenous inputs, a low amount of high HC-rich orange AOM but a higher relative proportion of brown AOM with a lower oil-generation potential (Fig. 5.2). This is well substantiated by the geochemical characterization which shows that group A samples contain a greater proportion of more oxygenated OM made up of a mixture of type II/III OM (Fig. 5.16). These samples thus correspond to non-productive periods that were less favorable to the production and the preservation of oil-prone phytoplanktonic material. Group B, which exhibits the typical features of samples of the top of the cycle, formed during periods of higher phytoplanktonic productivity, allowing a better preservation and exportation of this supplemental highly oil-prone phytoplanktonic material (orange AOM, Fig. 5.2). This is well substantiated by the molecular OM composition. The plot of Pr/n-17 versus Ph/n-C18 indeed shows the presence of less oxygenated type II OM formed in reducing conditions (Fig. 5.16). Known to be preserved by sulfurization processes (Boussafir and Lallier-Vergès, 1997), the higher relative proportion of orange AOM explains the higher content of organosulfur

compounds and DBT/Phe ratio in samples in group B (Tab. 5.4). This higher contribution of well-preserved phytoplanktonic material also appears to be responsible for the higher hopane + sterane concentrations, especially marked by more abundant 4-methyl- and regular steranes dominated by C_{27} (Fig. 5.10, 5.12). Previous work suggests that the predominance of C_{27} steranes marks a high contribution of zoo- and phyto- planktonic OM (Huang and Meinschein, 1979), while 4-methylsteranes are often considered as indicators of phytoplanktonic contributions in sediments, and more specifically of dinoflagellates (Brassell et al., 1986; Wolff et al., 1986). Despite slightly different n-alkane distributions between the two groups of KCF source rocks (Fig. 5.11), group B contains systematically higher concentrations of C_{14}-C_{25} and $\geq C_{25}$ n-alkanes indicating a higher n-alkane contribution of phytoplanktonic material than green microalgae cell-walls (Tab. 5.4).

In accordance with our previous investigations, brown AOM seems to be dispersed/diffuse in the organoclay-mineral matrix, responsible for the high fluorescence of the mineral matrix in light microscopy (Fig. 5.3B-D). In SEM, brown AOM appears as small and diffuse AOM domains closely mixed with clay (Fig. 5.5B, C). Orange AOM appears mainly as thick laminar particles, embedding clay minerals and pyrite framboids (Fig. 5.5A, C). KCF porosity before maturation is mainly composed of meso- and macropores ≥6 nm (Fig. 5.18) with a pore volume of ≈3.40 cm^3/100g mainly provided by the inter and intraparticle spaces located between rigid grains, microfossil remains and clay mineral extractible bitumen aggregates (Fig. 5.4). SEM images show that larger macropores (≤500 nm in diameter), too large to be measured using nitrogen adsorption, are also present (Fig. 5.4). As previously shown both thermally immature marine and terrigenous kerogen particles are non-porous (Fig. 5.5A-C). OM exhibits thus no contribution of OM-hosted pores to the total pore volume of small macropores to large micropores. The Rm of 0.42% measured on samples before maturation (Tab. 5.4) substantiates the Rc of 0.48%, the low S1 and PI and the Tmax ≈428°C previously determined (Tab. 5.3, 5.4). The studied samples are immature. The high content of compounds of low thermal stability (moretanes, 22R hopanes and ααα 20R steranes), the high proportion of long-chain TAS and MAS and the strong odd over even n-alkane predominance (CPI≈1.47) support the low maturity of the samples (Tab. 5.4, Fig. 5.17A, B). In general, samples showing 22S/(22S+R) < 0.50, 20S/(20S+R) < 0.20, TAS(I)/(I+II) and MAS(I)/(I+II) < 20% are immature (Mackenzie et al., 1980; Seifert and Moldowan, 1981; Peters et al., 2007).

5.1.2. OM thermal transformations during anhydrous confined thermal maturation

5.1.2.1. Evolution of bulk and molecular OM composition.

The evolution of Rock-Eval parameters, ratios of Phe and DBT, SAT, ARO, POL, condensable gas concentrations and mean Rc values are well substantiated by the Rm of 0.68%, 1.40% and 2.07% measured on KCF samples after thermal maturation at 325, 390 and 470°C for 72h respectively (Tab. 5.3, 5.4). This indicates the progressive increase in the thermal maturity from the early oil window to the dry gas zone after maturation. The evolution of biomarker thermal maturity parameters agrees with the maturity estimated with the other indicators (Fig. 5.16, 5.17). While only the early oil generation stage has been reached after maturation at 325°C/72h, the Rc of ≈0.85%, the Tmax of ≈446°C, the strong increase in S1, PI, bitumen, SAT and ARO concentrations as well as the increase in the amount of di- and polyaromatic HC and C_{14}-C_{25} n-alkanes without any odd over even predominance, indicate that the peak of oil generation is reached after maturation at 350°C (Tab. 5.3, Fig. 5.8, 5.9, 5.10). The production of abundant short-chain n-alkanes without odd over even carbon number predominance from heavier OM components is responsible for the progressive decrease in the CPI to ≈1.0 after maturation at 325°C and 350°C, the typical value observed in mature rocks (Tab. 5.4, Peters et al., 2007). At the same time, the strong decrease in steranes, hopanes, long-chain MAS and TAS concentrations mark the progressive degradation of the less thermally stable OM components (Fig. 5.10). MAS are known to be progressively aromatized and transferred into TAS through thermal maturation and microbiological processes (Moldowan et al., 1985; Peters et al., 2007). The aromatization of part of C-ring long-chain MAS into TAS and their degradation into short chain MAS (Moldowan et al., 1985; Peters et al., 2007) may thus explain the quick decrease in MAS concentrations, the slower decrease in TAS concentrations and the relatively high content of remaining long-chain TAS through these oil generation stages (Fig. 5.10, 5.13C). Accordingly, TAS(I)/(I+II), MAS(I)/(I+II), 22S/(22S+R) hopanes and 20S/(20S+R) steranes increase, reaching typical values of rocks in the peak oil generation stages (Tab. 5.4, Fig. 5.17, Mackenzie et al., 1980; Seifert and Moldowan, 1981; Peters et al., 2007). Pr/Ph increases in the same time to reach similar values of natural mature source rocks from the KCF or equivalent formations of the North Sea, confirming that these thermal maturation experiments have accurately simulated the OM thermal transformation (Fig. 5.17C, van Graas, 1990; Isaksen and Ledje, 2001). This is well-substantiated by the similitude existing between the Rock Eval parameters, the bulk and the molecular OM composition of the KCF samples and the oil-mature sample from the Viking graben at these maturity stage (Fig.5.8,

5.10, Tab.5.4, 5.5, 5.3). The thermal cracking of kerogen after heating at 350°C results mainly in the generation of n-alkanes C_{14}^{+}, and especially of C_{14}-C_{25} n-alkanes (Fig. 5.10, 5.11). $<C_{14}$ n-alkanes are present in small amounts. Only ≈27% and ≈ 8% of the total concentrations of C2-C5 and C1 have been generated during the peak oil generation respectively (Tab. 5.5, Fig. 5.8). These results well substantiate the previous work by Behar et al. (1992) which showed that the thermal cracking of a type II kerogen first results in the production of the C_{14}^{+} accompanied by the production of around 30 wt% of the C_2-C_5 but only 5 wt% of the methane fraction.

The evolution of Rock-Eval® parameters (increase of PI, RC/TOC, S1, Tab. 5.3), gas concentrations and the mean Rc of ≈1.24% and ≈2.50% previously calculated indicates that the beginning of the condensate wet gas zone and the dry gas zone have been reached after maturation at 390 and 470°C for 72h respectively Tab. 5.4). The mean Rm of 1.40% and 2.07% measured on these samples are consistent with these previous results. The mean Rc of ≈1.67% indicate that an intermediate stage of maturity corresponding to the end of the wet gas zone has been reached after maturation at 440°C for 72h (Tab. 5.3, 5.4). According to the available literature (Tissot, 1977; Chakhmakhchev et al., 1997; Peters et al., 2007), the evolution of thermal maturity parameters including 4,6-MDBT/1,4-MDBT (≈1.84-5.45) and Pr/Ph, Pr/n-C17, Ph/n-C18 up to the total degradation of C_{14}^{+} alkanes after maturation at 390-470°C, substantiates these degrees of maturity (Tab. 5.4, Fig. 5.17C, D). MDBT, MP1-1 and DPR thus provide a relatively good estimate of the vitrinite reflectance, especially from the low mature stage to the beginning of wet gas generation (Tab. 5.4). However, beyond, the standard deviation increases and the Rc calculated with each ratio vary greatly between samples. Only the mean value of the Rc provides a relatively good estimate of vitrinite reflectance. These results show that these ratios should be used with caution, especially for the highest levels of maturity and that they need to be compared with other maturity parameters to ensure a precise and reliable estimate of thermal maturity. Wet and dry gas generation are marked by the progressive thermal degradation of SAT and ARO (Tab. 5.5, Fig. 5.8). C_{14}+ alkanes, di-and heavier polyaromatic HC are progressively converted into C_1-C_5 components (Fig. 5.10, 5.11). After maturation at 390, 440, and 470°C, the secondary cracking of kerogen and bitumen left behind a residual inert OM with no remaining HC potential (RC/TOC≈1, Fig. 5.7). While about 64% of the n-alkanes generated during maturation are degraded during the early condensate wet gas zone to generate C_2-C_5, only ≈48% of the methane concentration is produced (Fig. 5.8, 5.10). n- alkanes $<C_{14}$ are still present in low amounts at this maturity stage, suggesting that even if these components are generated during OM thermal degradation processes, they are

probably quickly degraded into C_2-C_5 hydrocarbon gases. Methane appears to be mainly produced from the end of the wet gas zone to the dry gas generation, when all the C_{14}^+ alkanes have been degraded and the C_2-C_5 concentrations start to decrease (Fig. 5.8, 5.10, Tab. 5.5). Once again, all these results substantiate previous work on type II kerogen (Behar et al., 1992), and suggest that methane is mainly produced from the thermal degradation of the C_2-C_5 fraction (Fig. 5.8). Similar results are observed for the VMF, even if these natural samples contain lower amounts of residual extractible bitumen, probably more efficiently degraded under the longer duration of natural thermal degradation processes (Tab.5.5, 5.8).

All these results show that confined anhydrous maturation experiments have accurately simulated the thermal transformation of the selected KCF marine mudstones. Previous work suggests that the absence of water during maturation promotes C-C bond cross linking rather than C-C bond breaking, favoring the formation of an insoluble carbon-rich residue (solid bitumen, pyrobitumen) that may significantly limit and even prevent the generation of saturated enriched oil (Lewan, 1993, 1997). The increase in EB concentrations and relative proportions of SAT and ARO indicate, however, the production of abundant oil after maturation at 325°C for 72h (Tab. 5.5, Fig. 5.8). Moreover, gas analysis suggests that water was generated during confined experiments (Tab. 5.5). As previously envisaged by Behar et al. (2003) and Huang (1996) this result indicates that enough water could be produced in response to kerogen conversion during confined pyrolysis. This appears sufficient to make the system hydrous to promote kerogen conversion into oil. Nevertheless, only low quantities of water were produced, especially in the oil generation stage (Tab. 5.5). Part of the hydrogen from water probably hydrogenated aromatic and unsaturated components.

5.1.2.2. Variations of molecular OM composition between samples

The OM molecular analyses show that the concentration and the composition of bitumen and gas generated during maturation closely depend on the initial proportion of orange AOM (Fig. 5.15A, B). The thermal cracking of samples with a higher relative proportion of highly oil-prone phytoplanktonic OM (group B, Fig. 5.2) generated more abundant and less viscous oils during early and peak oil generation, characterized by lower amounts of POL, higher proportions of ARO and SAT richer in $\leq C_{25}$ alkanes and lighter aromatic HC, such as biphenyls, naphthalenes, and organosulfur components (Fig. 5.8, 5.10). The secondary cracking of this more hydrogenated kerogen and lighter bitumen then resulted in the formation of larger amounts of C_1-C_5 gases (Fig. 5.8, Tab. 5.5). On the contrary, the thermal degradation of the

initially more oxygenated OM of samples with higher relative proportions of brown AOM (group A, Fig. 5.2) and the apparent heavier and less abundant viscous oils produced from it, led to the formation of smaller quantities of C_1-C_5 HC gases and more abundant CO_2 (Fig. 5.8, Tab. 5.5). Our artificial maturation experiments appear thus to have successfully simulated the thermal degradation of KCF source rocks, revealing slight differences in the amount and the composition of oil and gas generated by algal cell walls and phytoplanktonic-rich samples during maturation

5.1.3. Thermal maturity and OM geochemical composition as controlling factor of KCF mudstones porosity

As suggested by previous work over the past ten years (Chalmers and Bustin, 2008; Bernard et al., 2012a; Loucks et al., 2012; Curtis et al., 2012; Milliken et al., 2013; Mastalerz et al., 2013; Chen and Xiao, 2014; Hackley and Cardott, 2016; Ko et al., 2018; Katz and Arango, 2018), the chemical transformations of OM and the subsequent HC generation as oil, gas and pyrobitumen are accompanied by complex evolutionary trends of OM-hosted pore development. Thermal maturation and OM composition play a complex but major role in the evolution of KCF mudstones porosity from the early oil generation to the dry gas zone. Kerogen and bitumen thermal transformation and the ensuing oil and gas generation appear responsible for most of the variations in pore volume and PSD (Fig. 5.8, Fig. 5.18).

5.1.3.1. Oil generation

In the studied mudstones, the early oil generation stage (~0.72% Ro), marked by the appearance of pyrobitumen in polished sections (Fig. 5.3E, F), is characterized by the strong decrease in the number of pores ranging from 1.6 to 100 nm, leading to lower total pore volumes and specific surface areas (Tab. 5.6, Fig. 5.18). PSD revealed the almost complete filling of micro and mesopores less than 10 nm in diameter by bitumen generated from the early OM conversion making them poorly accessible to nitrogen adsorption measurements (Fig. 5.18). SEM images showed that the vast majority of the intra and interparticle macropores observed in immature samples between rigid grains, and clay minerals, are also partly filled by a diffuse AOM gel-like, probably resulting from a mixture of bitumen and kerogen (Fig. 5.5D, Fig. 5.6A). Accordingly, the remaining pore volume decreases with the increase in the amount of oil generated after maturation at 325°C (Fig. 5.19A, C). Unsurprisingly, samples that initially

contained higher TOC and more oil-prone orange AOM (group B) produced a slightly higher quantity of oil and thus exhibit a lower number of meso and macropores in the 10-100 nm pore size range and thus, lower remaining pore volumes after the early conversion of OM (Tab. 5.6, Fig. 5.8, 5.19A, C). This phenomenon was commonly observed in mudstones at thermal maturity up to Ro=0.90% (Löhr et al., 2015; Furmann et al., 2016; DiStefano et al., 2016; Han et al., 2017; Ko et al., 2018; Katz and Arango, 2018; Wang et al., 2019). These results show that the early oil generation and migration appear to be sufficient to strongly limit the availability of the original mineral inter and intraparticle macro and mesoporosity. While only pores less than 10 nm in size are occluded in the early oil generation stage (Fig. 5.18B), the stage at 350°C for 72h shows that the peak oil generation results indeed in the occlusion and/or the destruction of about 89% of the initial total pore volume (Fig. 5.18C, Tab. 5.6). Hence, most of the mineral associated pores, predominant in immature KCF rocks before maturation, disappear during oil generation in favor of an increasingly well-connected OM network. Only a few residual micropores and mesopores (<30 nm) still remain accessible to N_2 gas adsorption measurements (Fig. 5.18C). While the occlusion of pores by oil generation and migration appears to be an obvious explanation for these phenomena, previous studies suggest that pore compaction, ductile deformations and collapse of the kerogen structure resulting from increased plasticity at the more elevated temperature and/or changes in the physical and chemical properties of kerogen may also explain part of the loss of pore space in response to oil generation (Löhr et al., 2015; Guo et al., 2018). During oil generation (Rc≈0.71 to 0.85%), the higher amounts of bitumen enriched in saturated and lighter aromatic components (lower amounts of heavier polyaromatic components such as phenanthrenes or pyrenes Fig. 5.8, 5.9, 5.10) generated by group B have probably led to a better and more complete impregnation of the mineral matrix by bitumen forming a more interconnected OM network. While this may explain the strong correlations existing between orange AOM contents, SAT + ARO concentrations, S1 and thus pore volume after maturation at 325°C (Fig. 5.15A, 5.19A, C), the remaining pore volume associated with the mineral matrix, probably too weakly connected after maturation at 350°C, cannot be correctly measured by nitrogen adsorption. These correlations are thus no longer visible during peak oil generation (Fig. 5.19B, D).

It is commonly assumed that the formation of OM-hosted pores occurs essentially at higher levels of maturity, during gas generation, but previous work suggests that the development of organic porosity can be initiated by pore rearrangements under compaction, mineral dissolution, or in kerogen and solid bitumen (pre-oil) in response to oil generation and

expulsion for Rm ≥ 0.70% (Loucks et al., 2009; Chen and Xiao, 2014; Juliao et al., 2015; Ko et al., 2018; Wang et al., 2019). Some rare isolated bubble-like pores, varying in size from a few hundred nm to a few µm, are indeed observed in KCF OM in the oil generation stage (Fig. 5.6A-C). Since no OM-hosted pores are observed in immature samples, some of these pores may result from petroleum generation and expulsion processes. Most of these pores are located near the interface of OM and clay minerals (Fig. 5.6B). Phyllosilicates are known to catalyze the formation of gas prior to petroleum (Tannenbaum and Kaplan, 1985), favoring early nucleation and the escape of gas bubbles along the surface of clay minerals (Milliken et al., 2013). These OM-hosted oval pores may result from OM-clay mineral interactions responsible for the early nucleation and devolatilization of condensable gases (especially C_2-C_5 and CO_2 at this low level of maturity, Tab. 5.5). The available literature suggests that these processes may reach a significant level at slightly higher thermal maturity levels (~0.80-0.85% Ro), where OM-hosted pores are known to develop further (Loucks et al., 2009; Bernard et al., 2012a; Han et al., 2017). Many irregular-shaped OM pores are, however, not associated with clay minerals (Fig. 5.6C). These pores are hosted by granular OM, probably bitumen that filled intergranular spaces between various minerals such as pyrite grains (Fig. 5.5D, 5.6C). This pore network may form from bitumen migration in the intergranular porosity that has partially filled the pore space allowing the trapping of water on the edges of various minerals. These different pore types are commonly observed in mudstones (Milliken et al., 2013; Guo et al., 2018). As for the natural sample from the Viking Graben (see chapter 4), the vast majority of OM is, nevertheless, non-porous at this low level of maturity (Ro≈0.72%). OM-hosted pores remain sparse, isolated, and largely outweighed by the volume of pores filled by oil/bitumen generation or lost by collapse and compression processes.

5.1.3.2. Gas generation

As commonly observed in thermally mature mudstones (Loucks et al., 2009; Bernard et al., 2012b; Curtis et al., 2012; Reed et al., 2014; Chen and Xiao, 2014; Cardott et al., 2015; Hackley and Cardott, 2016; Ko et al., 2016; Hackley, 2017; Ko et al., 2017, 2018), gas generation and expulsion from the end of the oil window to the wet gas zone result in the formation of abundant secondary products from oil/bitumen (Fig. 5.3E-H, pyrobitumen) and the re-increase in the number of macropores, mesopores and total pore volumes (Tab. 5.6, Fig. 5.8, 5.18). As previously observed for the VMF (see chapter 4), pores appear to be mainly hosted by OM (Fig. 5.5E-F). This is substantiated by the positive relationship existing between

TOC, specific surface areas and pore volume (Fig. 5.20A). While not all the OM is porous (Fig. 5.6F), the majority is at the SEM detection limit, indicating an intense pore development facilitated by OM transformation (Fig. 5.5E-F). Two main types of OM hosted pores are present. Many OM particles of various sizes and shapes exhibit a spongy texture characterized by the presence of abundant subrounded pores forming a complex interconnected 3D nanometer-scale pore network (≤100 nm, Fig. 5.5D, 5.6D). These well-developed OM-hosted spongy pores consist probably of devolatilization vacuoles formed from the homogeneous generation and expulsion of interconnected gas bubbles when gas nucleation becomes significant (C_1, CO_2, C_2-C_5, Tab. 5.5) or from the release of petroleum and/or water entrapped in bitumen (Loucks et al., 2017; Ko et al., 2017). Some of these pores and the large devolatilization cracks in spongy OM (Fig. 5.6D) may, however, be artefacts accentuated by sample preparation and SEM observations under vacuum and might not exist in the subsurface (Loucks and Reed, 2014; Klaver et al., 2016). Spongy OM-hosted pores are frequently observed in various marine and lacustrine mudstones (Bernard et al., 2012b; Loucks and Reed, 2014; Reed et al., 2014; Ko et al., 2016; Loucks et al., 2017; Ko et al., 2017; Guo et al., 2018; Ko et al., 2018). While this spongy OM is often considered to be solid bitumen/pyrobitumen (Bernard et al., 2012b; Milliken et al., 2013; Loucks et al., 2017; Ko et al., 2017), the laminar shape and the thickness of some spongy particles suggests that some of them are residual marine kerogen (Fig. 5.5E, 5.6D). Granular OM appears to be made up of the aggregation of small spheres of OM separated by large and complex irregular pores at the nanometer scale (Fig. 5.6E, G). These pores may result from a more complete nucleation and interconnection of pores created by the expulsion of oil and gas bubbles in OM or may be a consequence of the formation of pores in OM particles with different compositions. However, the rearrangement of structural units within kerogen with increasing thermal maturity and oil/gas expulsion processes may greatly contribute to the appearance of spongy and granular OM-hosted pores from the oil window to the condensate/wet gas zone (Romero-Sarmiento et al., 2014; Alcantar-Lopez, 2016). Alcantar-Lopez (2016) revealed that the progressive evolution of the kerogen structure from sub-spherical units to a more rigid crosslinked nanofiber network in SEM may significantly favor the formation of pores with increasing maturity. For samples containing relatively lower TOC (<6.0 wt%), these processes appear insufficient to allow the development of a large pore volume accessible for gas adsorption (Tab. 5.6, Fig. 5.18A, B), probably due to the poor interconnectivity of the less abundant OM pore network. Moreover, it is important to note that PSD can differ greatly between samples of group A and B, even in samples with comparable

TOC contents (Fig. 5.18), and that the relation between TOC and pore volume are not linear suggesting that other factors unrelated to thermal maturity and OM content are at work at this maturity stage (Fig. 5.20A). The decrease in pore volume and global pore size after thermal maturation at 440°C (Rc≈1.67%), and their re-increase after maturation at 470°C suggest that the secondary cracking of kerogen and bitumen does however not lead to a continuous and linear increase of porosity in OM but to a strong alternation of phases of growth and reduction of the total pore volume and pore sizes (Tab. 5.6, Fig. 5.8, 5.18) which seems more closely dependent on the amount of gas generated during maturation and thus on the initial OM composition than on the OM contents (Fig. 5.20, 5.15). We can suppose that the reduction of the pore volume is mainly due to collapse of the pore network in response to compaction and gas generation and expulsion.

In the dry gas zone, the massive generation of C_1, and the still abundant production of C_2-C_5 from OM (Tab. 5.5, Fig. 5.8) seem to result in a massive pore development in OM (Fig. 5.5F, 5.18). The almost complete conversion of some OM particles has left behind rare large conversion pores (a few µm in size, Fig. 5.5F) while the interconnection of spongy and granular OM-hosted pores has allowed the formation of more abundant irregular complex modified mineral pores (a few µm in diameter) lined with relic spongy and granular OM, (probably solid bitumen/pyrobitumen, Fig. 5.6I). Most of the pores seem, therefore, to be associated with primary mineral pores, filled first by bitumen, and partly freed after the expulsion of oil and gas. These pore types have been previously described in thermally-mature mudstones (Ko et al., 2016, 2017; Guo et al., 2018). The presence of this hybrid mineral-OM porosity in KCF samples may partly explain the absence of relationships between TOC, pore volume and specific surface area in the dry gas zone (Tab. 5.6, Fig. 5.20B). Type III kerogen, mainly composed of woody fragments, is the only type of OM which remains non-porous in thermally mature KCF mudstones (Fig. 5.6H). Although some dry-gas mature samples exhibit a slightly higher pore volume after thermal maturation than immature samples, most of the samples exhibit similar or lower total pore volumes (Tab. 5.6). It is important to note that thermal maturation influences the distribution of pores between mineral and OM phases rather than the total porosity of mudstones. Note that during artificial thermal maturation, no variations of the mineral texture and structure are visible in SEM as well as no variations of clay mineral composition (Fig. 5.5, 5.1). This suggests that the contribution of the inorganic phase to the variations of porosity is probably very limited.

5.1.3.3. Influence of the original OM particulate assemblage on porosity

The available literature suggests that the maceral composition of OM can influence the development of OM-hosted pores (Loucks et al., 2012; Mastalerz et al., 2013; Furmann et al., 2016; Ko et al., 2016, 2017; Liu et al., 2018; Ko et al., 2018). No real difference of PSD is observed between KCF samples during the early oil generation stage, probably masked by the filling of the porosity by entrapped oils and bitumen (Fig. 5.18). However, the size and the type of OM-hosted pores developed in kerogen/pyrobitumen in response to gas generation and expulsion, responsible for the progressive re-increase in the pore volume in the gas window, seems dependent on the content but especially on the composition of the OM. Significant differences are indeed observed during gas generation, indicating an impact of the maceral composition of the precursor of OM on pore development. The mineralogy, relatively homogeneous between the studied samples of Marton and Ebberston boreholes cannot explain this difference.

The different OM composition and concentrations of bitumen and gas generated between orange AOM-rich (group B) and brown AOM-rich (group A) samples has led to a slightly different timing of pore evolution. Through the immature stage (i), the condensate wet/gas zone (ii) and the dry gas zone (iii), the OM texture of orange AOM-rich samples (group B, bituminite-rich samples) evolves mainly from: (i) thick non-porous laminar amorphous particles (bituminite macerals, orange AOM) forming a continuous OM framework embedding clay minerals and pyrite (Fig. 5.5A); (ii) thick laminar particles (bituminite) which appear as non-porous at the SEM detection limit (Fig. 5.6F). Nitrogen adsorption measurements suggest, however, that these particles are porous, but contain abundant small mesopores and micropores less than 10 nm which are under the SEM detection limit (Fig. 5.18D-E) responsible for the re-increase in the total pore volume after maturation at 390°C; (iii) spongy and granular particles containing abundant larger meso and macropores (≥ 10 nm), probably formed from the coalescence of smaller pores (Fig. 5.18F, 5.5G). Only a few large modified mineral pores are observed, resulting in a relatively low total pore volume (Tab. 5.2, Fig. 5.8), which remains relatively stable throughout the gas window (Fig. 5.8). Contrary to group B, the OM texture of the relatively brown AOM-rich samples of group A evolve mainly from: (i) thin more dispersed elongated non-porous amorphous particles (alginite macerals) and diffuse AOM domains (brown AOM) mixed with clay minerals (Fig. 5.5B, C); (ii) abundant spongy and granular particles forming a more interconnected pore network made up of abundant meso and

macropores (≥ 10 nm) whose contribution to the total pore volume depends on the OM content (Fig. 5.5E, 5.6D, E, 5.18); (iii) more abundant modified mineral meso and macropores lined with relic granular/spongy OM, probably formed from the extensive conversion of residual spongy and granular OM (Tab. 5.2, Fig. 5.6 I). These pores are responsible for the stronger increase in total pore volume and the number of mesopores larger than 4 nm of group A samples in the dry gas zone (Fig. 5.8, 5.18). Despite a higher oil-prone quality, samples containing a higher content of oil-prone orange AOM (bituminite macerals) and lower content of brown AOM thus appear to be less favorable to the formation of large mesopores during thermal maturation, resulting in slightly lower pore volume in the dry gas zone.

One main process can be proposed to explain this different development of OM-hosted pores, the pore evolution model is shown in Fig. 5.21. The more efficient secondary conversion into C1-C5 hydrocarbon gases of the OM network formed by the more hydrogenated bitumen and kerogen in orange AOM-rich samples (group B, Fig. 5.8, 5.15B) abundant thick laminar bituminite particles forming a continuous ductile or brittle network (depending on the maturity) probably left behind a well-developed but more vulnerable OM porosity, more easily and repeatedly altered by collapsing processes in response to the high pressure generated during gas generation. Conversely, in samples with a higher relative proportion of brown AOM (group A), the lower porosity formed during the less efficient conversion into gas of the poorly connected and hydrogenated OM network (Fig. 5.8, 5.15), more dispersed in the matrix, seems to exhibit a better resistance to compaction processes, explaining their larger pore sizes in the early wet gas zone (Fig. 5.18D) and the more abundant OM hosted pores in SEM images (Tab. 5.2). For the two higher maturity stages, the concentrations of HC gases generated during the OM conversion are the main controlling factor of KCF porosity (Fig. 5.20D). However, the HC gases concentrations and pore volume are anticorrelated ($R^2 \geq 0.70$, Fig. 5.20D), suggesting that the more C_1-C_5 hydrocarbon gases the samples have generated, the more the resulting interconnected OM pore network, vulnerable to compaction, suffers severe collapse, leading to a significant loss of pore volume. Hence, the total pore volume of the studied samples decreases strongly with the amount of C1-C5 HC gases, and thus with the initial content of highly oil-prone orange AOM for Rc ≥ 1.67% (Fig. 5.15B, 5.20D). Samples with a higher relative proportion of brown AOM (group A) have, however, also suffered collapsing processes, as shown by the strong decrease in the pore volume and sizes after maturation at 440°C (Tab. 5.6, Fig. 5.8, 5.18E). But these collapsing events are probably less frequent in these samples, explaining their higher pore sizes after maturation at 390°C and their higher pore volume after

maturation at 470°C, even for the lower TOC samples (Tab. 5.6, Fig. 5.18D, F). This probably explained why no positive linear correlation are observed between TOC and pore volume in the condensate wet gas zone (Fig.5.20A).

Other concomitant mechanisms, probably less important, can also be suggested. The different OM precursor, group A and B samples have generated different concentrations and composition of bitumen and gas. These differences may have influenced the structure and the composition of pyrobitumen and its ability to develop pores during maturation. As suggested by Alcantar-Lopez (2016), the progressive evolution of the kerogen structure with increasing maturity may significantly favor the formation of pores from the oil window to the dry gas zone. Alternatively, we can assume that the structure of several macerals, with slightly different oil generation kinetics, may evolve differently or with a slightly different timing leading to the formation of pores that differ in number and size for the same maturity level. While these variations may not be significant in natural systems, the short duration and the higher temperature of our laboratory experiments may have strongly accentuated these differences, explaining part of the difference in pore distribution between the samples of groups A and B. Assessing the effect of the temperature-duration pairs used for the experiments need to be clarified.

While pores are mainly associated with the mineral matrix in the immature samples, it is not true for the higher maturity stages. In migrating in the adjacent mineral pores, the significant amount of bitumen generated during thermal OM conversion, leads to a significant increase of the OM connectivity in samples and to the significant decrease of the mineral matrix pore volume (Fig. 5.21A, B). Then, the significant volume expansion and the pressure generated during gas generation lead to the massive formation of a well interconnected pore network in the residual OM which became thus, the major contributor of the porosity of these organic-rich mudstones. While some interparticle pores of the mineral matrix are released in the form of conversion or modified mineral pores lined with relic of residual OM (Fig. 5.5E, F), the formation of these pores closely depends on the OM conversion rate and thus on the OM composition and thermal maturity.

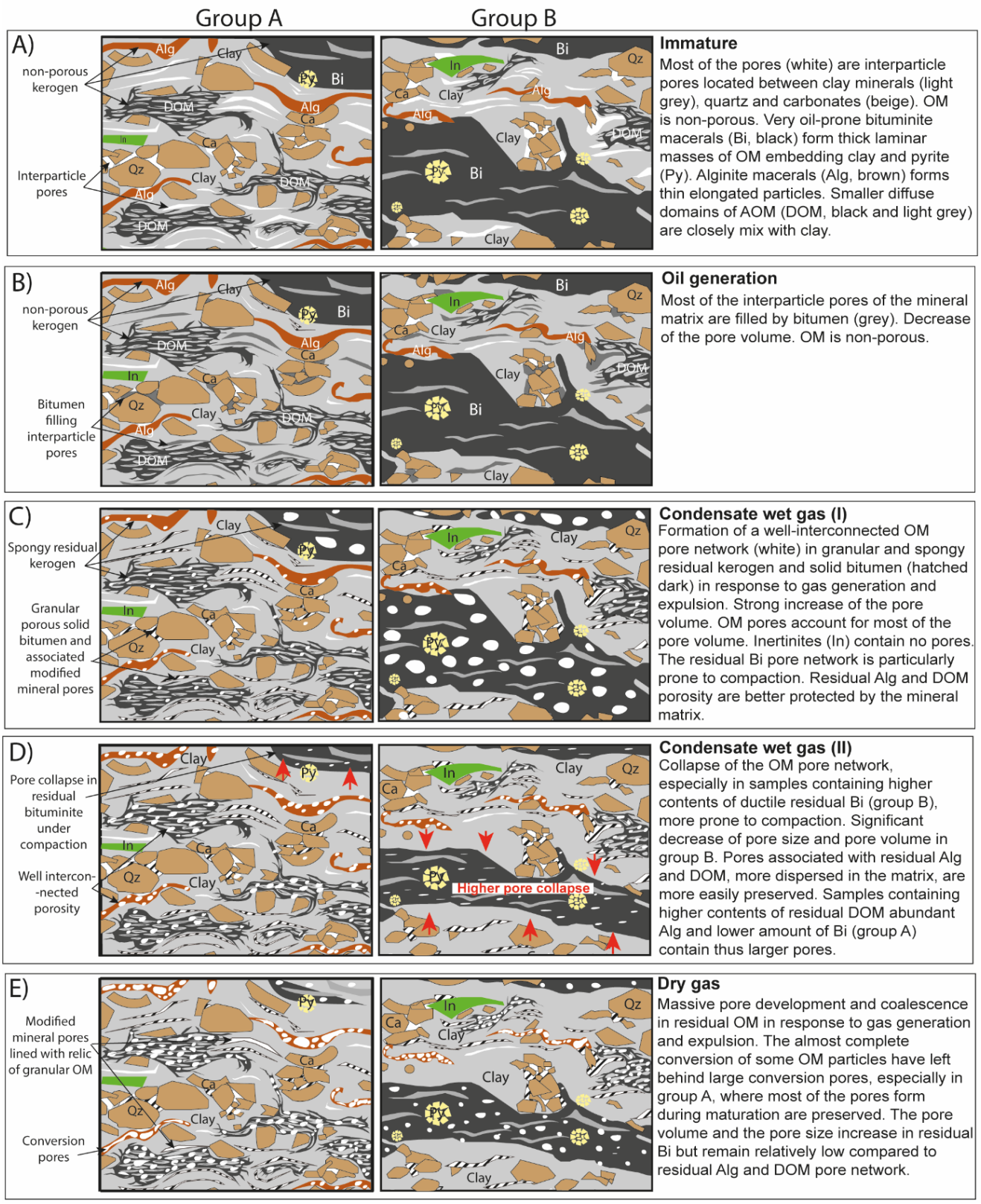

Fig. 5.21. Simplified synthetic pore evolution model of KCF mudstones with increasing thermal maturity. Group A: samples with higher relative proportion of brown AOM (diffuse patch of AOM mixed with the mineral matrix: DOM). Group B: samples with higher relative proportion of orange AOM (bituminite maceral: Bi). In: inertinite fragments. Py: pyrite. Alg: alginite macerals. Ca: carbonates. Qz: quartz.

In agreement with previous work (Chalmers and Bustin, 2008; Bernard et al., 2012a; b Loucks et al., 2012; Curtis et al., 2012; Milliken et al., 2013; Mastalerz et al., 2013; Chen and Xiao, 2014; Ko et al., 2018; Katz and Arango, 2018) all these results underscore the importance of the OM thermal degradation processes on the development of the porosity of organic-rich source rocks. Maturity appears to be the dominant factor controlling porosity but this work suggests that simply considering the amount and quality of OM and the level of maturity is clearly insufficient to estimate the porosity of organic-rich mudstones. Nevertheless, non-maturity-related factors such as the chemical properties of the OM particulate assemblage, the distribution of the OM particles in the mineral matrix and the ability of the rocks to resist compaction appear to affect pore generation and development. The oil-generation potential, the behavior of the OM particulate assemblage and its generation kinetics seem to significantly influence the evolution of porosity, even within the same formation containing a similar type II kerogen. That is probably the reason why so many different trends are observed in natural gas-mudstone systems. As previously observed in the VMF, no positive correlation is observed between TOC and pore volume in KCF samples in the condensate wet gas zone (Fig.4.16E, Fig.5.20A). This well substantiated our previous hypothesis which suggests that similar processes are at play in the KCF and the VMF. Variations of the OM composition, and probably various amounts and distribution of maceral types between samples are probably at the origin of different ability of the VMF rocks to develop and preserved pores during maturation explaining the decrease of the pore sizes with increasing TOC and the relatively low pore volume of samples with more than 5.5 wt.% of TOC.

As previously demonstrated by Monthioux et al. (1985) and Landais and Monthioux, (1988), a perfect experimental simulation of OM thermal maturation is not achievable. However, the similarities existing between our artificially matured samples, the natural oil-mature sample of the Viking graben, gas-mature samples from the VMF and natural trends from the available literature (similar biomarker ratios, bitumen and gas composition, OM surface texture…), indicate that anhydrous confined experiments give relatively comparable results to those of natural conditions. However, the differences in oil and gas generation potential that naturally exist between various organic components may be accentuated by the high temperature and the very short duration of our artificial maturation experiments. This may have emphasized some differences between orange and brown AOM-rich samples that are probably less marked in natural systems. A comparison of these results with natural equivalents and longer duration laboratory experiments thus remains essential to better understand the influence

of the thermal maturation kinetic on the simulated OM thermal degradation processes and pore development. This issue is addressed in the chapter 7.

Summary and conclusions

To investigate how variations in the composition of the total particulate OM assemblage and maceral types throughout the same formation influence the development and the evolution of porosity during the thermal maturation of marine mudstones, laboratory confined thermal maturation, geochemical characterization, organic petrography (SEM, palynofacies and macerals analysis), and porosimetry measurements were applied on six low-mature marine KCF mudstones with slightly different type II OM composition. The following conclusions can be drawn. The size and the PSD vary greatly within KCF mudstones with increasing thermal maturity. OM-hosted pores appear to develop mainly from the early condensate wet gas zone ($Rm \approx 1.24\%$). Although the mineral matrix is the predominant fraction in KCF mudstones, the initial molecular composition of the OM, the composition and the quantity of the products generated during its thermal degradation significantly influence the evolution of the total pore volume of KCF organic-rich mudstones during maturation. During oil generation samples containing higher amounts of phytoplanktonic orange AOM generated higher amounts of saturated and aromatic HC, richer in hydrogenated and lighter components (especially n- and isoalkanes) leading to a better and more complete impregnation of the mineral matrix by fluid and viscous bitumen and forming a well interconnected OM network. Then, the slightly more efficient secondary conversion of this OM network into C1-C5 hydrocarbon gases enabled the formation of a well-developed but more vulnerable OM porosity, more easily and repeatedly altered by collapsing processes during gas generation and expulsion. Hence, the total pore volume of the studied samples decreased strongly with the concentration of gas generated during maturation, and thus the initial content of highly oil-prone orange AOM. Thermal maturity can be considered as the principal factor controlling the formation and the progressive steps of pore evolution in organic-rich marine mudstones, but these results also demonstrate here that the amount and the quality illustrated by the palynofacies and chemical compositions of OM seem essential to better understand and predict the formation and the evolution of the porosity of natural thermally mature source-rocks. However, the contribution of the variations of the residual OM structure on the variations documented here during thermal maturation remains unclear. Further investigations on the isolated residual OM after thermal maturation are now required to better understand the origin of these processes. This is the aim of the next chapter.

Chapter 6: Influence of thermal maturation on the structure of the isolated OM of organic-rich mudstones

6. Influence of thermal maturation on the structure of the isolated OM of organic-rich mudstones

The work presented in this chapter will be submitted soon in Marine and Petroleum Geology.

Abstract

This chapter aims to better understand the role of the evolution of the kerogen structure on the OM porosity of organic-rich shales with increasing thermal maturation. To this end, the residual kerogen of KCF mudstones was isolated by acidic treatment after laboratory thermal maturation. The evolution of the composition, the chemical structure and the porosity of kerogen from the immature stage (Rc=0.48%) to the dry gas zone (Rc=2.57%) were documented using a combination of elemental analysis, SEM, TEM imaging techniques, Raman spectroscopy and SAXS. The results show that the progressive densification, reorganization and aromatization of the amorphous kerogen particles into a more ordered but heterogeneous carbon-rich residue is responsible for significant variations in the kerogen porosity with increasing maturity. Contrary to our previous observations on KCF mudstones, the variations that occur during the peak of oil generation (Rc≈0.88%) mark the onset of the OM-hosted pore development. There appears to be a natural close relationship between the evolution of kerogen porosity and KCF rock total pore volume during gas generation, as a similar alternation of pore collapse and pore development is observed in response to gas generation, indicating that the development and evolution of pores in these organic-rich shales is mainly driven by the evolution of the chemical structure and the composition of the OM during thermal maturation. In the dry gas zone, the porosity and the specific surface area of the kerogen are significant (19% and 57.1 $m^2.g^{-2}$ respectively). This highlights the importance of the organic phase in shale reservoir porosity and gas storage capacities, increasingly discussed in the available literature in recent years.

Introduction

Our previous investigations on artificially matured KCF mudstones suggested that the OM and especially its initial composition may strongly influence the quantity and composition of oil and gas generated as well as the evolution of porosity with increasing thermal maturity. The complex physico-chemical processes that occur during the thermal cracking of kerogen with burial lead to the progressive depletion in heteroatom-rich organic materials by the release of hydrogenated and oxygenated and other heteroatom-rich chemical groups in the form of liquid and gaseous hydrocarbons and CO_2, H_2S or N_2 (Tissot and Welte, 1984; Behar and Vandenbroucke, 1987; Peters et al., 2007). During these phenomena, previous TEM studies have demonstrated that kerogen becomes enriched in nm-size graphene-like polyaromatic layers which tend to pile up into increasingly well-ordered and larger basic structural units during thermal maturation (Boulmier et al., 1982; Oberlin, 1989; Rouzaud and Oberlin, 1989). The reorientation of these randomly distributed basic structural units into parallel structures in kerogen can result in the formation of a nano-scale porosity. (Romero-Sarmiento et al., 2014) proposed that the disorientation of the polyaromatic layers of kerogen at the nanoscopic scale and the ensuing generation of nanopores are responsible for most of the pore development in gas-mature organic-rich shales such as the Barnett Shales. Alternatively, the Raman spectroscopy and SEM investigations by Keel (2015) in the Ordovician Vila Group, the Cretaceous Niobrara Formation and the Silurian 'hot shales' suggest that the formation of pores in type II and III OM is mainly due to the creation of void spaces formed by the release of volatiles which surround 'aromatic islands'. This leads him to argue that the formation of these aromatic units is tied to the restructuring of kerogen macromolecules and the increase in aromaticity during thermal maturation. These processes may be largely involved in the development of KCF organic-rich shales porosity previously observed. In order to better investigate the role of the evolution of the chemical structure of the kerogen on the development of the porosity of KCF mudstones previously observed during thermal maturation, the OM of sample E19, which has the most representative/intermediate OM composition of the Marton and Ebberston well series (≈4.4 wt.% of orange AOM, and ≈3.5 wt.% of brown AOM), was isolated by acidic treatment after anhydrous thermal maturation. The evolution of the porosity, the chemical structure and composition of the OM with increasing thermal maturity was then assessed from the microscopic to the nanoscopic scale by the combination of elemental analyses, SEM, TEM imaging techniques, Raman spectroscopy and SAXS.

6.1. Results

6.1.1. Elemental composition and Raman spectroscopy

The elemental composition of the isolated residual OM of KCF samples before and after thermal maturation is presented in Tab. 6.1. The oxygen content was graphically determined from analyzed H/C and the mean Rc using the Van Krevelen diagram (Fig. 6.1). Hydrogen and Carbon are largely predominant but small amounts (≤ 0.51) of sulfur and nitrogen are also present.

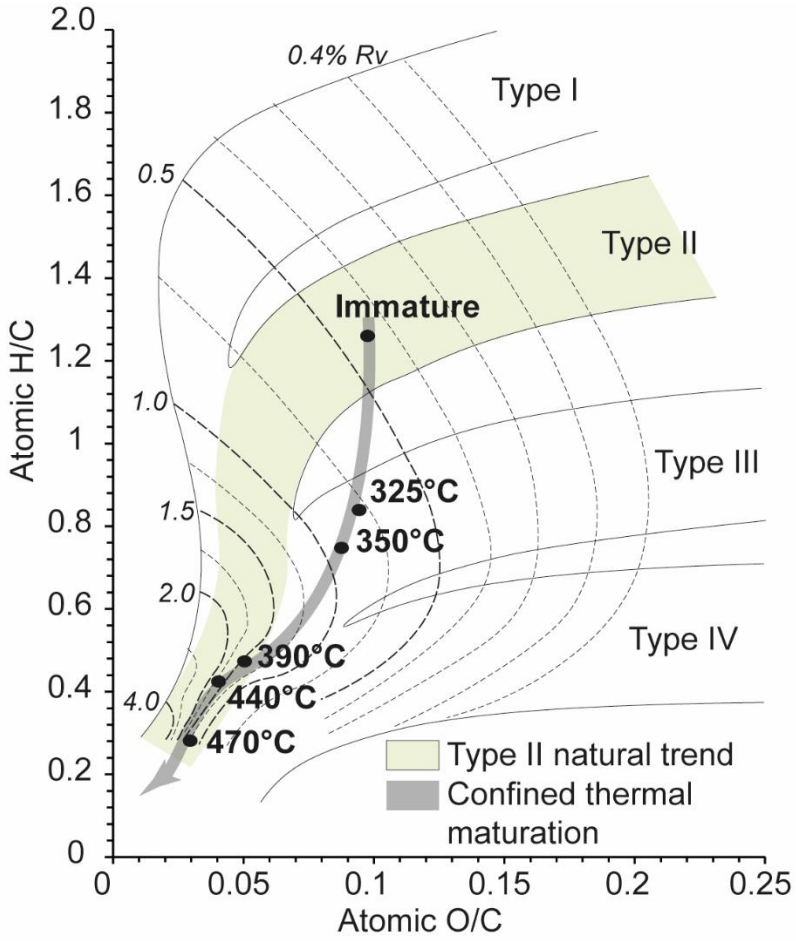

Fig. 6.1. Evolution of H/C and O/C atomic ratios with increasing maturation temperature.

The hydrogen and sulfur contents exhibit a strong decrease with the increase in thermal maturation temperature while the number of carbon and nitrogen atoms remains relatively constant. The H/C atomic ratio exhibits a strong decrease from 1.26 (immature) to ~0.30 (gas generation stages) during maturation (Tab. 6.1, Fig. 6.1).

Tab. 6.1. Elemental composition (wt.%), H/C and O/C atomic ratios of KCF isolated OM before (raw) and after maturation at 325-470°C for 72 hours.

Sample	*T mat (°C)*	*Rc (%)*	*Standard dev.*	*N*	*C*	*H*	*S*	*O*	*H/C*	*O/C*
K17019	Raw	0.48	0.02	4.84	69.29	7.30	9.32	9.24	1.26	0.10
K17005	325°C	0.74	0.06	4.29	71.93	4.89	9.30	9.57	0.82	0.10
K18004	350°C	0.88	0.12	4.93	71.27	4.46	11.41	7.93	0.75	0.08
K17012	390°C	1.30	0.03	5.14	79.36	3.00	7.00	5.50	0.45	0.05
K18010	440°C	1.60	0.20	5.42	83.65	2.91	3.44	4.57	0.42	0.04
K17026	470°C	2.57	0.06	5.01	84.34	2.04	5.57	3.04	0.29	0.03

Fig. 6.2 shows the evolution of measured Raman spectra of residual OM isolated in KCF samples. All the samples exhibit clean first order Raman spectra which consist of the two main bands characteristic of kerogen, G (~1600 cm^{-1}) and D (~1350 cm^{-1}).

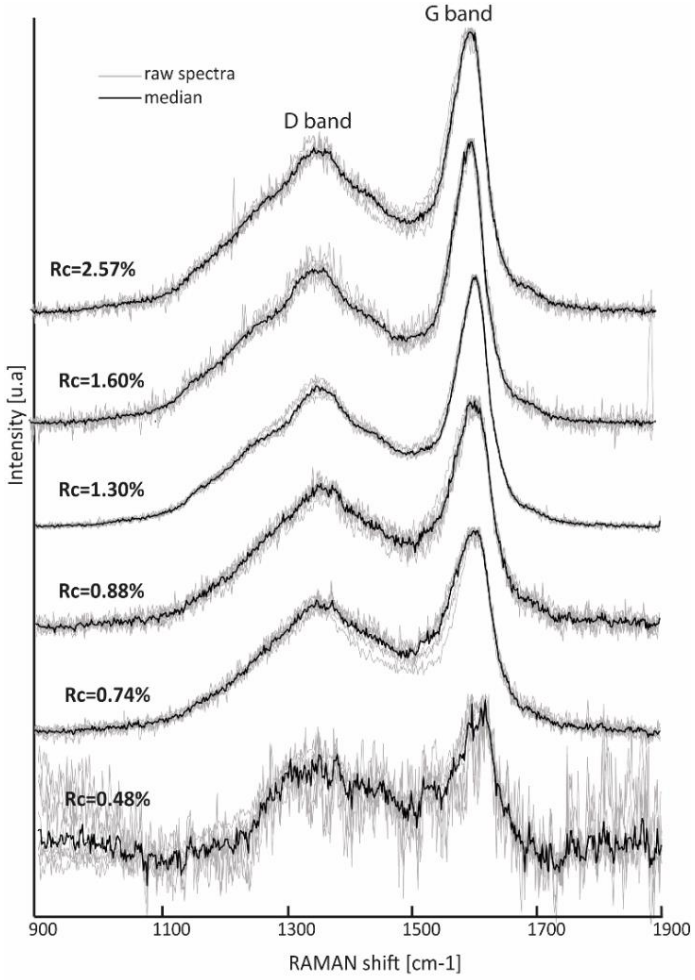

Fig. 6.2. Measured Raman spectra of KCF isolated OM at different thermal maturity and position of D and G bands. The spectra are offset for clarity. Light grey: superposition of the different raw spectra of each sample. Black: median spectrum.

The immature samples (raw) exhibit however a poorer signal-to-noise ratio. The G band, often called 'graphite band' is known to correspond to well-ordered graphite-like carbon structures and results more specifically from the longitudinal stretching vibration mode (E_{2G2} vibrational modes) of the C=C bond (sp^2 carbon) of well-structured aromatic rings with a D^4_{6h} symmetry (Tuinstra and Koenig, 1970). A D2 band is sometimes present as a shoulder on the G band, but it was often impossible to clearly separate the two components in our samples. G and D2 bands were thus considered as one broad band. The global D band (~1350 cm^{-1}) is generally assigned to discontinuities/ structural disorders of the kerogen sp^2 carbon network (Tuinstra and Koenig, 1970). Mernagh et al. (1984) and Beyssac et al.(2002) suggested that these defects result from specific in-plane vibrations of heteroatoms (H, O, N and S) or C=C groups present at the edge. According to the best fit (using only Lorentzian curves), the Raman spectra were deconvoluted into 6 peaks (Fig. 6.3).

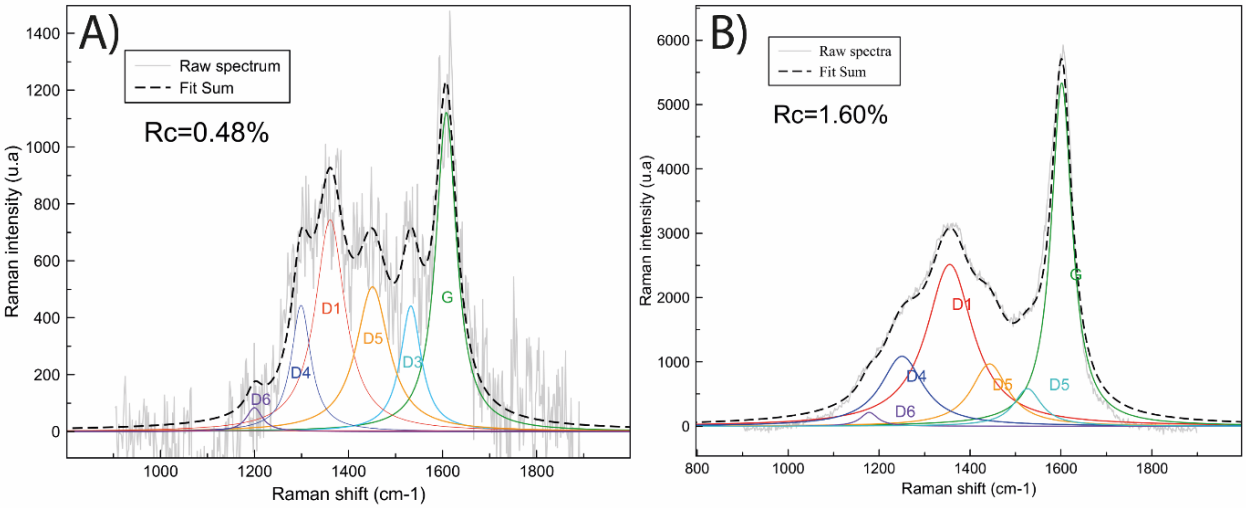

Fig. 6.3. Example of spectral deconvolution and identification of the main Raman bands in A) immature (Rc=0.48%) and B) gas-mature samples (Rc=1.60%). The deconvolution was carried out using Lorentzian curves.

The 'D band region' can be divided into a central D1 band (~1380 cm^{-1}) and three satellite bands: D4 (~1240 cm^{-1}), D5 (~1450 cm^{-1}) and D6 (~1185 cm^{-1}) commonly observed (Lin-Vien et al., 1991; Sadezky et al., 2005; Li et al., 2006) also in shale reservoirs (Liu et al., 2017). The 'G band region' can be divided into two bands: G (~1590 cm^{-1}) and D3 (~1540 cm^{-1}) which corresponds to the overlap between global G and D bands (Fig. 6.3). Each of these bands was assigned to the chemical functional groups summarized in Tab. 6.2 and referenced in Sadezky et al. (2005) and Li et al. (2006). During thermal maturation, the relative intensity of the raw G

band increases while the intensity of D bands decreases (Tab. 6.3). Consequently, D_{area}/G_{area} and D_{int}/G_{int} ratios decrease progressively (Fig. 6.4). A good correlation exists between the mean calculated vitrinite reflectance Rc previously determined using aromatic biomarker ratios, D_{area}/G_{area} (R^2=0.90) and D_{int}/G_{int} (R^2=0.94). The full width at half maximum (FWHM) of the G band decreases with increasing thermal maturity (R^2=0.95) while the FWHM of the D band increases (R^2=0.83).

Tab. 6.2. Summary of the position and the chemical functional groups correspondence of each Raman band. All the references can be found in Lin-Vien et al. (1991), Sadezky et al. (2005) and; Li et al. (2006).

Band name	*Mean band position (cm-1)*	*Description*
D6	~1185	C-C and C-H on aromatic rings; Caromatic-Calkyl in aromatic or aliphatic ethers.
D4	~1240	Para-aromatics; Aryl–alkyl ether.
D1	~1380	Amorphous carbon structures; methyl group; aromatic rings.
D5	~1450	Amorphous carbon structures; methyl or methylene, aromatic rings.
D3	~1540	Amorphous carbon structures; aromatics with 3-5 rings.
G	~1590	Alkene C=C; aromatic ring; ideal graphitic lattice.

Meanwhile, the raw D band positions are progressively shifted from ~1382 cm^{-1} to ~1349 cm^{-1} (Tab. 6.3). The G position decreases in the early oil generation stage from ~1607 cm^{-1} to ~1596 cm^{-1} and then re-increases progressively to ~1604 cm^{-1} from the early oil (Rc= 0.74%) to the dry gas zone (Rc=2.57%). Note however that the D and especially G positions exhibit a great variability within different organic particles of the same sample (Fig. 6.4). This variation of raw D and G positions results from a progressive increase in the Raman band separation (RBS) from 224 to 254 cm^{-1} (Tab. 6.3).

A good correlation is thus observed between the Rc and RBS (R^2=0.98, Fig. 6.4) and between the RBS of our artificially matured KCF samples and the data from Sauerer et al. (2017) obtained from natural organic-rich marine mudstones (Fig. 6.5A). The reference calibration curve from Sauerer et al. (2017) (in blue, Fig. 6.5A) was thus used to estimate the Raman vitrinite reflectance equivalence (Rr) from the RBS of KCF samples (Fig. 6.5B). The Rr values show a relatively high standard deviation due to the uncertainty of the G and D positions, even for the higher maturity stages (Fig. 6.4; Tab. 6.3). Rr and Rc give relatively comparable results (Fig. 6.5B). After thermal maturation from 325°C to 470°C for 72 hours, Rr increases from 0.86±0.17% to 2.34±0.44%.

Tab. 6.3. Median Raman parameters of KCF isolated kerogen including raw D and G band positions (Dpos and Gpos) and intensity (Dint and Gint), Dint/ Gint, Darea/ Garea, Raman band separation (RBS= Gpos-Dpos), Raman calculated vitrinite reflectance (Rr), G and D full width at half maximum (FWHM G and FWHM D).

Sample	D_{pos} *(cm^{-1})*	G_{pos} *(cm^{-1})*	*RBS (cm^{-1})*	Sd_{RBS}	D_{int}	G_{int}	D_{int}/G_{int}	D_{area}/G_{area}	*Rr * (%)*	Sd_{Rr}	*FWHM G (cm-1)*	*FWHM D (cm-1)*
K16026	1382	1607	224.2	3.8	619	736	0.86	2.22	0.50	0.09	38.54	86.87
K17005	1361	1596	234.7	3.6	1395	2049	0.68	1.95	0.86	0.17	35.69	99.23
K18004	1360	1596	237.6	2.7	1399	2049	0.68	1.81	1.00	0.14	33.48	101.56
K17012	1353	1599	245.4	1.3	1918	3384	0.57	1.86	1.50	0.10	26.76	107.28
K18010	1355	1604	248.1	2.4	1330	2441	0.55	1.55	1.80	0.23	27.31	106.58
K17026	1349	1604	253.9	3.8	1135	2237	0.48	1.46	2.34	0.44	23.89	107.78

**Rr: calculated using the RBS parameter from the data of Sauerer et al. (2017): Rr= 4.10^{-6}.exp(0.0523*RBS).*

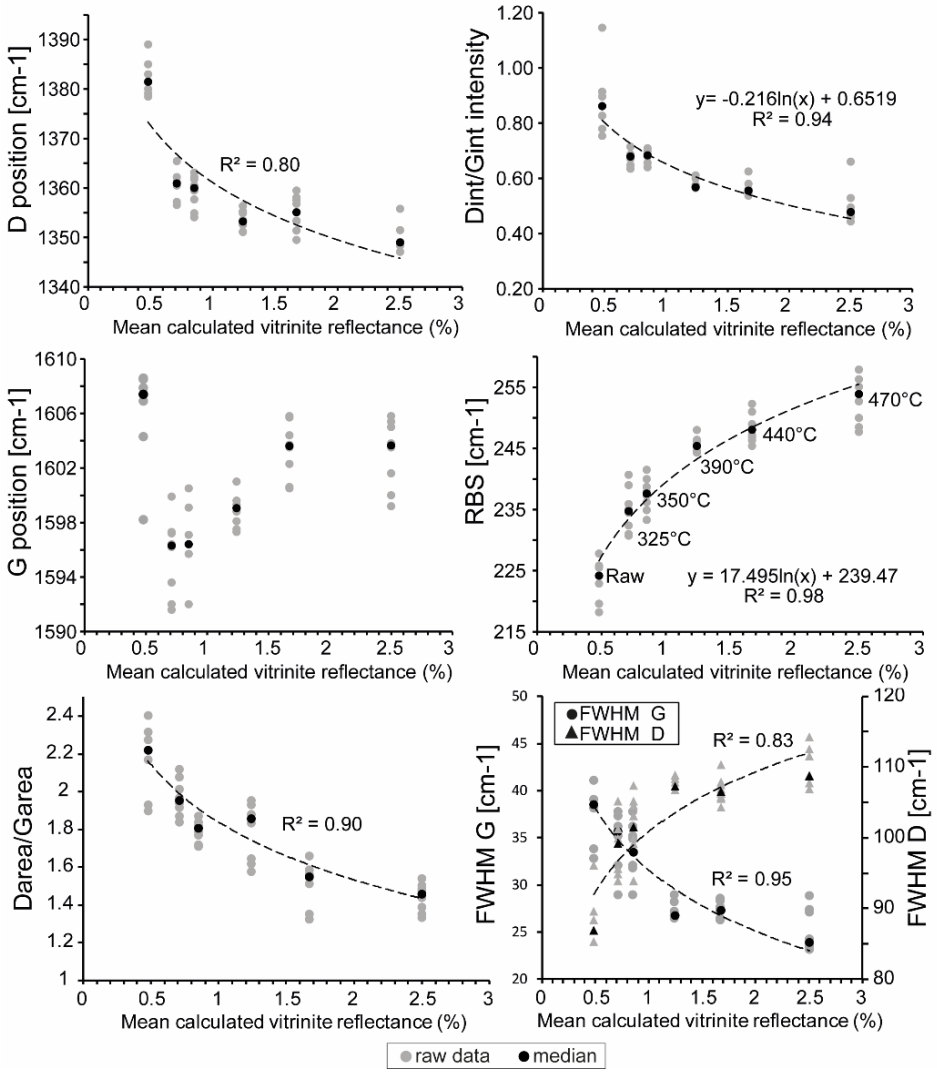

Fig. 6.4. Evolution of the raw D and G band positions, Raman band separation (RBS= G position – D position), Darea/Garea, Dint/Gint and G and D full width at half maximum (FWHM G, FWHM D) of isolated KCF residual OM as a function of maturity.

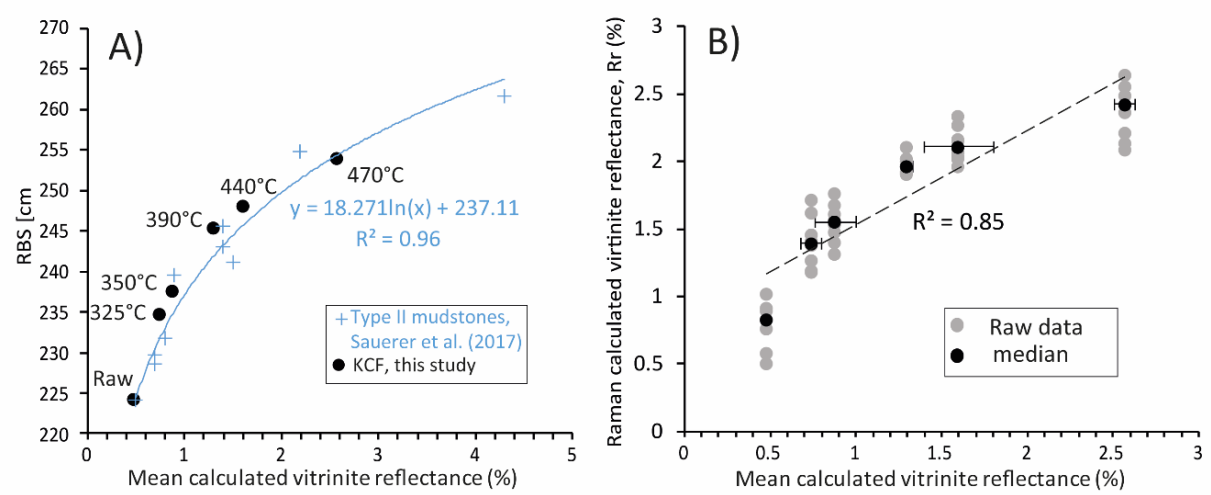

Fig. 6.5. A) Correlation between Rc and Raman band separation (RBS). The reference calibration curve was constructed using Raman data from natural organic-rich marine shales (Sauerer et al., 2017) and used to estimate the Raman vitrinite reflectance equivalence (Rr) from the RBS of artificially matured KCF isolated OM. B) Relationship between Rc and mean Rr.

6.1.2. SEM and TEM residual OM texture observations

In SEM images (SE), OM appears initially as AOM particles (Fig. 6.6A, B). These components exhibit no distinct shape or structure and have a perfectly homogeneous texture. Some of these particles present distinct edges and are closely associated with pyrite framboids (Fig. 6.7E) or contain inclusions of isolated pyrite grains (Fig. 6.6A). The other part of the amorphous OM appears as an agglomeration of various AOM particles without any distinct edges or shapes (Fig. 6.6B) probably stacked together after the dissolution of the mineral matrix by the acidic treatment. This AOM is accompanied by various structured components including scarce lignaceous debris (Fig. 6.7B) and various fragments of plant tissues (Fig. 6.7A). These particles (inertinite) of various sizes contain sharp edges and distinct arcuate shapes inherited from biological structures (Fig. 6.7B). The surface texture of these particles is perfectly homogenous at the micrometric scale (Fig. 6.7A). Lignaceous fragments contain however large macropores inherited from biological cell structure. The inertinite fragments exhibit no variation of texture at the micrometric scale during maturation. Their arcuate shapes and biological structure are still visible during dry gas generation and their surface texture still appears homogeneous (Fig. 6.7C, D). Contrary to inertinite fragments, the texture of the AOM shows significant changes with increasing thermal maturity (Fig. 6.6C-E).

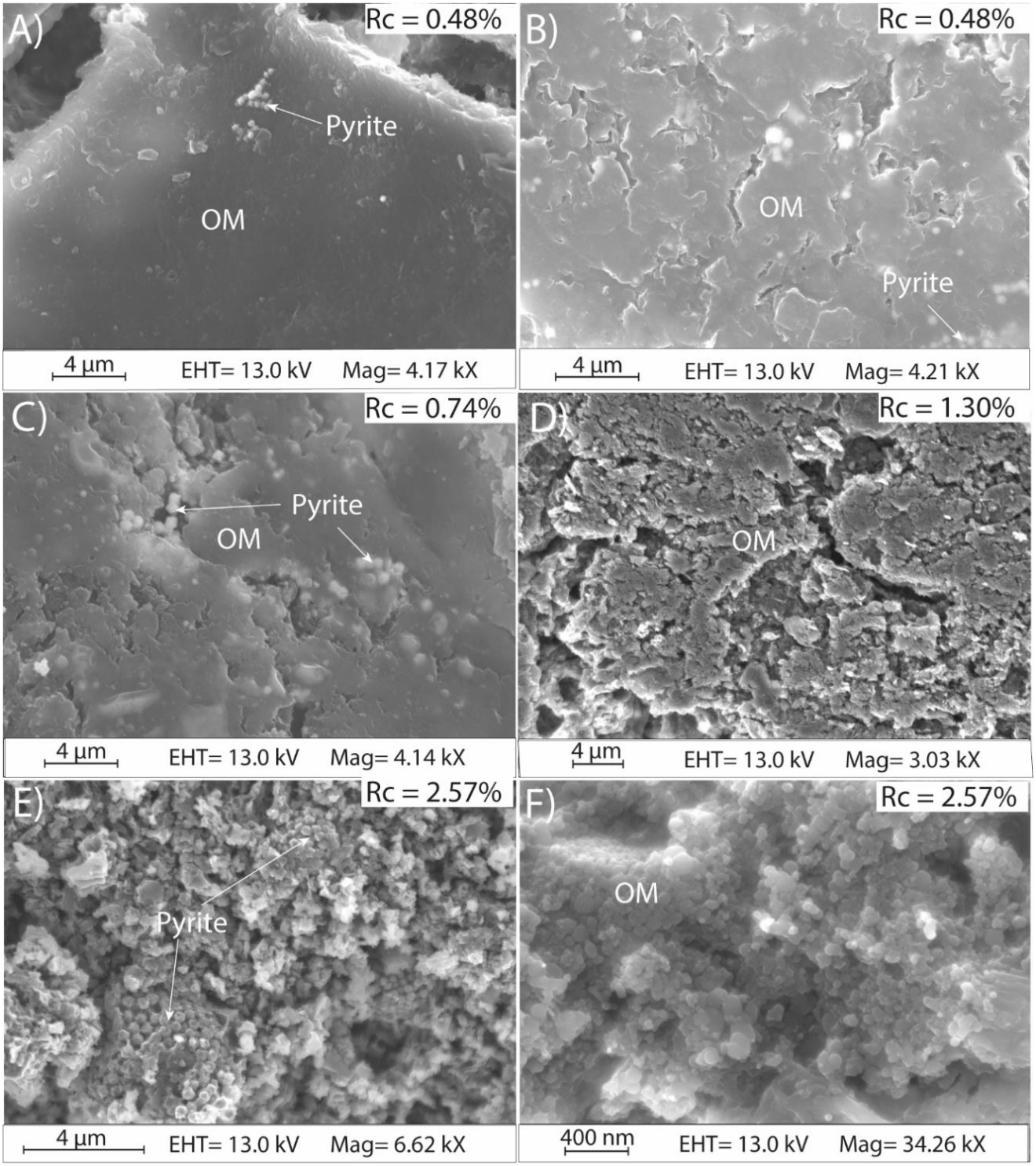

Fig. 6.6. A-D) SEM images (SE) showing the evolution of the texture of the isolated OM of KCF samples with increasing thermal maturity. A) Relatively massive amorphous particle with sharp edges. The large geometric pores are the imprint of minerals dissolved during acidic treatment. B) Agglomeration of various amorphous particles without distinct edges and shapes but with a homogeneous surface texture. C-E) Agglomeration of various amorphous particles showing an increasingly heterogeneous and granular texture. F) Zoom on the granular organic matter of gas-mature samples.

In the early oil generation stages (Rc= 0.74%, 325°C/72 hours), no real changes in the surface texture of OM are observed. The AOM still mainly exhibits a perfectly homogeneous microtexture. Locally, some amorphous OM aggregates present nevertheless a granular aspect, not observed in the immature sample (Fig. 6.6C). In the condensate wet gas zone (Rc= 1.30%, 390°C/72h), most of the AOM exhibits an irregular and granular surface texture at the micrometric scale (Fig. 6.6D). Some rare AOM particles still exhibit a relatively homogenous texture but the granular texture is predominant. In the dry gas zone (Rc =2.57%, 470°C/72h), the OM surface texture is highly heterogeneous (Fig. 6.6E). OM occurs mainly as an agglomeration of small spherical OM grains, less than 100 nm in diameter, stacked together and mixed with pyrite framboids and inertinite fragments (Fig. 6.6F). Pyrite framboids remain abundant in the dry gas zone and do not appear to be affected by thermal maturation (Fig. 6.7F).

In TEM observations different organic structures are present. No real differences are observed between the immature stage and the early oil generation stage (Fig. 6.8). Before thermal maturation (Rc= 0.48%), the OM is mainly composed of a diffuse OM material (light grey) which contains abundant imprints of minerals (white) dissolved by the acidic treatment (mainly Quartz, Carbonates and clay) (Fig. 6.8A, B). These areas also appear to contain different thin elongated particles (orange arrows, Fig. 6.8B) whose edges are often difficult to identify. In these areas, the OM exhibits a perfectly amorphous structure at the nanoscopic scale (Fig. 6.8A, B). Various structured components including mainly lignaceous fragments and debris from plant tissues are observed (Ld, Fig. 6.8E, 6.9A, E). These particles are easily identifiable by their distinct structure and sharp edges. They often exhibit a ‘scaly’ or a ‘shredded’ heterogeneous texture (Fig. 6.8E, 6.9A, E) at the nanoscopic scale. The ‘scaly’ texture of these particles shows parallel scratches which are probably artefacts created by the diamond knife during the cutting of ultrathin sections. Some of these structured particles show elongated bacterial-like shapes and irregular surface texture (Fig. 6.8C, D) suggesting the possible presence of nanopores. These particles are however, relatively scarce. Locally, more massive amorphous OM particles are present and exhibit a perfect nanoscopically amorphous texture (Fig. 6.8F). Contrary to the diffuse AOM, these massive particles have relatively distinct edges.

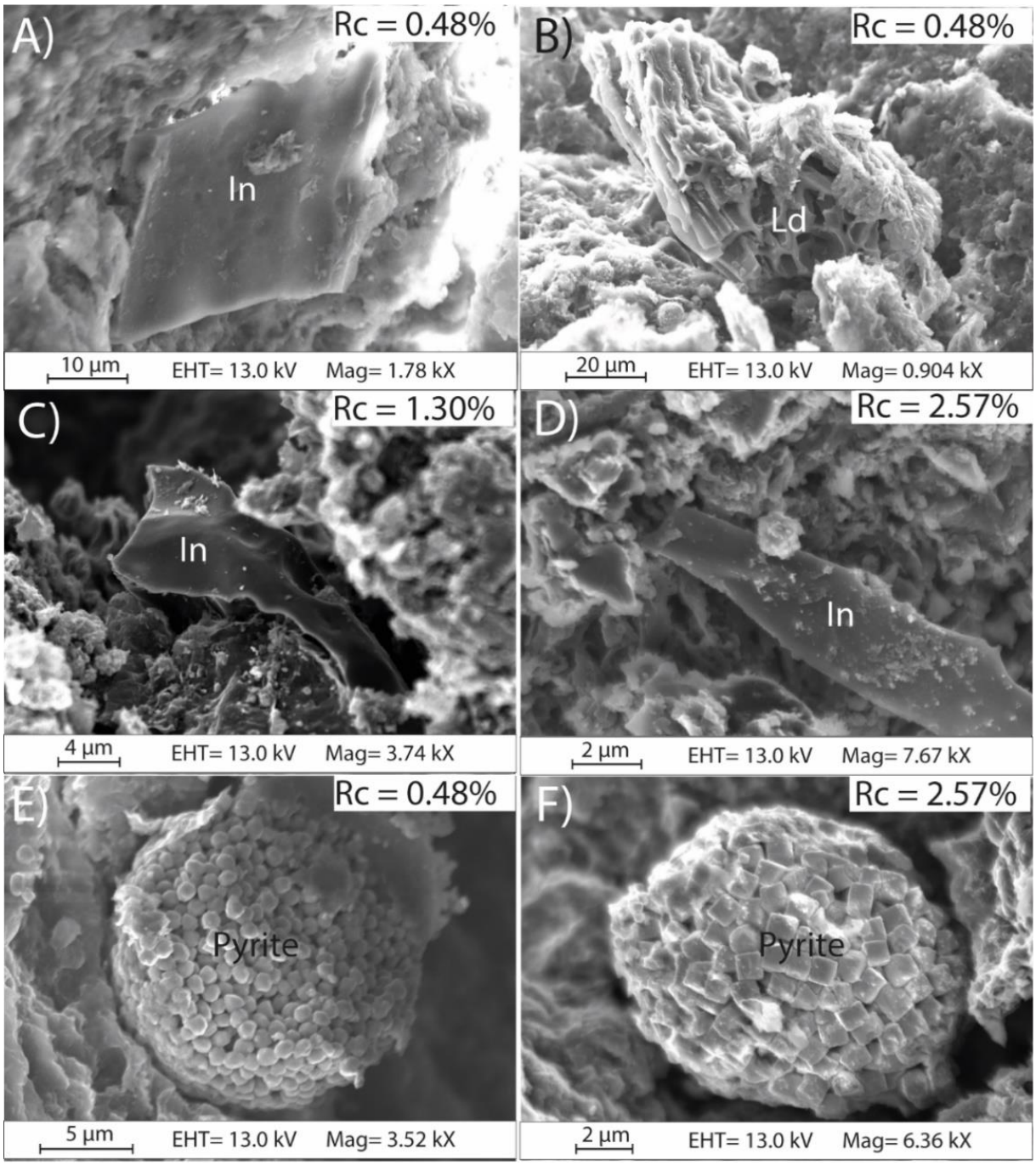

Fig. 6.7. A-D) SEM images (SE) of various inertinite fragments (In) and lignaceous debris (Ld) observed at different thermal maturity stages. E-F) Example of pyrite framboids observed for all maturity stages.

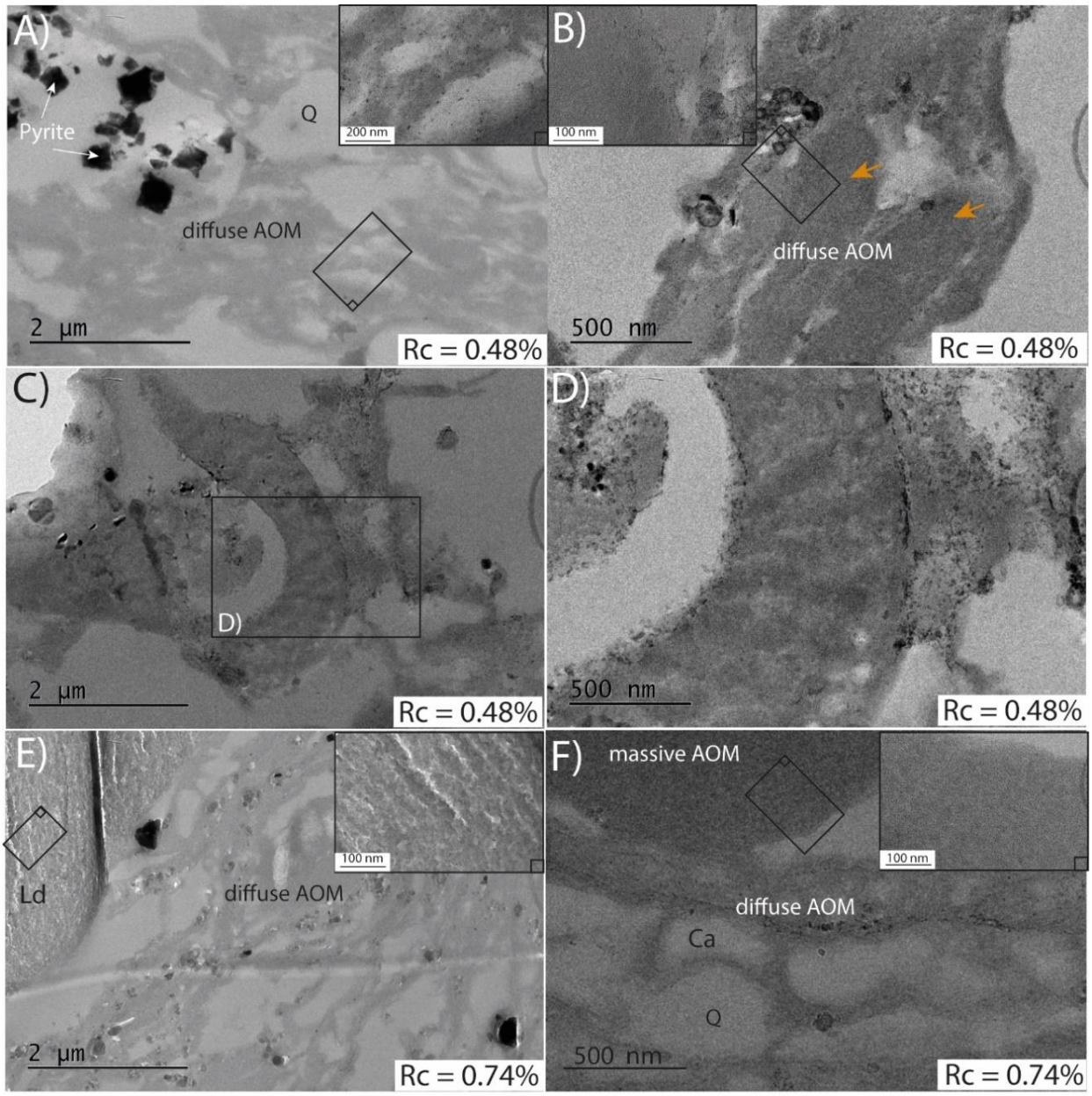

Fig. 6.8. TEM observation of various organic components of the isolated OM of low-mature KCF samples. A-B) Diffuse AOM between imprints of dissolved minerals (white) and isolated pyrite grains in immature kerogen. Orange arrows show different elongated amorphous particles in diffuse amorphous OM areas. C-D) Elongated bacterial-like structured components showing an irregular surface texture suggesting the possible presence of nanopores. E) Diffuse AOM with fragments of plant tissues (Ld). F). Diffuse AOM with massive AOM particles. The small black grains in the images are Osmium grains used to fix the OM. Rc: calculated vitrinite reflectance. The light grey areas are imprints of dissolved minerals (mainly Quartz (Q), carbonates (Ca), clays and albite).

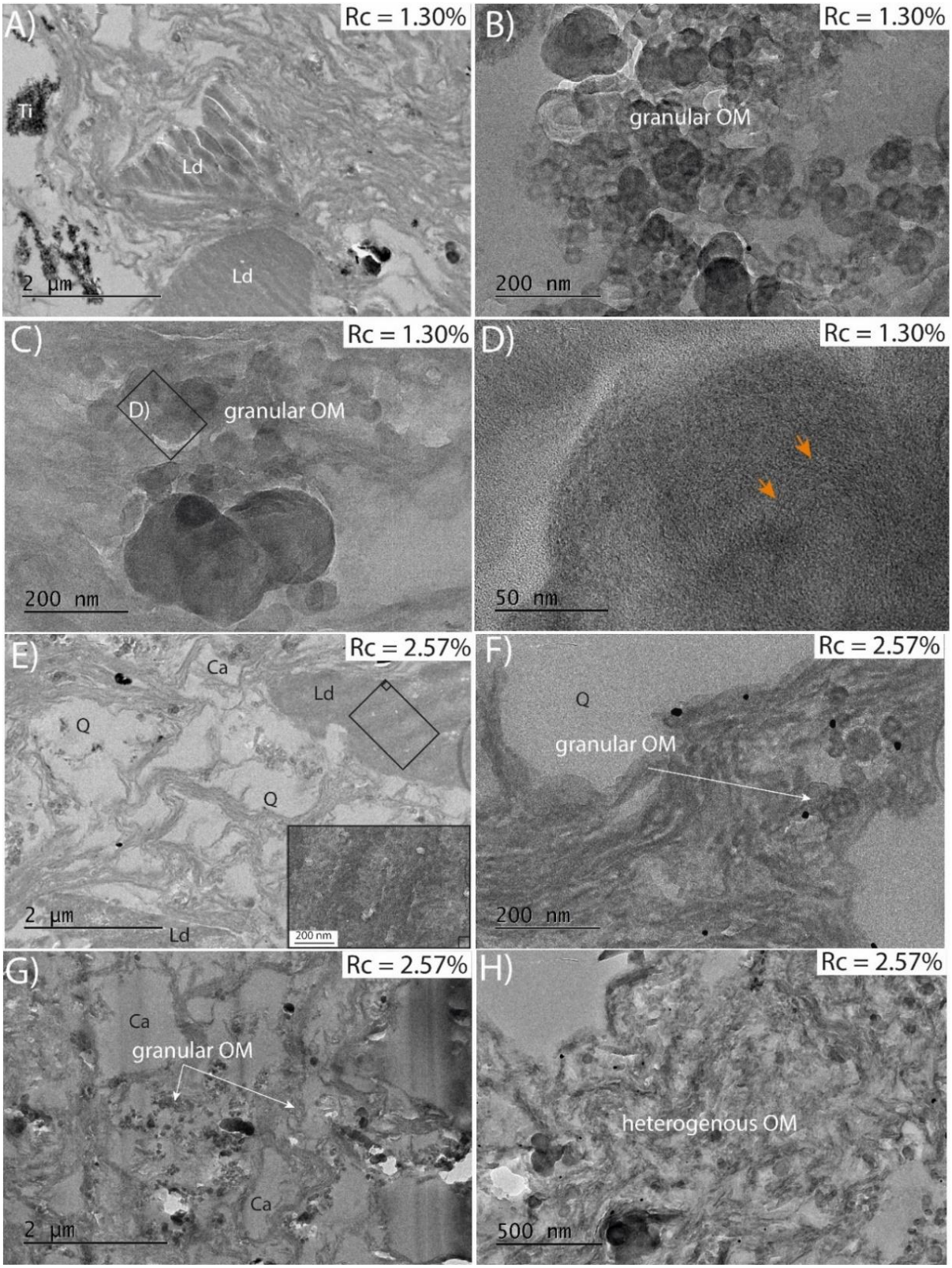

Fig. 6.9. TEM observations of organic components in isolated OM of thermally-mature KCF samples. Ld: lignaceous debris and various inertinite fragments. D) Granular OM particle showing local parallel orientation (orange arrows) of the basic structural units. The light grey areas are imprints of dissolved minerals (mainly Quartz (Q), carbonates (Ca), clays and albite).

After thermal maturation at 390°C (condensate wet gas zone, Rc= 1.24%) and 470°C (dry gas zone, Rc= 2.50%) for 72 hours, no variation in the texture of the plant tissues is visible at the nanoscopic scale (Fig. 6.9A, E). However, differences are observed for the diffuse and the massive amorphous OM (Fig. 6.9). In the condensate wet gas zone, the OM appears locally as an agglomeration of small grains of OM whose size varies from 20 to 200 nm in diameter (Fig. 6.9B, C). These granular areas are however still separated by relatively homogeneous diffuse particles (Fig. 6.9C). Locally, parallel orientations (orange arrows) of the basic structural units are observable in these OM grains (Fig. 6.9D). In the dry gas zone, these granular areas become more abundant (Fig. 6.9E, G) and all the OM particles exhibit a heterogeneous texture even at the nanoscopic scale (Fig. 6.9F, H).

6.1.3. SAXS measurements

Fig. 6.10 shows SAXS profiles of the scattering intensity of the isolated OM of KCF samples at different thermal maturities. Note that assuming a system composed of two homogeneous pore-matter phases, pore-OM in our case, the scattering intensity at the investigated scale varies in q^{-4} (Porod law) leading to a slope = -4 in a log-log scale system.

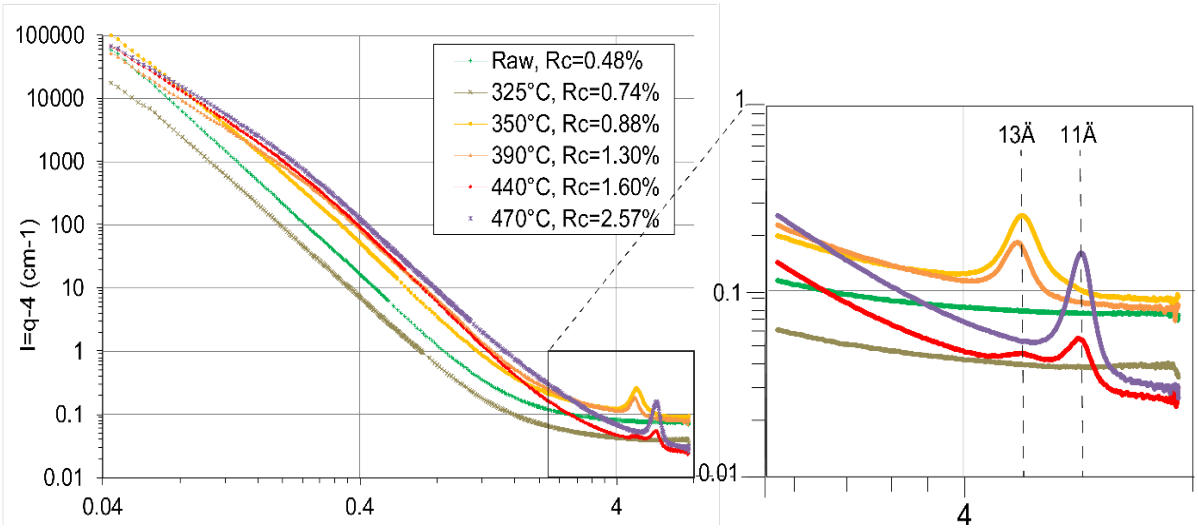

Fig. 6.10. SAXS profiles of isolated OM before and after thermal maturation at 325C to 470°C for 72 hours.

For our samples, the slope ranges between -3.7 to -3.8 due to the chemical heterogeneity of the OM (Tab.6.10). SAXS profiles reveal electronic fluctuations. For $q<2$ nm^{-1} ($d_{bragg} > 4$ nm), the measured scattering intensity depends on the porosity but also on the variations in the electronic density which can occur in pores or OM due to the filling of pores by fluids, or chemical heterogeneity of the OM during thermal maturation. Variations in the shape of SAXS

profiles are attributed to the change in the distribution of the pore phase in size and/or in quantity, whereas a change in the intensity of these curves without changes of shape indicates a variation in the electronic contrast between OM and pores. Firstly, after maturation at 325°C for 72 hours, a global decrease in the scattering intensity is observed without any changes in the shape of the curves (Fig. 6.10). This indicates a decrease in the global electronic contrast of the pore phase, probably filled by fluids. Above 325°C, the scattering power Q increases with increasing thermal maturation temperature (Tab.6.4). This is accompanied by a change in the shape of the scattering intensity curves (Fig. 6.10). This phenomenon suggests both an increase in the electronic contrast due to the progressive structuration and organization of the OM in response to thermal maturation and the development of pores in volume and size (open or not). Note that scattering intensities continue to rise with decreasing q instead of reaching a constant value, suggesting that the size of one of the homogeneous phases exceeds the lowest q-range of our measurements (Fig. 6.10).

Tab. 6.4. Main SAXS parameters of KCF isolated OM including the scattering power Q, the matrix density $\rho_{m\ (pores}$ excluded), the contrast term $\Delta\rho^2 = (\rho_m-\rho_{pores})^2$, the porosity P, the surface area S_{area}. The mean pore chord ld represents the mean pore diameter (nm).

Sample	*K16026*	*K17005*	*K18004*	*K17012*	*K18010*	*K17026*
T mat (°C)	Immature/Raw	325	350	390	440	470
Q ($nm^{-3}.cm^{-1}$)	6.79	2.51	16.9	18.4	21.8	27.1
ρ_m ($g.cm^{-3}$)	0.65	0.79	0.84	1.06	1.14	1.10
$\Delta\rho^2$	3.86	4.83	5.37	8.32	9.48	8.94
P	0.10	0.03	0.20	0.13	0.13	0.19
P(1-P)	8.91E-02	2.63E-02	1.59E-01	1.12E-01	1.16E-01	1.53E-01
Sv ($m^2.g^{-1}$)	16	5.34	37.6	46.5	39.7	57.1
ld (nm)	24.8	20.3	21.2	11.1	13.2	13.3

For q > 7.5 nm^{-1}, modulations are observable in SAXS profiles from 350°C to 470°C around d= 1.3 nm and 1.1 nm (Fig. 6.10). The modulations at 1.3 nm are present after maturation at 350°C, 390°C and 440°C for 72 hours. From 440°C this modulation is however less intense and disappears totally after heating at 470°C while the intensity of the modulation at 1.1 nm rises in intensity. The position of these reflections could be attributed to a dehydration of clay minerals with increasing temperature, embayed in the OM and thus protected from acidic treatment. However, these phases are not present for the immature and low-mature samples (raw and 325°C, Fig. 6.10). This is surprising if we assume that the irradiated volume is

representative of the overall sample composition (including both OM and mineral), since we assume that all the studied samples exhibit similar mineralogy.

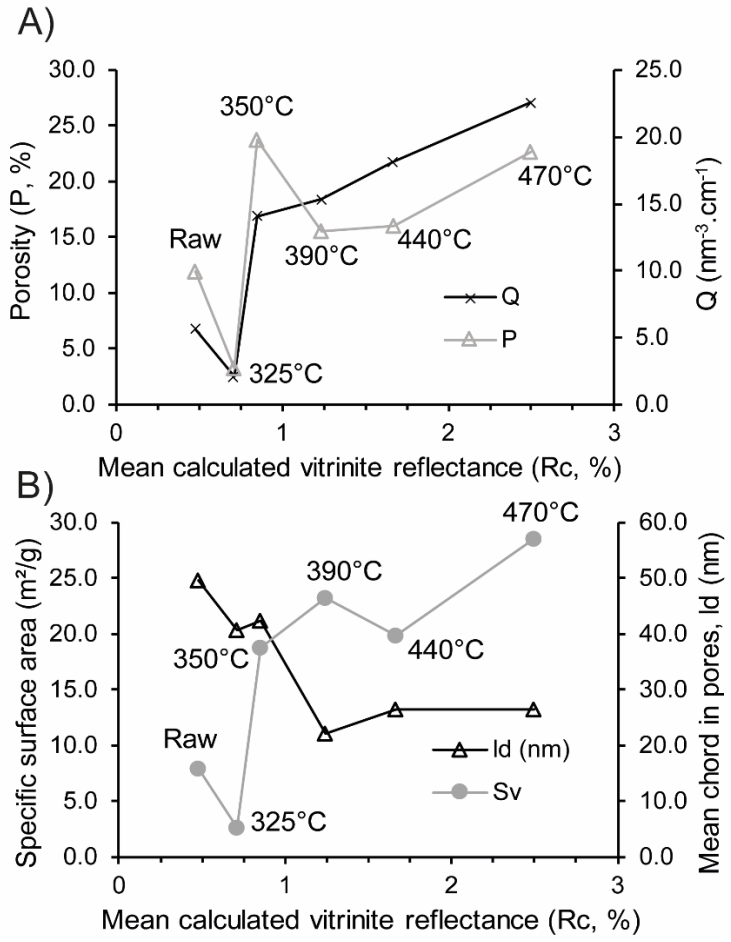

Fig. 6.11. Concomitant evolution of the scattering power Q, the porosity P, the specific surface area Sv and the mean pore chord length ld (mean pore size) of the isolated OM of KCF samples with increasing maturity.

These reflections may also be related to other mineral phases, not affected by acidic treatment, identified on the diffraction profiles at wide angle. Further investigations and especially replicates of these analyses are thus required to better understand these variations. The electronic contrast pore-OM ($\Delta\rho^2$), the porosity (P), the specific surface area (Sv) and the mean pore chord length (mean pore size) calculated after the scattering power of samples and the elemental composition are presented in Tab.6.4 (see chapter 3 for more details). According to SAXS profiles, the specific surface area, the porosity and the mean pore chord decrease after heating at 325°C for 72h, suggesting the loss of pore volume (Tab.6.4, Fig.6.11). The specific surface area and the porosity develop at the same time from 350°C to reach maximum values of about 57 m²/g and 20% respectively (Tab.6.4). The mean pore size decreases with increasing maturity to reach values ranging between 11.1 and 13.3 nm in diameter. Fluctuations in the

porosity, the specific surface area and the mean pore size are however observed after heating at 350°C to 470°C (Tab.6.4, Fig. 6.11) suggesting a non-linear increase in the OM porosity with increasing thermal maturity.

6.2. Discussion

6.2.1. Assessment of thermal maturity and OM structure evolution during thermal maturation using Raman spectroscopy

The first stage of thermal maturation is marked by the progressive breaking of some C-C bonds, leading to the elimination of functional groups, saturated cycles and chains. This results in the loss of the hydrogen-rich aliphatic carbon groups and N, S, O heteroatoms to yield bitumen, CO_2, N_2 and H_2S (Tissot and Welte, 1984; Tissot et al., 1987; Behar and Vandenbroucke, 1987; Peters et al., 2007). These processes leave behind a hydrogen-poor kerogen residue largely dominated by aromatic carbon structures and hydrogen-rich bitumen (Tissot and Welte, 1984; Tissot et al., 1987; Behar and Vandenbroucke, 1987; Peters et al., 2007). In higher thermal maturity stages, the secondary cracking of residual bitumen and kerogen leads to the progressive aromatization of the carbon-rich residue. In our samples, this is marked by the strong decrease in the H/C atomic ratio and H, N and S contents (Tab. 6.1, Fig. 6.1) and the increase in bitumen and CO_2 concentrations enriched in saturated and aromatic hydrocarbons. Raman spectroscopy provides useful information about the molecular vibrations of specific chemical bonds (Lin-Vien et al., 1991, p.; Beyssac et al., 2002; Sadezky et al., 2005; Li et al., 2006; Rebelo et al., 2016; Schito et al., 2017). Hence, each Raman band identified in our samples gives specific information (Tab. 6.2, Fig. 6.3). D1 is generally assigned to the vibration of methyl groups or to the breathing or aromatic rings in a relatively amorphous carbon structure (Lin-Vien et al., 1991). D3 results from the presence of polyaromatic components containing 3 to 5 rings in an amorphous carbon structure (Li et al., 2006) or polyacetylene-like structures (Rebelo et al., 2016; Schito et al., 2017). D4 is generally assigned to the presence of para-aromatics or aryl-alkyl ether (Lin-Vien et al., 1991). D5 results from the vibration of methylene and methyl groups or assigned to the breathing or aromatic rings (Lin-Vien et al., 1991). D3, D4 and D5 bands, sometimes called Gr, Dl and Dr respectively (Rebelo et al., 2016; Schito et al., 2017), are thus associated with the presence of low-size aromatic domains exhibiting structures analogous to those of polyaromatic hydrocarbons (Li et al., 2006; Rebelo et al., 2016; Schito et al., 2017). D6, sometimes called S (Rebelo et al., 2016; Schito et al., 2017) comes from the vibration of Caromatic-Calkyl, bonds, C-H bonds on aromatic rings,

aliphatic ethers or from long saturated and unsaturated alkane chains (Lin-Vien et al., 1991; Rebelo et al., 2016; Schito et al., 2017). Changes in these bands and Raman parameters thus clearly illustrate the progressive chemical variations in the kerogen chemical structure and composition that occur with increased maturity. Hence, in recent years, Raman spectroscopy parameters have become useful tools to quantitively assess the thermal maturity of various OM types (Beyssac et al., 2002; Quirico et al., 2005; Liu et al., 2013; Rebelo et al., 2016; Sauerer et al., 2017; Schito et al., 2017; Cheshire et al., 2017; Liu et al., 2017).

In this study, we indeed observed a good correlation between the Raman parameters investigated and the thermal maturity of KCF isolated OM (expressed as Rc, Fig. 6.5). According to previous work (Sauerer et al., 2017; Schito et al., 2017; Cheshire et al., 2017), RBS, G band FWHM, D_{int}/G_{int} and D_{area}/G_{area} are the Raman parameters that show the best correlation with maturity in the KCF (R^2>0.90, Fig. 6.4). In previous works (Li et al., 2006; Rebelo et al., 2016; Schito et al., 2017), the decrease in G band intensity and FWHM with increasing maturation temperature was considered to be mainly due to the progressive disappearance of the D3 band (often called Dl band) which marks the decrease of the polyacetylene-like structures and/or the small aromatic carbon rings (3-5 benzene rings) in amorphous carbon structures. The progressive decrease of D_{int}/G_{int} and D_{area}/G_{area} (Tab. 6.3, Fig. 6.4) is often attributed to the thinning of the G band in response to the clustering of the aromatic rings and the ensuing decrease in H, N, S and O heteroatoms leading to a concomitant decrease in D6, D4, D5, D3 and D1 bands (Tuinstra and Koenig, 1970; Ferrari and Robertson, 2000; Li et al., 2006). Meanwhile, the shift of the D position to a lower wavenumber and the ensuing progressive increase in the RBS (Fig. 6.4) are known to result from the progressive increase in the number of larger aromatic domains (Ferrari and Robertson, 2000). This substantiates the normal progressive aromatization of KCF OM and its transition from disordered to more ordered carbon materials with increasing maturation temperature as observed in natural sedimentary basins with increasing burial. As previously observed for many types of organic materials (Ferrari and Robertson, 2000; Quirico et al., 2005; Sauerer et al., 2017; Schito et al., 2017; Cheshire et al., 2017), the progressive increase in the RBS seems to be mainly driven by the shift of the D position while no clear variations are observed for the G band position (Fig. 6.4).

According to previous studies (Beyssac et al., 2002; Liu et al., 2013; Sauerer et al., 2017; Schito et al., 2017; Cheshire et al., 2017), the RBS appears to be a good parameter to estimate the equivalent vitrinite reflectance of OM with Rm ranging between 0.5 and 4.0%. A good

correlation exists between the RBS of our artificially-matured samples and that of the organic-rich marine shales from Sauerer et al. (2017) (Fig. 6.5A). Hence, the correlation of Sauerer et al. (2017) between Rm and RBS was used to estimate the mean Raman vitrinite reflectance (Rr) of KCF OM with increasing maturation temperature. The Rr and the Rc estimated using dibenzothiophene and phenanthrene ratios from bitumen give comparable values (Fig. 6.5B), which substantiates the punctual vitrinite reflectance values measured on total rocks. However, the error attached to these Rr values, generally greater than the Rc standard deviations, is significant and does not allow a precise estimation of thermal maturity (Fig. 6.5B). This variability, also visible for all the Raman parameters investigated (Fig. 6.4), may be due to internal variations in the KCF kerogen chemical structure and composition, which is initially composed of various particles of different origins and chemical compositions. Although the thermal cracking of kerogen and its aromatization during thermal maturation progressively blurs the difference of chemical composition between kerogen particles, this variability remains relatively high during thermal maturity stages. These results suggest that thermal maturity from Raman spectroscopy should be used with caution or in association with other maturity indicators for a precise estimation of vitrinite reflectance.

6.2.2. Concomitant evolution of the texture, the structure and porosity of KCF isolated OM with increasing thermal maturity

6.2.2.1. Initial OM texture from the microscopic to the nanoscopic scale

As previously observed in the bulk rock polished sections, SEM and TEM imaging on isolated OM shows that the OM is mainly composed of non-porous amorphous particles (Fig. 6.6A, B, 6.8A-D). This is in accordance with previous SEM and TEM observations on immature KCF mudstones (Boussafir et al., 1995a, b). In SEM, the larger AOM particles which often contain pyrite inclusions and distinct edges (Fig. 6.6A) seems to correspond to the massive AOM particles observed in TEM (Fig. 6.8F). These particles show a similar association with pyrite, a similar size and well-defined boundaries. According to Boussafir et al. (1995a), these particles probably correspond to orange AOM, which is abundant in the studied sample (4.4 wt.%). The other part of the AOM is present as an agglomeration of different amorphous particles without distinct edges in SEM (Fig. 6.6B) which likely corresponds to the diffuse AOM observed between mineral imprints in TEM (Fig. 6.8A, B). Boussafir et al. (1995a), suggested that these particles are mainly composed of black AOM with a probable contribution of brown AOM. In view of the low black AOM content in these samples (0.4 wt.%) compared

to brown AOM (3.5 wt.%) and the abundance of these diffuse AOM particles in the studied sample, a strong contribution of brown AOM is very likely. Both diffuse and massive AOM exhibit a perfectly non-porous and homogeneous amorphous texture from the microscopic to the nanoscopic scale. Contrary to the observations of Fishman et al. (2012) in KCF mudstones, this confirms the total absence of contribution of these KCF kerogen amorphous particles to the total pore volume of KCF mudstones before thermal maturation. Although the various structured components observed in samples exhibit a perfectly homogeneous microscopic surface texture in SEM (Fig. 6.7A-D), some of these particles show a heterogeneous 'shredded' texture in TEM which may suggest the presence of primary nanopores (Fig. 6.8C-E, 6.9A). Furthermore, the presence of large macropores inherited from the original biological structure of the organic components is sometimes visible in some lignaceous debris (Fig. 6.7B). In contrast with previous SEM observations in bulk low-mature KCF mudstones, these results reveal the presence of a primary OM-hosted porosity and thus, a contribution of the OM to the pore volume even in immature and low thermal maturity stages. This probably explains the low porosity observed for kerogen before thermal maturation (P=10%, Tab. 6.4). This provides support for previous observations made in various immature to low-mature rocks (Ro: 0.35-0.-63 %) (Löhr et al., 2015; Reed, 2017) including the KCF (Katz and Arango, 2018) and clearly indicates that some specific structured organic compounds can contain primary OM-hosted pores inherited mainly from cellulose and woody fragments' biological structures. Nevertheless, these lignaceous debris are relatively scarce in the studied samples, their contribution to the total pore volume is probably negligible.

6.2.2.2. Evolution of the structure of OM during oil and gas generation

The oil generation stage (325-350°C/72h, Rc=0.74-0.88%) is marked by a strong decrease in the kerogen H/C and N, S, O content due to the breaking of some C-C bonds of kerogen and the release of hydrogen-rich bitumen (Tab. 6.1). These processes mark a progressive structuration and aromatization of kerogen illustrated by a significant increase in the RBS, a decrease in the D_{int}/G_{int} and D_{area}/G_{area} (Fig. 6.4) and a densification of the kerogen structure (increase in the kerogen matrix density ρ_m, Tab. 6.4). In the early oil generation stage (Rc =0.74%), these processes have no impact on the OM surface texture at the microscopic to the nanoscopic scale (Fig. 6.6C, 6.8E, F). In SEM and TEM, amorphous kerogen particles still appear perfectly non-porous and amorphous and no changes are observed for the structured components. This is well substantiated by SAXS measurements which reveal a densification of

kerogen without any pore development. On the contrary, the decrease in the scattering intensity, the scattering power Q, the porosity P and the surface area suggest a significant loss of pore volume (Tab. 6.4, Fig. 6.10, 6.11). This decrease in kerogen-hosted porosity coincides with the decrease in pore volume observed for total KCF rocks after heating at 325°C for 72 hours. According to SAXS profiles these porosity variations are mainly due to the decrease in the global electronic contrast of the pore phase. This may indicate the filling of part of the pore volume by bitumen still trapped in the closed porosity and thus not totally extracted by dichloromethane/methanol treatments. These results thus reveal that the strong decrease in pore volume in the early oil generation stage in KCF mudstones is not only due to the filling of the interparticle pores associated with minerals by retained bitumen but also due to a loss of the primary OM porosity.

While the peak oil generation (350°C/72 hours, Rc=0.88%) corresponds to the loss of almost all the primary porosity in total rocks, SAXS measurements show a strong increase in the kerogen porosity marked by the concomitant rise of Q and porosity (Tab. 6.4, Fig. 6.11). The specific surface area and the porosity increase strongly to 37.6 $m^2.g^{-1}$ and 20% respectively. The progressive densification and aromatization of the kerogen related to the massive bitumen generation at this maturity stage lead to a massive development of nanopores. The variations in both scattering intensity and curve shape in SAXS profiles show indeed the clear onset of the structuration of kerogen in two distinct phases: OM and pores from the peak of oil generation (350°C/72 hours, Fig. 6.10). The mean pore chord length indicates the presence of mesopores (≈ 20 nm in diameter) (Tab. 6.4) but the still rising intensity with decreasing q in SAXS profiles indicates that larger pores, that exceed the lowest q-range of our measurements, are also present (Fig. 6.10). These new results show that pores start to develop in KCF kerogen from the peak of oil generation, at Rc ≈ 0.88%, and not only during gas generation and expulsion. This substantiates previous observations which show the presence of pores in OM at vitrinite reflectances ranging from 0.80 to 0.90% (Loucks et al., 2009; Reed et al., 2012, 2014; Han et al., 2017) as well as the model of (Romero-Sarmiento et al., 2013) which suggests the formation of pores from the onset of oil generation. This porosity, probably poorly interconnected and partly filled by entrapped bitumen, does not appear to be accessible by nitrogen adsorption in KCF mudstones. Hence this porosity was not observed during our previous investigations. These new results thus highlight the importance of using complementary methods such as SAXS, a powerful non-destructive global technique, to assess variations of the kerogen structure during the thermal maturation of organic-rich shales.

Gas generation (Rc=1.30-2.57%) is characterized by a strong decrease in N, S, O content and H/C which seems to reach a stable value around ≈2.2 (Tab. 6.1, Fig. 6.1). This chemical transformation is accompanied by a progressive and stronger aromatization of kerogen to form a more stable structure shown by the significant decrease in Raman 'disordered' D band areas and intensities and the increase in the 'graphitic' G band resolution (Fig. 6.2, 6.4). At these maturity stages, OM appears thus as a carbon-rich residue whose structure is increasingly ordered. This concomitant evolution of chemical structure and composition results in significant changes of the AOM texture in TEM and SEM observations and strong variations of porosity. From the condensate wet gas to the dry gas zone, the amorphous particles exhibit a granular texture which appears highly heterogeneous down to the nanoscopic scale, suggesting the presence of small nanopores (Fig. 6.6D-F, 6.9B, C, F, H). At the higher maturity stage, OM appears to be mainly composed of an agglomeration of grains (Fig. 6.6E, F). TEM observations reveal however, the presence of isolated concentric OM grains 50 to 200 nm in diameter dispersed in a heterogeneous amorphous OM matrix (Fig. 6.9B, C). These concentric nanostructures were previously described in the Barnett shale (Romero-Sarmiento et al., 2014) and are known to be derived from the secondary cracking of the retained hydrocarbons (Alfè et al., 2009). These structures may thus correspond to pyrobitumen, often described as the main contributor to the porosity of organic-rich shales (Bernard et al., 2012b; Milliken et al., 2013; Hackley and Cardott, 2016; Hackley, 2017). Locally the structure of these particles seems tied to the reorientation and the stacking of some aromatic structural units with increasing thermal maturity, forming locally a succession of parallel layers (Fig. 6.9D). Note however, that the rest of the OM remains relatively disordered in TEM observations (Fig. 6.9). These variations in OM structure and the formation of these concentric nanostructures are likely responsible for the massive OM-hosted pore development previously observed in KCF mudstones during gas generation. These observations provide support for the hypotheses of Keel (2015) and Romero-Sarmiento et al. (2014). Keel (2015) suggested that the increase in aromaticity and the ensuing reorganization of kerogen macromolecules with increasing maturity resulted in the formation of aromatic 'islands' separated by void spaces formed in response to the expulsion of volatiles. Alternatively, Romero-Sarmiento et al. (2014) demonstrated that the reorientation and the stacking of some structural units in residual OM during gas generation are responsible for the formation of OM-hosted nanopores in the Barnett Shales. The changes in kerogen nanostructure that occur from the peak oil generation to the dry gas zone are indeed accompanied by significant variations in the porosity, the specific surface

area and the mean pore size. Pores are about 11-13 nm in diameter (Tab.6.4). This substantiates nitrogen adsorption measurements carried out on total rocks which show that pores are mainly mesoporous in KCF samples. The continuous increase in the kerogen density, Q, the still rising RBS and the relative decrease in the area and intensity of disordered Raman D bands (Fig. 6.4), the fluctuations of the porosity, the specific surface area and the mean pore chord indicate that the OM porosity is non-linear during gas generation (Tab. 6.4, Fig. 6.4, 6.11). This may indicate that collapse processes occur in OM in response to gas generation, leading to variations in the size and the volume of OM-hosted pores. Note that none of the structured components derived from plant tissues and pyrite framboids exhibit any variations of structure during maturation (Fig. 6.7A-C, 6.9) and probably make no contribution to the porosity variations observed at these high maturity stages in the KCF.

In accordance with the observations made previously on KCF mudstones, OM porosity exhibits strong variations in porosity during oil and gas generation, marked by phases of destruction and growth. The similarity between the evolution of the porosity of KCF mudstones and the OM isolated through thermal maturation clearly demonstrates that the evolution of the chemical structure and the composition of kerogen during thermal maturation is the main factor responsible for the development and the evolution of pores in these organic-rich mudstones. Furthermore, the high porosity of OM (up to ≈20%) indicates that OM is indeed a significant contributor to the porosity, and thus to the gas storage capacity of shale reservoirs. This is in agreement with recent work which showed the strong influence of OM on the porosity and gas adsorption of shale reservoirs (Mastalerz et al., 2013; Yang et al., 2016; Ju et al., 2019; Song et al., 2019). However, most of these pores are probably not sufficiently interconnected or closed, explaining why this porosity was not detected with gas adsorption measurements, hence the need to use complementary methods such as SAXS to assess it. In leading to a different original chemical OM structure and variations during thermal maturation (Tissot and Welte, 1984; Behar and Vandenbroucke, 1987), it seems thus clear that variations in the original kerogen composition between shale reservoirs or samples should impact the development of pores, the features of pores or the resulting pore network. This is especially true for these clay and organic-rich mudstones, where most of the interparticle pores associated with this relatively ductile mineral matrix are quickly reduced by compaction or filled by entrapped bitumen in the early stages of thermal maturation and where OM thus rapidly becomes the main contributor to the porosity.

Summary and conclusions

In this chapter, the concomitant evolution of the chemical structure and the porosity of the isolated OM of KCF mudstones during maturation were investigated using a combination of SEM and TEM imaging techniques, Raman spectroscopy and SAXS. The following conclusions were drawn.

(1) Raman parameters can be good indicators of thermal maturity and allow a relatively reliable estimation of vitrinite reflectance.

(2) Raman spectroscopy, SEM and TEM show that even though the structure of the most mature sample remains relatively disordered, the increase in thermal maturity results in significant densification, reorganization and aromatization of kerogen, predominant in the studied sample. These residual organic components evolved progressively from a perfectly amorphous structure in immature and low-mature samples ($Rc \leq 0.74\%$) to a granular carbon-rich residue, highly heterogeneous at the nanoscopic scale and containing abundant concentric OM grains (likely pyrobitumens) in gas-mature samples ($Rc \approx 2.57\%$). As thermal degradation proceeds, these variations are responsible for significant changes in the OM nanoporosity.

(3) Contrary to the observations previously made on KCF mudstones, the peak of oil generation ($Rc \approx 0.88\%$) marks the onset of the OM-hosted pore development.

(4) As previously observed for KCF bulk rocks, the porosity of OM shows a complex evolution during gas generation marked by an alternation of collapse processes and pore development.

(5) The similarities existing between the evolution of the KCF mudstones and the isolated OM porosity through thermal maturation clearly show that the development and evolution of pores and gas adsorption capacities of these organic-rich mudstones are mainly driven by the evolution of the chemical structure and the composition of the OM during maturation.

While these analyses provide a better understanding of the processes involved in the evolution of the porosity of organic-rich source rocks, the representativeness of our results obtained from our artificial maturation experiments and especially the influence of the duration-temperature pairs of thermal maturation processes on OM thermal degradation and porosity need now to be verified. This is the aim of the last result chapter.

Chapter 7: Does the duration of the confined thermal maturation experiments influence the evolution of the porosity of organic-rich source rocks?

7. Does the duration of the confined thermal maturation experiments influence the evolution of the porosity of organic-rich source rocks?

The work presented in this chapter will be submitted soon in the journal Fuel.

Abstract

To investigate the influence of the duration-temperature pairs chosen for our laboratory thermal maturation experiments on the evolution of the OM and the porosity of the organic-rich KCF source rocks with increasing maturity, long duration (104 days) gold-tube confined thermal maturation, bulk, molecular geochemical OM characterization (Rock Eval, GC-TCD, GC/MS) and nitrogen adsorption porosimetry measurements were applied on the same six type II KCF mudstones studied. These results were then compared with the shorter duration experiments (72 hours). The increase in the duration of thermal maturation experiments enhanced the degradation of heavy polar OM components into saturated and aromatic hydrocarbons, leading to the production of similar amounts of bitumen enriched in saturated and ARO. Then, in preventing the early breaking of low energy bonds, the lower temperature used for the longer duration experiment led to a less pronounced early cracking of OM resulting in a different timing of gas generation. This process did not influence the general evolution of the pore volume, which increased in the two series due to the formation of pores in OM during gas generation. Whatever the duration-temperature pair chosen for the maturation experiments, highly oil-prone phytoplanktonic-rich samples appeared to suffer greater porosity collapse leading to the formation of lower pore volumes during gas generation. Increasing the duration of thermal maturation seemed, nevertheless, to influence the amplitude and the timing of pore collapse events that occur during gas generation, leading to slightly different pore size distributions and pore volumes between short and long duration experiments. These differences remain limited, however, suggesting that results from different time-duration experiments can be easily compared.

Introduction

As demonstrated by our previous experimental work, the use of these laboratory thermal maturations could be a key method to obtain rocks of various stages of maturity from the same initial material. However, various duration-temperature pairs can be selected for these experiments. While the effects of laboratory thermal maturation conditions on OM thermal degradation processes have been well studied in the past (Michels et al., 1992; Landais et al., 1994; Michels et al., 1995; Behar et al., 2003), the effects on the evolution and the development of porosity have never been assessed. As OM thermal degradation processes are governed by the first order Arrhenius law, a plethora of many duration-temperature pairs should be able to be used to reach the same stage of maturity (Wood, 1988; Landais et al., 1994). However, previous studies show that the experimental temperature and duration of these laboratory simulations are not really exchangeable parameters (Landais et al., 1994), as increasing the thermal maturation duration and lowering the experimental temperatures could significantly influence the yield, the composition and the timing at which bitumen and gas are generated during OM thermal maturation. In view of the strong relation existing between organic-rich source rocks porosity, OM thermal degradation processes, and oil and gas generation, these differences may influence the formation and the development of pores with increasing maturity. It seemed interesting therefore to test how the differences observed between short- and long-duration experiments can influence the formation and the development of organic-rich source rocks porosity. This may not only help to assess whether artificial maturation can accurately simulate the porosity evolution of natural source rocks, but also to better understand the relationships between the porosity, the composition and the amount of bitumen and gas generated during maturation. To this end, long duration (104 days) gold-tube anhydrous confined thermal maturation experiments were carried out on the same immature organic-rich KCF mudstones. The concomitant evolutions of the bulk, molecular organic geochemistry and porosity during maturation were determined using Rock Eval® pyrolysis, GC-TCD, GC/MS and nitrogen adsorption measurements. The results were then compared with the shorter duration experiments (72 hours) previously carried out. The present study aimed particularly to better understand the relation between the duration-temperature pair of anhydrous confined thermal maturation, the initial bulk and molecular composition of kerogen and the ability of rocks to develop and preserve with increasing maturity. Finally, to test the usefulness of other gas adsorption models that are more rarely used for the assessment of mudstone porosity, other models were used.

7.1. Results

7.1.1. Evolution of bulk and molecular OM geochemical composition during 104 days of thermal maturation

7.1.1.1. Bulk OM composition

After thermal maturation from 282 to 390°C for 104 days, the Rock Eval parameters follow the same evolution trend as those observed after maturation from 325°C to 470°C for 72 hours (Tab. 7.1, Fig. 7.1). The RC/TOC increases progressively to ≈0.97 indicating the presence of residual OM without any remaining HC potential (Tab. 7.1) after maturation at 390°C for 104 days. The S1 and the PI increase strongly after heating at 283 and 338°C for 104 days, especially for samples that initially had very high TOC and orange AOM contents (Tab. 7.1). After heating for 104 days at 390°C, the S1 and the PI decrease. After thermal maturation at 283°C, the Tmax and the mean calculated vitrinite reflectance (Rc) reached ≈443°C and 0.69%±0.07 respectively, indicating that the early oil generation stage had been reached (Tab. 7.1, 7.2).

Tab. 7.1. Main Rock-Eval parameters of KCF samples after thermal maturation at 283°C, 338°C and 390°C for 104 days. A: brown AOM rich samples. B: orange AOM rich samples.

Sample no.	*Sample name*			*TOC (wt.%)*	*S1 (mg HC/g rock)*	*S2 (mg HC/g rock)*	*Tmax (°C)*	*HI (mg HC/g TOC)*	*OI (mgCO2/g TOC)*	*IP*	*RC/TOC*
K16015	B2	A	Immature	3.0	0.1	12.4	429	418	20	0.00	0.64
K17001	B23	A		5.6	0.2	30.6	432	549	12	0.01	0.53
K16019	B31	B		6.8	0.2	38.9	431	574	16	0.01	0.51
K16026	E19	A		10.3	0.2	57.4	428	557	14	0.00	0.53
K16031	E38	B		14.4	0.5	86.4	422	599	15	0.01	0.49
K16032	E40	B		15.4	0.6	95.3	425	617	16	0.01	0.47
K17036	B2	A	283°C/104d	3.0	0.2	9.8	444	327	9	0.02	0.71
K17037	B23	A		5.4	1.0	25.3	445	471	3	0.04	0.58
K17038	B31	B		6.8	1.4	33.9	444	501	4	0.04	0.55
K17039	E19	A		10.0	0.6	47.1	443	469	4	0.01	0.59
K17040	E38	B		14.8	2.3	77.9	441	525	3	0.03	0.54
K17041	E40	B		15.4	4.1	87.2	441	530	2	0.05	0.52
K18013	B2	A	338°C/104d	2.03	0.5	2.1	/	101	7	0.19	0.87
K18014	B23	A		2.22	1.1	4.9	/	220	2	0.19	0.68
K18015	B31	B		4.05	3.1	6.6	/	162	1	0.32	0.70
K18016	E19	A		4.02	6.0	7.6	/	190	1	0.44	0.50
K18017	E38	B		13.27	13.3	13.5	/	102	1	0.50	0.75
K18018	E40	B		13.18	14.6	12.7	/	96	0	0.54	0.75
K17029	B2	A	390°C/104d	2.35	0.1	0.2	/	9	7	0.27	0.99
K17030	B23	A		3.72	0.1	0.7	/	19	3	0.12	0.98
K17031	B31	B		3.93	0.2	0.9	/	23	4	0.16	0.98
K17033	E19	A		4.47	0.5	1.5	/	34	1	0.25	0.99
K17034	E38	B		5.44	0.7	2.5	/	46	1	0.22	0.95
K17035	E40	B		5.02	0.7	3.6	/	72	1	0.17	0.93

/: unquantifiable Tmax values due to too flat and low an S2 peak.

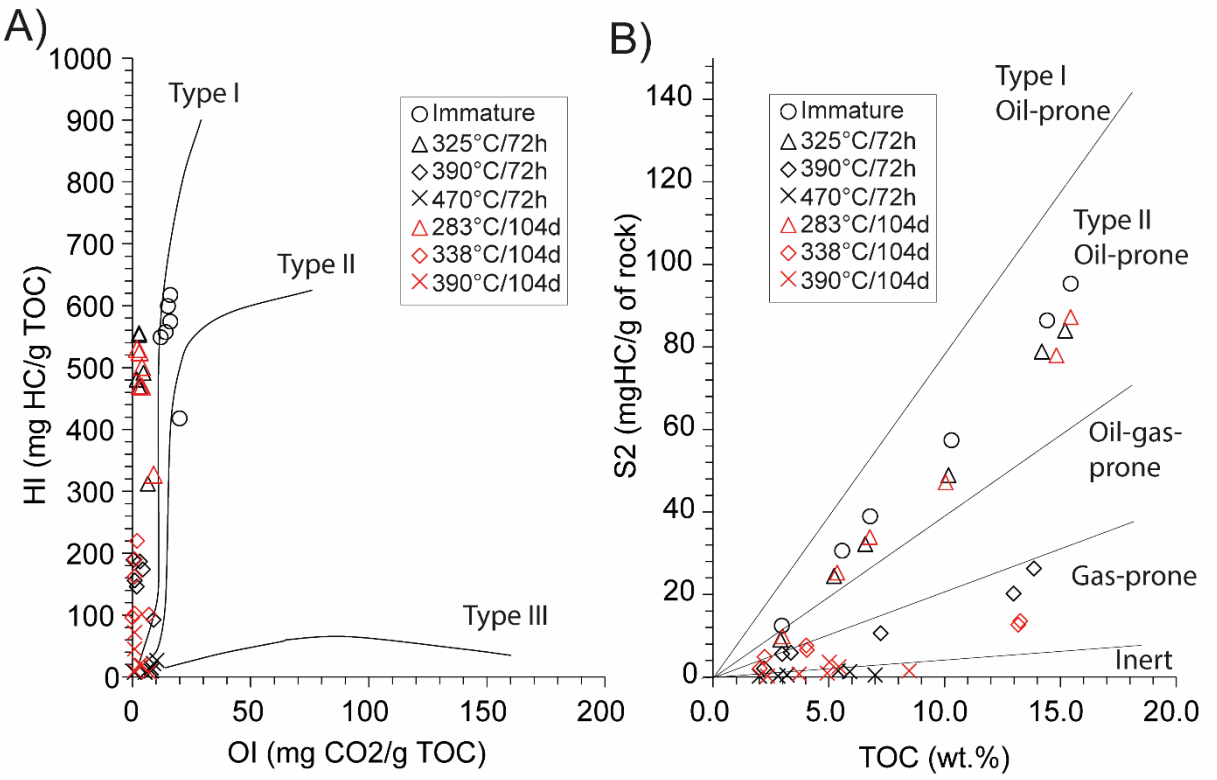

Fig. 7.1. A) Pseudo-Van Krevelen diagram of KCF samples and B) evolution of the S2 with increasing maturation temperatures. Comparison with the shorter experiments.

This stage of maturity is marked by the strong increase in bitumen, and especially of SAT and ARO hydrocarbon contents with only low concentrations of C_1-C_5 and CO_2 (Tab. 7.3, Fig. 7.2, 7.3). The S1 and the amount of SAT and ARO hydrocarbons increased linearly with the initial orange AOM content of samples ($R^2 \geq 0.82$, Tab. 7.3A). After heating for 104 days at 338 and 390°C S2 were two low and flat to allow a correct estimation of T_{max}. (Tab. 7.1) However, the increase in the mean Rc to 1.22% ±0.10 and 2.17% ±0.12 indicates that the condensate wet gas and the dry gas generation stages were reached after maturation at 338°C and 390°C respectively (Tab. 7.2). These two maturation stages are accompanied by a progressive and strong increase in CO_2 and C_1-C_5 hydrocarbon gas concentrations (Tab. 7.3, Fig. 7.2). C_2-C_5 are the main gases generated after heating at 338°C whereas C1 is mainly produced after heating at 390°C for 104 days (Tab. 7.3). The amount of C_1-C_5 and CO_2 produced during maturation depends on the initial phytoplanktonic orange AOM contents of samples. The concentration of C_1-C_5 increases with the orange AOM content ($R^2 \geq 0.71$) while the concentration of CO_2 decreases ($R^2 \geq 0.81$, Fig. 7.4B, C).

Tab. 7.2. Main biomarker ratios of aliphatic and aromatic fractions and calculated vitrinite reflectance (Rc) after maturation for 104 days.

Sample no.		Mean R_c[1] (%)	Stand Dev.	MAS(I)/ (I+II)[2]	TAS(I)/(I+II)[2]	TAS/ (TAS+MAS)[2]	20S/ (20S+R)[3]	22S/ (22S+R)[3]	αβ/(αβ+αα)[3]	Pr/n-C_{17}	Ph/n-C_{18}	Pr/Ph	CPI
K16015	Immature	0.47	0.03	2.9	2.2	57.1	0.12	0.34	0.25	3.01	1.48	1.14	1.73
K17001		0.45	0.04	4.7	4.6	64.1	0.17	0.42	0.32	3.38	1.47	1.07	1.4
K16019		0.50	0.07	2.7	4.2	32.9	0.18	0.47	0.28	1.7	2.16	0.72	1.42
K16026		0.48	0.02	2.6	3.9	58.3	0.19	0.4	0.29	2.88	2.06	0.6	1.71
K16031		0.48	0.02	2.1	11.2	15.7	0.1	0.39	0.31	1.78	2.29	0.9	1.52
K16032		0.51	0.04	6.0	18.6	16.3	0.14	0.35	0.35	2.24	2.56	0.73	1.98
Mean		**0.48**	**0.04**	**3.5**	**7.4**	**40.73**	**0.15**	**0.40**		**2.50**	**2.00**	**0.86**	**1.63**
K17002	283°C	un	un	13.6	24.1	89	0.29	0.50	0.51	1.02	0.63	1.07	1.19
K17003		0.70	0.07	11.7	un	100	0.35	0.51	0.42	1.25	0.85	1.03	1.15
K17004		0.71	0.09	12.6	un	100	0.29	0.53	0.37	0.75	0.98	1.42	1.08
K17005		0.72	0.10	7.3	un	100	0.27	0.49	0.38	0.82	0.52	1.08	1.12
K17007		0.67	0.06	6.9	26.6	91	0.36	0.48	0.42	0.65	0.6	1.37	1.16
K17008		0.66	0.03	8.6	un	100	0.42	0.51	0.41	0.74	1.02	1.53	1.32
Mean		**0.69**	**0.07**	**10.11**	**25.3**	**96.58**	**0.33**	**0.50**	**0.42**	**0.87**	**0.77**	**1.25**	**1.17**
K18013	338°C	1.20	0.11							0.13	0.09	0.57	1.05
K18014		1.27	0.14							0.08	0.08	0.68	1.01
K18015		1.22	0.09							0.09	0.13	0.76	1.05
K18016		1.21	0.09							0.07	0.06	0.50	1.05
K18017		1.24	0.12							0.04	0.07	0.59	1.02
K18018		1.19	0.04							0.08	0.14	0.94	1.03
Mean		**1.22**	**0.10**							**0.08**	**0.10**	**0.67**	**1.04**
K17029	390°C	un	un										
K17030		un	un										
K17031		un	un										
K17032		un	un										
K17034		2.15	0.13										
K17035		2.19	0.10										
Mean		**2.17**	**0.12**										

un: unquantifiable, too low concentrations. [1] MAS(I)/(I + II) (in %) where MA(I) = C_{21} ring-C monoaromatic steroids and MA(II) = C_{28} ring-C MAS. TAS(I)/(I + II) (in %), where TA(I) is C_{20} triaromatic steroids and TA(II) = C_{28} TAS 20S + 20R isomers. TAS/(TAS+MAS) where TAS= C_{28} TAS 20S + 20R isomers and MAS= C_{29} ring-C MAS 20S+20R. [2] 20S/(20S+R) where 20S and 20R are epimers at C-20 in the C_{29} 5α,14α,17α steranes. 22S/(22S+R) where 22S is C_{32} 17α21β 22S hopane and 22R is C_{32} 17α21β 22R hopane. αβ/(αβ+αα) where αβ= C_{29} 5α,14β,17β steranes (20S+20R) and αα = C_{29} 5α,14α,17α steranes (20S+20R). CPI: Carbon preference index. Pr: pristane. Ph: phytane. DBT: dibenzothiophene. Phe: phenanthrene.

Tab. 7.3. Concentration of C_1, C_2-C_5, water, CO_2 and bitumen and relative abundance of SAT, ARO and POL (NSO) hydrocarbons after thermal maturation. Group A: brown AOM-rich samples. Group B: orange AOM-rich rocks.

Sample no.	Sample name	Gr		Concentration (mg/g of TOC)					%		
				C1	C2-C5	H2O	CO2	Bitumen	SAT	ARO	POL
K16015	B2	A	Immature	0	0	0	0	79.7	11.8	11.8	76.5
K17001	B23	A		0	0	0	0	54.2	9.5	19	71.4
K16026	E19	A		0	0	0	0	117.3	7.2	15.6	77.2
K16019	B31	B		0	0	0	0	124.2	5.6	13	81.5
K16031	E38	B		0	0	0	0	167.4	14.9	15.6	69.5
K16032	E40	B		0	0	0	0	162.1	10.7	16.4	72.9
K17036	B2	A	283°C/104d	0.5	3.3	6.1	28.4	200.6	24.6	21.1	54.4
K17037	B23	A		4.7	3.5	3	20.6	211.6	21.4	24.1	54.5
K17039	E19	A		1.1	2.1	4.5	6.2	235.1	24.1	24.6	51.3
K17038	B31	B		0.4	2.9	17.6	3.8	257.2	26.9	30.1	42.9
K17040	E38	B		2.1	3.7	5.1	0.9	308.2	29.5	30.5	40
K17041	E40	B		1.8	1.4	4.5	4.3	366	34.2	25.5	40.2
K18013	B2	A	338°C/104d	3.7	221	13.1	357.5	110.8	5	9.1	85.9
K18014	B23	A		12.8	256.8	3.4	318.8	88.1	10.2	12.5	77.4
K18016	E19	A		24.5	373.6	2.9	301	97.2	17.2	28.6	54.3
K18015	B31	B		15.8	399.6	3.1	232.6	115.8	14.9	40.4	44.7
K18017	E38	B		17.1	360.2	1	131.5	109	12.8	30.1	57.1
K18018	E40	B		17.7	484.3	0.7	119.6	142	10.6	29.2	60.2
K17029	B2	A	390°C/104d	123	147.8	54.6	356.9	26.5	22.8	15.4	61.8
K17030	B23	A		97.1	168.6	39.3	395.1	16.4	14.6	12.9	72.5
K17033	E19	A		133.4	135.1	9.7	308.8	38.3	6.4	7.9	85.7
K17031	B31	B		203.1	178.9	27.7	281.4	18.9	11.3	19.2	69.5
K17034	E38	B		230.3	194.1	14.3	217.7	47.9	8.1	30.7	61.1
K17035	E40	B		287.9	232.3	65.4	248.9	75.7	8.6	34.3	57.1

5.1.1.1. Molecular OM composition

C_{15}-C_{38} n-alkanes, accompanied by a few isoprenoids, methylated and alkylcycloalkanes (alkylcyclohexanes and pentanes), are predominant in samples up to their total degradation after heating at 390°C for 104 days (Fig. 7.2). With a distribution initially maximizing at C_{23} with a strong odd over even predominance (CP1≈1.63), the increase in short chain n-alkane (<C_{23}) concentrations without any odd over even predominance after heating at 283 and 338°C leads to the decrease in the CPI to ≈1.00 (Tab. 7.2, Fig. 7.2). Pr/n-C_{17} and Ph/n-C_{18} and Pr/Ph show a progressive decrease with increasing thermal maturity (Tab. 7.2, Fig. 7.5). Whatever the thermal maturity stage, C_6-C_{14} n-alkanes are present in very small amounts or are totally absent in KCF samples. Hopanes and steranes as well as triaromatic (TAS) and ring-C monoaromatic steroids (MAS) are quickly degraded during maturation and completely disappear after heating 104 days at 338°C (Fig. 7.2).

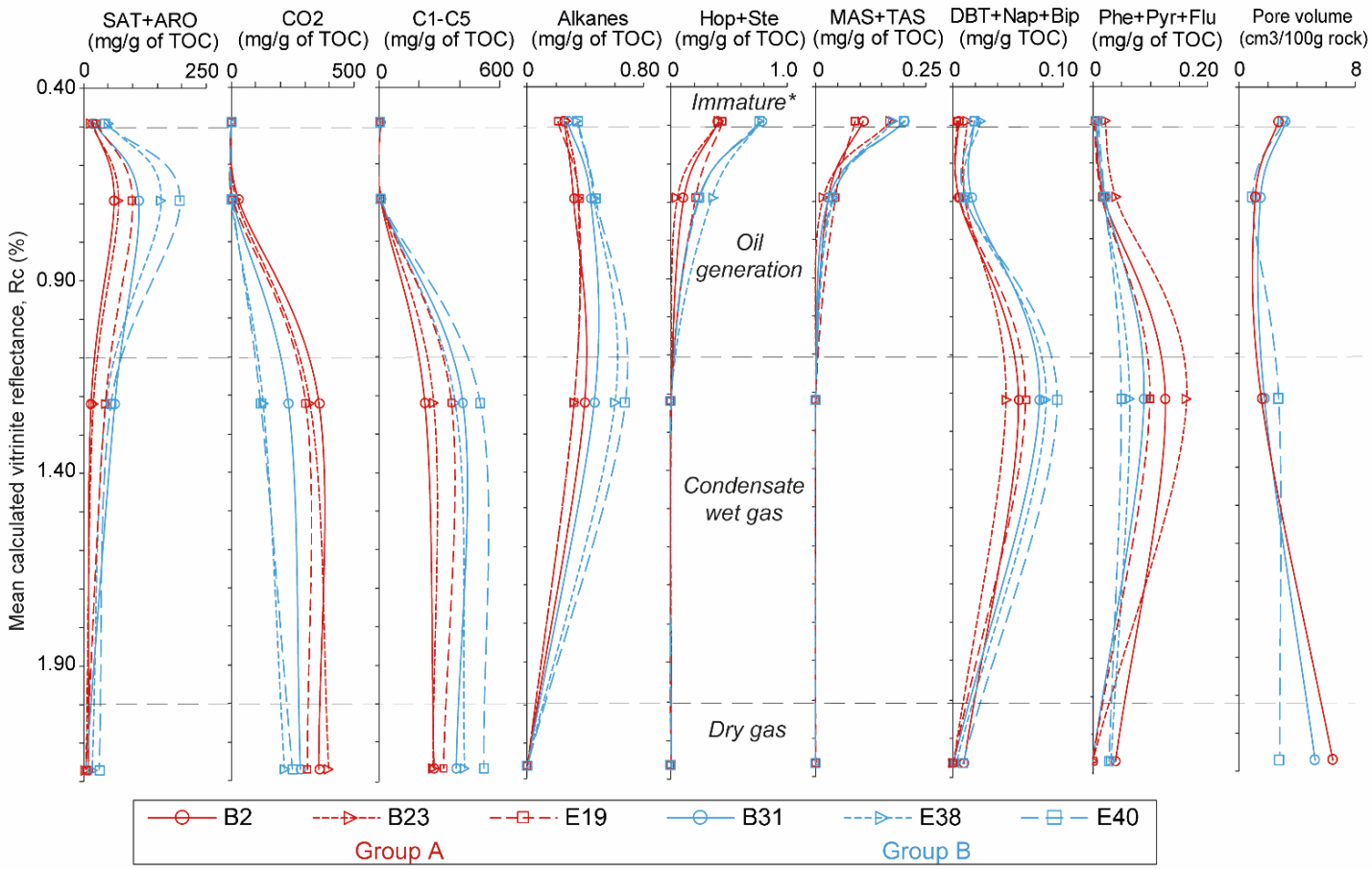

Fig. 7.2. Evolution of the concentrations of aromatic (ARO), saturated (SAT) hydrocarbons, CO2, C1-C5 hydrocarbon gases, alkanes (n-alkanes, alkylcycloalkanes and isoalkanes), hopanes (Hop), sterane (Ste), monoaromatic (MAS) and triaromatic steroids (TAS), dibenzothiophenes (DBT), naphthalenes (Nap), biphenyls (Bip), phenanthrenes (Phe), pyrenes (Pyr), and fluorenthenes (Flu) (including methylated derivatives) after maturation at 283°C (Rc≈0.69%), 338°C (Rc≈1.22%) and 390°C for 104 days (Rc≈2.17%).

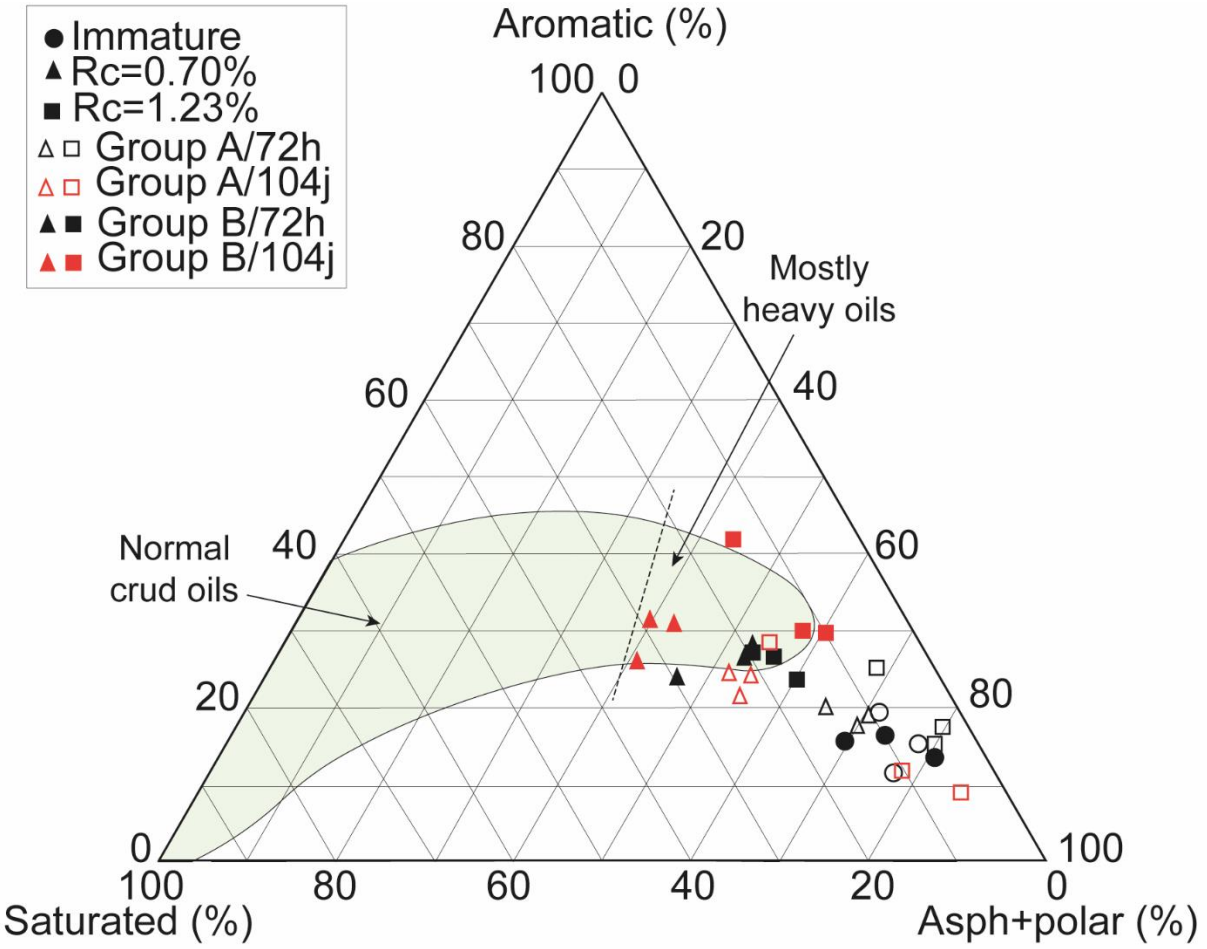

Fig.7.3. Ternary diagram of the saturated, aromatic and polar hydrocarbon fractions (NSO) of bitumen after thermal maturation during 72h (black) and 104 days (red). Group A: brown AOM-rich samples. Group B: orange AOM-rich rocks.

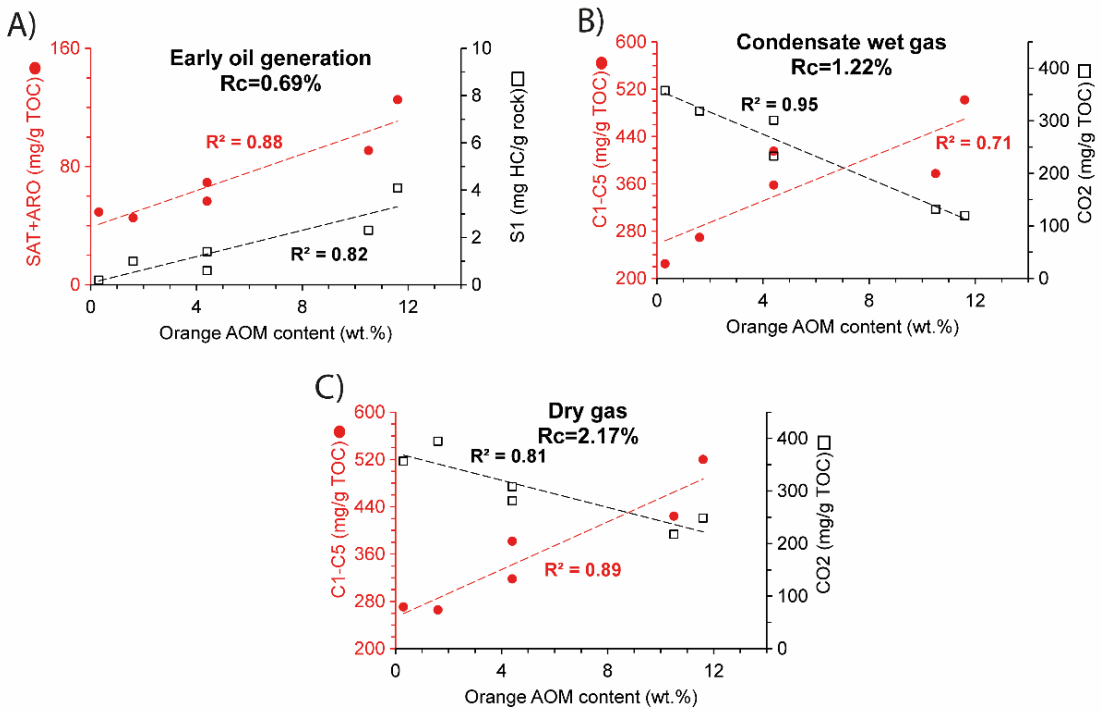

Fig. 7.4. A) Evolution of S1, SAT and ARO concentrations with the initial orange AOM content after maturation at 283°C for 104 days. B, C) Evolution of C_1-C_5 and CO_2 concentrations with the initial orange AOM content during gas generation.

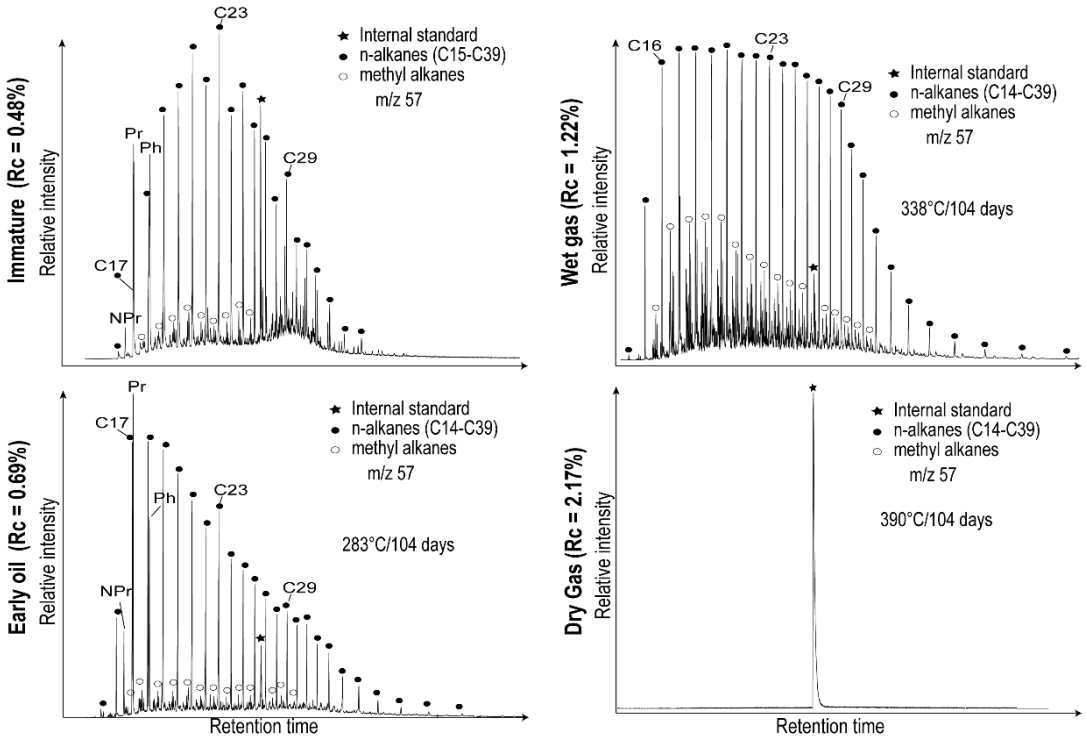

Fig. 7.5. Ion chromatograms of n-alkanes (m/z 57+71+85) of the saturated HC fractions from one representative KCF mudstone at different maturities.

Comparison with shorter duration maturation experiments

Comparable Rock Eval® parameters and mean Rc are obtained after maturation for 104 days and 72 hours (Tab. 7.2, Fig. 7.1), indicating that similar stages of thermal maturity have been reached after maturation for 104 days and 72 hours (Tab. 7.2, Fig. 7.6). The Rc obtained after maturation at 470°C for 72 hours (≈2.50%) is slightly higher than the mean Rc of 2.17% reached after maturation at 390°C for 104 days. As the variability of the Rc between samples is however greater at this maturity stage, this difference should not be significant. Similar thermal maturity biomarker ratios, including MAS(I)/(MASI+II), αβ/(αβ+αα), 20S/(20S+R), 22S/(22S+R), pristane/phytane (Pr/Ph), Pr/n-C_{17} and Ph/n-C_{18} ratios, are obtained after maturation for 104 days and 72 hours (Tab. 7.2, Fig. 7.6).

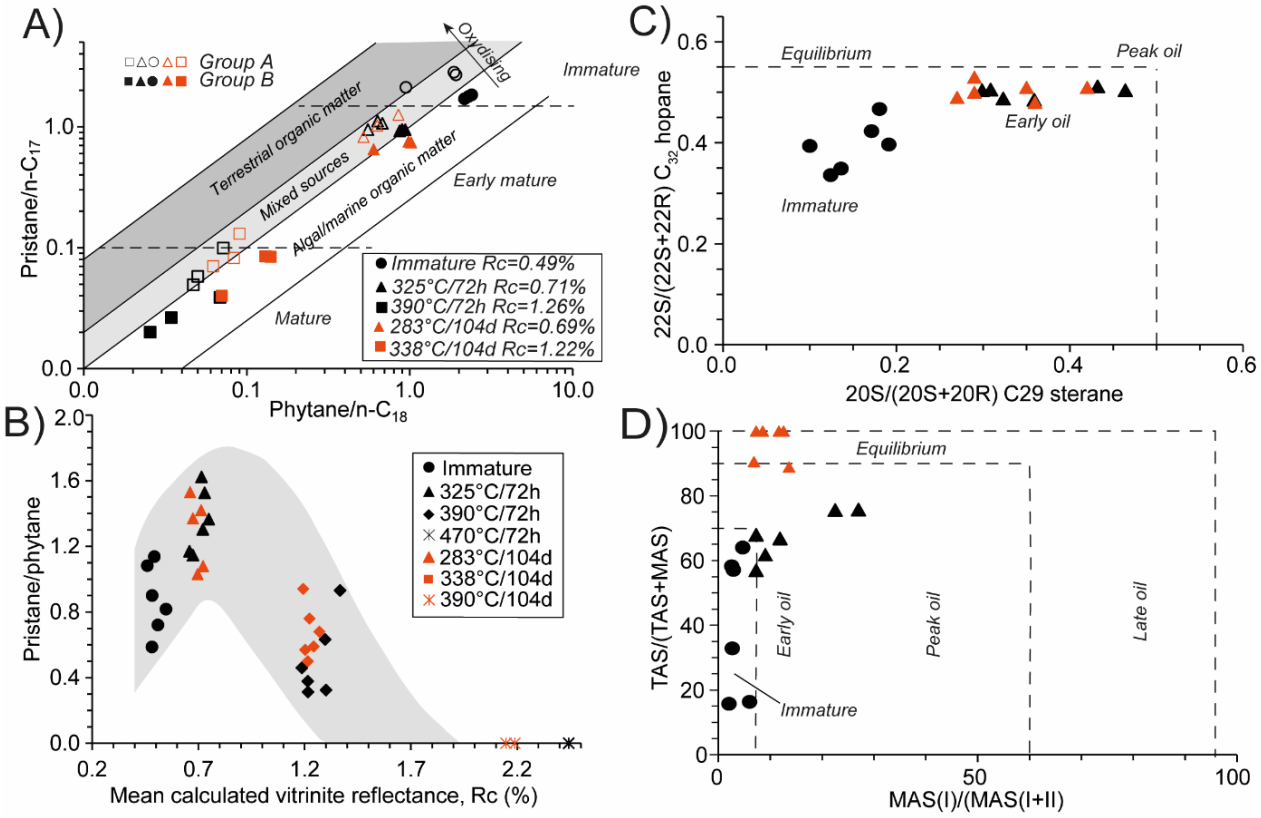

Fig. 7.6. A) Pristane/n-C_{17} versus phytane/n-C_{18}. B) Pristane/phytane as a function of Rc (from Shanmugam, 1985). C) 22S/(22S+22R) C_{32} hopane as a function of 20S/(20S+20R) C_{29} sterane. 22S: C_{32} 17α21β 22S hopane. 22R:C_{32} 17α21β 22R hopane. 20S and 20R: epimers at C-20 in the C_{29} 5α,14α,17α steranes. D) TAS/(TAS+MAS) versus MAS(I)/MAS(I+II). TAS: C_{28} triaromatic 20S+20R isomers. MAS: C_{29} ring-C monoaromatic steroids 20S+20R. MAS(II): C_{28} ring-C monoaromatic steroids. MAS(I): C_{21} ring-C monoaromatic steroids.

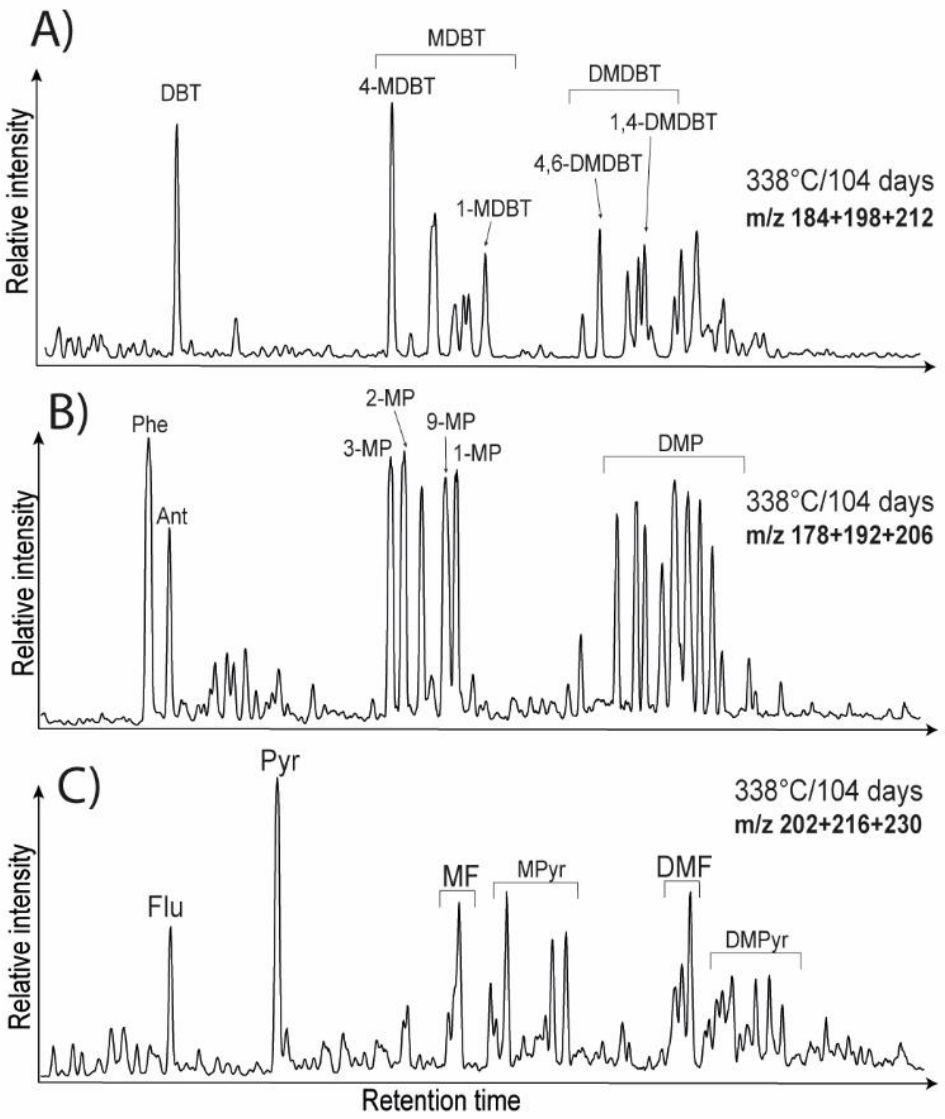

Fig. 7.7. Distribution of A) dibenzothiophenes (DBT), B) phenanthrenes (Phe), C) pyrenes (Pyr), fluorenthenes (Flu) and their methylated (M) and dimethylated derivatives (DM) in samples after maturation at 338°C for 104 days.

This substantiates the Rc and suggests that equivalent stages of thermal maturity have been reached: the early oil generation, the condensate wet gas zone, and the dry gas zone. MAS(I)/(MASI+II) of ≈10, αβ/(αβ+αα) of ≈0.42, 20S/(20S+R) of ≈0.33 and 22S/(22S+R) of ≈0.50 obtained after thermal maturation at 283°C for 104 days are typical values of the early oil generation stage (Fig. 7.6A, C) (Mackenzie et al., 1980; Seifert and Moldowan, 1981; Peters et al., 2007). Similar distributions of DBT and Phe are observed (Fig.7.7). Similar differences of Pr/n-C_{17} and Ph/n-C_{18} ratios are observed between samples containing a higher relative proportion of orange AOM (group B) and samples with a higher proportion of brown AOM (group A) after maturation for 104 days and 72 hours (Fig. 7.6A). Whatever the duration of the

maturation, samples of group A still contain slightly higher Ph/n-C_{18} indicating the presence of a less oxygenated OM from the early oil to the condensate wet gas zone. Similar relations are also observed between SAT, ARO, S1 CO_2 and C_1-C_5 concentrations and the initial orange AOM contents of samples (Fig. 7.4). However, some differences are observable between the longer and the shorter maturation experiments. In the early oil generation stage, higher TAS/(TAS+MAS) are obtained for the longer maturation experiment, suggesting a quicker degradation of the C-ring MAS (Fig. 7.6D). While the total bitumen HC concentrations generated in the early oil generation stage are similar between the two maturation series, samples matured for 104 days exhibit lower POL, CO_2, C_1-C_5 and slightly higher SAT, ARO, and alkane concentrations (including n-alkanes but also methylalkanes, isoprenoids and alkylcycloalkanes) than samples matured for 72 hours (Fig. 7.8, 7.9A). The difference in alkane concentrations is more pronounced for samples with a higher relative proportion of orange AOM contents: B31, E19 and E40. Similar concentrations of C_1, DBT, Nap, Bip, Flu, Phe and Pyr are obtained (Fig. 7.9A). In the condensate wet gas zone, the increase in the maturation duration resulted in the production of higher C_2-C_5 concentrations for samples with an initial higher oil generation potential (B31-E40), and lower C_1 and lower CO_2 concentrations (especially for less oil-prone samples B2, B23, E19, Fig. 7.10A). KCF samples show comparable alkane, DBT, Nap and Bip concentrations in the condensate wet gas zone after maturation for 104 days and 72 hours (Fig. 7.9B). However, significantly lower concentrations of Phe, Pyr and Flu are observed after maturation for 104 days. Lower POL concentrations are obtained for most of the samples for the longer duration experiment (Fig. 7.10). In the dry gas zone, the increase in the duration of maturation allows the production of higher C_1 concentrations and still higher concentrations of CO_2, especially for the less oil prone samples (Fig. 7.10B). C_2-C_5 are however generated in slightly lower amounts after maturation for 104 days in the dry gas zone. The concentrations of POL in residual OM do not appear to have been influenced by the duration of the experiments (Fig. 7.10B). The concentration of DBT, Bip, Naph, Flu, Pyr and Phe are two low at this maturity stage to allow a good comparison between the two series. .

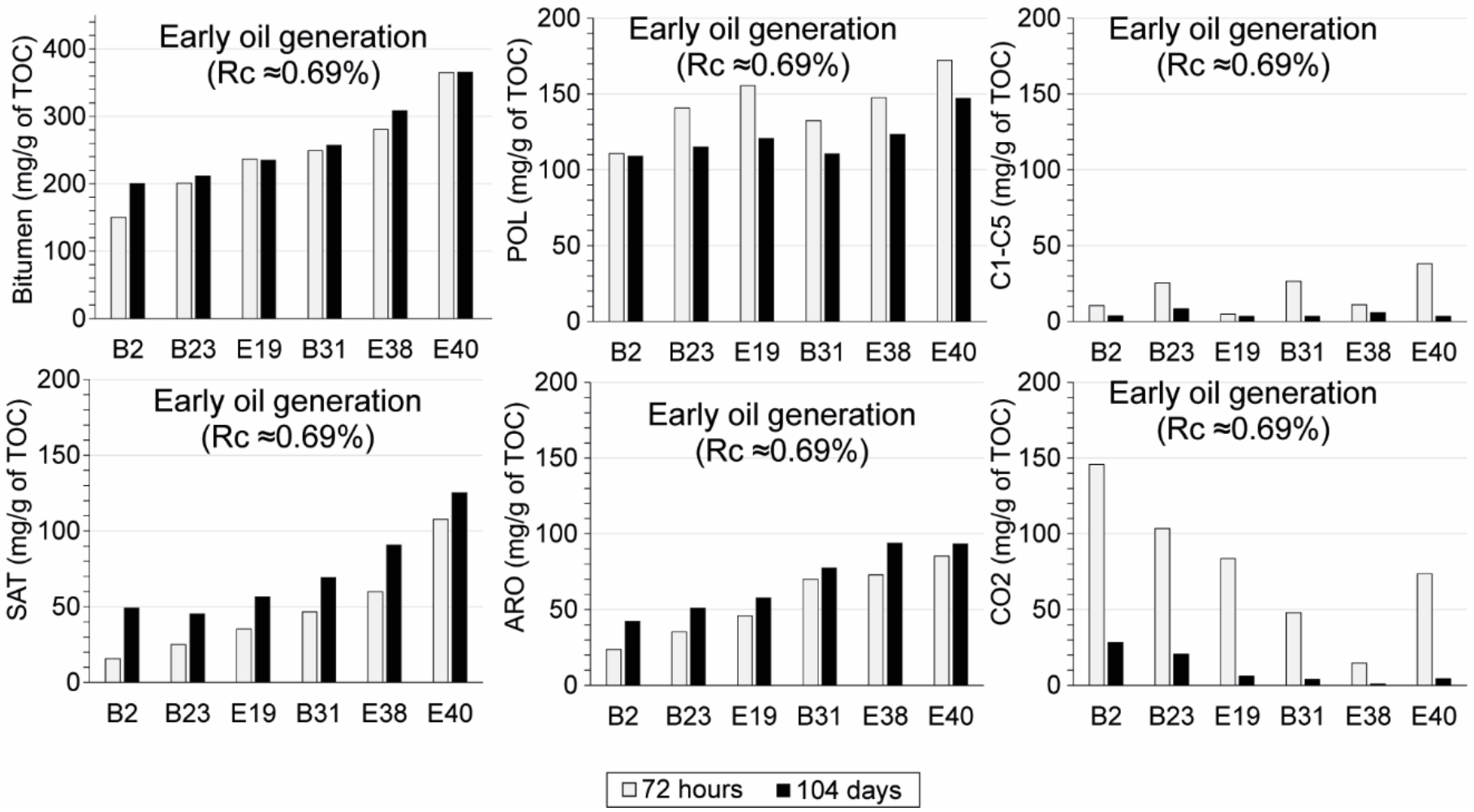

Fig. 7.8. Comparison of total bitumen, POL, SAT, ARO, C_1-C_5 hydrocarbon and CO_2 concentrations in the early oil generation stage as a function of the thermal maturation duration.

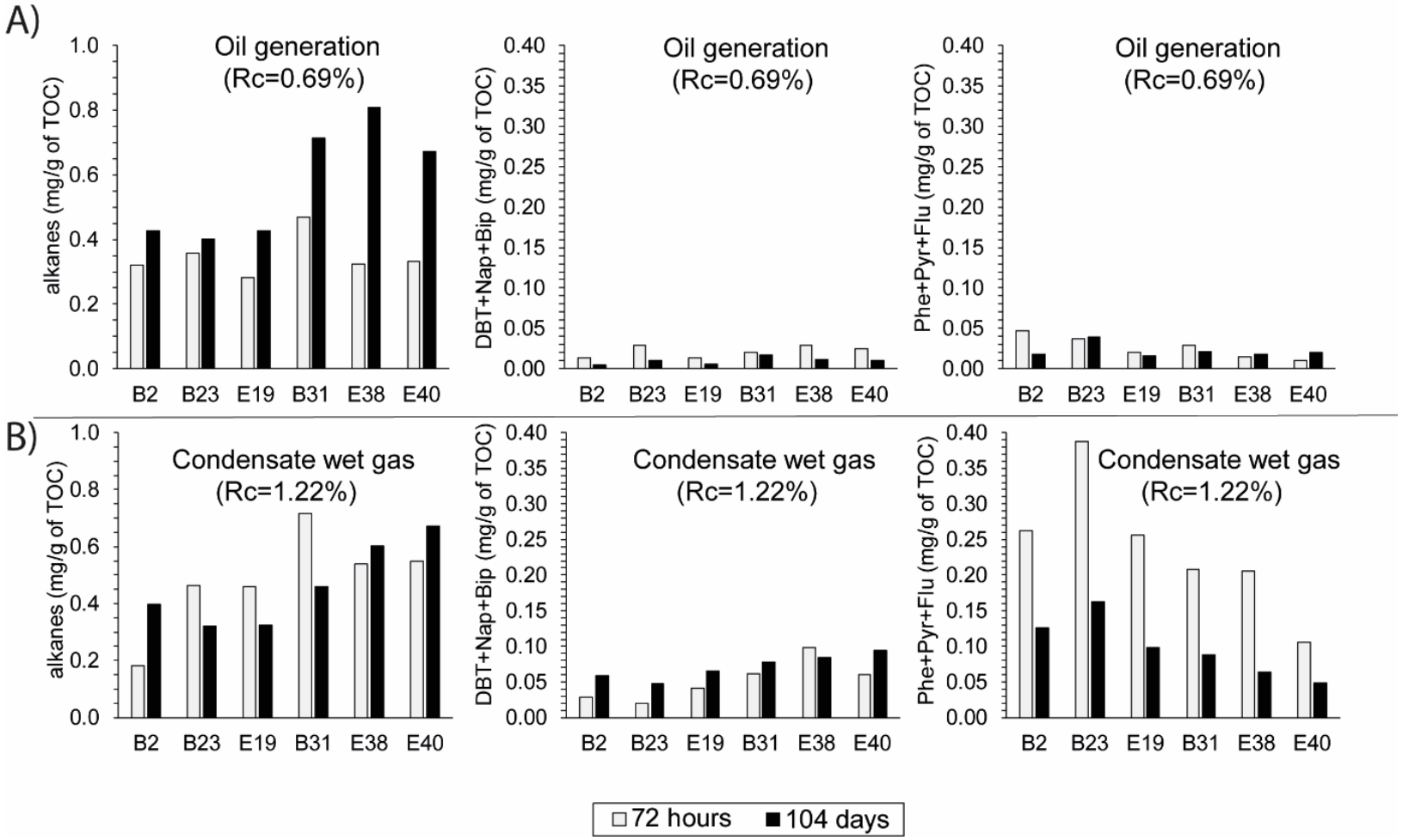

Fig. 7.9. Comparison of alkane (including n-alkanes, isoalkanes, cycloalkanes, hopanes and steranes), dibenzothiophene (DBT)+ naphthalene (Nap)+ biphenyl (Bip), phenanthrene (Phe)+ pyrene (Pyr)+ fluoranthene (Flu) concentrations in the oil generation (A) and the condensate wet gas zone (B) as a function of the thermal maturation duration.

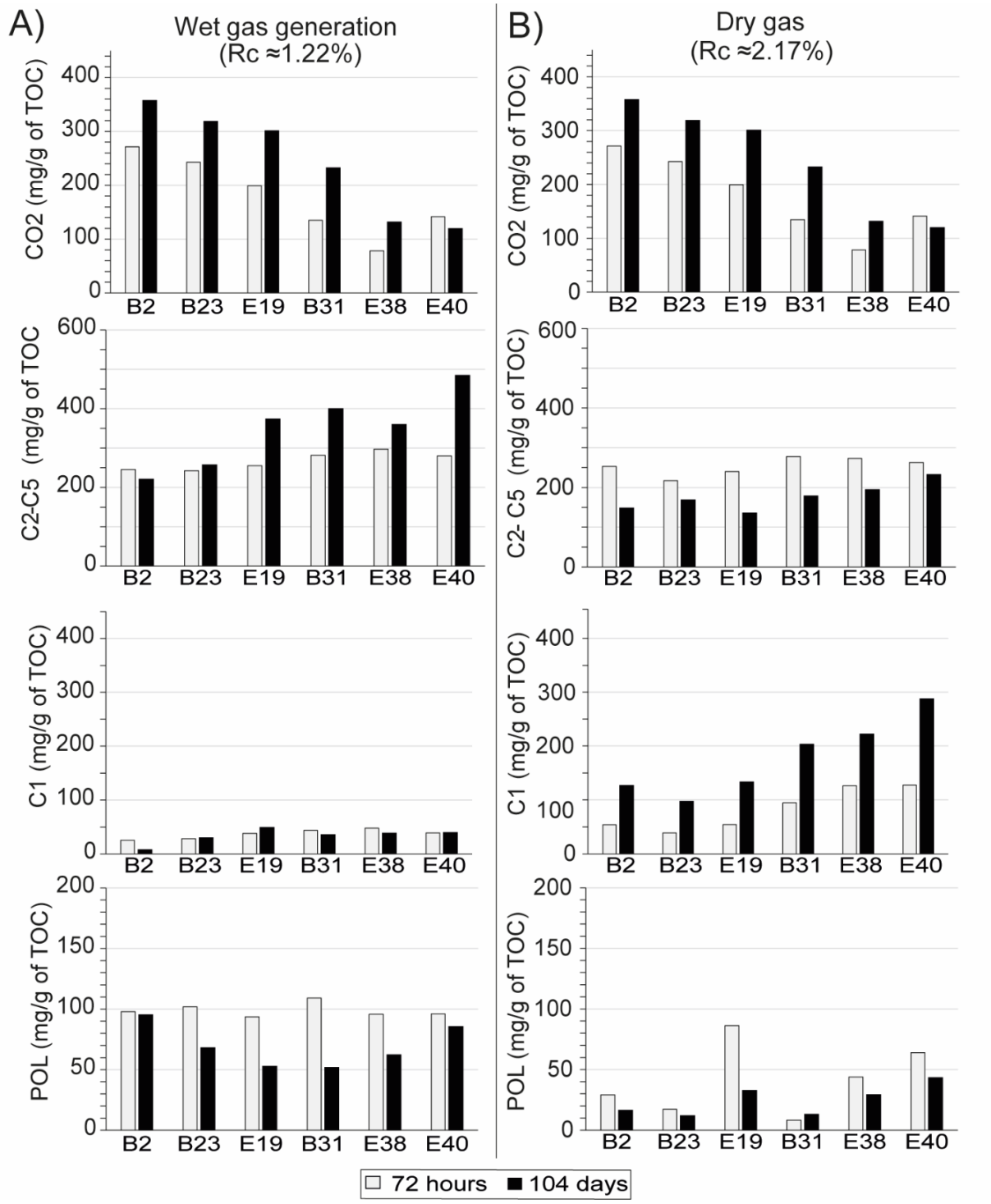

Fig. 7.10. Comparison of POL, C1, C2-C5 hydrocarbon and CO2 concentrations in the condensate wet gas (A) and the dry gas zone (B) as a function of the thermal maturation duration.

5.1.2. Evolution of pore volume and surface area during 104 days of maturation and comparison with shorter duration experiments.

5.1.2.1. Isotherms

An example of the evolution of nitrogen adsorption and desorption isotherms at 77K with increasing maturity is presented in Fig. 7.11. Whatever their initial composition and maturity, all samples show type IV isotherms, indicating the presence of mainly mesoporous materials (Sing, 1985). The shape of the hysteresis loops indicates the presence of slit-shaped pores associated with aggregated plate-like particles (Sing, 1985). However, in natural materials such as shale rocks, previous studies revealed that the assumption of slit-shaped pores could be subject to error and has thus to be considered with caution (Schmitt et al., 2013; Clarkson et al., 2013). The volume of gas adsorbed around p/p0 0.992, low after maturation at 283°C for 104 days (Rc=0.69%, Fig. 7.11) increases progressively after maturation at 338°C and 390°C for 104 days for all samples, indicating the increase in the total pore volume.

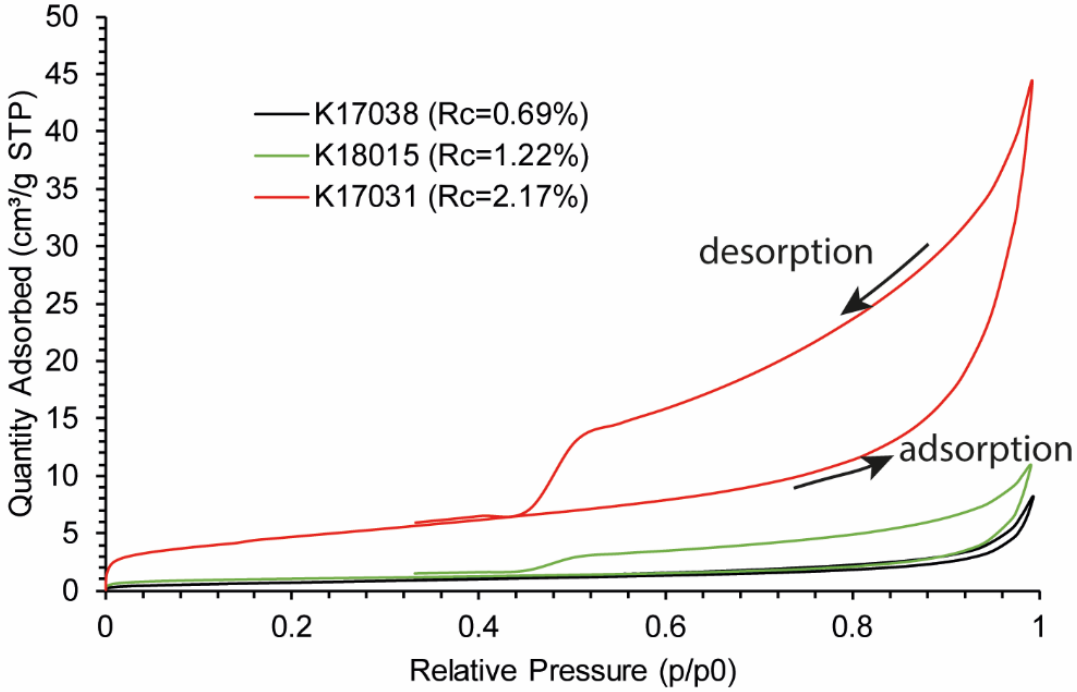

Fig. 7.11. Example of the evolution of KCF samples' nitrogen gas adsorption and desorption isotherms (at 77K) with increasing thermal maturity (sample B31).

5.1.2.2. Pore volumes and specific surface areas and pore size

The total pore volumes (Vp) and the BET specific surface areas (S_{BET}) of the three samples decrease after heating for 104 days at 283°C. At this maturity stage, the Vp (≤1.59 cm3/100g) and the S_{BET} (≤ 9.31 m²/g) decrease from B2 to E40 and thus, decrease with the increase in the initial TOC and oil-prone phytoplanktonic orange AOM contents (Tab. 7.4). The t-plot model appeared to be reaching its limits for many samples because some external micropore surface areas were negative and could not be interpreted (Tab. 7.4). The PSD determined using the DFT and the BJH methods give similar results and show that all KCF samples exhibit a large pore distribution mainly ranging from meso to macropores (Fig. 7.12, 7.13) after maturation at 283°C. However, there are some differences between B2 and the other two samples. B2, the least oil prone sample, exhibits a BET constant (C_{BET}) four times higher than that of samples B31 and E40 after heating at 283°C, suggesting the presence of a more polar surface with a higher ability to interact with gas (Tab. 7.4). C_{BET} is, indeed, related to the affinity of the solid with the nitrogen molecules (the adsorbate) and thus, to the heat of the adsorption (Brunauer et al., 1938). The BJH method was used to characterize the mesoporosity, the DFT to determine the mesoporosity and part of the microporosity, and the DR to assess the microporosity. A comparison of the surface areas and the pore volume calculated with these different models with the S_{BET} and the Vp enabled the relative contribution of the meso and the micropore surface area and pore volume of each sample to be estimated. As shown by the pore volume determined using the BJH (in adsorption, $V_{BJH, ads}$) close to the Vp, most of the pore volume of all the samples is provided by meso and macropores (Tab. 7.4). However, contrary to the other two samples, the lower $S_{BJH, ads}$/ $S_{BET,}$ far from 1.0, the slightly higher S_{DFT} / S_{BET} and especially the higher S_{DR} / S_{BET} close to 1 after heating at 283°C indicate that most of the specific surface area of B2 is provided by micropores (Tab. 7.4). The V_{DR}/Vt indicate that micropores account for about 22% of the total pore volume in this sample and less than 6% in the other two samples (Tab. 7.4). This is well substantiated by the PSD from the DFT methods which showed the presence of two controlled-size porosities about 1.3 and 4 nm in diameter in B2.

Tab. 7.4 Total pore volumes (V_p), BET specific surface areas (S_{BET}), BET constants (C_{BET}), surface areas (S_{BJHad}) and pore volumes in adsorption (V_{BJHad}) determined using the Barrett, Johner and Halenda method (BJH) and density functional theory (DFT), micropore volumes (V_{micro}) and micropore surface areas (S_{micro}) determined using the t-plot method and the Harkins-Jura model (HJ) and the Dubinin-Radushkevich model (DR) of samples B2, B31and E40 before and after thermal maturation, BET (D_{BET}) and BJH (D_{BJH}) mean pore width.

			t-plot (HJ)							*BJH meso*				*DFT micro+ meso*			*DR micro*			
Sample no.	***Sample name***	***T_{mat} (°C)***	***V_p (cm3/100 g)***	***S_{ext} (m^2/g)***	***S_{micro} (m^2/g)***	***V_{micro} (cm3/100g)***	***S_{BET} (m^2/g)***	***C_{BET}***	***D_{BET} (nm)***	***S_{BJHads} (m^2/g)***	***$V_{BJH, ads}$ (cm3/ 100g)***	***$D_{BJH, ads}$ (nm)***	***$S_{BJH, ads}$/ S_{BET}***	***S_{DFT} (m^2/g)***	***V_{DFT} (cm3/100 g)***	***S_{DFT} / S_{BET}***	***$S_{micro, DR}$ (m^2/g)***	***$V_{micro, DR}$ (cm3/100g)***	***S_{DR} / S_{BET}***	***V_{DR}/Vt (%)***
K17036	B2		1.59	8.13	1.18	0.05	9.31	165	6.9	3.10	1.20	15.5	0.35	5.92	1.49	0.64	9.99	0.35	1.13	22.3
K17038	B31	283	1.26	3.49	/	/	2.64	41	19.1	1.70	1.19	28.0	0.64	1.55	1.12	0.59	2.02	0.07	0.77	5.7
K17041	E40		0.97	2.52	/	/	1.89	39	20.6	1.24	0.92	30.0	0.69	1.05	0.95	0.55	1.18	0.04	0.65	4.3
K18013	B2		1.89	3.37	0.39	0.02	3.76	168	20.1	2.63	1.82	27.8	0.70	2.46	1.76	0.65	4.18	0.15	1.11	7.9
K18015	B31	338	1.69	0.96	0.96	0.04	3.60	160	18.8	2.04	1.62	31.7	0.57	2.23	1.55	0.62	4.02	0.14	1.12	8.5
K18018	E40		2.91	6.34	0.28	0.00	6.61	83	17.6	3.33	2.72	32.7	0.50	3.90	2.74	0.59	5.57	0.20	0.84	6.8
K17029	B2		5.62	19.64	/	/	19.48	5	11.5	18.22	5.08	18.2	0.94	14.36	5.25	0.74	20.92	0.74	1.33	13.2
K17031	B31	390	6.87	18.59	/	/	16.86	102	16.3	11.21	6.49	23.2	0.67	11.36	6.47	0.67	16.56	0.59	0.97	8.6
K17035	E40		2.85	6.96	/	/	5.36	45	21.3	3.83	2.75	28.7	0.72	3.04	2.81	0.57	3.97	0.14	0.74	4.9

/ negative values of micropore surface areas suggesting that the t-plot model is reaching its limits.

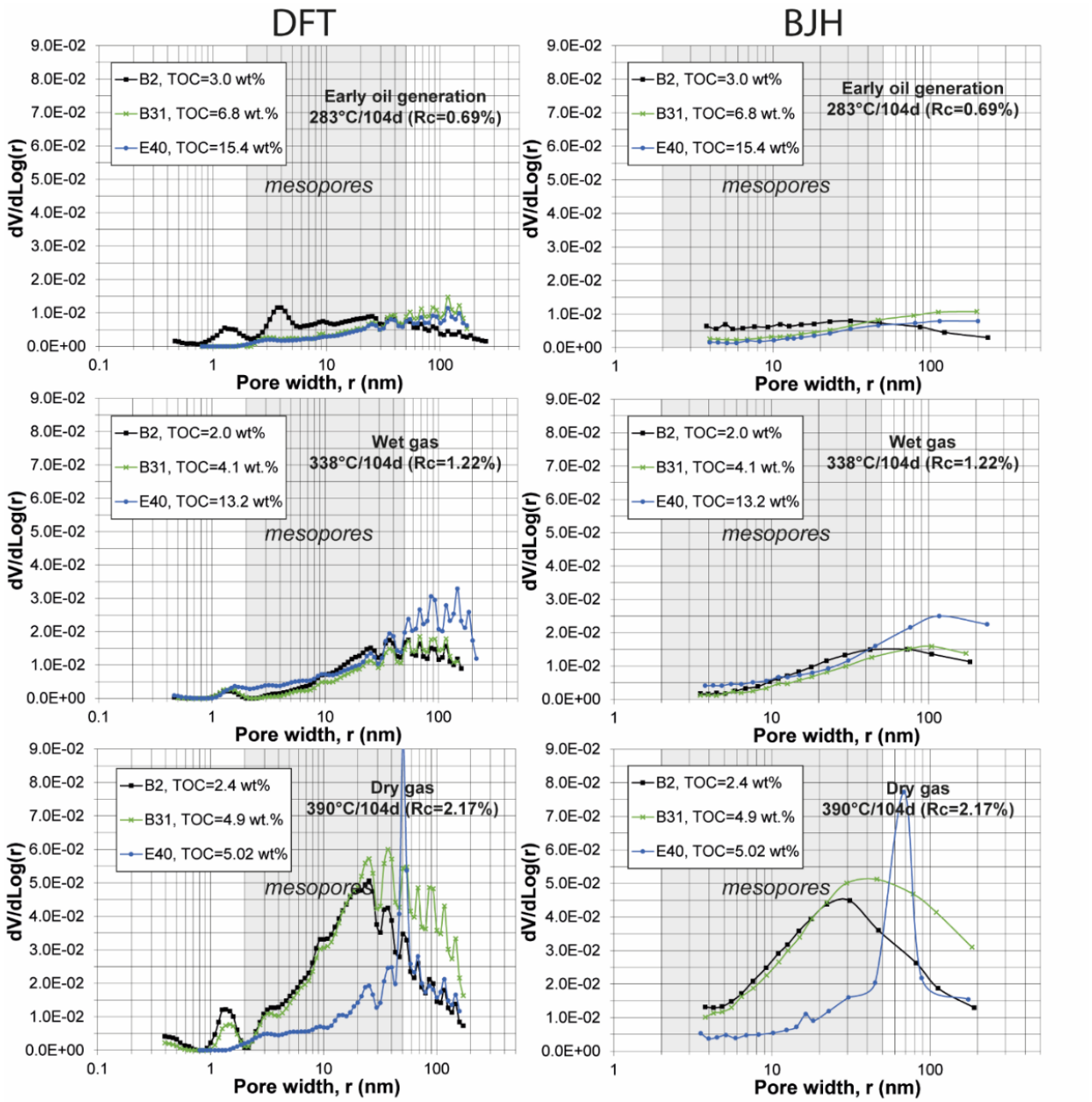

Fig. 7.12. Evolution of BJH and DFT pore size distributions of samples B2, B31 and E40 after thermal maturation at 283°C, 338°C and 390°C for 104 days.

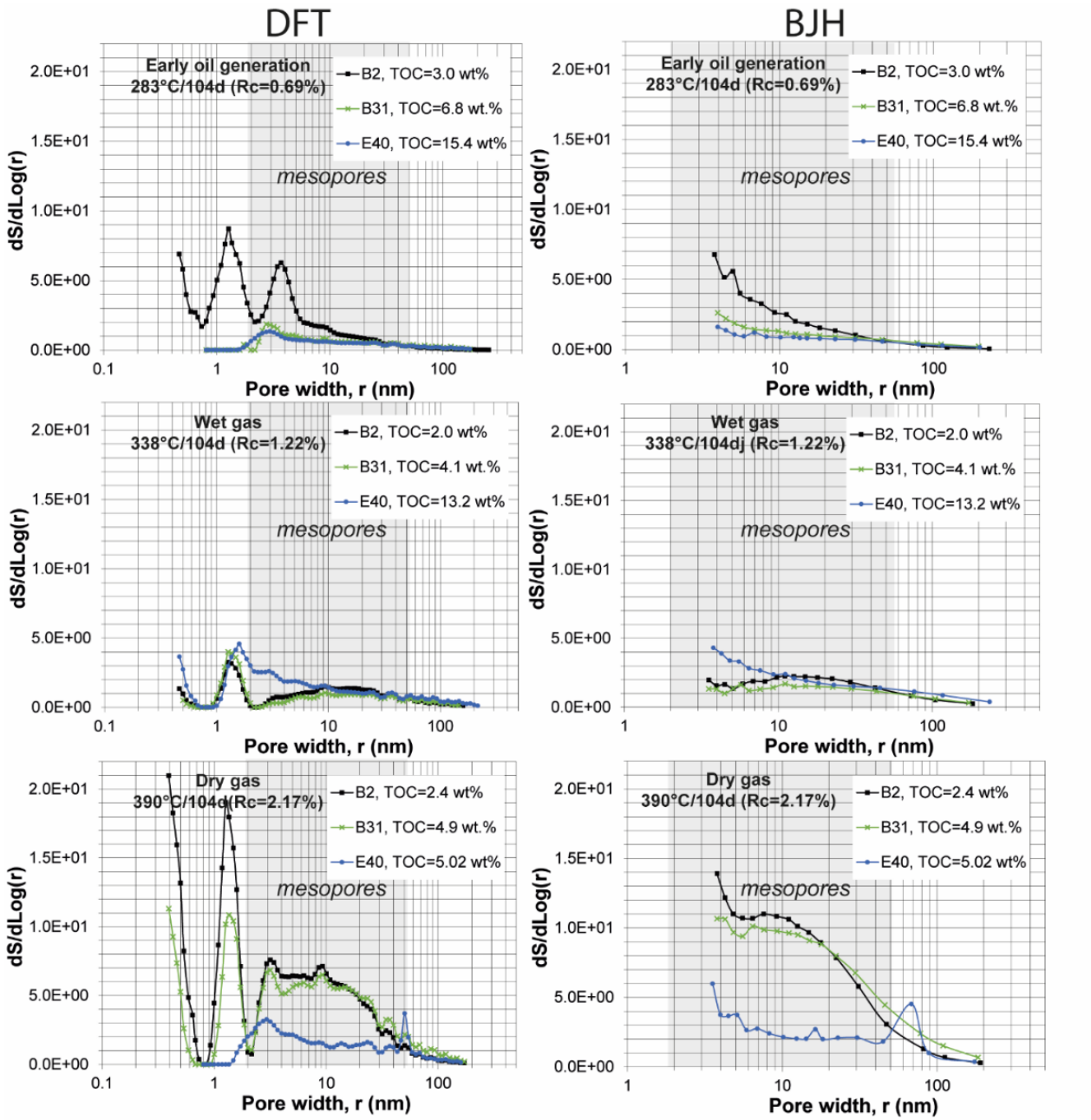

Fig. 7.13. Evolution of BJH and DFT surface area distributions of samples B2, B31 and E40 after thermal maturation at 283°C, 338°C and 390°C for 104 days.

These porosities have a significant contribution to the total specific surface after maturation at 283°C for 104 days (Fig. 7.12, 7.13). Consequently, B2 exhibits a lower mean pore diameter (D_{BET}≈7.0 nm) and mean mesopore diameter (D_{BJH}≈16.0 nm) than B31 and E40 for which D_{BET} ≈20 nm and D_{BJH}≈ 29.0 nm after heating at 283°C (Tab. 7.4). After heating at 338°C for 104 days, the Vp, the $V_{BJH, ads}$ and the V_{DFT} increase (Tab. 7.4, Fig. 7.14). While the S_{BET} increase for B31 and E40, they strongly decrease for B2 due to the decrease in its number of micropores around 1.3 nm in diameter after maturation at 338°C (Tab. 7.4, Fig. 7.12). E40, the highly oil-prone sample, exhibits higher Vp and S_{BET} than B2 and B31 which show similar features (Tab. 7.4). The differences between samples are less significant at this maturity stage. All samples exhibit a similar pore size distribution, with a predominance of mesopores ranging mainly from 4 to 150 nm in diameter (Fig. 7.12). Their D_{BJH} is about 30 nm and their D_{BET}≈ 19 nm in diameter (Tab. 7.4). As shown by the $V_{BJH, ads}$ close to the Vp, these mesopores account for most of the pore volume after maturation at 338°C. The PSD from the DFT shows however, the presence of a controlled size microporosity around 1.3 nm with a relatively low contribution to the pore volume (V_{DR}/Vt ≈8%, Tab. 7.4, Fig. 7.12) but a significant contribution to the specific surface area (Fig. 7.13). This may explain the S_{DR} / S_{BET} close to 1 in all samples and the S_{DFT} / S_{BET} and S_{BJH} / S_{BET} far from 1.0 (Tab. 7.4). As shown by the $V_{DR}/Vt_{(\%)}$, these micropores account for about 8% of the pore volume of KCF samples after maturation at 338°C for 104 days. The C_{BET}, which remains relatively constant for B2, increases strongly for B31 and E40 after heating at 338°C. While B2 and B31 exhibit similar C_{BET} at this maturity stage, E40 shows a lower C_{BET} suggesting the presence of slightly more apolar and hydrophobic surfaces. After maturation at 390°C for 104 days, the Vp and the S_{BET} increase strongly except for E40 for which these values remain relatively stable (Tab. 7.4, Fig. 7.2, 7.14). The Vp and the S_{BET} thus decrease with the increase in the initial TOC and orange AOM contents of the samples. The $V_{BJH, ads}$ still close to the Vp indicate that the total pore volume of samples is still mainly provided by meso and macropores (Tab. 7.2), widely distributed between 2 and 150 nm after maturation at 390°C for 104 days (Fig. 7.14). The PSD from the DFT shows however the increase in the number of pores at ≈1.3 nm and 4 nm for B2 and B31 (Fig.7.12). While these micro and small mesopores make a relatively low contribution to the total pore volume (VDR/Vt (%) from 8.6 to 13.2%) they provide a significant part of the specific surface area marked by a high DR micropore surface area (SDR) (Fig.7.13, Tab. 7.4). After heating at 390°C, the CBET decrease especially for B2 indicating a less polar material (Tab. 7.2). The PSD from the DFT method suggest that micropores less than 0.4 nm in diameter with a high

contribution to the specific surface area are present after heating at 390°C for 104 days but are not quantifiable by nitrogen adsorption.

Comparison of porosity evolution with shorter duration experiments.

Similar trends of pore evolution are observed in the same maturation stage for 104 days and the previous series for 72 hours (Fig. 7.14): the total pore volume, very low in the early oil generation stage, increases progressively to the dry gas zone. While no real differences are observed during oil generation, some slight differences are however visible between the two series during gas generation (Fig. 7.14). Slightly lower pore volumes are observed in the condensate wet gas zone. Increasing the duration of thermal maturation does not allow the formation of a greater pore volume at this stage of maturity.

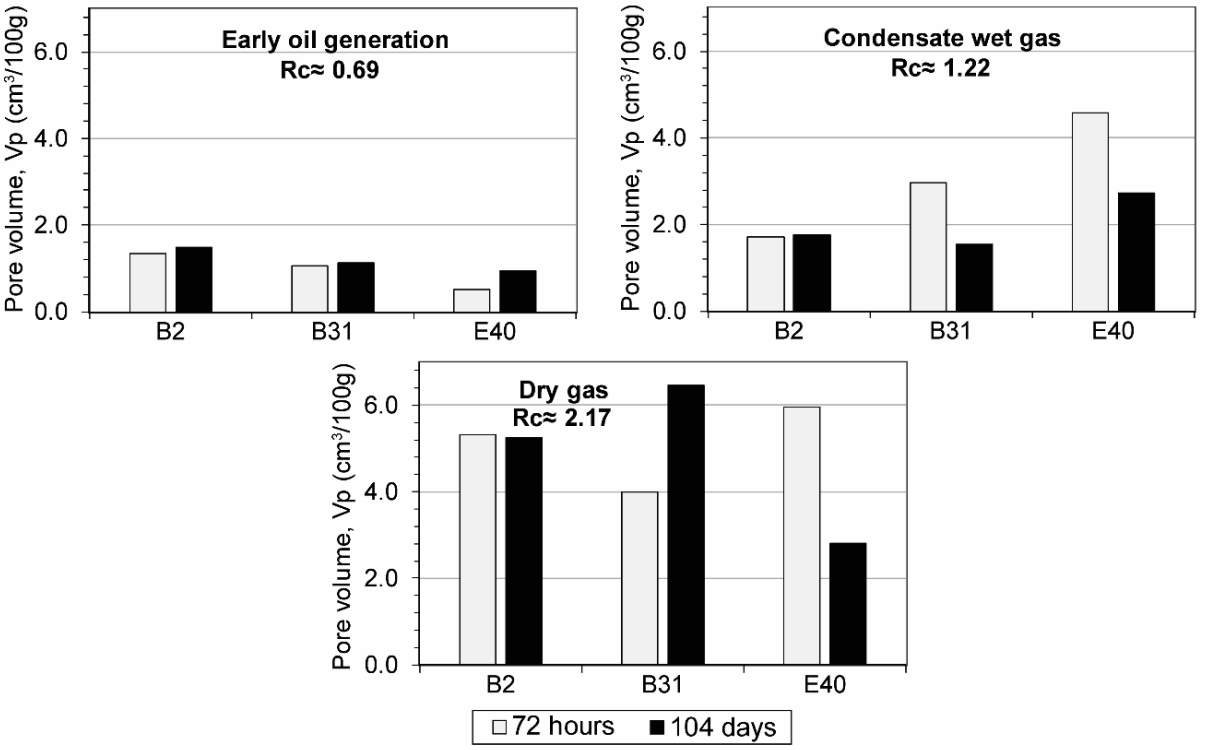

Fig. 7.14. Evolution of total pore volumes after thermal maturation at 283°C, 338°C and 390°C for 104 days. Comparison with the shorter experiments.

In the dry gas zone, the relation between the pore volume and the thermal maturation duration is not clear. While B2 exhibits a similar pore volume after maturation for 72 hours and 104 days, B31 exhibits a higher pore volume and E40 a lower pore volume after maturation for 104 days (Fig. 7.14). Differences in pore size distribution are observed between the two series, especially in the condensate wet gas zone but all samples exhibit a similar porosity mainly composed of widely distributed mesopores and macropores.

5.2. Discussion

5.2.1. How useful is it to combine different models for nitrogen adsorption measurements?

The concomitant use of different models for nitrogen adsorption measurements such as the DFT and the DR allows one to learn more about the poral structure of KCF rocks. In accordance with BJH pore size distribution and previous work, DFT pore size distributions show that most of the remaining pore volume in KCF rocks is provided by meso and macropores which vary widely in diameter from 2 to 160 nm in the early oil generation stage. However, the PSD curves from the DFT, which are more precise for microporosity and small mesoporosity assessment, reveal the presence of two controlled-size porosities at about 1.3 and 4 nm in diameter, only visible in the sample with the lowest oil generation potential in the early oil generation stage (B2, Fig. 7.12). These two controlled-size porosities are also observed in the condensate wet gas zone and are clearly visible in B2 and B31 in the dry gas zone (Fig. 7.12). According to the shape of the isotherms hysteresis loops (Fig. 7.11), these micro and small regular mesoporosities could correspond to slit-shaped pores associated with the plate-like clay particle aggregates previously observed in KCF rocks using SEM imaging. While these small meso and micropores generally make a limited contribution to the pore volume (Fig. 7.12), they provide a high specific surface area (Fig. 7.13) at the origin of the higher total BET and DR specific surface area of B2. Their role in gas storage and adsorption phenomena should thus not be neglected. In previous SEM images, the phytoplanktonic orange AOM appeared as a 'gel' which seems to fill the interlayer space between minerals, reducing the mineral associated pore volume of orange AOM-rich samples before maturation. We can thus suggest that B31 and E40 which initially contain higher amounts of orange AOM than B2, exhibit initially a lower micro and mesoporosity associated with clay sheet aggregates. Then, the filling of the porosity of these two higher oil prone samples by bitumen during oil generation makes the rest of these pores inaccessible to nitrogen adsorption, hence their lower porosity at ≈1.3 and 4 nm in diameter during oil generation. During the progressive conversion of residual kerogen and bitumen into gas and the ensuing generation of well interconnected secondary pores in OM, some micro and mesopores associated with clay minerals may be progressively released and/or become more accessible to nitrogen adsorption. This probably explains their increasing contribution to the pore volume and specific surface area (increase in $S_{micro,\ DR}$ and $V_{micro,\ DR,}$) from the condensate wet gas to the dry gas zone in samples B2 and B31 (Tab. 7.4, Fig. 7.12, 7.13). Indeed, the $S_{DR} / S_{BET} \geq 1$ in B2 and B31 indicates that most of the specific surface area

is provided by micropores (Tab. 7.4). In E40, the more extensive collapses of the pore structure in response to gas generation may have limited the accessibility of these pores to nitrogen adsorption, explaining the absence of pores 1.3 nm in diameter in the dry gas zone (Fig. 7.10, 7.13). Although this relatively scarce porosity associated with clay sheet aggregates makes a small contribution to the total pore volume, it is a major contributor to the specific surface area and may have a significant ability to adsorb and retain gas. These pores could thus also contribute to the gas storage capacity of these source rocks and may partly explain the greater CBET of some samples reflecting a better affinity of nitrogen for these clay mineral surfaces than for less polar residual OM particle surfaces. We can nevertheless exclude the possibility that the difference in OM composition, which, as previously observed hosts a large majority of pores in gas matured KCF samples, plays also a role in the variation of this constant between rich and poor phytoplanktonic orange OM samples.

5.2.2. Effect of the duration of confined thermal maturation on OM thermal degradation

As previously demonstrated (Wood, 1988; Landais et al., 1994), different time-temperature pairs can thus be used to reach the same stage of maturity. As expected, comparable Rc and thermal maturity biomarker ratios (Tab. 7.1, 7.2) are obtained after thermal maturation for 72 hours and 104 days, indicating indeed that similar stages of maturity have been reached: the early oil generation (Rc≈0.70%), the condensate wet gas (Rc≈1.23%) and the dry gas zone (Rc: 2.2-2.5%). It is thus possible to compare the bulk, the molecular composition of OM and the porosity between the two series as a function of the duration of maturation experiments. Our results show that Pr/Ph, Pr/n-C17, Ph/n-C18 and the relative proportion of the different hopane and sterane configurations do not depend on the duration of the maturation (Tab. 7.2, Fig. 7.14). The Rock Eval® parameters do not exhibit variations related to the duration-temperature pairs chosen for the experiments (Tab. 7.1, Fig. 7.1). This well substantiates the results of Landais et al. (1994) on type II source rocks and kerogen isolated from the Paris basin. Similar evolution of bitumen, CO_2 and C_1-C_5 concentrations and comparable OM components with similar distributions are observed in SAT and ARO fractions for long (104 days) and short (72 hours) maturation experiments. Furthermore, the choice of the time-temperature pairs does not influence the differences observed between samples with various initial relative proportions of orange and brown AOM. In both cases, the S1, the concentration of bitumen (especially of

SAT and ARO) in the early oil generation stage and thus the concentration of C_1-C_5 hydrocarbon gases during gas generation increase with the initial content of highly hydrogenated phytoplanktonic orange AOM. Samples containing a higher relative proportion of algal brown AOM systematically generated lower amounts of bitumen, slightly richer in POL components and higher CO_2 concentrations (Tab. 7.3, Fig. 7.2, 7.3, 7.4). These longer maturation experiments thus confirm the influence of the slight variations in the initial OM composition of KCF mudstones on the amount and the composition of bitumen generated, as previously discussed.

Some differences are, however, visible between the two series during oil and gas production. Shorter duration experiments (72 hours) appear to favor the production of bitumen extracts enriched in polar hydrocarbons while longer duration experiments (104 days) seem to favor the production of bitumen enriched in SAT and, to a lesser extent, ARO hydrocarbons in the early oil generation stage (Fig. 7.8). Hence, residual bitumen extracts exhibit lower POL and especially lower polyaromatic concentrations such as phenanthrenes, pyrenes or fluorenthenes during gas generation stages (Fig. 7.9B, 7.10). The increase in the maturation duration, and thus the increase in the residence time in the thermal maturation system, thus appears to enhance the degradation of heavy polar OM components into SAT and ARO hydrocarbons. This probably explains the higher alkane concentrations in the SAT fraction after the longer duration experiment in the early oil generation stage (Fig. 7.9A). Similar results were previously found on type II Paris Basin source rocks and type III Mahakam coal (Landais, 1991; Landais et al., 1994). On the contrary, lower C_1-C_5 concentrations are generated in the early oil generation stage after the longer duration experiment (Fig. 7.8). As previously suggested by Landais et al. (1994), the lower temperature used for the longer duration experiment (283°C for 104 days) probably led to a less pronounced early cracking of OM into light components by preventing low energy bonds from being broken during the early stage of maturation. This may also explain the slightly lower C_1 concentration for the longer duration experiment in the condensate wet gas (Fig. 7.10A). This lower early transformation of OM then leads to a more efficient secondary cracking of OM at higher maturity stages. This results in C_2-C_5 concentrations in the condensate wet gas zone and to a more efficient conversion of C_2-C_5 into C_1 in the dry gas zone responsible for the lower remaining C_2-C_5 concentrations and the significantly higher C_1 concentration of the longer maturation experiment (Fig. 7.10B). Note however, that contrary to the Paris basin source rocks, where CO_2 concentrations did not appear to be influenced by these processes (Landais et al., 1994), in the KCF increasing the duration

of the experiments also seems to lead to the production of lower CO2 concentrations in the early oil generation stage but higher concentrations during gas generation (Fig. 7.8, 7.10). Nevertheless, the difference in CO_2 concentrations between the two series seems to depend on the initial OM composition of KCF samples, especially during condensate wet gas generation. This difference, which is significant for the less oil-prone samples which initially contain a higher relative proportion of algal brown AOM, does not exist in the two highly oil-prone samples (E38 and E40, Fig. 7.10A). This suggests that the effect of the duration-temperature pair choice on OM thermal degradation may also depend on the original OM composition.

5.2.3. Does the duration of confined thermal maturation affect the evolution of porosity?

Similar variations in pore volume are observed form the early oil generation to the dry gas zone after maturation for 104 days (Fig. 7.2, 7.8) and 72 hours. Total pore volumes and specific surface areas decrease during early oil generation (filled by bitumen) and then exhibit a progressive increase (formation of pores in OM) which depends on the initial OM content and composition for the two maturation series.

As for the shorter maturation duration, samples with a higher content of OM and highly oil-prone orange AOM have lost a higher volume of pores during oil generation, occluded by the larger quantity of bitumen (Tab. 7.3). The increase in maturation duration allows the production of less viscous bitumen enriched in SAT and ARO hydrocarbons but does not influence the total amount of bitumen generated during oil generation (Fig. 7.3, 7.8). This probably explains why similar BJH pore size distributions and similar pore volumes are observed after 72 hours and 104 days of maturation in the early oil generation stage (Fig. 7.12, 7.14). The relative proportion of SAT, ARO and POL components in bitumen appears thus to have a limited effect on pore occlusion processes during the early stages of thermal maturation.

In the condensate wet gas zone, the samples which exhibit the higher total, meso-, micropore volume and specific surface area after heating at 338°C for 104 days are also the ones which exhibit the highest TOC content (13.18 wt.%) and hydrocarbon gas concentration in the condensate wet gas zone (≈500 mg/g of TOC, Tab. 7.4). Samples with a higher content of OM, and especially of phytoplanktonic AOM, exhibit a still higher pore collapse during gas generation that is responsible for the destruction of part of their pore network. This confirms that collapsing processes, closely related to the amount of gas generated, the initial OM

composition and content, occur during gas generation. The increase in maturation duration causes an increase in the amount of C_2-C_5 generated in the condensate wet gas zone, especially for samples with a higher content of phytoplanktonic OM such as B31 and E40 (Fig. 7.10A). We can thus suggest that these samples may have suffered earlier or more pronounced collapse processes leading to slightly lower pore volumes than for the shorter duration experiments (Fig. 7.14A). The less oil-prone sample B2, which generates similar amounts of hydrocarbon gases after heating for 72 hours and 104 days, exhibits comparable pore volume and PSD (pores widely distributed from 8 to 160 nm in diameter) in the condensate wet gas zone providing support for this hypothesis (Fig. 7.12, 7.14). This different timing and amplitude of collapsing processes between the two series of maturation may explain the different BJH PSD observed for the highly oil-prone samples B31 and E40. After maturation for 72 hours, B31 and E40 are composed of meso and micropores less than 40 nm while they contain mainly meso and macropores more than 8 nm after heating for 104 days (Fig. 7.12). We can suggest that the lower temperature used by the longer maturation experiments, which seems to prevent low energy bonds from being broken early on, may result in a slower and more homogeneous gas generation throughout the OM particles forming a better interconnected and distributed OM-hosted porosity in the condensate wet gas zone. Despite frequent collapse events, this may have enhanced early pore coalescence at the origin of the larger pore sizes after heating for 104 days.

In the dry gas zone, as previously observed after maturation for 72 hours, the specific surface area and the pore volume of samples increase more or less as a function of the initial OM composition and gas concentrations (Fig. 7.2). Moreover, the BJH PSD indicates a comparable porosity mainly composed of pores larger than 10 nm in the two series. As observed for the shorter duration experiments, the sample with the highest phytoplanktonic OM (E40) generated higher amounts of SAT and ARO enriched in hydrogenated components (such as n-alkanes) and exhibits lower pore volume than less oil prone samples in the dry gas zone (Fig. 7.14). This confirms that the pore volume formed during gas generation is not linearly correlated with the OM oil generation potential. However, the slightly different timing of generation and concentrations of C_1-C_5 hydrocarbon gases have probably influenced the timing and the amplitude of the collapsing processes that have affected the pore volume, probably causing the differences in pore volume between samples of the two series of maturation.

Our results show that increasing the duration of thermal maturation experiments influences the composition of bitumen, the amount and the timing at which HC gases are generated. Nevertheless, these differences, relatively small between 72h and 104 days of

maturation, do not significantly affect the development and the evolution of KCF mudstones' porosity with increasing maturity. Similar trends of pore volume and specific surface area are observed with increasing maturity and similar variations of porosity are observed between samples with a slightly different initial OM composition. The choice of duration-temperature pairs for thermal maturation experiments seems thus to have a limited impact on the porosity of organic-rich source rocks. Nevertheless, the results obtained from these longer duration experiments clearly substantiate the significant role of the chemical compositions of OM on the ability of organic-rich source rocks to develop and preserve pores during thermal maturation.

Summary and conclusions

To investigate how the choice of the duration-temperature-pairs of laboratory thermal maturation experiments can influence the evolution of OM and porosity of organic-rich source rocks with increasing maturity, long duration (104 days) confined thermal maturation, bulk, molecular geochemical OM characterization and porosimetry measurements were applied on the same immature marine KCF mudstones. The results were compared with shorter duration experiments (72 hours). The following conclusions can be drawn.

While increasing the duration of thermal maturation experiments does not influence the amount of bitumen generated, the increase of the residence time in the confined thermal maturation system enhances the degradation of heavy polar OM components into SAT and ARO hydrocarbons, leading to the production of bitumen enriched in SAT and ARO. This difference has however no significant impact on the evolution of KCF rocks' porosity at the early oil generation stage, which is controlled more by the amount of bitumen filling the interparticle mineral associated porosity than by its composition.

In preventing the early breaking of low energy bonds, the lower temperature used for the longer duration experiments results in a less pronounced early cracking of OM, resulting in a different timing of gas generation, more gradual and probably more homogeneous throughout the OM particles. This process does not influence the general evolution of the pore volume, which increases in the two series due to the formation of pores in OM. However, it seems to influence the amplitude and the timing of pore collapse events that occur during gas generation, leading to slightly different PSD and pore volumes in highly oil-prone phytoplanktonic-rich samples. The impact of the duration-temperature pairs of thermal maturation experiments on the development of KCF mudstones porosity remains, however, very limited, suggesting that results from different time-duration experiments and natural samples can be easily compared.

The results from the longer duration maturation experiments fully substantiate the significant role of the chemical compositions of OM on the ability of organic-rich source rocks to develop and preserve pores during maturation. As previously observed for the shorter experiments, phytoplanktonic OM rich samples seem to have generated a well-developed but more vulnerable OM porosity during gas generation, more repeatedly altered by collapsing processes. Hence, despite their higher initial higher OM content and the larger amounts of gas generated during their maturation, these highly oil-prone samples have not systematically developed greater pore volumes.

Summary and general discussion

Summary and general discussion

The variation in the OM composition of organic-rich mudstones selected from the Kimmeridge-Clay formation (KCF, Yorkshire, UK and Viking graben, North Sea) and the Vaca Muerta-formation (VMF, Neuquén basin, Argentina) with increasing thermal maturity was assessed by different techniques such as maceral and palynofacies analyses, Rock Eval pyrolysis, GC/MS and GC-TCD. These results were then related to the evolution of the structure and the porosity documented in the bulk rock and/or the OM isolated by SEM, TEM, nitrogen adsorption, mercury intrusion porosimetry, small angle X-ray scattering and Raman spectroscopy. This work aimed to investigate how the geochemical composition of the OM and its thermal degradation processes influence the development and the evolution of the porosity of organic-rich source rocks during thermal maturation.

The thermal maturation experiments, carried out on KCF samples compared with natural analogues from the VMF and the Viking graben, fully substantiate the available literature (Curtis et al., 2012; Milliken et al., 2013; Chen and Xiao, 2014; Ko et al., 2017; Ko et al., 2018; Katz and Arango, 2018) in showing that OM thermal degradation processes are responsible for significant changes in the porosity of organic-rich marine mudstones. A summary of the main observations made on KCF rocks with increasing maturity is presented on Fig.8.1. While pores are mainly associated with the mineral matrix in immature and low-mature samples, this is not the case for the higher maturity stages, where OM-hosted porosity is abundant. In migrating to the adjacent mineral pores, the significant amount of bitumen generated during the thermal conversion of the OM leads to a significant increase in the OM network connectivity in samples and to a significant decrease in the pore volume associated with the mineral matrix (Fig.8.1). Then, variations in the residual OM structure at the nanoscopic scale, together with the significant volume expansion that occurs during oil and gas generation, lead to the massive formation of a well-interconnected pore network in the residual OM which becomes the major contributor to the porosity. The similitude between the evolution of the porosity of KCF mudstones and the residual OM isolated through thermal maturation clearly demonstrated that the evolution of the chemical structure and the composition of kerogen during thermal maturation is the main factor responsible for the development and the evolution of pores from the late oil generation stage (Rm≈0.85%) to the dry gas zone (Rm≈2.50%). Our TEM studies show that these processes are accompanied by a progressive variation of the kerogen and residual bitumen structure from a perfectly homogeneous non-

porous texture to a heterogeneous porous granular structure at the nanoscopic scale accompanied by the formation of isolated grains of residual pyrobitumen (Fig.8.1).

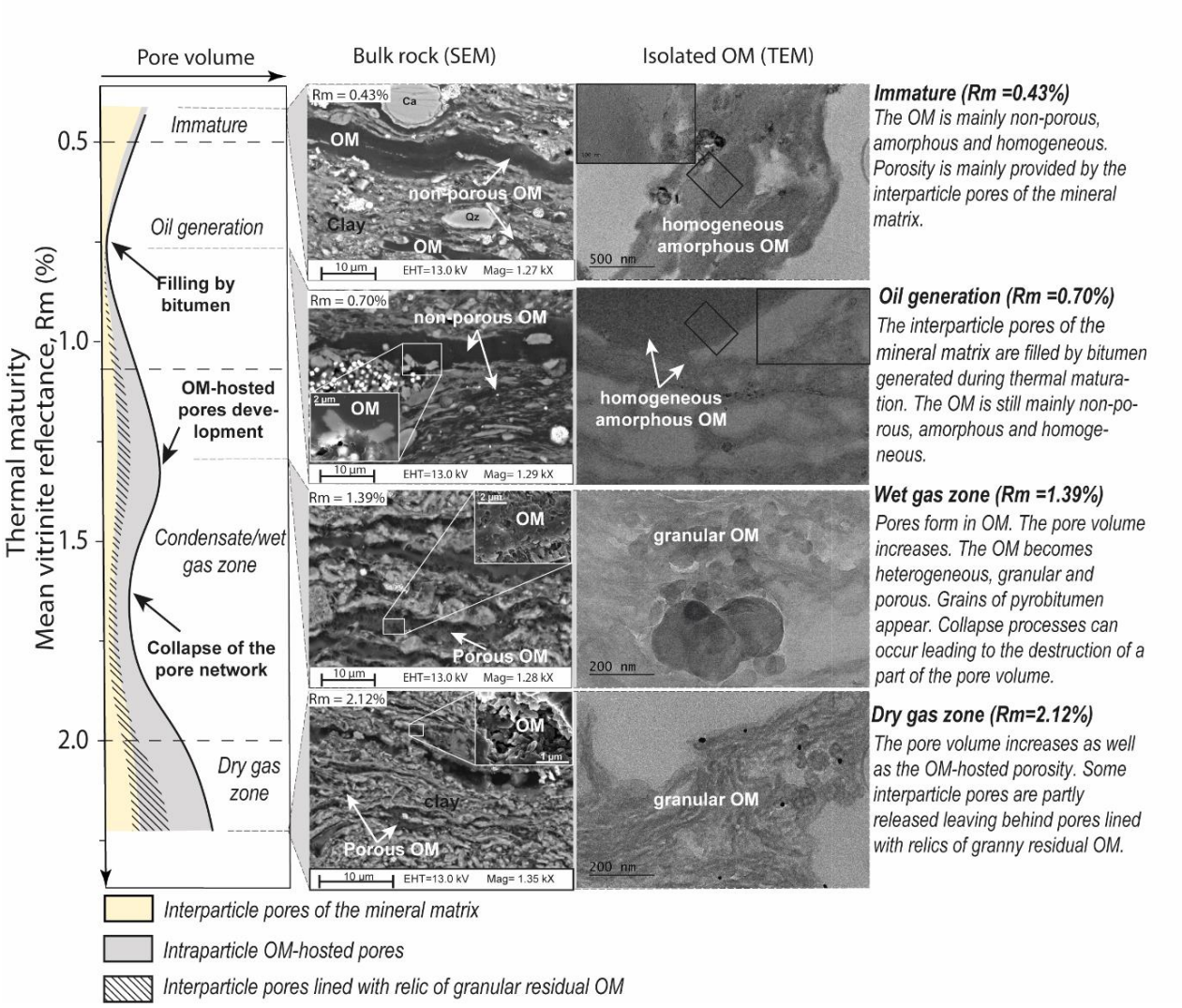

Fig. 8.1. Summary of the main observations made on the pore volume, the total rock framework (SEM images, backscattered electron) and the isolated OM structure (TEM) of KCF mudstones with increasing thermal maturity.

According to the hypothesis from (Keel, 2015), the creation of pores in OM thus seems linked with the progressive organization of the residual kerogen structure. Furthermore, the high porosity of OM (up to ≈20%) indicates that OM can indeed be a significant contributor to the porosity and the gas storage capacity of shale reservoirs.

In controlling the different steps at which bitumen and gas are generated and the progressive aromatization and evolution of the residual OM structure, thermal degradation processes are indeed the main factor controlling the porosity of these organic-rich marine claystones. However, the comparison of the evolution of porosity between KCF samples

containing various original OM particulate assemblages during artificial thermal maturation showed that simply considering the amount, the oil-prone quality and the maturity of the OM is insufficient to estimate the porosity. Our investigations reveal that during oil generation samples containing higher amounts of phytoplanktonic orange AOM, which appears as ductile thick bituminite particles, generated higher amounts of saturated and aromatic hydrocarbons, richer in lighter components. This leads to a better and more complete impregnation of the mineral matrix by bitumen forming a well-interconnected but ductile OM network (Fig.8.2). Then, the more efficient conversion of this OM network into hydrocarbon gases enabled the formation of a well-developed but more vulnerable OM porosity, which seems to be more easily and repeatedly altered by collapsing processes during gas generation (Fig.8.2). Hence, contrary to what is generally accepted in the literature (Katz and Arango, 2018), these results show that the ability of the studied mudstones to preserve pores strongly decreases with the increase in the amount of hydrocarbon gases generated during maturation and thus, with the original OM oil generation potential. Chen et al. (2015) suggested that a type I kerogen has about 40 times more potential for pore development than a type III and that the ability of kerogen to develop an OM-hosted porosity strongly depends on its oil-proneness. Even if the pore volume formed in rocks during maturation is dependent on the OM content (which hosts most of the porosity) and its oil and gas generation potential (which influences the ability of the OM to develop pores) our results reveal, however, that this relation is not straightforward. It is true that inertinite fragments do not exhibit any pore development during thermal maturation, suggesting that less oil-prone type III organic components have indeed a low ability to develop pores. Nevertheless, our investigations on a type II kerogen indicate that the distribution in the mineral matrix, the shape of the different macerals and their ability to form a well-connected and ductile (or brittle depending on the maturity) OM network can strongly influence the ability of the rock to preserve these pores from collapsing and compaction process (Fig.8.2). Consequently, no direct positive linear correlation exists between porosity, TOC and the OM oil-generation potential. That is probably the reason why so many different trends are observed in natural gas shale systems or even within the same formation (Katz and Arango, 2018) where the OM original composition is often heterogeneous. Our study reveals that these variations may indeed lead to different development, evolution and preservation of the OM porosity during maturation. This may locally mask the effect of thermal maturity and could explain why TOC is sometimes considered as the main factor controlling porosity as in the Marcellus (Milliken et al., 2013) or the Lower Yangtze region (Pan et al., 2015) and why the effect of thermal maturation processes

are not systematically clearly observed (Schieber, 2010; Curtis et al., 2012; Fishman et al., 2012; Milliken et al., 2013; Pan et al., 2015; Löhr et al., 2015; Guo et al., 2018; Ko et al., 2018).

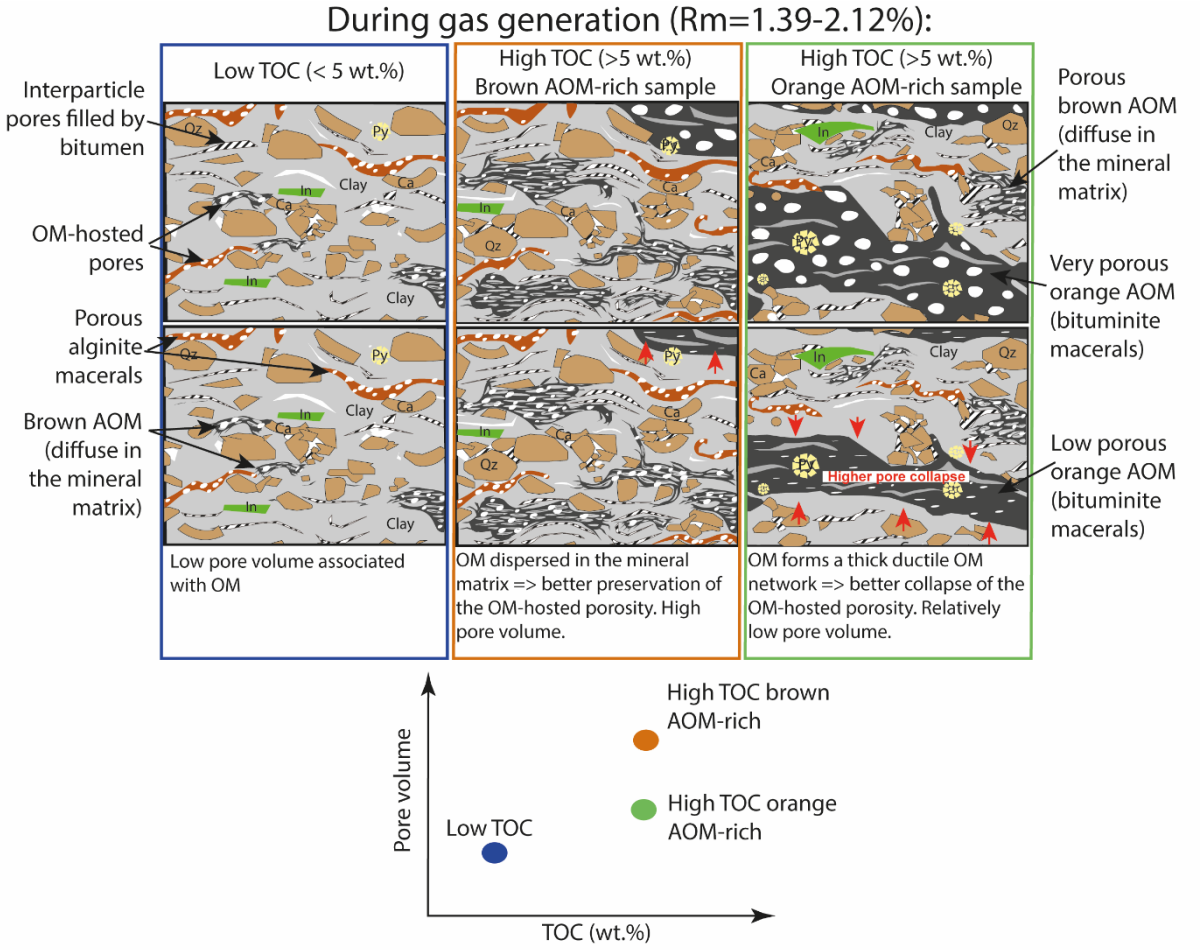

Fig. 8.2. Main differences observed between artificially matured KCF samples as a function of TOC and OM composition during gas generation. In light grey: clay minerals. In: inertinite fragments. Py: pyrite framboids.

Furthermore, the similar trends existing between TOC and the pore volume in our artificially matured KCF samples in the condensate wet gas zone (Fig.5.20A), in natural gas-matured samples from the VMF (Fig.4.16E), in the Marcellus (Milliken et al., 2013) or the Lower Yangtze region (Pan et al., 2015) suggest that the processes highlighted in this work are likely at play in various natural formations.

While the differences observed between samples appear mainly due to differential compaction phenomena tied with the original maceral composition and the OM distribution in rock, the effect of the OM composition on the evolution of the isolated kerogen structure was not investigated. The work on the isolated OM has only been applied to a single sample through different degrees of thermal maturity and deserves, therefore, further investigations. In

particular, it could be interesting to see whether the differences in the original OM particulate assemblage can influence the variation of the kerogen structure at the nanoscopic scale and thus the total porosity of mudstones. This could help us to know whether differences in the internal structure of the OM contribute to the differences in porosity observed between samples with various OM particulate assemblages during thermal maturation. Multiplying the observations on the isolated OM of various original compositions and maturity could therefore be of paramount importance.

Although the OM accounts for less than 15 wt.% of the total KCF rocks, which are dominated by minerals, these results show that the initial OM composition and transformations during thermal maturation are crucial factors controlling the ability of marine mudstones to develop and to preserve pores. This is especially true for these organic-rich claystones (> 50 wt.% of clay minerals), where most of the interparticle pores associated with this relatively ductile mineral matrix are quickly reduced by compaction or filled by entrapped bitumen in the early stages of thermal maturation. In this case OM thus rapidly becomes the main contributor to the porosity and the OM original content, maturity and oil-proneness become important controlling factors. While some interparticle pores of the mineral matrix are also released in the form of conversion or modified mineral pores lined with relics of residual OM, the formation of these pores closely depends on the OM conversion rate and thus on the OM composition and thermal maturity. These pores cannot be considered as OM-hosted pores but their abundance and features are thus also tied with the OM properties. This trend may however be very different in rocks containing more abundant rigid mineral grains such as quartz, carbonates or feldspaths, where a greater proportion of interparticle pores are associated with the mineral matrix. In this case the contribution of the OM and its properties are likely less important. Increasing the number of thermal maturation experiments on rocks containing different mineralogical and organic assemblages remains thus now essential to better identify the extent of the impact that these variations can have on the evolution of the global porosity of these organic-matter rich shales. This should also contribute to a better identification of the key parameters required to establish pore evolution models that would better reflect the complexity of natural shale gas systems.

While a perfect experimental simulation of OM thermal maturation processes is not achievable, the similarities existing between our artificially matured samples, the natural oil-mature and gas-mature samples and natural trends from the available literature (similar biomarker ratios, similar concentrations and composition of bitumen and gas, similar variations

of the OM porosity and surface texture…), indicate that anhydrous confined experiments give relatively comparable results to those obtained from natural conditions. We can thus suggest that our results can be applied to natural gas shale systems. This is well substantiated by the similar relation observed between the pore volume and TOC in artificially matured KCF samples (390°/72 hours) and the gas-mature samples from the VMF (Fig.4.16E, Fig.5.20A). However, the results from the longer thermal maturation experiments suggest that the lower temperature and the longer duration time allowed for the OM degradation processes in natural sedimentary basins lead to a more progressive and more efficient conversion of the OM. This seems to strengthen the differences in pore volume existing between samples with different OM compositions. For example, this may lead to a greater loss of pore volume for the orange AOM-rich sample by collapsing and compaction processes under natural sedimentary basin conditions rather than during the experimental simulations. Furthermore**,** the only slight variations in the mineralogical composition and the structure of clay minerals during artificial thermal maturation measured by XRD and observed in SEM, show that the very short durations of the experiments are incapable of simulating properly the clay diagenetic transformation that occurs during burial. However, the physical processes and the chemical alteration of the inorganic phase such as the conversion of smectite into increasingly well-ordered illite layers or the possible precipitation of cements, may also greatly influence the development and especially the preservation of pores during maturation. A comparison of these results with natural equivalents of similar but also various mineralogy and OM composition and/or longer duration laboratory experiments remains therefore essential to better understand the exact role of the OM content and particulate assemblage and the influence of the thermal maturation kinetic on the simulated OM thermal degradation processes and pore development.

Conclusions

Conclusions

To investigate how the geochemical composition of the organic matter (OM) and its thermal degradation processes influence the development and the evolution of the porosity of organic-rich source rocks during thermal maturation, organic-rich marine mudstones from the Kimmeridge Clay formation were artificially matured using different duration-temperature pairs. The concomitant variations of the bulk, the molecular OM composition and the porosity were assessed by a combination of different petrographical and geochemical techniques. These results were compared with natural oil-mature rocks from the Viking graben and gas-mature samples from the Vaca Muerta formation. The main following conclusions can be drowned:

The OM thermal degradation processes play a complex but major role in the development of pores in organic-rich source rocks. In controlling the progressive reorganization of the residual OM structure and the concomitant production of oil and gas, thermal maturation processes are responsible for significant variations of the OM-hosted porosity, which is the main contributor to the porosity of the studied samples. The onset of the OM-hosted pore development starts during the peak of oil generation (Rc≈0.88%) and continue during gas generation interrupted by collapse processes.

Nevertheless, this study reveals that slight differences of the OM composition between the studied samples have strongly influenced the ability of the rock to form and preserve pores from compaction leading to different pore evolution models during maturation. Hence, contrary to what is generally accepted in the literature, these results show that the ability of the studied mudstones to preserve pores strongly decreases with the increase of the amount of the hydrocarbons gases generated during maturation and thus, with the original OM oil generation potential. These variations seem closely tied with the stronger framework compaction that have occurred in orange amorphous OM-rich samples facilitated by the presence of a more continuous ductile or brittle framework formed by the thick laminar shape of amorphous OM and the greater volume lost during the expulsion of a greater amount of hydrocarbons generated during gas generation. This result show that the shape, the size and the distribution of the maceral types in mudstones can also play an important role on organic-rich mudstones pore development.

Finally, comparison between the two series of laboratory thermal maturation using different temperature-duration pairs show that the increase of the duration of the experiments

lead to the formation of bitumen enriched in lighter saturated and aromatic components and higher amount of gas. These factors have however a very limited influence on pores development. These results, compared with natural samples, show that the influence of the kinetic of thermal degradation processes on porosity are very weak. We can assume that our results should thus be applied to natural gas shale systems.

References

References

Alcantar-Lopez L. (2016) Understanding organic matter structural changes with increasing thermal maturity from oil shale plays through SEM imaging. In *Unconventional Resources Technology Conference, San Antonio, Texas, 1-3 August 2016* Society of Exploration Geophysicists, American Association of Petroleum …. pp. 1372–1389.

Alfè M., Apicella B., Barbella R., Rouzaud J.-N., Tregrossi A. and Ciajolo A. (2009) Structure–property relationship in nanostructures of young and mature soot in premixed flames. *Proceedings of the Combustion Institute* **32**, 697–704.

Ardakani O. H., Sanei H., Ghanizadeh A., Lavoie D., Chen Z. and Clarkson C. R. (2018) Do all fractions of organic matter contribute equally in shale porosity? A case study from Upper Ordovician Utica Shale, southern Quebec, Canada. *Marine and Petroleum Geology* **92**, 794–808.

Barrett E. P., Joyner L. G. and Halenda P. P. (1951) The determination of pore volume and area distributions in porous substances. I. Computations from nitrogen isotherms. *Journal of the American Chemical society* **73**, 373–380.

Behar F., Kressmann S., Rudkiewicz J. L. and Vandenbroucke M. (1992) Experimental simulation in a confined system and kinetic modelling of kerogen and oil cracking. *Organic Geochemistry* **19**, 173–189.

Behar F., Lewan M. D., Lorant F. and Vandenbroucke M. (2003) Comparison of artificial maturation of lignite in hydrous and nonhydrous conditions. *Organic Geochemistry* **34**, 575–600.

Behar F., Lorant F. and Lewan M. (2008) Role of NSO compounds during primary cracking of a Type II kerogen and a Type III lignite. *Organic Geochemistry* **39**, 1–22.

Behar F., Roy S. and Jarvie D. (2010) Artificial maturation of a Type I kerogen in closed system: Mass balance and kinetic modelling. *Organic Geochemistry* **41**, 1235–1247.

Behar F. and Vandenbroucke M. (1987) Chemical modelling of kerogens. *Organic Geochemistry* **11**, 15–24.

Behar F., Vandenbroucke M., Tang Y., Marquis F. and Espitalié J. (1997) Thermal cracking of kerogen in open and closed systems: determination of kinetic parameters and stoichiometric coefficients for oil and gas generation. *Organic Geochemistry* **26**, 321–339.

Bernard S., Horsfield B., Schulz H.-M., Wirth R., Schreiber A. and Sherwood N. (2012a) Geochemical evolution of organic-rich shales with increasing maturity: A STXM and TEM study of the Posidonia Shale (Lower Toarcian, northern Germany). *Marine and Petroleum Geology* **31**, 70–89.

Bernard S., Wirth R., Schreiber A., Schulz H.-M. and Horsfield B. (2012b) Formation of nanoporous pyrobitumen residues during maturation of the Barnett Shale (Fort Worth Basin). *International Journal of Coal Geology* **103**, 3–11.

Bertrand P., Bordenave M. L., Brosse E., Espitalié J., Houzay J. P., Pradier B., Vandenbroucke M. and Walgenwitz F. (1993) Other methods and tools for source rock appraisal. In *Applied Petroleum geochemistry* Bordenave M.L. pp. 279–371.

Beyssac O., Goffé B., Chopin C. and Rouzaud J. N. (2002) Raman spectra of carbonaceous material in metasediments: a new geothermometer: RAMAN SPECTROSCOPY OF CARBONACEOUS MATERIAL. *Journal of Metamorphic Geology* **20**, 859–871.

Bishop K. (2015) Mechanical stratigraphy of the Vaca Muerta Formation, Neuquen Basin, Argentina. Doctoral dissertation, Colorado School of Mines.

Boreham C. J., Crick I. H. and Powell T. G. (1988) Alternative calibration of the Methylphenanthrene Index against vitrinite reflectance: Application to maturity measurements on oils and sediments. *Organic Geochemistry* **12**, 289–294.

Boulmier J. L., Oberlin A., Rouzaud J. N. and Villey M. (1982) NATURAL ORGANIC MATTERS AND CARBONACEOUS MATERIALS-A PREFERENTIAL FIELD OF APPLICATION FOR TRANSMISSION ELECTRON-MICROSCOPY. *Scanning electron microscopy*, 1523–1538.

Bourbonniere R. A. and Meyers P. A. (1996) Sedimentary geolipid records of historical changes in the watersheds and productivities of Lakes Ontario and Erie. *Limnology and Oceanography* **41**.

Boussafir M. (1994) Microtexture et structure ultrafine des roches et matières organiques pétroligènes : nature et fossilisation de la matière organique dans les séries organo-sédimentaires cycliques du Kimméridgien d'Angleterre. Université d'Orléans.

Boussafir M., Gelin F., Lallier-Vergès E., Derenne S., Bertrand P. and Largeau C. (1995a) Electron microscopy and pyrolysis of kerogens from the Kimmeridge Clay Formation, UK: source organisms, preservation processes, and origin of microcycles. *Geochimica et Cosmochimica Acta* **59**, 3731–3747.

Boussafir M. and Lallier-Vergès E. (1997) Accumulation of organic matter in the Kimmeridge Clay Formation (KCF): an update fossilisation model for marine petroleum source-rocks. *Marine and Petroleum Geology* **14**, 75–83.

Boussafir M., Lallier-Vergès E., Bertrand P. and Badaut-Trauth D. (1995b) SEM and TEM studies on isolated organic matter and rock microfacies from a short-term organic cycle of the Kimmeridge Clay Formation (Yorkshire, GB). In *Organic Matter Accumulation* Berlin, Heidelberg. pp. 15–30.

Brassell S. C., Eglinton G. and Mo F. J. (1986) Biological marker compounds as indicators of the depositional history of the Maoming oil shale. *Organic Geochemistry* **10**, 927–941.

Brunauer S., Emmett P. H. and Teller E. (1938) Adsorption of Gases in Multimolecular Layers. *J. Am. Chem. Soc.* **60**, 309–319.

Bustin R. M., Bustin A., Ross D. J. K., Chalmers G. R. L., Murthy V., Laxmi C. and Cui X. (2009) Shale gas opportunities and challenges. In American Association of Petroleum Geologists Annual Convention,. San Antonio, TX.

Cardott B. J., Landis C. R. and Curtis M. E. (2015) Post-oil solid bitumen network in the Woodford Shale, USA — A potential primary migration pathway. *International Journal of Coal Geology* **139**, 106–113.

Cavelan A., Boussafir M., Le Milbeau C., Rozenbaum O. and Laggoun-Défarge F. (2019a) Effect of organic matter composition on source rock porosity during confined anhydrous thermal maturation: Example of Kimmeridge-clay mudstones. *International Journal of Coal Geology* **212**.

Cavelan A., Boussafir M., Rozenbaum O. and Laggoun-Défarge F. (2019b) Organic petrography and pore structure characterization of low-mature and gas-mature marine organic-rich mudstones: Insights into porosity controls in gas shale systems. *Marine and Petroleum Geology* **103**, 331–350.

Chakhmakhchev A., Suzuki M. and Takayama K. (1997) Distribution of alkylated dibenzothiophenes in petroleum as a tool for maturity assessments. *Organic Geochemistry* **26**, 483–489.

Chalmers G. R., Bustin R. M. and Power I. M. (2012) Characterization of gas shale pore systems by porosimetry, pycnometry, surface area, and field emission scanning electron microscopy/transmission electron microscopy image analyses: Examples from the Barnett, Woodford, Haynesville, Marcellus, and Doig units. *AAPG Bulletin* **96**, 1099–1119.

Chalmers G. R. L. and Bustin R. M. (2017) A multidisciplinary approach in determining the maceral (kerogen type) and mineralogical composition of Upper Cretaceous Eagle Ford Formation: Impact on pore development and pore size distribution. *International Journal of Coal Geology* **171**, 93–110.

Chalmers G. R. L. and Bustin R. M. (2008) Lower Cretaceous gas shales in northeastern British Columbia, Part I: geological controls on methane sorption capacity. *Bulletin of Canadian Petroleum Geology* **56**, 1–21.

Charpentier D., Worden R. H., Dillon C. G. and Aplin A. C. (2003) Fabric development and the smectite to illite transition in Gulf ofMexico mudstones: an image analysis approach. *Journal of Geochemical Exploration* **78–79**, 459–463.

Chen J. and Xiao X. (2014) Evolution of nanoporosity in organic-rich shales during thermal maturation. *Fuel* **129**, 173–181.

Chen Z., Wang T., Liu Q., Zhang S. and Zhang L. (2015) Quantitative evaluation of potential organic-matter porosity and hydrocarbon generation and expulsion from mudstone in continental lake basins: A case study of Dongying sag, eastern China. *Marine and Petroleum Geology* **66**, 906–924.

Cheshire S., Craddock P. R., Xu G., Sauerer B., Pomerantz A. E., McCormick D. and Abdallah W. (2017) Assessing thermal maturity beyond the reaches of vitrinite reflectance and Rock-Eval pyrolysis: A case study from the Silurian Qusaiba formation. *International Journal of Coal Geology* **180**, 29–45.

Clarkson C. R., Freeman M., He L., Agamalian M., Melnichenko Y. B., Mastalerz M., Bustin R. M., Radliński A. P. and Blach T. P. (2012) Characterization of tight gas reservoir pore structure using USANS/SANS and gas adsorption analysis. *Fuel* **95**, 371–385.

Clarkson C. R., Solano N., Bustin R. M., Bustin A. M. M., Chalmers G. R. L., He L., Melnichenko Y. B., Radliński A. P. and Blach T. P. (2013) Pore structure characterization of North American shale gas reservoirs using USANS/SANS, gas adsorption, and mercury intrusion. *Fuel* **103**, 606–616.

Cohaut N., Blanche C., Dumas D., Guet J. M. and Rouzaud J. N. (2000) A small angle X-ray scattering study on the porosity of anthracites. *Carbon* **38**, 1391–1400.

Combaz A. (1980) Les kérogènes vus au microscope. In *Kerogen* Paris. pp. 55–11.

Comisky J. T., Santiago M., McCollom B., Buddhala A. and Newsham K. E. (2011) Sample Size Effects on the Application of Mercury Injection Capillary Pressure for Determining the Storage Capacity of Tight Gas and Oil Shales. In Canadian Unconventional Resources Conference. Society of Petroleum Engineers.

Cooper B. S., Bernard P. C. and Telnaes N. (1995) The Kimmeridge Clay formation of the North Sea. In *Petroleum Source Rocks* Katz, B.J. (Ed.),. pp. 89–110.

Cornford C. (1984) Source rocks and hydrocarbons of the North Sea. In: Glennie, K.W. (Ed.), Introduction to the Petroleum Geology of the North Sea. *Blackwell Scientific Publications, Oxford*, 171–209.

Cox B. M. and Gallois R. W. (1981) The stratigraphy of the Kimmeridge Clay of the Dorset type area and its correlation with some other Kimmeridgian sequences. *Republic Institute of Geological Sciences.* **80**, 44.

Curiale J. A. (1986) Origin of solid bitumens, with emphasis on biological marker results. *Organic Geochemistry* **10**, 559–580.

Curtis M. E., Cardott B. J., Sondergeld C. H. and Rai C. S. (2012) Development of organic porosity in the Woodford Shale with increasing thermal maturity. *International Journal of Coal Geology* **103**, 26–31.

Day-Stirrat R. J., Aplin A. C., Środoń J. and Pluijm B. A. V. der (2008) DIAGENETIC REORIENTATION OF PHYLLOSILICATE MINERALS IN PALEOGENE

MUDSTONES OF THE PODHALE BASIN, SOUTHERN POLAND. *Clays and Clay Minerals* **56**, 100–111.

De Boer J. H., Lippens B. C., Linsen B. G., Broekhoff J. C. P., Van den Heuvel A. and Osinga T. J. (1966) Thet-curve of multimolecular N2-adsorption. *Journal of Colloid and Interface Science* **21**, 405–414.

Dembicki Jr. Harry (2017) Chapter 2 - The Formation of Petroleum Accumulations. In *Practical Petroleum Geochemistry for Exploration and Production* (ed. Jr. Dembicki Harry). Elsevier. pp. 19–60.

Desprairies A., Bachaoui M., Ramdani A. and Tribovillard N. (1995) Clay diagenesis in organic-rich cycles from the Kimmeridge Clay Formation of Yorshire (G.B.): implication for palaeoclimatic interpretations. In *Organic Matter Accumulation* Springer Berlin Heidelberg, Berlin, Heidelberg. pp. 63–91. Available at: http://www.springerlink.com/index/10.1007/BFb0117668 [Accessed April 8, 2019].

Disnar J. R. and Ramanampisoa L. (1995) Palaeoproduction control on anoxia and organic matter preservation and accumulation in the Kimmeridge Clay Formation of Yorkshire (GB): molecular assessment. In *Organic Matter Accumulation* Berlin Heidelberg. pp. 49–62.

DiStefano V. H., McFarlane J., Anovitz L. M., Stack A. G., Gordon A. D., Littrell K. C., Chipera S. J., Hunt R. D., Lewis S. A., Hale R. E. and Perfect E. (2016) Extraction of organic compounds from representative shales and the effect on porosity. *Journal of Natural Gas Science and Engineering* **35**, 646–660.

Dow W. G. (1977) Journal of Geochemical Exploration. *Kerogen studies and geological interpretations* **7**, 79–99.

Drouin S. (2007) Rôle des argiles dans la préservation et la fossilisation de la Matière Organique. Université d'Orléans.

Dubinin M. M. (1966) *Chemistry and Physics of Carbon*. Marcel Dekker,., P.L. Walker, New York.

Dubinin M. M. (1947) Sorbtsiya I Struktura Aktivnykh Uglei 1. Issledovanie Adsorbtsii Organicheskikh Parov. *Zhurnal Fizicheskoi Khimii* **21**, 1351–1362.

EIA (2015) Energy Information Administration. Technically recoverable shale oil and shale gas resources: Argentina. *Tech. Rep. September.*

Espitalié J., Deroo G. and Marquis F. (1985a) ROCK-EVAL PYROLYSIS AND ITS APPLICATION. 2. *Revue De L Institut Francais Du Petrole* **40**, 755–784.

Espitalié J., Deroo G. and Marquis F. (1985b) Rock-Eval pyrolysis and its applications. *Revue De L Institut Francais Du Petrole* **40**, 563–579.

Ferrari A. C. and Robertson J. (2000) Interpretation of Raman spectra of disordered and amorphous carbon. *Phys. Rev. B* **61**, 14095–14107.

Ficken K. J., Li B., Swain D. L. and Eglinton G. (2000) An n-alkane proxy for the sedimentary input of submerged/ ¯oating freshwater aquatic macrophytes. *Organic Geochemistry* **31**, 745–749.

Field J. D. (1985) Organic geochemistry in exploration of the northern North Sea. In *Petroleum geochemistry in exploration of the Norwegian Shelf* Dordrecht. pp. 39–57.

Fisher A. T. and Underwood M. B. (1995) 3. Calibration of an X-ray diffraction method to determine relative mineral abundances in bulk powders using matrix singular value decomposition: a test from the barbados accretionary complex. In *Proceedings of the Ocean Drilling Program, 156 Initial Reports* Proceedings of the Ocean Drilling Program. Ocean Drilling Program.

Fishman N. S., Hackley P. C., Lowers H. A., Hill R. J., Egenhoff S. O., Eberl D. D. and Blum A. E. (2012) The nature of porosity in organic-rich mudstones of the Upper Jurassic

Kimmeridge Clay Formation, North Sea, offshore United Kingdom. *International Journal of Coal Geology* **103**, 32–50.

Furmann A., Mastalerz M., Bish D., Schimmelmann A. and Pedersen P. K. (2016) Porosity and pore size distribution in mudrocks from the Belle Fourche and Second White Specks Formations in Alberta, Canada. *Bulletin* **100**, 1265–1288.

Gallois R. (2004) The Kimmeridge Clay: the most intensively studied formation in Britain. *Journal Open University Geological Society* **25**, 33–38.

Garcia M. N., Sorenson F., Bonapace J. C., Motta F., Bajuk C. and Stockman H. (2013) Vaca Muerta Shale Reservoir Characterization and Description: The Starting Point for Development of a Shale Play with Very Good Possibilities for a Successful Project. In Unconventional Resources Technology Conference. Society of Exploration Geophysicists, American Association of Petroleum Geologists, Society of Petroleum Engineers., Denver, Colorado. pp. 863-899).

Gautier D. L. (2005) *Kimmeridgian Shales Total Petroleum System of the North Sea Graben Province.*, Reston, Virgnia.

Goff J. C. (1983) Hydrocarbon generation and migration from Jurassic source rock in East Shetland Basin and Viking Graben of the northern North Sea. *Journal of Geological Society of London* **140**, 445–474.

van Graas G. W. (1990) Biomarker maturity parameters for high maturities: Calibration of the working range up to the oil/condensate threshold. *Organic Geochemistry* **16**, 1025–1032.

Guo H., He R., Jia W., Peng P., Lei Y., Luo X., Wang X., Zhang L. and Jiang C. (2018) Pore characteristics of lacustrine shale within the oil window in the Upper Triassic Yanchang Formation, southeastern Ordos Basin, China. *Marine and Petroleum Geology* **91**, 279–296.

Guo H., Jia W., Peng P., Zeng J. and He R. (2017) Evolution of organic matter and nanometer-scale pores in an artificially matured shale undergoing two distinct types of pyrolysis: A study of the Yanchang Shale with Type II kerogen. *Organic Geochemistry* **105**, 56–66.

Hackley P. C. (2017) Application of Organic Petrology in High Maturity Shale Gas Systems. In *Geology: Current and Future Developments: The Role of Organic Petrology in the Exploration of Conventional and Unconventional Hydrocarbon Systems* sabel Suárez-Ruiz and João Graciano Mendonça Filho, Sharjah, UAE. pp. 205–235.

Hackley P. C. and Cardott B. J. (2016) Application of organic petrography in North American shale petroleum systems: A review. *International Journal of Coal Geology* **163**, 8–51.

Hackley P. C., Zhang L. and Zhang T. (2017) Organic petrology of peak oil maturity Triassic Yanchang Formation lacustrine mudrocks, Ordos Basin, China. *Interpretation* **5**, SF211–SF223.

Han Y., Horsfield B., Wirth R., Mahlstedt N. and Bernard S. (2017) Oil retention and porosity evolution in organic-rich shales. *Bulletin* **101**, 807–827.

Hedges J. I. and Keil R. G. (1995) Sedimentary organic matter preservation: an assessment and speculative synthesis. *Marine Chemistry* **49**, 81–115.

Herbin J. P., Boreham C., Geyssant J. R., Mélières F. and Penn I. E. (1991) Hétérogénéité quantitative et qualitative de la matiére organique dand les argiles du Kimméridgien du Val de Pickering (Yorkshire, UK): cadre sédimentologique et stratigraphique. *Revue de l'Institut français du pétrole* **46**, 675–712.

Herbin J. P., Fernandez-Martinez J. L., Geyssant J. R., Albani A. El., Deconinck J. F., Proust J. N., Colbeaux J. P. and Vidier J. P. (1995) Sequence stratigraphy of source rocks applied to the study of the Kim meridgian/Tithonian in the north-west European shelf

(Dorset/UK, Yorkshire/UK and Boulonnais/France). *Marine and Petroleum Geology* **12**, 177–194.

Howell J. A., Schwarz E., Spalletti L. A. and Veiga G. D. (2005) The Neuqu6n Basin: an overview. *Geological Society, London, Special Publications* **252**, 1–14.

Hu H., Zhang T., Wiggins-Camacho J. D., Ellis G. S., Lewan M. D. and Zhang X. (2015) Experimental investigation of changes in methane adsorption of bitumen-free Woodford Shale with thermal maturation induced by hydrous pyrolysis. *Marine and Petroleum Geology* **59**, 114–128.

Huang W.-L. (1996) Experimental study of vitrinite maturation: effects of temperature, time, pressure, water, and hydrogen index. *Organic Geochemistry* **24**, 233–241.

Huang W.-Y. and Meinschein W. G. (1979) Sterols as ecological indicators. *Geochimica et Cosmochimica Acta* **43**, 739–745.

Huang Y., Street-Perrott F. A., Perrott R. A., Metzger P. and Eglinton G. (1999) Glacial–interglacial environmental changes inferred from molecular and compound-specific δ13C analyses of sediments from Sacred Lake, Mt. Kenya. *Geochimica et Cosmochimica Acta* **63**, 1383–1404.

Hunt J. M. (1996) *Petroleum Geochemistry and Geology*., W.H. Freeman.

Isaksen G. H. and Ledje K. H. (2001) Source rock quality and hydrocarbon migration pathways within the greater Utsira High area, Viking Graben, Norwegian North Sea. *AAPG Bulletin* **85**.

Jarvie D. M., Hill R. J., Ruble T. E. and Pollastro R. M. (2007) Unconventional shale-gas systems: The Mississippian Barnett Shale of north-central Texas as one model for thermogenic shale-gas assessment. *Bulletin* **91**, 475–499.

Johnson H., Leslie A. B., Wilson C. K., Andrews I. and Cooper R. M. (2005) Middle Jurassic, Upper Jurassic and Lower Cretaceous of the UK central and northern North Sea. *British Geological Survey*.

Ju Y., He J., Chang E. and Zheng L. (2019) Quantification of CH4 adsorption capacity in kerogen-rich reservoir shales: An experimental investigation and molecular dynamic simulation. *Energy* **170**, 411–422.

Juliao T., Suárez-Ruiz I., Marquez R. and Ruiz B. (2015) The role of solid bitumen in the development of porosity in shale oil reservoir rocks of the Upper Cretaceous in Colombia. *International Journal of Coal Geology* **147–148**, 126–144.

Katz B. J. and Arango I. (2018) Organic porosity: A geochemist's view of the current state of understanding. *Organic Geochemistry* **123**, 1–16.

Keel M. B. (2015) Organic Porosity Distribution: A Function of Aromaticity in Organic-Rich Mudrocks. University of Kansas.

Kietzmann D. A., Ambrosio A. L., Suriano J., Alonso M. S., Tomassini F. G., Depine G. and Repol D. (2016) The Vaca Muerta–Quintuco system (Tithonian–Valanginian) in the Neuquén Basin, Argentina: A view from the outcrops in the Chos Malal fold and thrust belt. *AAPG Bulletin* **100**, 743–771.

Kietzmann D. A., Martin-Chivelet J., Palma R. M., López-Gómez J., Lescano M. and Concheyro A. (2011) Evidence of precessional and eccentricity orbital cycles in a Tithonian source rock: the mid-outer carbonate ramp of the Vaca Muerta Formation, Northern Neuquén Basin, Argentina. *AAPG bulletin* **95**, 1459–1474.

Kietzmann D. A., Palma R. M., Riccardi A. C., Martin-Chivelet J. and López-Gómez J. (2014) Sedimentology and sequence stratigraphy of a Tithonian–Valanginian carbonate ramp (Vaca Muerta Formation): a misunderstood exceptional source rock in the Southern Mendoza area of the Neuquén Basin, Argentina. *Sedimentary geology* **302**, 64–86.

Killops S. and Killops V. (2004) *Introduction to Organic Geochemistry*. Blackwell Publishing., Malden, Massachussetts.

King Jr. H. E., Eberle A. P. R., Walters C. C., Kliewer C. E., Ertas D. and Huynh C. (2015) Pore Architecture and Connectivity in Gas Shale. *Energy Fuels* **29**, 1375–1390.

Klaver J., Desbois G., Littke R. and Urai J. L. (2015) BIB-SEM characterization of pore space morphology and distribution in postmature to overmature samples from the Haynesville and Bossier Shales. *Marine and petroleum Geology* **59**, 451–466.

Klaver J., Desbois G., Littke R. and Urai J. L. (2016) BIB-SEM pore characterization of mature and post mature Posidonia Shale samples from the Hils area, Germany. *International Journal of Coal Geology* **158**, 78–89.

Klaver J., Desbois G., Urai J. L. and Littke R. (2012) BIB-SEM study of the pore space morphology in early mature Posidonia Shale from the Hils area, Germany. *International Journal of Coal Geology* **103**, 12–25.

Ko L. T., Loucks R. G., Milliken K. L., Liang Q., Zhang T., Sun X., Hackley P. C., Ruppel S. C. and Peng S. (2017) Controls on pore types and pore-size distribution in the Upper Triassic Yanchang Formation, Ordos Basin, China: Implications for pore-evolution models of lacustrine mudrocks. *Interpretation* **5**, SF127–SF148.

Ko L. T., Loucks R. G., Zhang T., Ruppel S. C. and Shao D. (2016) Pore and pore network evolution of Upper Cretaceous Boquillas (Eagle Ford–equivalent) mudrocks: Results from gold tube pyrolysis experiments. *AAPG Bulletin* **100**, 1693–1722.

Ko L. T., Ruppel S. C., Loucks R. G., Hackley P. C., Zhang T. and Shao D. (2018) Pore-types and pore-network evolution in Upper Devonian-Lower Mississippian Woodford and Mississippian Barnett mudstones: Insights from laboratory thermal maturation and organic petrology. *International Journal of Coal Geology* **190**, 3–28.

Kouketsu Y., Mizukami T., Mori H., Endo S., Aoya M., Hara H., Nakamura D. and Wallis S. (2014) A new approach to develop the Raman carbonaceous material geothermometer for low-grade metamorphism using peak width: Raman CM geothermometer using FWHM. *Island Arc* **23**, 33–50.

Kugler R. L. (1985) Source Rock Characteristics, Los Molles and Vaca Muerta Shales, Neuquen Basin, West-Central Argentina. *AAPG Bulletin* **69**, 276–276.

Kuila U., McCarty D. K., Derkowski A., Fischer T. B., Topór T. and Prasad M. (2014) Nano-scale texture and porosity of organic matter and clay minerals in organic-rich mudrocks. *Fuel* **135**, 359–373.

Kuila U. and Prasad M. (2013) Specific surface area and pore-size distribution in clays and shales: *Specific surface area and pore-size distribution in clays and shales*. *Geophysical Prospecting* **61**, 341–362.

Kuila U. and Prasad M. (2011) Understanding pore-structure and permeability in shales. In *SPE Annual Technical Conference and Exhibition* Society of Petroleum Engineers.

Kuila U., Prasad M., Derkowski A. and McCarty D. K. (2012) Compositional controls on mudrock pore-size distribution: An example from Niobrara Formation. In *SPE Annual Technical Conference and Exhibition* Society of Petroleum Engineers.

Kus J., Araujo C. V., Borrego A. G., Flores D., Hackley P. C., Hámor-Vidó M., Kalaitzidis S., Kommeren C. J., Kwiecińska B., Mastalerz M., Mendonça Filho J. G., Menezes T. R., Misz-Kennan M., Nowak G. J., Petersen H. I., Rallakis D., Suárez-Ruiz I., Sýkorová I. and Životić D. (2017) Identification of alginite and bituminite in rocks other than coal. 2006, 2009, and 2011 round robin exercises of the ICCP Identification of Dispersed Organic Matter Working Group. *International Journal of Coal Geology* **178**, 26–38.

Lafargue E., Espitalié J., Marquis F. and Pillot D. (1998) ROCK-EVAL 6 APPLICATIONS IN HYDROCARBON EXPLORATION, PRODUCTION AND IN SOIL CONTAMINATION STUDIES. , 23.

Lahfid A., Beyssac O., Deville E., Negro F., Chopin C. and Goffé B. (2010) Evolution of the Raman spectrum of carbonaceous material in low-grade metasediments of the Glarus Alps (Switzerland): RSCM in low-grade metasediments. *Terra Nova* **22**, 354–360.

Lallier-Vergès E., Bertrand B. and Tribovillard N. (1995) Short-term organic cyclicities from the Kimmeridge Clay Formation of Yorkshire (G.B.): combined accumulation and degradation of organic carbon under the control of primary production variations | SpringerLink. In *In Organic Matter Accumulation* Berlin, Heidelberg. pp. 3–13.

Landais P. (1991) Assessment of coal potential evolution by experimental simulation of natural coalification. *Organic Geochemistry* **17**, 705–710.

Landais P., Michels R. and Elie M. (1994) Are time and temperature the only constraints to the simulation of organic matter maturation? *Organic Geochemistry* **22**, 617–630.

Landais P. and Monthioux M. (1988) Closed system pyrolysis : an efficient technique for simulating natural coal maturation. *Fuel Processing Technology* **20**, 123–132.

Largeau C., Casadevall E., Kadouri A. and Metzger P. (1984) Formation of Botryococcus-derived kerogens—Comparative study of immature torbanites and of the extent alga Botryococcus braunii. *Organic Geochemistry* **6**, 327–332.

Lazar O. R., Bohacs K. M., Macquaker J. H. S., Schieber J. and Demko T. M. (2015) Capturing Key Attributes of Fine-Grained Sedimentary Rocks In Outcrops, Cores, and Thin Sections: Nomenclature and Description Guidelines. *Journal of Sedimentary Research* **85**, 230–246.

Legarreta L. and Uliana M. A. (1991) Jurassic—Marine Oscillations and Geometry of Back-Arc Basin Fill, Central Argentine Andes. In *Sedimentation, Tectonics and Eustasy* John Wiley & Sons, Ltd. pp. 429–450.

Legarreta L. and Uliana M. A. (1996) The Jurassic succession in west-central Argentina: stratal patterns, sequences and paleogeographic evolution. *Palaeogeography, Palaeoclimatology, Palaeoecology* **120**, 303–330.

Legarreta L. and Villar H. J. (2011) Geological and Geochemical Keys of the Potential Shale Resources, Argentina Basins. In AAPG Geoscience Technology Workshop, "Unconventional Resources: Basics, Challenges, and Opportunities for New Frontier Plays,." Buenos Aires, Argentina.

Legarreta L. and Villar H. J. (2015) The Vaca Muerta Formation (Late Jurassic - Early Cretaceous), Neuquén Basin, Argentina: Sequences, Facies and Source Rock Characteristics. In Unconventional resources technology conference. San Antonio, Texas, USA.

Lejay A., Monkenbusch J., Martinez L., Boitnott G. N., Louis L. and Gelin F. (2018) When the Syn-Depositional Climatic Variations Influence My Source Rock Properties –The Case Study of the Vaca Muerta. In AAPG Annual Convention and Exhibition 2018. Salt Lake City, Utah.

Leu L., Georgiadis A., Blunt M. J., Busch A., Bertier P., Schweinar K., Liebi M., Menzel A. and Ott H. (2016) Multiscale Description of Shale Pore Systems by Scanning SAXS and WAXS Microscopy. *Energy Fuels* **30**, 10282–10297.

Lewan M. D. (1997) Experiments on the role of water in petroleum formation. *Geochimica et Cosmochimica Acta* **61**, 3691–3723.

Lewan M. D. (1993) Laboratory simulation of petroleum formation. In *Organic geochemistry* Boston, MA. pp. 419–442.

Li X., Hayashi J. and Li C. (2006) FT-Raman spectroscopic study of the evolution of char structure during the pyrolysis of a Victorian brown coal. *Fuel* **85**, 1700–1707.

Lin-Vien D., Colthup N. B., Fateley W. G. and Grasselli J. G. (1991) *The handbook of infrared and Raman characteristic frequencies of organic molecules.*, Elsevier.

Liu D., Xiao X., Tian H., Min Y., Zhou Q., Cheng P. and Shen J. (2013) Sample maturation calculated using Raman spectroscopic parameters for solid organics: Methodology and geological applications. *Chin. Sci. Bull.* **58**, 1285–1298.

Liu K., Ostadhassan M., Zhou J., Gentzis T. and Rezaee R. (2017) Nanoscale pore structure characterization of the Bakken shale in the USA. *Fuel* **209**, 567–578.

Liu Y., Xiong Y., Li Y. and Peng P. A. (2018) Effect of thermal maturation on chemical structure and nanomechanical properties of solid bitumen. *Marine and Petroleum Geology* **92**, 780–793.

Löhr S. C., Baruch E. T., Hall P. A. and Kennedy M. J. (2015) Is organic pore development in gas shales influenced by the primary porosity and structure of thermally immature organic matter? *Organic Geochemistry* **87**, 119–132.

Loucks R. G. and Reed R. M. (2014) Scanning-Electron-Microscope petrographic evidence for distinguishing organic-matter pores associated with despositional organic matter versus migrated organic matter in mudrocks. **3**, 51–60.

Loucks R. G., Reed R. M., Ruppel S. C. and Hammes U. (2012) Spectrum of pore types and networks in mudrocks and a descriptive classification for matrix-related mudrock pores. *Bulletin* **96**, 1071–1098.

Loucks R. G., Reed R. M., Ruppel S. C. and Jarvie D. M. (2009) Morphology, Genesis, and Distribution of Nanometer-Scale Pores in Siliceous Mudstones of the Mississippian Barnett Shale. *Journal of Sedimentary Research* **79**, 848–861.

Loucks R. G., Ruppel S. C., Wang X., Ko L., Peng S., Zhang T., Rowe H. D. and Smith P. (2017) Pore types, pore-network analysis, and pore quantification of the lacustrine shale-hydrocarbon system in the Late Triassic Yanchang Formation in the southeastern Ordos Basin, China. *Interpretation* **5**, SF63–SF79.

Mackenzie A. S., Patience R. L., Maxwell J. R., Vandenbroucke M. and Durand B. (1980) Molecular parameters of maturation in the Toarcian shales, Paris Basin, France—I. Changes in the configurations of acyclic isoprenoid alkanes, steranes and triterpanes. *Geochimica et Cosmochimica Acta* **44**, 1709–1721.

Mastalerz M., Schimmelmann A., Drobniak A. and Chen Y. (2013) Porosity of Devonian and Mississippian New Albany Shale across a maturation gradient: Insights from organic petrology, gas adsorption, and mercury intrusion. *AAPG Bulletin* **97**, 1621–1643.

Mastalerz M., Schimmelmann A., Lis G. P., Drobniak A. and Stankiewicz A. (2012) Influence of maceral composition on geochemical characteristics of immature shale kerogen: Insight from density fraction analysis. *International Journal of Coal Geology* **103**, 60–69.

Mathia E. J., Bowen L., Thomas K. M. and Aplin A. C. (2016) Evolution of porosity and pore types in organic-rich, calcareous, Lower Toarcian Posidonia Shale. *Marine and Petroleum Geology* **75**, 117–139.

Mernagh T. P., Cooney R. P. and Johnson R. A. (1984) Raman spectra of Graphon carbon black. *Carbon* **22**, 39–42.

Meyers P. A. (2003) Applications of organic geochemistry to paleolimnological reconstructions: a summary of examples from the Laurentian Great Lakes. *Organic geochemistry* **34**, 261–289.

Michels R., Landais P., Elie M., Gerard L. and Mansuy L. (1992) Evaluation of factors influencing the thermal maturation of organic matter during confined pyrolysis experiments. *ABSTRACTS OF PAPERS OF THE AMERICAN CHEMICAL SOCIETY* **204**, 76.

Michels R., Landais P., Philp R. P. and Torkelson B. E. (1994) Effects of pressure on organic matter maturation during confined pyrolysis of Woodford kerogen. *Energy & fuels* **8**, 741–754.

Michels R., Landais P., Torkelson B. E. and Philp R. P. (1995) Effects of effluents and water pressure on oil generation during confined pyrolysis and high-pressure hydrous pyrolysis. *Geochimica et Cosmochimica Acta* **59**, 1589–1604.

Milliken K. L., Pommer M. and Marsaglia K. M. (2014) SEM petrography of eastern Mediterranean sapropels: Analogue data for assessing organic matter in oil and gas shales. *Journal of Sedimentary Research* **84**, 961–974.

Milliken K. L., Rudnicki M., Awwiller D. N. and Zhang T. (2013) Organic matter-hosted pore system, Marcellus Formation (Devonian), Pennsylvania. *Bulletin* **97**, 177–200.

Mitchum R. M. and Uliana M. A. (1985) Seismic Stratigraphy of Carbonate Depositional Sequences, Upper Jurassic-Lower Cretaceous, Neuquen Basin, Argentina: Chapter 15. *AAPG Special Volumes*, 255–274.

Modica C. J. and Lapierre S. G. (2012) Estimation of kerogen porosity in source rocks as a function of thermal transformation: Example from the Mowry Shale in the Powder River Basin of Wyoming. *Bulletin* **96**, 87–108.

Moldowan J. M., Seifert W. K. and Gallegos E. J. (1985) Relationship between petroleum composition and depositional environment of petroleum source rocks. *AAPG bulletin* **69**, 1255–1268.

Monkenbusch J., Lejay A., Martinez M. and Pälicke H. (2017) ORBITAL FORCING OF ORGANIC MATTER QUALITY AND QUANTITY IN A SOURCE-ROCK FORMATION: THE CASE OF THE VACA MUERTA FORMATION, TITHONIAN-VALANGINIAN, NEUQUÉN BASIN, ARGENTINA. In International Meeting of Sedimentology. Toulouse, France. p. 622.

Monthioux M. (1988) Expected mechanisms in nature and in confined-system pyrolysis. *Fuel* **67**, 843–847.

Monthioux M., Landais P. and Monin J.-C. (1985) Comparison between natural and artificial maturation series of humic coals from the Mahakam delta, Indonesia. *Organic Geochemistry* **8**, 275–292.

Mosquera A., Ramos V. A. and Kay S. M. (2006) Intraplate deformation in the Neuquén Embayment. *SPECIAL PAPERS-GEOLOGICAL SOCIETY OF AMERICA* **407**, 97.

Oberlin A. (1989) High-resolution TEM studies of carbonization and graphitization. *Chemistry and physics of carbon* **22**.

Oschmann W. (1988) Kimmeridge clay sedimentation — A new cyclic model. *Palaeogeography, Palaeoclimatology, Palaeoecology* **65**, 217–251.

Pan C., Geng A., Zhong N., Liu J. and Yu L. (2009) Kerogen pyrolysis in the presence and absence of water and minerals: Amounts and compositions of bitumen and liquid hydrocarbons. *Fuel* **88**, 909–919.

Pan L., Xiao X., Tian H., Zhou Q., Chen J., Li T. and Wei Q. (2015) A preliminary study on the characterization and controlling factors of porosity and pore structure of the Permian shales in Lower Yangtze region, Eastern China. *International Journal of Coal Geology* **146**, 68–78.

Patruno S., Hampson G. J., Jackson C. A.-L. and Dreyer T. (2015) Clinoform geometry, geomorphology, facies character and stratigraphic architecture of a sand-rich subaqueous delta: Jurassic Sognefjord Formation, offshore_Norway. *Sedimentology* **62**, 350–388.

Peters K. E., Walters C. C., Moldowan J. M. and Peters K. E. (2007) *Biomarkers and isotopes in the environment and human history*. 2. ed., reprinted with corrections, digitally printed version 2007., Cambridge Univ. Press, Cambridge, UK.

Pommer M. and Milliken K. L. (2015) Pore types and pore-size distributions across thermal maturity, Eagle Ford Formation, southern Texas. *American Association of Petroleum Geologists Bulletin* **99**, 1713–1744.

Powell J. H. (2010) Jurassic sedimentation in the Cleveland Basin: a review. *Proceedings of the Yorkshire Geological Society* **58**, 21–72.

Quirico E., Rouzaud J.-N., Bonal L. and Montagnac G. (2005) Maturation grade of coals as revealed by Raman spectroscopy: Progress and problems. *Spectrochimica Acta Part A: Molecular and Biomolecular Spectroscopy* **61**, 2368–2377.

Radke M. (1988) Application of aromatic compounds as maturity indicators in source rocks and crude oils. *Marine and Petroleum Geology* **5**, 224–236.

Radke M., Welte D. H. and Willsch H. (1986) Maturity parameters based on aromatic hydrocarbons: Influence of the organic matter type. *Organic Geochemistry* **10**, 51–63.

Ramanampisoa L. and Disnar J. R. (1994) Primary control of paleoproduction on organic matter preservation and accumulation in the Kimmeridge rocks of Yorkshire (UK). *Organic Geochemistry* **21**, 1153–1167.

Rawson P. F. and Riley L. A. (1982) Latest Jurassic - Early Cretaceous Events and the "Late Cimmerian Unconformity" in North Sea Area. *AAPG Bulletin* **66**, 2628–2648.

Rebelo S. L. H., Guedes A., Szefczyk M. E., Pereira A. M., Araújo J. P. and Freire C. (2016) Progress in the Raman spectra analysis of covalently functionalized multiwalled carbon nanotubes: unraveling disorder in graphitic materials. *Phys. Chem. Chem. Phys.* **18**, 12784–12796.

Reed R. M. (2017) Organic-matter pores: new findings from lower-thermal maturity mudrocks. *GCAGS Journal* **6**, 99–110.

Reed R. M., Loucks R. G. and Milliken K. L. (2012) Heterogeneity of shape and microscale spatial distribution in organic-matter-hosted pores of gas shales. In Proceedings AAPG Annual Convention and Exhibition.

Reed R. M., Loucks R. G. and Ruppel S. C. (2014) Comment on "Formation of nanoporous pyrobitumen residues during maturation of the Barnett Shale (Fort Worth Basin)" by Bernard et al. (2012). *International Journal of Coal Geology* **127**, 111–113.

Robert P. (1971) Etude pétrographique des matières organiques insolubles par la mesure de leur pouvoir réflecteur: contribution à l'exploration pétrolière et à la connaissance des bassins sédimentaires. *Rev. Inst. Franç. Pétrole* **26**, 104–135.

Rodriguez R., Crandall D., Song, X., Verba, C. and Soeder D. (2014) *Imaging techniques for analyzing shale pores and minerals.*, National Energy Technology Laboratory, Morgantown, WV, USA.

Romero-Sarmiento M.-F., Ducros M., Carpentier B., Lorant F., Cacas M.-C., Pegaz-Fiornet S., Wolf S., Rohais S. and Moretti I. (2013) Quantitative evaluation of TOC, organic porosity and gas retention distribution in a gas shale play using petroleum system modeling: Application to the Mississippian Barnett Shale. *Marine and Petroleum Geology* **45**, 315–330.

Romero-Sarmiento M.-F., Rouzaud J.-N., Bernard S., Deldicque D., Thomas M. and Littke R. (2014) Evolution of Barnett Shale organic carbon structure and nanostructure with increasing maturation. *Organic Geochemistry* **71**, 7–16.

Ross D. J. K. and Bustin M. R. (2009) The importance of shale composition and pore structure upon gas storage potential of shale gas reservoirs. *Marine and Petroleum Geology* **26**, 916–927.

Rouquerol J., Avnir D., Fairbridge C. W., Everett D. H., Haynes J. M., Pernicone N., Ramsay J. D. F., Sing K. S. W. and Unger K. K. (1994) Recommendations for the characterization of porous solids (Technical Report). *Pure and Applied Chemistry* **66**, 1739–1758.

Rouquerol J., Rouquerol F., Llewellyn P., Maurin P. and Sing K. S. (2013) *Adsorption by powders and porous solids: principles, methodology and applications*. Academic press.,

Rouzaud J. N. and Oberlin A. (1989) Structure, microtexture, and optical properties of anthracene and saccharose-based carbons. *Carbon* **27**, 517–529.

Sadezky A., Muckenhuber H., Grothe H., Niessner R. and Pöschl U. (2005) Raman microspectroscopy of soot and related carbonaceous materials: Spectral analysis and structural information. *Carbon* **43**, 1731–1742.

Sanei H., Wood J. M., Ardakani O. H., Clarkson C. R. and Jiang C. (2015) Characterization of organic matter fractions in an unconventional gas siltstone reservoir. *International Journal of Coal Geology* **150_151**, 296–305.

Sauerer B., Craddock P. R., AlJohani M. D., Alsamadony K. L. and Abdallah W. (2017) Fast and accurate shale maturity determination by Raman spectroscopy measurement with minimal sample preparation. *International Journal of Coal Geology* **173**, 150–157.

Schieber J. (2013) 13 SEM Observations on Ion-milled Samples of Devonian Black Shales from Indiana and New York: The Petrographic Context of Multiple Pore Types. , 153–171.

Schieber J. (2010) Common Themes in the Formation and Preservation of Intrinsic Porosity in Shales and Mudstones – Illustrated with Examples Across the Phanerozoic. In SPE Unconventional Gas Conference. Pittsburgh, Pennsylvania, USA. p. 10.

Schito A., Romano C., Corrado S., Grigo D. and Poe B. (2017) Diagenetic thermal evolution of organic matter by Raman spectroscopy. *Organic Geochemistry* **106**, 57–67.

Schmitt M., Fernandes C. P., da Cunha Neto J. A. B., Wolf F. G. and dos Santos V. S. S. (2013) Characterization of pore systems in seal rocks using Nitrogen Gas Adsorption combined with Mercury Injection Capillary Pressure techniques. *Marine and Petroleum Geology* **39**, 138–149.

Seifert W. R. and Moldowan J. M. (1981) Paleoreconstruction by biological markers. **45**, 783–794.

Sigal R. F. (2009) A methodology for blank and conformance corrections for high pressure mercury porosimetry. *Measurement Science and Technology* **20**.

Sikes E. L., Uhle M. E., Nodder S. D. and Howard M. E. (2009) Sources of organic matter in a coastal marine environment: evidence from n-alkanes and their δ13C distributions in the Hauraki Gulf, New Zealand. *Marine Chemistry* **113**, 149–163.

Sing K. S. (1985) Reporting physisorption data for gas/solid systems with special reference to the determination of surface area and porosity (Recommendations 1984). *Pure and applied chemistry* **57**, 603–619.

Song L., Martin K., Carr T. R. and Ghahfarokhi P. K. (2019) Porosity and storage capacity of Middle Devonian shale: A function of thermal maturity, total organic carbon, and clay content. *Fuel* **241**, 1036–1044.

Stinco L. P. and Barredo S. P. (2014) Vaca Muerta Formation: An example of shale heterogeneities controlling hydrocarbon accumulations. In Unconventional Resources Technology Conference. Society of Exploration Geophysicists, American Association of Petroleum Geologists, Society of Petroleum Engineers., Denver, Colorado. pp. 2854–2868.

Strąpoć D., Mastalerz M., Schimmelmann A., Drobniak A. and Hasenmueller N. R. (2010) Geochemical constraints on the origin and volume of gas in the New Albany Shale (Devonian–Mississippian), eastern Illinois Basin. *Bulletin* **94**, 1713–1740.

Sylwan C. (2014) SOURCE ROCK PROPERTIES OF VACA MUERTA FORMATION, NEUQUINA BASIN, ARGENTINA. In IX Congreso de Exploración y Desarrollo de Hidrocarburos. IAPG, Mendoza, Argentina.

Tannenbaum E. and Kaplan I. R. (1985) Role of minerals in the thermal alteration of organic matter—I: Generation of gases and condensates under dry condition. *Geochimica et Cosmochimica Acta* **49**, 2589–2604.

Tegelaar E. W., de Leeuw J. W., Derenne S. and Largeau C. (1989) A reappraisal of kerogen formation. *Geochimica et Cosmochimica Acta* **53**, 3103–3106.

Teichmüller M. (1989) The genesis of coal from the viewpoint of coal petrology. *International Journal of Coal Geology* **12**, 1–87.

Tian H., Pan L., Xiao X., Wilkins R. W. T., Meng Z. and Huang B. (2013) A preliminary study on the pore characterization of Lower Silurian black shales in the Chuandong Thrust Fold Belt, southwestern China using low pressure N2 adsorption and FE-SEM methods. *Marine and Petroleum Geology* **48**, 8–19.

Tian H., Pan L., Zhang T., Xiao X., Meng Z. and Huang B. (2015) Pore characterization of organic-rich Lower Cambrian shales in Qiannan Depression of Guizhou Province, Southwestern China. *Marine and Petroleum Geology* **62**, 28–43.

Tissot B. (1977) Utilisation des alcanes comme fossiles géochimiques indicateurs des environnements géologiques. *Advance in Organic Geochemistry*.

Tissot B. P., Pelet R. and Ungerer P. (1987) Thermal History of Sedimentary Basins, Maturation Indices, and Kinetics of Oil and Gas Generation. *Bulletin* **71**.

Tissot and Welte D. H. (1984) *Petroleum formation and occurence*. 2. rev. and enl. ed., Springer, Berlin, Heidelberg [usw.].

Tuinstra F. and Koenig J. L. (1970) Raman Spectrum of Graphite. *The Journal of Chemical Physics* **53**, 1126–1130.

Uliana M. A., Legarreta L., Laffitte G. A. and Villar H. J. (1999) Estratigrafía y geoquímica de las facies generadoras de hidrocarburos en las cuencas petrolíferas de Argentina. In Congreso de Exploración y Desarrollo de Hidrocarburos. pp. 1–61.

Vergani G., Arregui C. and Carbone O. (2011) SISTEMAS PETROLEROS Y TIPOS DE ENTRAMPAMIENTOS EN LA CUENCA NEUQUINA. In XVIII CONGRESO GEOLÓGICO ARGENTINO. NEUQUÉN. p. 12.

Wang F., Guan J., Feng W. and Bao L. (2013) Evolution of overmature marine shale porosity and implication to the free gas volume. *Petroleum Exploration and Development* **40**, 819–824.

Wang Y., Liu L., Zheng S., Luo Z., Sheng Y. and Wang X. (2019) Full-scale pore structure and its controlling factors of the Wufeng-Longmaxi shale, southern Sichuan Basin, China: Implications for pore evolution of highly overmature marine shale. *Journal of Natural Gas Science and Engineering* **67**, 134–146.

Wang Y., Zhu Y., Chen S. and Li W. (2014) Characteristics of the Nanoscale Pore Structure in Northwestern Hunan Shale Gas Reservoirs Using Field Emission Scanning Electron Microscopy, High-Pressure Mercury Intrusion, and Gas Adsorption. *Energy & Fuels* **28**, 945–955.

Washburn E. W. (1921) The dynamics of capillary flow. *Physical review* **17**, 273.

Webb P. A. and Orr C. (1997) Analytical methods in fine particle technology: Norcross. *Georgia, Micromeritics Instrument Corporation.*

Wiliams C. J., Hesselbo S. P., Jenkyns H. C. and Morgans-Bell H. S. (2001) Quartz silt in mudrocks as a key to sequence stratigraphy (Kimmeridge Clay Formation, Late Jurassic, Wessex Basin, UK). *Terra Nova* **13**, 449–455.

Wolff G. A., Lamb N. A. and Maxwell J. R. (1986) The origin and fate of 4-methyl steroids—II. Dehydration of stanols and occurrence of c30 4-methyl steranes. *Organic Geochemistry* **10**, 965–974.

Wood D. A. (1988) Relationships between thermal maturity indices calculated using Arrhenius equation and Lopatin method: implications for petroleum exploration. *Assoc. Pet. Geol. Bull.* **72**, 115–134.

Wu S., Zhu R., Cui Jinggang, Cui Jingwei, Bai B., Zhang X., Jin X., Zhu D., You J. and Li X. (2015) Characteristics of lacustrine shale porosity evolution, Triassic Chang 7 Member, Ordos Basin, NW China. *Petroleum Exploration and Development* **42**, 185–195.

Yang F., Ning Z., Wang Q., Zhang R. and Krooss B. M. (2016) Pore structure characteristics of lower Silurian shales in the southern Sichuan Basin, China: Insights to pore development and gas storage mechanism. *International Journal of Coal Geology* **156**, 12–24.

Yang S., Chen G., Lv C., Li C., Yin N., Yang F. and Xue L. (2018) Evolution of nanopore structure in lacustrine organic-rich shales during thermal maturation from hydrous pyrolysis, Minhe Basin, Northwest China. *Energy Exploration & Exploitation* **36**, 265–281.

Zargari S., Canter K. L. and Prasad M. (2015) Porosity evolution in oil-prone source rocks. *Fuel* **153**, 110–117.

Zhang T., Ellis G. S., Ruppel S. C., Milliken K. L., Lewan M. D. and Sun X. (2013) Effect of organic matter properties, clay mineral type and thermal maturity on gas adsorption in organic-rich shale systems. In Unconventional Resources Technology Conference. Society of Exploration Geophysicists, American Association of Petroleum Geologists, Society of Petroleum Engineers. pp. 1996–2001.

Amélie CAVELAN

Rôle de la maturité thermique et des propriétés chimiques de la matière organique sédimentaire dans la structuration du réseau poral d'argilites pétroligènes à gaz

L'objectif de cette thèse était d'étudier l'influence de la composition géochimique, des transformations de la matière organique (MO) et du degré de maturité thermique sur le développement de la porosité d'argilites pétroligènes, dont dépend la capacité de stockage des réservoirs non conventionnels. Ces travaux ont été menés sur des échantillons naturels issus de la « Kimmeridge-Clay- formation » d'Angleterre et de la « Vaca Muerta-formation » en Argentine. Les variations de la composition de la MO et l'augmentation de la maturité thermique ont été caractérisées par différentes méthodes (analyse macérale, palynofaciès, Rock Eval, GC/MS, GC-TCD) et mises en relations avec les variations de porosité observées (MEB, MET) et quantifiées (adsorption de diazote, porosimetry au mercure, SAXS, spectroscopie Raman) au sein de la roche totale et/ou de la MO isolée. Les expériences de maturation, montrent que les processus de dégradation thermique de la MO sont à l'origine de fortes variations de la porosité en lien avec le développement de pores au sein de la MO suite à la production des hydrocarbures et les variations de structure du kérogène et des bitumes à l'échelle nanoscopique. Néanmoins, cette étude révèle que de légères différences de composition de la MO entre les échantillons affectent la capacité de la roche à former et préserver la porosité au cours de la maturation thermique. Ainsi, contrairement à ce qui est admis dans la littérature, la capacité des argilites étudiées à préserver leur volume poral diminue avec la concentration d'hydrocarbures gazeux générés au cours de la maturation et la qualité pétroligène de la MO. Finalement, l'augmentation de la durée des expériences de maturation n'influencent que très peu la dégradation thermique de la MO et le volume poral. La cinétique des réactions de dégradation thermique sont peu influentes. Nos résultats peuvent donc être applicables aux environnements naturels.

Mots clés : roche mère, argilite pétroligène, maturité thermique, porosité, matière organique, schiste à gaz

Role of the chemical properties and the chemical transformations of organic matter with increasing thermal maturity on the development of the porosity of organic-rich shales

This work aimed to investigate how the geochemical composition of the organic matter (OM) and its thermal degradation during artificial maturation influence the development and the evolution of the porosity of organic-rich source rocks which controlled the gas storage capacity of many unconventional reservoirs. This work was carried out on natural mudstones selected from the "Kimmeridge-Clay-formation" (UK) and the "Vaca Muerta-formation" (Argentina). The variations of the OM composition with increasing maturity were assessed by different techniques (maceral and palynofacies analyses, Rock Eval, GC/MS, GC-TCD) and brought into relationship with the variations of the porosity observed (SEM, TEM) and quantified (nitrogen adsorption, mercury intrusion porosimetry, SAXS, Raman spectroscopy) in the bulk rock and/or the isolated OM. Thermal maturation experiments on KCF rocks compared with natural analogues, show that the OM thermal degradation plays a major role in the development of pores. These variations are closely tied with the formation of OM-hosted pores in response to the production of oil and gas and the variation of the residual OM structure at the nanoscopic scale. Nevertheless, this study reveals that differences of the OM composition between samples can influenced the ability of the rock to form and preserve pores from compaction. Hence, contrary to what is accepted in the literature, these results show that the ability of the studied mudstones to preserve pores strongly decreases with the increase of the amount of the hydrocarbons gases generated during maturation and the original oil generation potential of the OM. Finally, the increase of the duration of the experiments lead to variations of the composition of bitumen and gas. These factors have however a very limited influence on the OM thermal degradation and pore development. The influence of the kinetic of thermal degradation processes on porosity are weak. Our results should thus be applied to natural gas shale systems.

Keywords: source rocks, oil-prone mudstones, thermal maturity, porosity, organic matter, gas shale

Earth Sciences Institute of Orléans ISTO

Institut des Sciences de la Terre,
1A rue de la Férollerie 45100 Orléans

UNIVERSITE D'ORLEANS